

Advances in
Geosciences

Volume 9: Solid Earth (SE)
Ocean Science (OS) and Atmospheric Science (AS)



Editor-in-Chief

Wing-Huen Ip

Volume Editor-in-Chief

Yun-Tai Chen

A d v a n c e s i n

Geosciences

Volume 9: Solid Earth (SE)
Ocean Science (OS) and Atmospheric Science (AS)

ADVANCES IN GEOSCIENCES

Editor-in-Chief: Wing-Huen Ip (*National Central University, Taiwan*)

A 5-Volume Set

Volume 1: Solid Earth (SE)
ISBN-10 981-256-985-5

Volume 2: Solar Terrestrial (ST)
ISBN-10 981-256-984-7

Volume 3: Planetary Science (PS)
ISBN-10 981-256-983-9

Volume 4: Hydrological Science (HS)
ISBN-10 981-256-982-0

Volume 5: Oceans and Atmospheres (OA)
ISBN-10 981-256-981-2

A 4-Volume Set

Volume 6: Hydrological Science (HS)
ISBN-13 978-981-270-985-1
ISBN-10 981-270-985-1

Volume 7: Planetary Science (PS)
ISBN-13 978-981-270-986-8
ISBN-10 981-270-986-X

Volume 8: Solar Terrestrial (ST)
ISBN-13 978-981-270-987-5
ISBN-10 981-270-987-8

Volume 9: Solid Earth (SE), Ocean Science (OS) & Atmospheric Science (AS)
ISBN-13 978-981-270-988-2
ISBN-10 981-270-988-6

A d v a n c e s i n
Geosciences

Volume 9: Solid Earth (SE)
Ocean Science (OS) and Atmospheric Science (AS)

Editor-in-Chief

Wing-Huen Ip

National Central University, Taiwan

Volume Editor-in-Chief

Yun-Tai Chen

*Institute of Geophysics,
Chinese Academy of Sciences, China.*



World Scientific

NEW JERSEY • LONDON • SINGAPORE • BEIJING • SHANGHAI • HONG KONG • TAIPEI • CHENNAI

Published by

World Scientific Publishing Co. Pte. Ltd.

5 Toh Tuck Link, Singapore 596224

USA office: 27 Warren Street, Suite 401-402, Hackensack, NJ 07601

UK office: 57 Shelton Street, Covent Garden, London WC2H 9HE

British Library Cataloguing-in-Publication Data

A catalogue record for this book is available from the British Library.

ADVANCES IN GEOSCIENCES

A 4-Volume Set

Volume 9: Solid Earth (SE), Ocean Science (OS) & Atmospheric Science (AS)

Copyright © 2007 by World Scientific Publishing Co. Pte. Ltd.

All rights reserved. This book, or parts thereof, may not be reproduced in any form or by any means, electronic or mechanical, including photocopying, recording or any information storage and retrieval system now known or to be invented, without written permission from the Publisher.

For photocopying of material in this volume, please pay a copying fee through the Copyright Clearance Center, Inc., 222 Rosewood Drive, Danvers, MA 01923, USA. In this case permission to photocopy is not required from the publisher.

ISBN-13 978-981-270-781-9 (Set)

ISBN-10 981-270-781-6 (Set)

ISBN-13 978-981-270-988-2 (Vol. 9)

ISBN-10 981-270-988-6 (Vol. 9)

Typeset by Stallion Press
Email: enquiries@stallionpress.com

Printed in Singapore.

EDITORS

Editor-in-Chief: Wing-Huen Ip

Volume 6: Hydrological Science (HS)

Editor-in-Chief: Namsik Park

Editors: Chunguang Cui
Eiichi Nakakita
Simon Toze
Chulsang Yoo

Volume 7: Planetary Science (PS)

Editor-in-Chief: Anil Bhardwaj

Editors: C. Y. Robert Wu
Francois Leblanc
Paul Hartogh
Yasumasa Kasaba

Volume 8: Solar Terrestrial (ST)

Editor-in-Chief: Marc Duldig

Editors: P. K. Manoharan
Andrew W. Yau
Q.-G. Zong

Volume 9: Solid Earth (SE), Ocean Science (OS) & Atmospheric Science (AS)

Editor-in-Chief: Yun-Tai Chen

Editors: Hyo Choi
Jianping Gan

This page intentionally left blank

CONTENTS

| | |
|---|----|
| Editors | v |
| SOLID EARTH (SE) | 1 |
| Tracking the High-Frequency Energy Radiation Sources of the 2004 Sumatra-Andaman M_w 9.0 Earthquake Using the Short-Period Seismic Data: Preliminary Result | 3 |
| <i>H.-L. Du, L.-S. Xu, Y.-T. Chen, C.-L. Li and K. Stammle</i> | |
| Rupture Process of the 2005 Southern Asian (Pakistan) M_w 7.6 Earthquake from Long-Period Waveform Data | 13 |
| <i>Y. Zhang, Y.-T. Chen and L.-S. Xu</i> | |
| Seismic Characteristics of Strong Deep Focal Earthquakes and Associated Phenomena in Northeastern Asia | 23 |
| <i>J. Wang, X.-S. He and Y.-Q. Li</i> | |
| Moho Depths in the Indian Ocean Based on the Inversion of Satellite Gravity Data | 41 |
| <i>D. N. Arabelos, G. Mantzios and D. Tsoulis</i> | |
| Post Earthquake Debris Management — an Overview | 53 |
| <i>R. Sarkar</i> | |
| OCEAN SCIENCE (OS) | 65 |
| Buried and Surface Polymetallic Nodule Distribution in the Eastern Clarion–Clipperton Zone: Main Distinctions and Similarities | 67 |
| <i>R. Kotlinski and V. Stoyanova</i> | |
| Iron Organic Complexation in the Oligotrophic Subtropical Waters in the Tasman Sea | 75 |
| <i>F. Tian, R. Frew, R. Strzepek and M. Ellwood</i> | |

| | |
|---|-----|
| Coastal Processes with Improved Tidal Opening in Chilika Lagoon (East Coast of India) | 91 |
| <i>G. Jayaraman and A. Dube</i> | |
| ATMOSPHERIC SCIENCE (AS) | 109 |
| Semi-Idealized COAMPS® Simulations of Sumatra Squall Lines: The Role of Boundary Forcing | 111 |
| <i>L. Yi and H. Lim</i> | |
| Sand Dust Weather in Beijing from the Late 19th Century | 125 |
| <i>X. Z. Zhang and X. Fang</i> | |
| Ensemble Projection of Climate Change in East Asia | 135 |
| <i>C.-M. Liu, Y.-C. Chen, S.-F. Chen, S. Paul, S.-H. Lin, Y.-C. Lee, M.-C. Wu, R.-Y. Tzeng, H.-H. Hsu and C.-T. Chen</i> | |
| Atmospheric Deposition of Nutrients and its Role on Coastal Eutrophication in Southeast Asia | 149 |
| <i>S. Palani, R. Balasubramanian, S. Karthikeyan and P. Tkalich</i> | |
| Study of Temporal Variation of Equatorial Tropopause Due to Atmospheric Waves in CPEA Campaign 2004 at Koto Tabang, Indonesia | 167 |
| <i>S. K. Dhaka, R. Bhatnagar, Y. Shibagaki, S. Fukao, T. Kozu, V. Malik, S. Malik and A. Dutta</i> | |
| The Winter Anomaly of the Night-to-Day Ratio of Ozone in the Middle to Upper Mesosphere in Middle Latitudes — A Comparison Between Measurements and Model Calculations | 177 |
| <i>G. R. Sonnemann, P. Hartogh, C. Jarchow, M. Grygalashvily and U. Berger</i> | |
| MM5 Simulated Evolution and Structure of Typhoon Vamei (2001) | 191 |
| <i>F. T. Tangang, L. Juneng and C. J. Reason</i> | |

| | |
|--|-----|
| Influences of Secondary Chemical Gas Processes on PM₁, PM_{2.5} and PM₁₀ Concentrations Over the Korean Coast | 209 |
| <i>H. Choi and M. S. Speer</i> | |
| Seasonal Variation Characteristics of Gradient of Refractivity Over a Humid Region of India | 225 |
| <i>S. Duttagupta</i> | |

This page intentionally left blank

SOLID EARTH (SE)

This page intentionally left blank

TRACKING THE HIGH-FREQUENCY ENERGY RADIATION SOURCES OF THE 2004 SUMATRA-ANDAMAN M_W 9.0 EARTHQUAKE USING THE SHORT-PERIOD SEISMIC DATA: PRELIMINARY RESULT

HAI-LIN DU*, LI-SHENG XU†, YUN-TAI CHEN‡, CHUN-LAI LI
and KLAUS STAMMLER§

*Institute of Geophysics, China Earthquake Administration,
Beijing 100081, China*

*Seismologisches Zentralobservatorium
Mozartstr, 57, 91052 Erlangen, Germany*

*hailin_du@hotmail.com

†txuls@cea-igp.ac.cn

‡chenyt@cea-igp.ac.cn

§klaus@szgrf.bgr.de

Thirty-three stations of short-period seismometers of the Capital Region Digital Seismograph Network, Beijing, China, are organized into an array, and the beam power analysis in time domain is used to track the rupture front of the 2004 Sumatra-Andaman M_W 9.0 earthquake. The analysis indicates that the earthquake has rupture duration time of 440 s and rupture length of at least 1347 km, and that the rupture started at the initiation point, firstly propagated southward about 160 km with an average rupture velocity of 3.71 km/s, then propagated northward about 1200 km with an average rupture velocity of 2.86 km/s. The success of tracking the rupture front of this earthquake at teleseismic distance further extended the application field of seismic array technique.

1. Introduction

A great earthquake occurred off the western coast of northern Sumatra Island at 00:58:53 UTC on December 26, 2004, which generated the most devastating tsunami in recorded history, and eventually resulted in nearly 300,000 fatalities across the Indian Ocean region.¹ The earthquake initiated at 3.3°N, 96.0°E, and at a depth of about 30 km according to the NEIC's determination. The German Regional Seismic Network (GRSN) gave an almost same location for the earthquake, initiating at 3.4°N, 95.8°E.²

There have been many studies on this earthquake. The focal mechanism and magnitude were determined.^{3–5} The rupture length and width were estimated by various approaches.^{1–3,6–8} The duration time was measured by different techniques.^{2,4,6,8} The rupture process was imaged by means of various techniques using different types of data.^{2,7} The rupture velocities were analyzed and discussed by various methods using different datasets.⁸

Among all the works done so far, as mentioned above, two works are more interesting: one done by Kruger and Ohrnberger² and another by Ishii *et al.*⁶ Kruger and Ohrnberger² modified the standard array-seismological approach and processed the broadband recordings of GRSN for tracking the propagating rupture front. Ishii *et al.*⁶ used the Hi-Net seismic array in Japan to map the progression of slip by monitoring the direction of high-frequency radiation. These are for the first time the teleseismic recordings used to track the rupturing trace by means of the array-seismological technique although the similar works had been done in the case of near or local distances.^{9–11} In this paper, we apply the moving-window power beam forming technique in time domain to the short-period seismic recordings of the Capital Region Digital Seismograph Network, Beijing, China, and track the propagating rupture front of the 2004 Sumatra-Andaman $M_W 9.0$ earthquake. Hopefully, it will be helpful for further understanding the kinematical, even dynamic characteristics of the disastrous earthquakes.

2. Data

The Capital Region Digital Seismograph Network (CRDSN) consists of 107 seismic stations, including 59 short-period seismometer stations and 48 broadband seismometer stations. The geometry of the CRDSN is irregular, and the distances between stations vary very much from station to station. To have an array good enough, we choose 33 stations equipped with short-period seismometers and take them as elements of an array as shown in Fig. 1. The station depicted with the bigger triangle was used as the reference station. In this way, the geometry of the array becomes more regular, and the array becomes denser. The aperture of the array is about 200 km. All these instruments have a flat velocity response between 2 Hz and 20 Hz. The distances of the stations from the 2004 Sumatra-Andaman $M_W 9.0$ earthquake is about 40°. At these distances the phases PP, PPP, and other secondarily generated phases should be recorded besides P. However, the frequencies of the later phases should be lower than 2 Hz, as pointed by Ni *et al.*⁸ We selected the recordings of 600 s from the first arrivals to analyze the propagating rupture front.

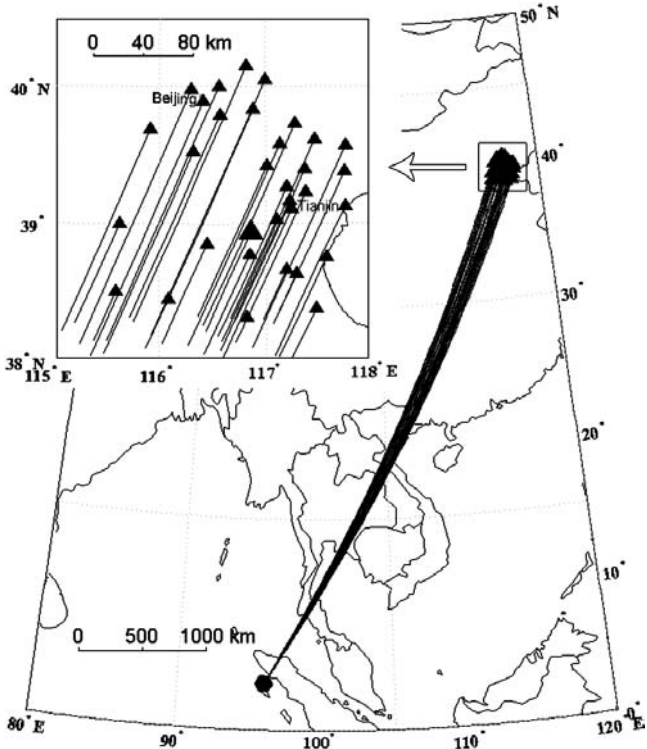


Fig. 1. The epicenter of the 2004 Sumatra-Andaman $M_w 9.0$ earthquake (black hexagon), the locations of the stations of the seismic array (black triangles), and the reference station (the bigger triangle).

3. Method

The method of beam power analysis in time domain is used in this study.¹² Here we have a brief description of this method.

A signal arriving at a reference point within the array with horizontal velocity v_s and a back azimuth θ is described as $s(t)$. The n th seismometer with the location vector \mathbf{r}_n , relative to the array reference point, records the signal $x_n(t)$:

$$x_n(t) = s(t - \mathbf{u}_0 \cdot \mathbf{r}_n) \quad (1)$$

where \mathbf{u}_0 is the horizontal slowness vector with:

$$\mathbf{u}_0 = \frac{1}{v_s}(\cos \theta, \sin \theta) \quad (2)$$

The maximum amplitude of the sum of all the recordings of array seismometers is reached as the signals of all stations are in phase, that is, if the time shifts $\mathbf{u}_0 \cdot \mathbf{r}_n$ disappear. The output of the array can be computed with:

$$y(t) = \frac{1}{N} \sum_{n=1}^N x_n(t + \mathbf{u}_0 \cdot \mathbf{r}_n) \quad (3)$$

for an array of N elements. For signals with different slowness vector \mathbf{u} the beam trace is computed as:

$$y(t) = \frac{1}{N} \sum_{n=1}^N s \{ t + [(\mathbf{u}_0 - \mathbf{u}) \cdot \mathbf{r}_n] \} \quad (4)$$

The total energy recorded at the array can be calculated by the integration of the squared summed amplitudes over time:

$$E(\mathbf{u} - \mathbf{u}_0) = \int_{-\infty}^{\infty} y^2(t) dt \quad (5)$$

Considering Eqs. (4) and (5), the maximum energy will be reached when $\mathbf{u} = \mathbf{u}_0$. In this way, we can have the horizontal slowness of the array reference point.

The relation between slowness and distance is linked with the IASPEI91 earth model.¹³ In this way, the locations from where the energy radiates could be determined. For a large earthquake which has a finite fault, seismic recording could be divided into a number of segments by moving time window. The locations determined using the signals within different time windows form the rupture trace of the whole earthquake.

4. Correction for the Slowness Vectors Using Aftershocks

As is known, the slowness vector determined by the array technique is always biased from the truth because of the geometry of the array and/or the heterogeneity of the medium. It is necessary to make correction for the slowness vector directly determined by the data analysis.

The 2004 Sumatra-Andaman $M_w 9.0$ earthquake was followed by a number of moderate-size aftershocks. Until June 27, 2006, the Capital Region Digital Seismograph Network well recorded 25 aftershocks with magnitudes greater than 5.8. These aftershocks have been well located by

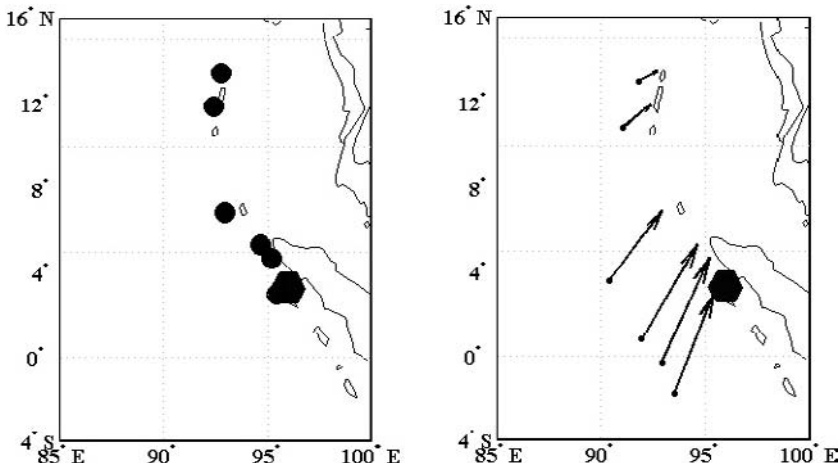


Fig. 2. Locations of the main shock (black hexagon) and the selected aftershocks (black dot) (left). The location correction vectors determined using the seismic recordings of the aftershocks (right).

some institutions such as Harvard University, NEIC, among others, so they could be used to correct the slowness vector in this area. In this study, the locations of the aftershocks published by NEIC were assumed to be correct or true, and compared these with the locations we determine using our approach to have difference vectors for the locations of all the aftershocks. By linear interpolation between any two locations, we could have the difference vectors for all the locations of interests, that is, the locations where the main shock ruptured ran through. Among the 25 aftershocks, we choose six aftershocks which occurred near or on the ruptured region of the main shock as shown on the left panel of Fig. 2, and obtained the corresponding difference vectors as shown on the right panel of Fig. 2. The right panel of Fig. 2 indicates that the different locations (different epicentral distances and/or back azimuth) have different correction vectors (both scales and directions). Using a constant vector to correct all the locations seems to be unreasonable.

5. Tracking the Energy Sources

As mentioned above, the first 600 s of the initial arrivals were used in this study. The width of the time windows to be shifted is 10 s, and the shift step is 4 s. Therefore, 150 time windows of the signals are analyzed for

slowness vectors. In finding the solutions, we used the grid-search method. The search step for scalar slowness is 0.005 s° , which yields only distance variations less than 8.6 km at the southern end of the ruptured region and less than 10.4 km at the northern end. The search step for the back azimuth is 0.07° , which yields distance variations less than 5.2 km at the southern end of the ruptured region and less than 4.2 km at the northern end. For each of the time windows, we have one best slowness vector which corresponds to a specific geographic location. In this way, we could have 150 locations for the whole rupture process of the 2004 Sumatra-Andaman $M_{\text{W}}9.0$ earthquake, which represent the locations from where high-frequency signals were radiated during the earthquake rupture process. However, the fitness of the beamed signal with the signal recorded at the reference stations became worse when the window was shifted after 440 s. That is the noises were stronger than the source signals after 440 s. Thus to be the duration time of the earthquake is determined to be 440 s. Therefore, the 109 locations determined in the first 440 s are considered to be reliable. The left and right panels of Fig. 3 show the locations before and after being corrected, respectively.

Figure 4 clearly presents the locations where the rupture had gone through, which is from the northwestern shore of the Sumatra Islands to the northeastern shore of the Andaman Islands. The general feature of the rupture geometry fits the trench of islands well. It is very similar to the

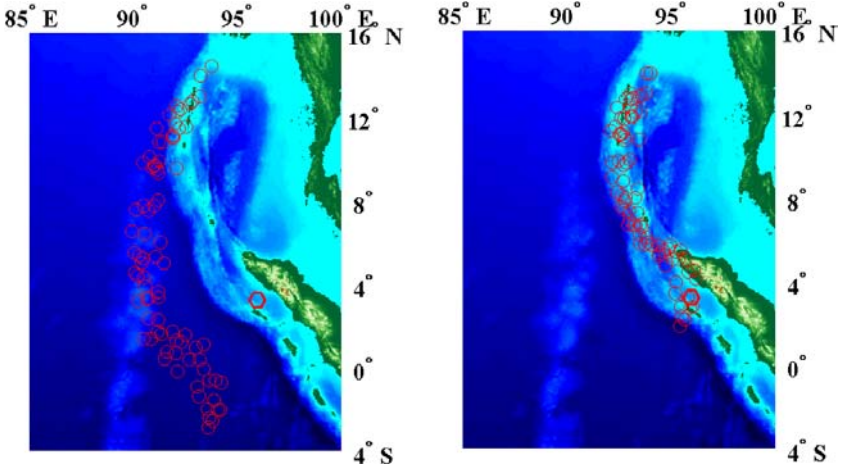


Fig. 3. Locations of high-frequency energy sources before (left) and after (right) being corrected.

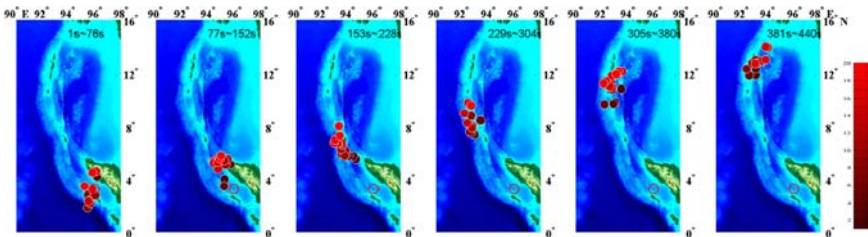


Fig. 4. Snapshots of the progression of rupture front. Each of the snapshots shows the locations of rupture fronts within a time window of 76 s. The solid dots represent the locations of rupture fronts and the open hexagon is the epicenter of the main shock. The color of the dots in the same time window indicates the time progression of rupture fronts.

results obtained by Kruger and Ohrnberger² and Ishii *et al.*⁶ The rupture length was estimated to be at least 1347 km by calculating the distances between the most northern location and the most southern location. From Fig. 4, we notice that the initial location is not the most southern one indicating that southward rupture occurred. Based on the lengths of rupture toward south and north, respectively, as well as the corresponding times, the average rupture velocities are estimated to be 3.71 and 2.86 km/s.

Figure 4 shows the progression of rupture front. Each of the snapshots shows the rupture spots within a time window of 76 s and in each the color indicates the time order of the ruptured spots. It is clear that overall the rupture initiated at the south, propagated northward, and stopped at the north. More details about the rupture process could be seen in this group of images, but they are preferred to be discussed in the coming paper.

6. Discussion and Conclusions

The analysis of the 33 stations recordings indicates that the rupture length of the 2004 Sumatra-Andaman M_w 9.0 earthquake was at least 1347 km. It is much larger than the length suggested by the aftershock distribution¹ and by the analysis of Japanese Hi-Net Array data,⁶ also slightly larger than the length of 1200 km suggested by the short-period seismic body waves⁸ and the analysis of the Earth's normal modes,³ and even larger than the length of 1150 km suggested by the analysis of GRSN data.²

The analysis suggested that the 2004 Sumatra-Andaman M_w 9.0 earthquake has rupture duration time of 440 s. This is a little shorter than 500 s suggested by the analysis of short-period seismic body waves⁸ and

480 s resulted in by the Japanese Hi-Net Array analysis,⁶ very close to 430 s suggested by the analysis of GRSN teleseismic data,² but much shorter than 600 s yielded by the analysis of Earth's free oscillations.⁴

Our result suggested that the rupture velocities during the earthquake process were variable. Only the average velocity of southward rupture and the average velocity of northward rupture were estimated in this work, which were 3.71 km/s and 2.86 km/s, respectively. These velocities seemed to be larger than those obtained by the analysis of the high-frequency signals⁸ and the Japanese Hi-Net Array data.⁶

The array made up of the 33 stations of the Capital Region Digital Seismograph Network, Beijing, China, is good enough for tracking the rupture front of the 2004 Sumatra-Andaman M_W 9.0 earthquake. The beam power analysis in time domain led to a very similar result to those obtained from the analysis of GRSN broadband recordings² and Hi-Net Array short-period recordings⁶ clearly and generally describing the progression of rupture front. It is indeed a significant extension of the seismic array technique application besides the application of the local and near-fault recordings.^{9–11}

Acknowledgments

This study is supported by the NSFC (40474018 and 40574025) and the Program of the National Fundamental Research (2004CB418404-4 and 2001CB711005), and the Joint Foundation of Earthquake Science (A07047). Contribution No. of IGCEA: 07FE3004.

References

1. T. Lay, H. Kanamori, C. J. Ammon, M. Nettles, S. N. Ward, R. C. Aster, S. L. Beck, S. L. Bilek, M. R. Brudzinski, R. Butler, H. R. DeShon, G. Ekstrom, K. Satake and S. Sipkin, *Science* **308** (2005) 1127.
2. F. Krüger and M. Ohrnberger, *Nature* **435** (2005) 937.
3. S. Stein and E. A. Okal, *Nature* **434** (2005) 581.
4. J. Park, T. A. Song, J. Tromp, E. Okal, S. Stein, G. Roult, E. Clevede, G. Laske, H. Kanamori, P. Davis, J. Berger, C. Breitenberg, M. V. Camp, X. Lei, H. P. Sun, H. Z. Xu and S. Rosat, *Science* **308** (2005) 1139.
5. M. K. Giovanni, S. L. Beck and L. Wagner, *Geophys. Res. Lett.* **29** (2002) 2018, doi: 10.1029/2002GL015774.
6. M. Ishii, P. Shearer, H. Houston and J. Vidale, *Nature* **435** (2005) 933.

7. C. J. Ammon, C. Ji, H. Thio, D. Robinson, S. D. Ni, V. Hjorleifsdottir, H. Kanamori, T. Lay, S. Das, D. Helmberger, G. Ichinose, J. Polet and D. Wald, *Science* **308** (2005) 1133.
8. S. Ni, H. Kanamori and D. Helmberger, *Nature* **434** (2005) 582.
9. P. Spudich and E. Cranswick, *Bull. Seismol. Soc. Am.* **74** (1984) 2083.
10. P. Goldstain and R. J. Archuleta, *J. Geophys. Res.* **96** (1991) 6187.
11. B. S. Huang, *Geophys. Res. Lett.* **28** (2001) 3377.
12. S. Rost and C. Thomas, *Rev. Geophys.* **40**(3) (2002) 1.
13. B. L. N. Kennett and E. R. Engdahl, *Geophys. J. Int.* **105** (1991) 429.

This page intentionally left blank

RUPTURE PROCESS OF THE 2005 SOUTHERN ASIAN (PAKISTAN) M_w 7.6 EARTHQUAKE FROM LONG-PERIOD WAVEFORM DATA

YONG ZHANG^{†,‡,*}, YUN-TAI CHEN^{‡,†,§} and LI-SHENG XU^{‡,¶}

[†]*Peking University, Beijing 100871, China*

[‡]*Institute of Geophysics, China Earthquake Administration*

Beijing 100081, China

^{*}*zhygn@163.com*

[§]*chenyt@cea-igp.ac.cn*

[¶]*xuls@cdsn.org.cn*

On October 8, 2005, an M_w 7.6 earthquake occurred in the Southern Asia (Pakistan) and was followed by a number of aftershocks. The long-period waveform data from 53 worldwide stations were usable, and 18 moderate-size aftershocks can be used as empirical Green's function (EGF) events. For the spatial and temporal complexity of the source, 127 azimuth-dependent relative source time functions (RSTFs) were retrieved when those aftershocks were used as EGF events individually, and 53 average RSTFs were used in imaging the evolution of rupture on the fault plane. From both the retrieved RSTFs and the imaged spatio-temporal rupture process, the Southern Asia M_w 7.6 earthquake had duration time of 25 s. From the inverted static slip distribution, the fault length was about 80 km, the fault width was 35 km, the maximum slip value was 11 m, the average slip value was 5 m, the maximum slip-rate was 1.6 m/s, and the average slip-rate was 0.8 m/s. On a basis of the inverted results, the maximum stress drop on the fault plane was estimated to be 105 MPa, and the average one was 20 MPa. From the snapshots of the slip-rate variation with space and time, the rupture process could be divided into two periods: rupture propagation of the first 10 s and rupture healing of the last 15 s. The first period seemed to be regular and in order. In more details, the rupture took place mainly in down-dip direction around the hypocenter in the first 2 s, and then the rupture took place in the strike direction, which seemed to be asymmetrical. Eventually, the rupture length in the SSE direction was shorter than that in the NNW direction, and the spot of the strongest rupture, where both the slip-rate and slip are largest, was 10 km NNW of the epicenter.

1. Introduction

An M_w 7.6 earthquake occurred in the Southern Asia (Pakistan) on October 8, 2005. The earthquake caused a huge loss of lives and properties. From the

official report of Pakistan government, the earthquake caused the casualty of about 86,000 people, more than 10,000 people injured, more than 9000 people missing, and millions of people homeless.

Since the earthquake occurrence, some studies have been done. Ji¹ inverted 11 stations of P phases and 9 stations of SH phases of teleseismic waveforms for the slip distribution on the fault plane. His results suggested that the area with the maximum slip of about 6.5 m was in the northwest of the epicenter near Muzaffarabad. From both the P and SH waves coming from FDSN-GeoScope networks, Vallée² obtained results different from the above by means of the slip patch method, that is, the main slip distributed at the southeast of epicenter and above the hypocenter rupture initiation point. After processing the ASTER images and teleseismic waveform data, Avouac *et al.*³ suggested that the average offset on the ground surface was 4 m, the peak value reached 7 m which was at the northwest of Muzaffarabad, and the rupture duration was about 25 s. Similarly, Pathier⁴ determined the fault trace of around 80 km and the distribution of ground surface displacement using ENVISAT SAR images. His results indicated that the main slip occurred in the upper 10 km of the crust and between the cities of Muzaffarabad and Balakot. According to the study of Parsons *et al.*,⁵ there were two asperities lying NNW and SSE to the hypocenter, respectively, and the asperity of 12 m maximum slip was in the NNW.

After the main shock, still there was a high seismic activity in the epicentral region. During the period of only 20 days, between October 8 and October 28, there occurred 18 stronger aftershocks whose magnitudes were greater than M_W 5.5. In this study, the relative source time functions (RSTFs) were retrieved when the 18 selected aftershocks were used as the events of empirical Green's function (EGF), and the spatio-temporal rupture process was imaged by means of the technique of inverting RSTFs.⁶

2. Data and Processing

The data used in this study were from the Data Center of the IRIS. There are 53 stations which clearly recorded the earthquake and whose epicentral distances are between 20° and 90° (Fig. 1). The raw velocity recordings were filtered with a third-order Butterworth filter of 0.01–0.2 Hz only when they are put in use.

In order to obtain an image of the spatial and temporal variation of slip on the fault plane, the focal mechanism of the earthquake is firstly



Fig. 1. Distribution of the stations from which the long-period data were used in this study. The black hexagon represents the epicenter.

required to be determined. The focal mechanism of this earthquake was obtained by moment tensor inversion in frequency domain⁷ by means of the Green's functions calculated using the IASPEI91 earth model⁸ and the reflectivity method.⁹ The corresponding best double couple solution is presented in Fig. 2. The strike, dip, and rake are 111° , 71° , and 70° for the nodal plane I, and 339° , 27° , and 135° for the nodal plane II, respectively. The scalar seismic moment determined by moment tensor inversion is $M_0 = 2.2 \times 10^{20}$ N m. Accordingly, the moment magnitude is $M_W = 7.5$.

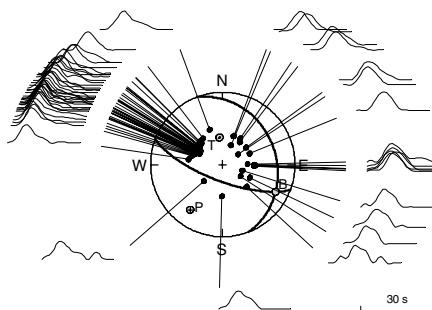


Fig. 2. Azimuth-dependent RSTFs averaged over those retrieved when the 18 aftershocks were used as EGF events, respectively, the geometrical representation of the best double couple solution obtained by means of the moment tensor inversion and the projected station positions.

Another important step in obtaining the image of spatial and temporal variation of slip on the fault plane is to retrieve RSTFs from the waveform data of different stations using EGF technique.^{10–12} As mentioned above, there were 18 aftershocks which can be used as the EGF events. Therefore, we firstly used each of them as the EGF event to retrieve the RSTFs of the main shock. In this way, 18 RSTFs were obtained for all the stations when each of the aftershocks was used as an EGF event. Then the unique RSTF was obtained for each station by averaging those 18 RSTFs. Figure 2 shows the average RSTFs of the 18 stations. It is worth noticing that the RSTFs from various stations appear stable and vary systematically with variation of azimuths, which implies that these RSTFs are reliable, and in the meantime, reflects the complexity of rupture process.

3. Spatio-temporal and Rupture Process

A time domain inversion technique was used for imaging the rupture process. That is, the observed azimuth-dependent RSTFs from different stations are inverted in time domain to obtain temporal and spatial distribution of slip on fault plane.⁶

The above analysis indicates that the causative or seismogenic fault of the earthquake is of strike 339° /dip 27° /rake 135° . While performing the inversion, the extent and geometry of rupture area is unnecessary to be assigned *a priori*, and the ruptured area is determined automatically by inversion. In order to objectively obtain a ruptured area, the area size or extent to be used in inversion should be chosen to be large enough to contain the true ruptured area. Thus, a fault plane 160 km long along the strike direction, 80 km in the north of the epicenter and 80 km in the south of the epicenter, respectively, and 45 km wide along the down-dip direction, was used as the area for inverting the spatial and temporal slip distribution, and was equally divided into 32 segments in the strike direction and 9 segments in the down-dip direction. In other words, a rectangular fault of $160\text{ km} \times 45\text{ km}$ was divided into $32 \times 9 = 288$ sub-faults of $5\text{ km} \times 5\text{ km}$.

As mentioned above, 53 azimuth-dependent RSTFs were available. However, the rectangular fault for imaging the slip distribution was divided into 288 sub-faults. For a time instant, the number of the observation equations is 53, while the number of the unknowns is 288. Therefore, the inversion problem is an underdetermined one. To stabilize

the inversion, three constraints were imposed as done before.^{13,14} The first one is that the slip-rate be greater than or equal to zero. It physically means that no backward slip occurs during earthquake rupture process. This is a kinematical condition, but up to now, no backward motion has been observed during real source rupture processes at least in the current precision. The second one is that the rupture velocity should not be greater than 2.8 km/s, which was about 0.8 times the local shear wave velocity. The third one is that the gradient of the slip-rates on the neighboring sub-faults at a certain time should not be greater than some constant. This is a smoothness condition. In our work, the smoothness constant was determined to be 0.003 by trial-and-error technique.

In this inversion, the conjugate gradient method was used.¹⁵ The result from this kind of inversion, to some extent, depends on initial model. To obtain a stable and reliable result, we used a random scheme to produce initial models. A number of the numerical tests indicated that the main feature of the inverted results were rather stable in spite of the differences corresponding to the different initial models. We performed many inversions using randomly produced initial models. It is found that little difference existed among the inverted results.

Figure 3 depicts the distribution of static slip or final slip on the fault plane obtained by the inversion, where the white octagon denotes the hypocenter or rupture initiation point. From the static slip distribution, the ruptured area with slip amplitude greater than 3 m is about 35 km wide and about 70 km long, 50 km in the north of the epicenter and 20 km in the south of the epicenter, respectively. The area with slip amplitude greater than 5.0 m is about 20 km wide and about 35 km long, 25 km in the north of the epicenter and 10 km in the south of the epicenter, respectively. The area with slip amplitude greater than 8.0 m is about 15 km wide and about 25 km long, 20 km in the north of the epicenter and 5 km in the south of

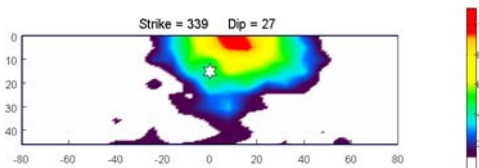


Fig. 3. Static slip distribution on the fault plane. The white hexagon denotes the rupture initiation point.

the epicenter, respectively. The location of the 11 m maximum slip value is 10 km north of the epicenter. Based on the circular fault mode,^{16,17}, we calculated the stress drop on each sub-fault. The maximum stress drop is 105 MPa, and the average one is 20 MPa.

Figure 4 demonstrates the spatial and temporal rupture process of the earthquake. The hexagon denotes the rupture initiation point or the hypocenter. From the snapshots of the slip-rate variation, the rupture process consisted of two phases in general, with the first 10 s for rupture propagation and the last 15 s for rupture healing. In more details, in the first 2 s, the rupture propagated downwards and upwards; in the first 2 s the rupture propagated mainly in the horizontal direction asymmetrically toward the NNW and toward the SSE; between the eleventh second and the end time, the ruptured areas were fragmentary and irregular. The main rupture took place in the first phase, that is, before the tenth second. It is noticed that the rupture extended almost bilaterally in this phase; however, the leftward (SSE) rupturing was rather slower than the rightward (NNW) rupturing, which eventually appeared as an overall unilateral rupture from SSE to NNW. The spot of the maximum slip-rate was at the 10 km NNW of the epicenter. The value of the maximum slip-rate was 1.6 m/s.

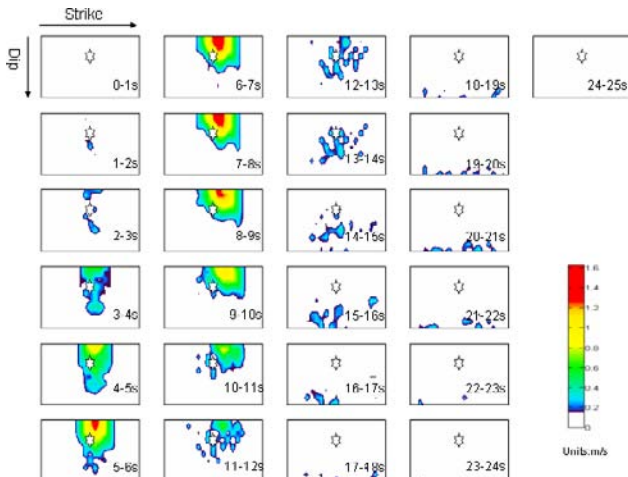


Fig. 4. Snapshots of the spatial and temporal variation of the slip-rate. Each rectangle represents the given fault plane with the length of 160 km and the width of 45 km. The white hexagon denotes the rupture initiation point.

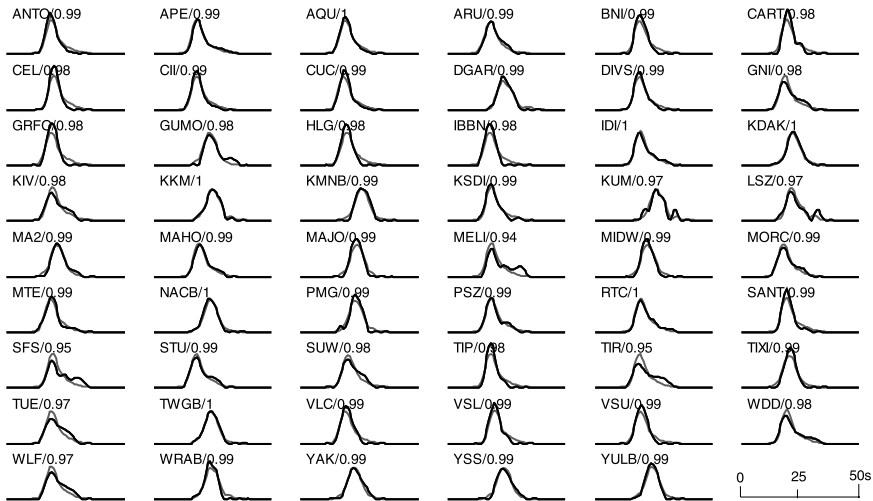


Fig. 5. Fitness of the observed RSTFs with the synthetic ones calculated using the dynamic rupture model which was calculated by inverting the observed RSTFs as shown in Fig. 2.

Figure 5 shows the fitness of the average observed RSTFs retrieved from the waveform data of 53 stations when the 18 aftershocks were used as EGF events with the synthetic RSTFs calculated using the dynamic rupture model as shown in Fig. 4. It is obvious that almost all the features of the observed RSTFs were explained well by the inverted dynamic rupture model.

4. Discussion and Conclusions

To study the complexity of rupture process of the 2005 Southern Asian $Mw7.6$ earthquake, the long-period waveform data from 53 worldwide stations, including the data of the main shock and 18 aftershocks, were used. A total of 127 azimuth-dependent RSTFs of the main shock were retrieved when the 18 aftershocks were used as the EGF events, and the 53 average RSTFs were used in imaging the spatio-temporal rupture process on the fault plane.

From both the retrieved RSTFs and the imaged spatio-temporal rupture process, the Southern Asian $Mw7.6$ earthquake had a rupture duration time of 25 s. From the inverted final (static) slip distribution, the fault length was about 70 km, the fault width was 35 km, the maximum

slip value was 11 m, the average slip was 5 m, the maximum slip-rate was 1.6 m/s, and the average slip-rate was 0.8 m/s. According to the inverted results, the maximum stress drop on the fault plane was estimated to be 105 MPa, and the average stress drop was about 20 MPa. From the snapshots of the slip-rate variation with space and time, the rupture process could be divided into two phase, that is, the period of rupture propagation of the first 10 s and the period of rupture healing of the last 15 s. The rupture propagation phase seemed to be regular and in order. The rupture took place mainly in down-dip direction around the hypocenter in the first 2 s, and then the rupture took place in the strike direction. The bilateral rupture in the strike direction was asymmetrical. Eventually, the rupture length in the SSE direction was shorter than that in the NNW direction, and the spot of the strongest rupture, where both the maximum slip-rate and maximum slip occurred, was 10 km to the NNW of the epicenter. The results obtained by this study indicated that the total rupture duration time of the earthquake was about 25 s. This result is consistent with that obtained by Avouac *et al.*³ The fault length was estimated to be about 70 km, which is very close to the result obtained from ENVISAT SAR images by Pathier *et al.*⁴ However, the fault width estimated by this study was about 35 km while Pathier *et al.*⁴ suggested the main slip occurred in the upper 10 km of the crust. The maximum slip on the fault plane obtained by this study was about 11 m. It is in good agreement with the result of 12 m obtained by Parsons *et al.*⁵ but different from the result of 6.5 m obtained by Ji¹ and the result of 7 m obtained by Avouac *et al.*³ The results inverted from this study indicates that the rupture length in the NNW direction was longer than that in the SSE direction. It is similar to the result obtained by Ji¹ and is also similar to the result obtained by Avouac *et al.*³ but different from the result obtained by Vallée² According to this study, the maximum slip was 10 km to the NNW of the epicenter. This result is consistent with the results obtained by Ji,¹ Avouac *et al.*³ and Parsons *et al.*⁵

Acknowledgments

This study is supported by the Program of the National Fundamental Research (2001CB711005 and 2004CB418404-4), the NSFC (40574025 and 40474018), and the Joint Foundation of Earthquake Science (No.106018). Contribution No. of IGCEA: 07FE3005.

References

1. C. Ji, Finite-fault slip model preliminary result for the 05/10/08 PAKISTAN earthquake. <http://earthquake.usgs.gov/eqcenter/eqintheneWS/2005/usdyae/finitefault/> (2006).
2. M. Vallée, <http://www-geoazur.unice.fr/SEISME/PAKISTAN081005/note1.html> (2005).
3. J. P. Avouac, F. Ayoub, S. Leprince, O. Konca and D. V. Helmberger, *Earth Planet. Sci. Lett.* **249** (2006) 514.
4. E. Pathier, E. J. Fielding, T. J. Wright, R. Walker, B. E. Parsons and S. Hensley, *Geophys. Res. Lett.* **33**(20) (2006) CiteID L20310.
5. T. Parsons, R. S. Yeats, Y. Yagi and A. Hussain, *Geophys. Res. Lett.* **33** (2006) L06304, doi: 10.1029/2005GL025429.
6. Y. T. Chen and L. S. Xu, *Geophys. J. Int.* **143** (2) (2000) 407.
7. L. S. Xu and Y. T. Chen, *Acta Seismol. Sin.* **12**, 5 (1999) 495.
8. B. L. N. Kennett and E. R. Engdahl, *Geophys. J. Int.* **105** (1991) 429.
9. B. L. N. Kennett, *Seismic Wave Propagation in Stratified Media* (Cambridge University Press, Cambridge, 1983), p 1.
10. D. S. Dreger, *Geophys. Res. Lett.* **21** (1994) 2633.
11. S. E. Hough and D. S. Dreger, *Bull. Seism. Soc. Am.* **85** (1995) 1576.
12. L. S. Xu and Y. T. Chen, *Acta Seismol. Sin.* **9**(2) (1996) 209.
13. L. S. Xu, Y. T. Chen and G. Patau, *Bull. Seism. Soc. Am.* **92**(8) (2002) 3210.
14. L. S. Xu and Y. T. Chen, *Sci. China D Earth Sci.* **48**(1) (2005) 112.
15. S. N. Ward and S. E. Barrientos, *J. Geophys. Res.* **91**(B5) (1986) 4909.
16. J. N. Brune, *J. Geophys. Res.* **75** (1970) 4997.
17. J. N. Brune, Correction, *J. Geophys. Res.* **76** (1971) 5002.

This page intentionally left blank

SEISMIC CHARACTERISTICS OF STRONG DEEP FOCAL EARTHQUAKES AND ASSOCIATED PHENOMENA IN NORTHEASTERN ASIA

JIAN WANG,* XUE-SONG HE and YI-QUN LI

*Institute of Geophysics, China Earthquake Administration
No.5 Minzu Daxue Nan Rd., Haidian District
Beijing 100081, China*
**wangjcsb@hotmail.com*

In Northeastern Asia, strong deep focal earthquakes ($M_S \geq 5.8$, generally focal depths > 430 km) distribute approximately north-south trending, which is very similar to the trend of the slab structure. From 1900, temporal distribution of strong deep focal earthquakes is non-stationary. Based on the wavelet transform, relative active and quiet periods are divided. Each active or quiet period is about 12 years. In terms of energy index (square root of energy released by earthquakes), in total about 79% of strong deep focal earthquakes occurred in active periods. For strong shallow earthquakes in Northeastern Asia, seismic characteristics in the eastern part are different from that in the western part. Temporal distribution of strong shallow earthquakes in the eastern part is very similar to that of strong deep focal. The results of the territorial limit test show that in the eastern part of 120°E , the ratios of energy index in active periods are stable in high level. In the western part of 117°E , the ratios are stable in low level. There is a transition belt between 117°E and 120°E . The north-east trending Tan-Lu fault is an important boundary. The strong deep focal earthquakes have a correlation with shallow earthquakes in Northeastern Asia. The relationship cannot be understood as an accidental event. The mechanism of the relationship is analyzed. The mantle convection and its attenuation take important role.

1. Introduction

The Pacific plate subducts beneath the Japan Islands with a convergence rate of about 90 mm/year. The dip angle is almost constant of about 35° .¹ Beneath Northeastern China and Korean Peninsula, the slab has the shallowest dip and the depth ranges from about 400 km to about 600 km. The trend of the slab structure, shown by slab contours, is approximately north-south trending.² The strong deep focal earthquakes

distribute approximately north–south trending, which is very similar to the trend of the slab structure.

Seismic characteristics can constraint on mechanisms of strong deep focal earthquakes and give very important information about geodynamic processes.³ Many geoscientists analyzed the hypocentral distribution of earthquakes to mark subduction structure of a down-going oceanic plate.^{4–6} Some seismologists paid attention to the relationship between deep focal earthquakes and strong shallow earthquakes. A strong shallow earthquake in a region is preceded and sometimes followed by the marked increase of deep seismic activity in the same down-dip seismic zone perpendicular to the trend of an arc structure. The increase of the deep seismic activity before the strong shallow earthquake cannot be understood as an accidental event, nor as a mere trigger of the great shallow earthquake, but as an essential forerunning phenomenon of it.⁷ Wu *et al.*⁸ compared the seismicity in Northern China and in Japan with data from 1918 to 1976. They found that there was a correlation between the strong earthquakes in these two regions. They explained the phenomena as the earthquakes in Northern China are under the control of the down-going movement of the Pacific plate along the Japan Trench.

Geodynamics in Northeastern Asia are debated for several decades. How to recognize the collision of the Indian Plate with the Eurasian Plate and the roles of the Pacific plate is an important issue. Seismic characteristics can provide constraint on this issue. In this paper, we will firstly analyze the temporal distribution of deep focal earthquakes in Northeastern Asia by using wavelet analysis. Spatial distribution of deep focal earthquake in each period will be analyzed. Meanwhile, the seismicity in continent of Northeastern Asia and its relationship with deep focal earthquakes and the mechanism will be discussed.

2. Seismic Data

The earthquake catalogues used in this paper come from several sources. The seismic data from 1900 to 1963 mainly root from ISS, but recomposed with local recordings.^{9–12} The data from 1964 to 1998 come from ISC relocated with improved travel times and procedures for depth determination.¹³ The data after 1998 come from the *Annual Bulletin of Chinese Earthquakes*¹⁴ and the *Bulletin of Digital Seismological Observations of Chinese Stations*.¹⁵ The strong deep focal earthquakes in Northeastern Asia were listed in Table 1.

Table 1. The catalogue of strong deep focal earthquakes in Northeastern Asia.

| No. | Year-month-date | Lat ($^{\circ}$ N) | Long ($^{\circ}$ E) | H (km) | M_S | Location | Source |
|-----|-----------------|---------------------|----------------------|--------|-------|---------------------|----------------------------------|
| 1 | 1905-08-25 | 43.00 | 129.00 | 470 | 6.8 | Jilin, China | Min <i>et al.</i> ⁹ |
| 2 | 1917-07-31 | 42.50 | 131.00 | 460 | 7.5 | Jilin, China | Wang <i>et al.</i> ¹⁰ |
| 3 | 1918-02-10 | 43.00 | 130.00 | 450 | 6.5 | Jilin, China | Wang <i>et al.</i> ¹⁰ |
| 4 | 1918-04-10 | 43.50 | 130.50 | 570 | 7.2 | Jilin, China | Wang <i>et al.</i> ¹⁰ |
| 5 | 1920-05-06 | 43.00 | 131.50 | 520 | 6.3 | Jilin, China | Wang <i>et al.</i> ¹⁰ |
| 6 | 1923-07-27 | 43.00 | 130.00 | 430 | 5.8 | Jilin, China | Wang <i>et al.</i> ¹⁰ |
| 7 | 1927-05-18 | 44.00 | 131.00 | 430 | 6.5 | Heilongjiang, China | Wang <i>et al.</i> ¹⁰ |
| 8 | 1928-06-07 | 44.00 | 131.00 | 430 | 6.0 | Heilongjiang, China | Wang <i>et al.</i> ¹⁰ |
| 9 | 1931-06-06 | 42.60 | 129.50 | 500 | 6.8 | Jilin, China | Wu <i>et al.</i> ¹² |
| 10 | 1933-07-24 | 42.50 | 131.00 | 550 | 5.8 | Jilin, China | Wang <i>et al.</i> ¹⁰ |
| 11 | 1933-09-09 | 44.00 | 130.00 | 590 | 6.3 | Heilongjiang, China | Wang <i>et al.</i> ¹⁰ |
| 12 | 1935-03-29 | 43.00 | 131.00 | 550 | 6.3 | Jilin, China | Wang <i>et al.</i> ¹⁰ |
| 13 | 1938-10-21 | 43.50 | 131.00 | 550 | 6.3 | Heilongjiang, China | Wang <i>et al.</i> ¹⁰ |
| 14 | 1940-07-10 | 44.00 | 131.00 | 580 | 7.3 | Heilongjiang, China | Wang <i>et al.</i> ¹⁰ |
| 15 | 1940-11-22 | 43.70 | 131.50 | 540 | 6.0 | Heilongjiang, China | Wang <i>et al.</i> ¹⁰ |
| 16 | 1945-08-21 | 41.50 | 130.50 | 540 | 7.0 | East Sea, Korea | Wu <i>et al.</i> ¹² |

Table 1. (continued)

| No. | Year-month-date | Lat ($^{\circ}$ N) | Long ($^{\circ}$ E) | H (km) | M_S | Location | Source |
|-----|-----------------|---------------------|----------------------|----------|-------|---------------------|-------------------------------------|
| 17 | 1946-01-11 | 44.00 | 129.50 | 580 | 7.2 | Heilongjiang, China | Wang <i>et al.</i> ¹⁰ |
| 18 | 1949-04-05 | 42.00 | 131.00 | 600 | 6.8 | East Sea, Korea | Li <i>et al.</i> ¹¹ |
| 19 | 1950-05-17 | 39.00 | 130.30 | 580 | 6.8 | East Sea, Korea | Li <i>et al.</i> ¹¹ |
| 20 | 1954-11-19 | 41.20 | 131.80 | 600 | 6.5 | East Sea, Korea | Li <i>et al.</i> ¹¹ |
| 21 | 1957-01-03 | 43.90 | 130.60 | 593 | 7.0 | Heilongjiang, China | Wang <i>et al.</i> ¹⁰ |
| 22 | 1957-01-03 | 43.90 | 130.60 | 580 | 5.8 | Heilongjiang, China | Wang <i>et al.</i> ¹⁰ |
| 23 | 1959-10-29 | 42.80 | 131.10 | 547 | 6.3 | Jilin, China | Wang <i>et al.</i> ¹⁰ |
| 24 | 1960-10-08 | 39.50 | 130.00 | 650 | 6.8 | East Sea, Korea | Li <i>et al.</i> ¹¹ |
| 25 | 1969-04-10 | 42.05 | 131.05 | 553 | 5.8 | East Sea, Korea | Engdahl <i>et al.</i> ¹³ |
| 26 | 1973-09-10 | 42.43 | 131.05 | 562 | 6.6 | East Sea, Korea | Engdahl <i>et al.</i> ¹³ |
| 27 | 1973-09-29 | 41.90 | 130.99 | 570 | 7.7 | East Sea, Korea | Engdahl <i>et al.</i> ¹³ |
| 28 | 1975-06-29 | 38.73 | 130.08 | 556 | 6.1 | East Sea, Korea | Engdahl <i>et al.</i> ¹³ |
| 29 | 1977-03-09 | 41.60 | 131.05 | 569 | 5.9 | East Sea, Korea | Engdahl <i>et al.</i> ¹³ |
| 30 | 1979-08-16 | 41.60 | 130.90 | 582 | 6.0 | East Sea, Korea | Engdahl <i>et al.</i> ¹³ |
| 31 | 1999-04-08 | 43.72 | 130.45 | 573 | 6.8 | Jilin, China | Cheng <i>et al.</i> ¹⁴ |
| 32 | 2002-06-29 | 43.68 | 130.66 | 578 | 7.1 | Jilin, China | Liu <i>et al.</i> ¹⁵ |
| 33 | 2002-09-15 | 44.79 | 129.90 | 586 | 6.0 | Jilin, China | Liu <i>et al.</i> ¹⁵ |

Wang *et al.*

The epicentral distribution of strong deep focal earthquakes and slab contours are depicted in Fig. 1. These strong deep focal earthquakes concentrate in a belt of 38°N to 45°N and 129°E to 132°E (area A), similar to slab contours. The focal distribution of these strong deep focal earthquakes is also consistent with slab depth.

Our research region covers Northern China, Northeast China, Yellow Sea, and Korean Peninsula. In the region, the Tan-Lu fault (T-L fault) is an important fault cutting through the lithosphere.¹⁶ It directs from northeast to southwest. Beside T-L fault, there are two other important faults. The Yinshan-Yanshan fault (Y-Y fault) trends east to west, which is the boundary of North China and Northeast China. The Qinlin-Dabieshan fault (Q-D fault) is the south boundary of Northern China. In Fig. 1, strong shallow earthquakes from 1900 to 2004 are depicted. The parameters of strong shallow earthquakes mainly come from the *Catalogue of Chinese Historical Strong Earthquakes*⁹ and the *Catalogue of Chinese Earthquakes*.¹⁰

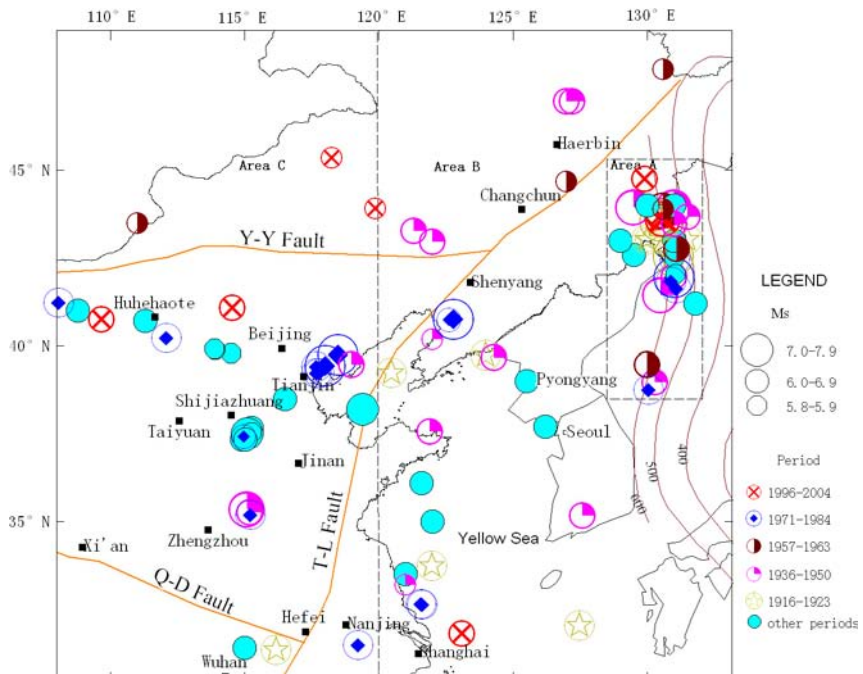


Fig. 1. Epicentral distribution of strong deep focal and shallow earthquakes.

3. Spatial–Temporal Characteristics of Deep Focal Earthquakes

From Table 1 we can notice that temporal distribution of strong deep focal earthquakes in Northeastern Asia is non-stationary. We will apply wavelet transform to study its characteristics.

3.1. Wavelet analysis on temporal–frequency characteristics

Wavelet analysis has higher resolution in both time and frequency domains, although it is developed based on the Fourier transform. With wavelet analysis, we transform the temporal distribution of earthquake occurrence to frequency domain. In frequency domain, it is easy to analyze the dominant periods of earthquake sequences. The processes are as the followings:

If a squared integrable function $\psi(t)$ satisfies the condition:

$$\int_{-\infty}^{+\infty} |\psi(t)|^2 |t|^{-1} dt < \infty \quad (1)$$

where the $\psi(t)$ is a wavelet fundamental function, $\psi(t) \in L^2(R)$.

Suppose a continuous wavelet function from the fundamental function is:

$$\varphi_{a,b}(t) = \frac{1}{\sqrt{|a|}} \varphi\left(\frac{t-b}{a}\right), \quad a, b \in R, \quad a \neq 0 \quad (2)$$

Suppose a function $f(t) \in L^2(R)$, the wavelet transform of a function $f(t)$ is defined as the integral transform:

$$W_f(a, b) = \frac{1}{\sqrt{|a|}} \int_{-\infty}^{+\infty} f(t) \psi\left(\frac{t-b}{a}\right) dt \quad (3)$$

In Eqs. (2) and (3), a is a scale parameter, which influences the frequency and window of the wavelet; b is a location parameter.¹⁷

The sequence of earthquake events is denoted by the following formula:

$$f(t) = \sum_i \sqrt{E_i(t)} \quad (4)$$

where, f is an energy index and E expresses the energy released by an earthquake:

$$\text{Log } E = 1.5 M + 11.8 \quad (5)$$

Table 2. The catalogue of strong shallow earthquakes.

| No. | Year-month-date | Lat (°N) | Long (°E) | H (km) | M_S | Location |
|-----|-----------------|----------|-----------|--------|-------|------------------|
| 1 | 1906-04-06 | 37.70 | 126.20 | | 6.0 | Yellow Sea |
| 2 | 1910-01-08 | 35.00 | 122.00 | | 6.8 | Yellow Sea |
| 3 | 1911-01-25 | 39.80 | 114.50 | | 5.9 | Hebei |
| 4 | 1917-01-24 | 31.30 | 116.20 | | 6.3 | Anhui |
| 5 | 1917-05-28 | 39.70 | 124.00 | | 6.1 | Lianin, China |
| 6 | 1921-12-01 | 33.70 | 122.00 | | 6.5 | Yellow Sea |
| 7 | 1922-09-29 | 39.20 | 120.50 | | 6.5 | Behai, China |
| 8 | 1923-12-09 | 32.00 | 127.50 | | 6.0 | East Sea, China |
| 9 | 1927-02-03 | 33.50 | 121.00 | | 6.5 | Yellow Sea |
| 10 | 1927-02-03 | 33.50 | 121.00 | | 6.5 | Yellow Sea |
| 11 | 1929-01-14 | 40.70 | 111.30 | | 6.0 | Inner-Mongolia |
| 12 | 1932-04-06 | 31.40 | 115.00 | | 6.0 | Hubei |
| 13 | 1932-08-22 | 36.10 | 121.60 | | 6.3 | Yellow Sea |
| 14 | 1934-01-21 | 41.10 | 108.30 | | 6.3 | Inner-Mongolia |
| 15 | 1936-07-04 | 35.20 | 127.60 | | 6.0 | Korea Peninsular |
| 16 | 1937-08-01 | 35.40 | 115.10 | | 7.0 | Shandong |
| 17 | 1937-08-01 | 35.30 | 115.20 | | 6.8 | Shandong |
| 18 | 1940-01-19 | 43.30 | 121.30 | | 6.0 | Inner-Mongolia |
| 19 | 1940-08-05 | 40.10 | 122.10 | | 5.8 | Liaoning, China |
| 20 | 1941-05-05 | 46.70 | 127.10 | | 6.0 | Heilongjiang |
| 21 | 1942-07-09 | 43.50 | 121.90 | | 6.0 | Inner-Mongolia |
| 22 | 1942-09-02 | 47.00 | 127.00 | | 6.0 | Heilongjiang |
| 23 | 1944-12-19 | 39.70 | 124.30 | | 6.8 | Liaoning, China |
| 24 | 1945-09-23 | 39.50 | 119.00 | | 6.3 | Hebai |
| 25 | 1948-05-23 | 37.60 | 121.90 | | 6.0 | Shandong, China |
| 26 | 1949-01-14 | 33.20 | 121.00 | | 5.8 | Yellow Sea |
| 27 | 1952-03-19 | 39.00 | 125.50 | | 6.5 | Korea Peninsular |
| 28 | 1959-12-31 | 43.50 | 111.00 | | 5.8 | Inner-Mongolia |
| 29 | 1960-04-13 | 44.70 | 127.00 | | 5.8 | Jilin |
| 30 | 1963-06-21 | 47.90 | 130.60 | | 5.8 | Heilongjiang |
| 31 | 1966-03-08 | 37.35 | 114.91 | 8 | 6.8 | Hebai |
| 32 | 1966-03-22 | 37.50 | 115.08 | 9 | 6.7 | Hebai |
| 33 | 1966-03-22 | 37.50 | 115.10 | 9 | 7.2 | Hebai |
| 34 | 1966-03-26 | 37.68 | 115.26 | 15 | 6.2 | Hebai |
| 35 | 1966-03-27 | 37.55 | 115.27 | 20 | 5.8 | Hebai |
| 36 | 1966-03-29 | 37.35 | 115.03 | 25 | 6.0 | Hebai |
| 37 | 1967-03-27 | 38.50 | 116.50 | 30 | 6.3 | Hebai |
| 38 | 1969-07-18 | 38.20 | 119.40 | | 7.4 | Behai Sea |
| 39 | 1975-02-04 | 40.70 | 122.70 | 16 | 7.3 | Liaoning, China |
| 40 | 1976-04-06 | 40.20 | 112.10 | 18 | 6.2 | Inner-Mongolia |
| 41 | 1976-07-28 | 39.40 | 118.00 | 22 | 7.8 | Hebei (Tangshan) |
| 42 | 1976-07-28 | 39.20 | 117.80 | 19 | 6.2 | Hebei |
| 43 | 1976-07-28 | 39.70 | 118.50 | 22 | 7.1 | Hebei (Tangshan) |
| 44 | 1976-11-15 | 39.40 | 117.70 | 17 | 6.9 | Tianjin |
| 45 | 1977-05-12 | 39.20 | 117.70 | 19 | 6.2 | Hebei |
| 46 | 1978-05-18 | 40.75 | 122.63 | 13 | 5.9 | Liaoning, China |

Table 2. (*Continued*)

| No. | Year-month-date | Lat (°N) | Long (°E) | H (km) | M_S | Location |
|-----|-----------------|----------|-----------|--------|-------|----------------|
| 47 | 1979-07-09 | 31.47 | 119.25 | 12 | 6.0 | Jiangsu, China |
| 48 | 1979-08-25 | 41.20 | 108.05 | 18 | 6.0 | Inner-Mongolia |
| 49 | 1981-11-09 | 37.40 | 114.99 | 20 | 5.8 | Hebei |
| 50 | 1983-11-07 | 35.17 | 115.25 | 15 | 6.0 | Shandong |
| 51 | 1984-05-21 | 32.60 | 121.67 | 11 | 6.1 | Yellow Sea |
| 52 | 1984-05-21 | 32.63 | 121.60 | 18 | 6.2 | Yellow Sea |
| 53 | 1989-10-19 | 39.97 | 113.83 | 13 | 5.9 | Shanxi |
| 54 | 1991-03-26 | 39.93 | 113.88 | 12 | 5.9 | Shanxi |
| 55 | 1996-05-03 | 40.72 | 109.57 | 23 | 6.4 | Inner-Mongolia |
| 56 | 1996-11-09 | 31.83 | 123.10 | 16 | 6.1 | Yellow Sea |
| 57 | 1998-01-10 | 41.11 | 114.55 | 10 | 6.3 | Hebei |
| 58 | 2003-08-16 | 43.92 | 119.87 | 20 | 5.9 | Inner-Mongolia |
| 59 | 2004-03-24 | 45.38 | 118.25 | 18 | 5.9 | Inner-Mongolia |

where M is the magnitude of earthquakes. Using Eq. (4), we calculate the energy indexes of strong deep focal earthquakes varying with time. The sampling unit of time is 1 year. The result is displayed in Fig. 3. using Eq. (3), the real part of wavelet transforms is calculated and the contours are depicted in Fig. 2. From the Figure, multi-periods of strong deep focal earthquakes are obvious characteristics.

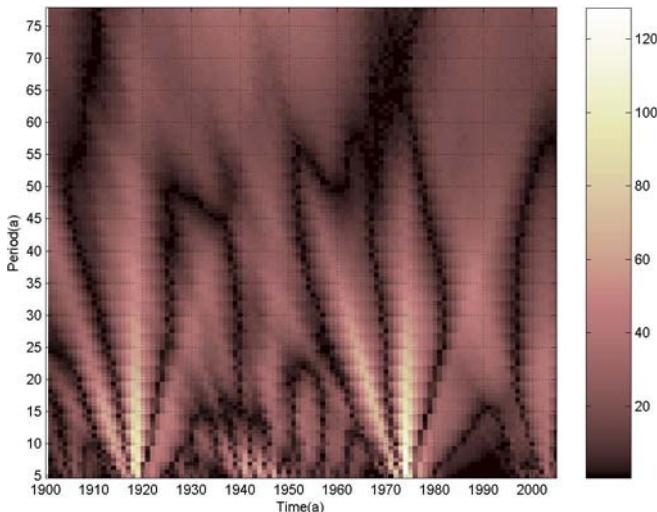


Fig. 2. Wavelet real part contour of the energy index.

We take db3 wavelet as fundamental functions and make multi-resolution analysis (MRA). The MRA maybe taken as a series of low- and band-pass filters. After the MRA, we obtain two coefficients in each layer denoted as a and d , respectively; a is the coefficient of low-pass filter, while d expresses that of band-pass filter. If sign f is transformed to fifth layer, then $f = d_1 + d_2 + d_3 + d_4 + d_5 + a_5$. Because sampling unit is 1 year and statistic period is about 100 years, the available periods should be from 2 to 100 years. The coefficient of each layer corresponds to the available period listed as following: d_1 (2–4 years), d_2 (4–8 years), d_3 (8–16 years), d_4 (16–32 years), and d_5 (32–64 years). As layers increasing, the corresponding periods become larger. The energy index of strong deep focal earthquakes and its multi-scale transform are shown in Fig. 3.

Further, the modulus of wavelet coefficients (namely the square of amplitude, which is equivalent to power spectrum) is calculated. The result of the modulus varying with periods is illustrated in Fig. 4. The salient peaks appear in the periods of 16 and the prominent period is from 16 to 32, corresponding to the d_4 layer. We will analyze the temporal characteristics quantitatively based on the d_4 layer. From Fig. 3, it is worth to note that the

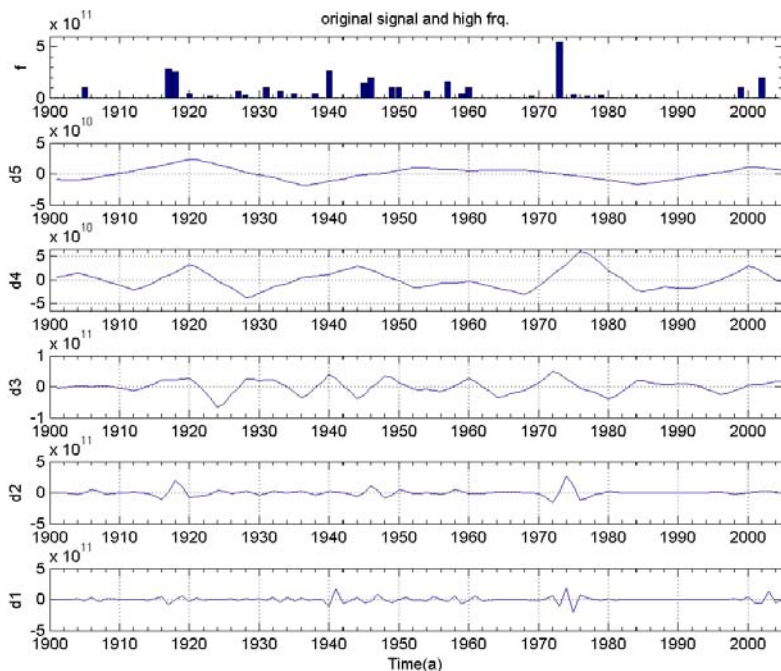


Fig. 3. The energy index and its wavelet coefficients in multi-scales.

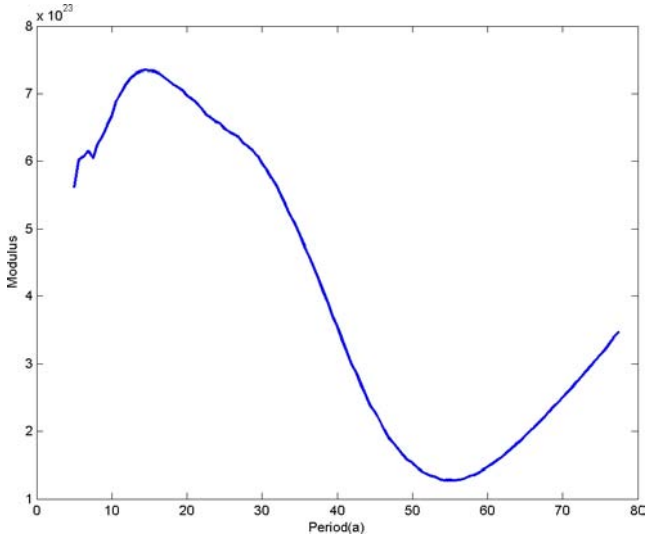


Fig. 4. Modulus of the wavelet coefficient.

coefficient is about balance around the value of zero. We use the coefficient around zero as an important criterion to distinguish active or quiet periods.

3.2. Relative active and quiet periods of deep focal earthquakes

Based on the results of multi-scale wavelet transform, we identify the relative active and quiet periods. We stipulate that the total time intervals of active periods should be approximately equal to that of quiet periods. Based on wavelet coefficients of the d4 layer, the periods are partitioned. From Fig. 3, we notice that the period before 1908 is not complete. Since 1908–2004, in total there are four complete periods, i.e., four active and four quiet periods. Detail parameters are listed in Table 3.

In Table 3, N represents the number of earthquakes in corresponding period and EI represents the energy index in the period. Time interval of four quiet periods is 50 years. Average interval of each quiet period is 12.5 years, while average interval of each active is 11.5 years. Earthquake number and energy index of strong deep focal earthquakes in each period are also listed in Table 3. For strong deep focal earthquakes (area A), 78.4% of energy index distribute in the four active periods.

Beside four active periods, there is a sub-active period of great deep focal earthquakes. From Fig. 4, the peak of wavelet coefficient appears in

Table 3. Active and quiet periods of strong deep focal earthquakes.

| Periods | Intervals | Years | Area A | | Area B | | Area C | |
|---------------------|-----------|-------|--------|--------|--------|--------|--------|---------|
| | | | N | EI | N | EI | N | EI |
| First quiet period | 1908–1915 | 7 | 0 | 0 | 1 | 1 | 1 | 2.1135 |
| Second quiet period | 1924–1935 | 12 | 6 | 2.8681 | 3 | 1.613 | 3 | 0.92407 |
| Third quiet period | 1951–1970 | 20 | 6 | 3.7856 | 3 | 0.9513 | 9 | 8.0384 |
| Fourth quiet period | 1985–1995 | 11 | 0 | 0 | 0 | 0 | 2 | 4.227 |
| Total ratio | | 50 | 12 | 21.6% | 7 | 30.5% | 15 | 38.6% |
| First quiet period | 1916–1923 | 8 | 5 | 6.5401 | 4 | 1.7411 | 1 | 4.217 |
| Second quiet period | 1936–1950 | 15 | 7 | 8.4521 | 9 | 2.8628 | 3 | 2.8342 |
| Third quiet period | 1971–1984 | 14 | 5 | 6.2005 | 4 | 3.2361 | 10 | 1.0487 |
| Fourth quiet period | 1996–2004 | 9 | 3 | 2.93 | 1 | 2.9854 | 5 | 1.5569 |
| Total ratio | | 46 | 20 | 78.4% | 18 | 69.5% | 19 | 61.4% |

1960. The sub-active period started from 1957 and ended in 1963, when a deep focal earthquake M_S7 occurred in 1957 and another $M_S6.8$ in 1960.

3.3. Spatial distribution of strong deep focal earthquakes

We analyze the spatial distribution of deep focal earthquakes in different active periods. From Table 1 and Fig. 1, we know that the strong deep focal earthquakes concentrate in a narrow belt from 129°E to 132°E. Here we only discuss difference along the north–south direction from 38°N to 45°N. For the second active period (1936–1950), two largest earthquakes located in the north end of area A. The epicenters of earthquake $M_S7.3$ in 1940 and $M_S7.2$ in 1946 are both in 44°N. For the fourth active period (1996–2004), the deep focal earthquakes are also located in the northern end. The epicenters of earthquake $M_S7.1$ in 2004 and $M_S6.8$ in 1999 located near 43.7°N. The epicenters of earthquake $M_S6.0$ in 2004 located in 44.79°N. The earthquake M_S7 in 1957 located in 43.9°N, which belongs to the sub-active period. There are strong deep focal earthquakes belonging to the second, fourth active periods and the sub-active periods reach the northern end of area A.

4. Characteristics of Strong Shallow Earthquakes and Tests

4.1. Spatial-temporal distribution of strong shallow earthquakes

In Fig. 1 we use different signs to express earthquakes in each active periods and other time intervals. For strong shallow earthquakes, we find that earthquakes in other time intervals in the western part seem more than

that in the eastern part. To confirm this cognition, we use 120°E meridian to divide the region in two parts. The eastern part is area B and the western is area C. For area B and area C, we calculate the earthquake number and energy index in each period separately. The data are also listed in Table 3. For strong shallow earthquakes in area B, 69.5% of energy index distributes in the four active periods, while 61.4% in area C. That is, about 80% energy index distributes in active periods in area A, about 70% in area B, and around 60% in area C. The ratios of energy index in active periods decline from eastern to western part.

4.2. Test of seismic characteristics

To test the territorial limits, we change split line from 115°E meridian to 123°E meridian. In each step, we calculate the ratio of energy index in active periods in the western part. The result is illustrated in Fig. 5. We notice that in the eastern part of 120°E meridian, the ratios are stable in high level. In the western part of 117°E meridian, the ratios are stable in low level. Between 117°E and 120°E meridian, the ratios are variable. We have tested magnitude cutoffs with $M_0 = 5.8$ and 6.0 , respectively. The result is also illustrated in Fig. 5. The curves have same tendency with $M_0 = 5.8$ and 6.0 .

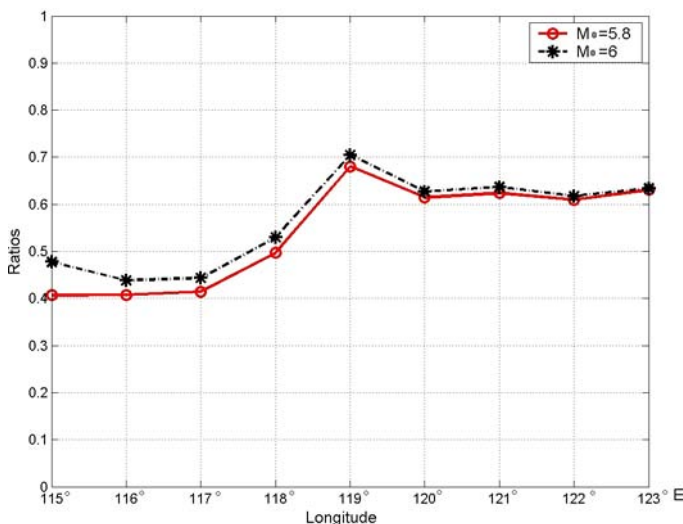


Fig. 5. Ratios of energy index change along longitude.

4.3. Seismic characteristics of Northeastern China

Seismicity in Northeastern China is relative weak comparing with that in Northern China. There have been only nine strong earthquakes since 1900, which can be divided as three clusters. The first cluster lasted about two years from 1940 to 1942 with four strong earthquakes. The second cluster started in 1959 and lasted about half and three years with three earthquakes. Till now only two strong earthquakes occurred in the third cluster, which started in 2003. The occurring times of the three clusters coincide with the second and fourth active periods and the sub-active period of strong deep focal earthquakes, respectively. From Sec. 3.3, we know that epicenters of strong deep focal earthquakes in the second, fourth active, and the sub-active periods reached the northern end around 44°N. That means strong earthquakes in Northeastern China correspond to the special active periods, when strong deep focal earthquakes reach the northern end.

4.4. Mechanism of the relationship between strong shallow earthquakes and great deep focal earthquakes

It is a common consensus that the relationship between great deep focal earthquakes and strong shallow earthquakes is not accidental and the mantle convection takes an important role. Here, we suggest a simple model to explain the relationship.

The Pacific plate subducts beneath the Japan Islands with almost constant dip angle of about 35°. Beneath Northeastern China and Korean Peninsula, the slab has the shallowest dip and where the great deep earthquakes concentrated. These great deep earthquakes distribute very similar with the trend of the slab structure and the largest depression of the 660-km discontinuity is located near the deepest earthquakes. The oceanic lithosphere is pushed downward by external forces, but encounters resistance in the 660-km discontinuity. The slab material piles up at the bottom of the mantle transition zone and sinks locally into the lower mantle because of the increasing mass and decreasing temperature. The slab penetration is limited in a spatial extent along the trending of the slab. The correlation of the deep earthquakes and the depression of the 660-km discontinuity might give some insight in understanding the occurrence of the deep earthquakes.¹⁸

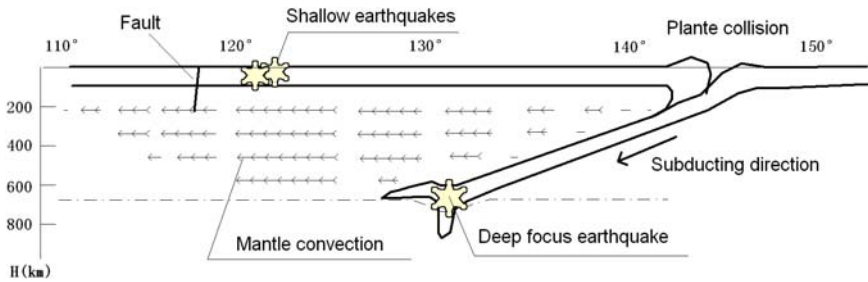


Fig. 6. Relationship among slab subduection, shallow, and deep focal earthquakes.

For last century, the movement of the slab is not stationary. When the slab moves faster, the resistance slab meet in the 660-km discontinuity reinforced. As a result of this faster movement, great deep focal earthquakes are active. Meanwhile, the mantle convection is stirred up. Owing to viscosity, the mantle convection will be quicken up gradually. The effect of mantle convection up to continental plate should be strongest just outside the mouth of the triangle region formed between the subducting slab and the continental plate. The synchronization of great deep focal earthquakes and strong shallow earthquakes in area B reveals that they are all resulted from the same geodynamical process. Spatial distribution of strong shallow earthquakes area B can also been explained in this mechanism.

5. Discussion and Conclusions

Although the seismic data are limited, only about 100 years and 33 strong deep focal earthquakes, it is clear that the temporal distribution of deep focal earthquakes is non-stationary. Through comparing seismicity of strong deep focal and shallow earthquakes, we can obtain some information of geodynamics in Northeastern Asia. Geodynamics in Northeastern Asia are debated for several decades. The collision of the Indian Plate with the Eurasian Plate would cause compression which may push the continent of eastern China eastward.¹⁹ An alternative source of the driving force for the movement of the continent of eastern China may be due to the convection of the material in the mantle.²⁰ The roles of the Pacific plate and Philippine Sea plate could not be ignored.^{21,22} From the seismic constraints, in the east of 120°N, the effect of the Indian Plate is less than that of the

Pacific plate. In Northeastern China, the seismicity might be affected by the subduction of Pacific plate, but only the strong deep focal earthquakes occurred northwards.

The Pacific plate subducts beneath the Japan, Northeastern China and Korean Peninsula, might stir up the mantle convection. Owing to viscosity, the mantle convection should attenuate gradually. The effect of mantle convection should be stronger just in the front of the subducting slab. The ratios of energy index in active periods declining from east to west might reveal the effects of subduction and its attenuation.

Temporal distribution of strong deep focal earthquakes is non-stationary. Since 1908, there have been four complete periods. Each active or quiet period averages about 12 years. From the view of energy index, total 79% of strong deep focal earthquakes occurred in active periods. Spatial distribution of strong deep focal earthquakes is inhomogeneous. The epicenters of strong deep focal earthquakes vary along the north-south direction from 39°N to 44°N. For second (1936–1950), the fourth (1995–2004) active period, and the sub-active period (1957–1963), the strong deep focal earthquakes reach the north end around 44°N.

For strong shallow earthquakes in Northeastern Asia, seismic characteristics in the eastern part are different from that in the western part. Temporal distribution of strong shallow earthquakes in the eastern part is more similar with that of strong deep focal earthquakes. In the eastern part of 120°E meridian, the ratios of energy index in active periods are stable in high level. In the western part of 117°E meridian, the ratios are stable in low level. There is a transition belt between 117°E and 120°E, where ratios are variable. Magnitude cutoffs with $M_0 = 5.8$ and $M_0 = 6.0$ have been tested. The results show that they have the same tendency as varying with longitudes.

Seismicity in Northeastern China is relative weak. There have been only nine strong shallow earthquakes since 1900, which can be divided into three clusters. The occurrence times of the three clusters are coincident with that of the second and fourth active periods and the sub-active period, respectively, when the strong deep focal earthquakes reached the northern end around 44°N.

In Northeastern Asia, strong deep focal earthquakes seem to have relationship with shallow earthquakes. The mantle convection and its attenuation might be the main mechanism.

Acknowledgments

The authors thank Ms. Xuan Wu for preparing figures for this paper. This study was supported by Grants-in-Aid for Research on Physical Mechanism of Mid-term Strong Earthquake Prediction from Department of Earthquake Monitoring and Prediction, China Earthquake Administration (No.10-5-08-09).

References

1. A. Gorbatenko and V. Kostoglodov, *Tectonophysics* **277** (1997) 165–187.
2. O. Gudmundsson and M. Sambridge, *J. Geophys. Res.* **103** (1998) 7121–7136.
3. C. H. Estabrook, *J. Geophys. Res.* **109**(B02306) (2004) doi: 10.1029.
4. R. Willemann and C. Frohlich, *J. Geophys. Res.* **92** (1987) 13927–13943.
5. S. X. Zang and J. Y. Ning, *Acta Geophys. Sin.* **39** (2) (1996) 188–202.
6. S. Omori, T. Komabayashi and S. Maruyama, *Phys. Earth Planet. Interiors* **146** (1–2) (2004) 297–311.
7. K. Mogi, *Tectonophysics* **17** (1973) 1–22.
8. J. Y. Wu, S. J. Yu and S. Y. He, *Acta Geophys. Sin.* **22** (4) (1979) 425–438 (in Chinese with English abstract).
9. Z. Q. Min, G. Wu, Z. S. Jiang, C. S. Liu and Y. L. Yang, *The Catalogue of Chinese Historical Strong Earthquakes* (Earthquake Publish House, Beijing, 1995) (in Chinese).
10. S. Y. Wang, G. Wu and Z. L. Shi, *The Catalogue of Chinese Earthquakes (from 1912 to 1990)* (Chinese Science and Technology Publish House, Beijing, 1999) (in Chinese).
11. Y. C. Li, *The Catalogue of Korea Peninsula Earthquakes* (Earthquake Publish House, Beijing, 2001) (in Chinese).
12. G. Wu, C. S. Liu, W. J. Zhai, Z. S. Jiang and D. Wu, *The Catalogue of Yellow Sea and its Coast Earthquakes* (Earthquake Publish House, Beijing, 2001) (in Chinese).
13. E. R. Engdahl, R. D. Van der Hilst and R. P. Buland, *Bull. Seism. Soc. Am.* **88** (1998) 722–743.
14. P. S. Cheng, C. M. Yin and X. L. Wang, *The Annual Bulletin of Chinese Earthquakes (1999)* (Earthquake Publish House, Beijing, 2002) (in Chinese).
15. R. F. Liu, C. M. Yin, P. S. Cheng, *The Bulletin of Digital Seismological Observations of Chinese Stations (2002)*. (Earthquake Publish House, Beijing, 2002) (in Chinese).
16. X. Y. Ma, G. Y. Ding and W. X. Gao et al., *Lithospheric Dynamics Atlas of China* (China Cartographic Publishing House, Beijing, China, 1989), pp. 16–21.
17. P. Kumar and E. F. Georgiou, *Rev. Geophys.* **35** (1997) 385–412.
18. X. Q. Li and X. H. Yuan, *Earth Planet. Sci. Lett.* **216** (2003) 679–691.

19. P. Molnar and P. Tapponnier, *Geology* **5** (1977) 212–216.
20. P. H. Huang and R. S. Fu, *Acta Geophys. Sin.*, **26** (1983) 39–47 (in Chinese with English Abstract).
21. Z. L. Shi, W. L. Huan, H. Y. Wu and X. L. Cao, *Geol. Sci.* **4** (1973) 281–293 (in Chinese with English abstract).
22. S. Y. Wang and P. S. Chen, *Acta Geophys. Sin.* **23** (1980) 35–45 (in Chinese with English abstract).

This page intentionally left blank

MOHO DEPTHS IN THE INDIAN OCEAN BASED ON THE INVERSION OF SATELLITE GRAVITY DATA

D. N. ARABELOS*, G. MANTZIOS and D. TSOULIS

Department of Geodesy and Surveying

Aristotle University of Thessaloniki

GR-54124 Thessaloniki, Greece

*arab@eng.auth.gr

An experiment for the estimation of the Moho interface was carried out in a part of the Indian Ocean, stretching over the high seismicity area between the east coasts of Africa and the west coasts of Sumatra. The estimation was based on the inversion of satellite-deduced gravity data using Least Squares Collocation and a statistical model consisting of two layers. The parameters for the construction of the necessary covariance functions were selected taking into account the statistical characteristics of the global elevation model DTM2002 and the global crustal database CRUST 2.0. The latter were treated in the frame of the prediction algorithm as *a-priori* values, which were tuned on the basis of a good agreement between the covariance function of the gravity anomalies and the covariance function of the gravity response of the two layers. An assessment of the estimated Moho depths was attempted, comparing the results of isostatically reduced sea surface heights from Jason-1 satellite altimetry. The isostatic reduction was computed using the DTM2002 topography and Moho depths resulting from (i) the Airy isostatic model, (ii) the CRUST 2.0 database, and (iii) the estimated Moho interface obtained from the present prediction method. The results showed a better smoothing of the sea surface heights when the estimated Moho depths were used.

1. Introduction

A powerful statistical tool that has been established in geodetic research over the last decades is Least Squares Collocation (LSC), a method which was initially proposed for the determination of the anomalous gravitational field from the combination of heterogeneous primary geodetic measurements.¹ Taking in account the fact that certain linear expressions of the disturbing potential are associated with further gravity field-related functionals, some of which represent observable quantities, LSC can be applied for the prediction of some geometrical-type quantities related to the

disturbing potential, such as geoidal heights or deflections of the vertical, provided that direct observations of gravity anomalies, which represent the fundamental observable in the frame of LSC, are available. In some recent investigations^{2,3} the possibility of applying the LSC approach as an inversion tool for the prediction of bathymetry in local and regional scales has been examined, by using marine gravity or gravity derived from altimeter data as the input observable data. The method used in these investigations was based on a two-layer model of the upper crust. The first layer was defined by the ocean bottom topography and the second one by the Moho interface, the discontinuity surface separating crust and mantle. The procedure was aimed to define the gravity response of these layers at sea surface, starting from their *a-priori* statistical information. The *a-priori* statistical characteristics that were used therefore included the mean and the standard deviation of the location of the interfaces (i.e. depth of each layer) with respect to mean sea level, the density contrast between the neighboring layers, the correlation length of the depths of each interface and its correlation with the previous layer. The construction of the covariance functions that were used for the computation of the resulting gravity response was initially based on some predefined numerical values for the aforementioned statistical parameters. Then, the computed gravity response was compared with the gravity at sea surface (observed or emerged from the analysis of satellite altimetry data). In the sequel, an iterative procedure was initiated in order to minimize the differences, between observed and computed gravity response by changing the *a-priori* given statistical characteristics of the two interfaces. The initial values for these statistical characteristics were taken from the existing digital terrain models (DTMs) and the application of Airy's isostatic model to the available terrain data in order to evaluate the corresponding Moho interface. A previous level of iterative optimization was elaborated for the construction of the necessary covariance functions entering into the LSC algorithm. The computed covariance function of the gravity response of the two layers according to the input statistical information that was chosen exploiting the available terrain information was compared with the empirical covariance of the real observations and an optimum agreement was pursued, by tuning properly these *a-priori* statistical characteristics of the layers.

In the implementation process of the aforementioned approach we elaborated new recently released terrain and gravity data of the best available resolution and accuracy at the present moment. More precisely we

exploited the improved global DTM2002 of Ref. 4, CRUST 2.0, a prototype 2-degree global crustal model,⁵ including apart from other information, the thickness and seismic/density structure of sedimentary basins more completely than in existing earlier models, as well as the detailed gravity model of Ref. 6 obtained from the analysis of satellite altimetric data.

The availability of these data motivated the present work, i.e., to investigate the possibility of an independent determination of the Moho interface based on an LSC inversion algorithm. Such a determination seems plausible only over oceanic areas, if one intends to use gravity data derived from satellite altimetry. More specifically, the idea would be to use the statistical characteristics of the bathymetry data directly from the DTM2002 model and the corresponding quantities for the Moho boundary surface directly from CRUST 2.0 database as the starting values for the computation of the covariance of the gravity response of the two layers at sea surface. Then, in order to tune this covariance function for the best possible agreement with the empirical covariance function of the gravity anomalies (according to the procedure described above) we can keep the statistical characteristics of the depth model unchanged (considering this as more accurate) and allow the parameters taken from CRUST 2.0 to vary. For a first numerical investigation of the aforementioned prediction process we have selected a part of the Indian Ocean bounded by $-18^\circ \leq \varphi \leq 0^\circ$, $50^\circ \leq \lambda \leq 96^\circ$.

2. Data

2.1. Gravity anomalies

From the 2' KMS2.0 gravity model derived from the analysis of altimeter data a $20' \times 20'$ grid was averaged covering the test area (see Fig. 1, black dots). In Fig. 2, the free-air gravity field is shown. The statistics of these free-air gravity anomalies are given in Table 1.

In Fig. 3, the empirical covariance function which is computed from these available altimetric gravity anomalies is shown.

2.2. Digital terrain model

The bottom topography from the recent DTM2002 was used for our experiments. From Fig. 4 it is evident that the bottom topography in the test area is very rough, especially in its western part, with mountains

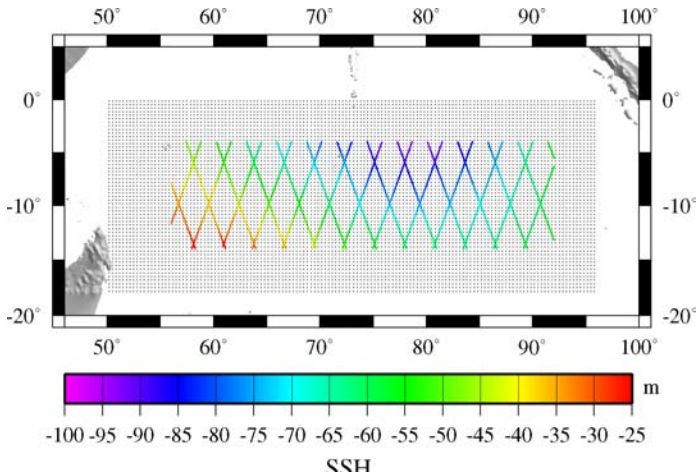


Fig. 1. The gravity grid in the Indian Ocean used for the estimation of the Moho interface (black dots) and the Jason-1 data used for the assessment of the results (colored dots).

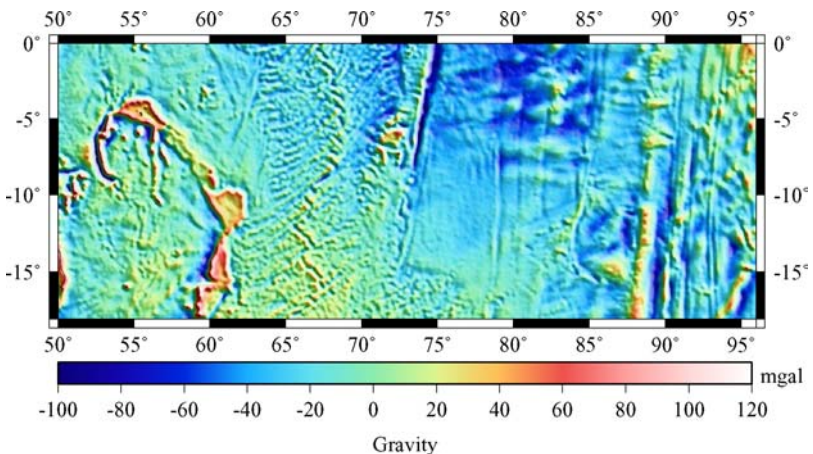


Fig. 2. Free-air gravity anomalies in the test area derived from satellite altimeter data.

Table 1. Statistics of gravity anomalies derived from altimeter data in the Indian Ocean (7452 data points). Unit is mgal.

| | Mean value | Standard deviation | Minimum | Maximum |
|----------|------------|--------------------|----------|---------|
| Free-air | 15.380 | 21.469 | -100.556 | 110.436 |

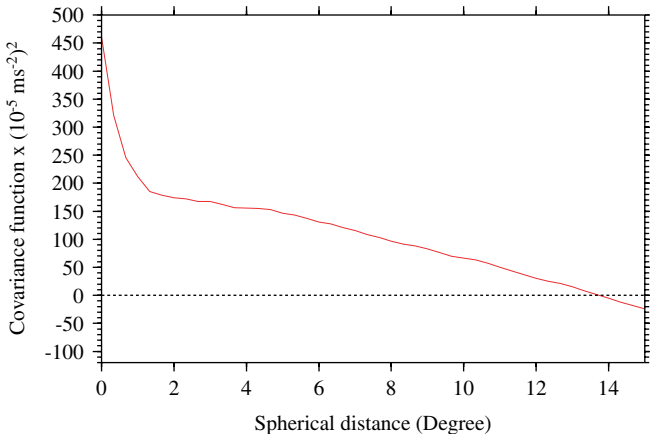


Fig. 3. The empirical covariance function of the free-air gravity anomalies in the test area.

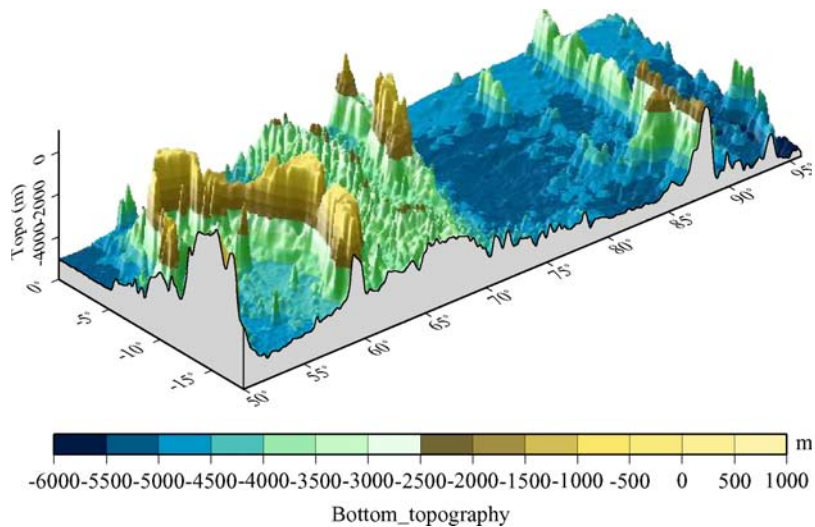


Fig. 4. Bathymetry in the test area according to the model of Ref. 4.

reaching the height of 5000 m. Some peaks are exceeding the sea surface, as it is shown in Fig. 1. This is a problem for the two-layer model used for the representation of the upper crust in the test area. Note the very strong correlation between the two patterns of Figs. 2 (gravity) and 4 (bottom topography) (Table 2).

Table 2. Statistics of the bathymetry in the test area. Unit is km.

| | Mean value | Standard deviation | Minimum | Maximum |
|--------|------------|--------------------|---------|---------|
| Depths | -4.21 | 1.09 | -6.28 | 0.92 |

2.3. CRUST 2.0

CRUST 2.0 is a global database of the Earth's crust with density and distinct layer thickness information. The model consists of seven distinct layers, namely ice, water, soft sediments, hard sediments, upper, middle and lower crust. The information related to each of these layers (density, depth of each layer with respect to mean sea level, compressional and shear wave velocity) is provided with a common resolution of $2^\circ \times 2^\circ$ for all layers. This spatial resolution implies that in our test area a total of 207 2-degree blocks are included. The statistical characteristics of the corresponding depths of the seventh CRUST 2.0 layer for this area are shown in Table 3.

2.4. Altimetry

In order to assess the estimated Moho interface sea surface heights (SSH) from JASON-1 mission have been used in a sub-area of the test area bounded by $-14^\circ \leq \varphi \leq -4^\circ$, $56^\circ \leq \lambda \leq 92^\circ$ (see Fig. 1, colored dots). The data (28,934 point values) are distributed on 26 tracks, extracted from cycle 105 of JASON-1 orbit. After the application of the usual geophysical corrections their statistics are shown in Table 4.

Table 3. Statistical characteristics of the CRUST2.0 depths in the test area. Unit is km.

| | Mean value | Standard deviation | Minimum | Maximum |
|--------|------------|--------------------|---------|---------|
| Depths | -12.17 | 2.73 | -24.74 | -9.27 |

Table 4. Statistics of the JASON-1 altimeter data used for the assessment of the results. Unit is m.

| | Mean value | Standard deviation | Minimum | Maximum |
|-----|------------|--------------------|---------|---------|
| SSH | -61.431 | 15.703 | -97.615 | -24.278 |

3. Inversion of the Gravity Anomalies Using LSC

According to the description in Sec. 1, the statistical characteristics of the two interfaces between ocean–lithosphere and lithosphere–mantle are needed for the construction of the necessary covariance functions used in the LSC prediction method. More specifically, initial values of the mean depth, the standard deviation, the correlation length, the density contrast, and correlation coefficient of each layer with respect to the one preceding it have to be defined. These values for the interface between ocean and lithosphere were taken from the statistics of the DTM2002 (see Table 5, row 1). For the second interface an independent source of information can be obtained either from the application of Airy's compensating mechanism based on the bathymetry data provided by the DTM2002 database, or by employing the depth information given by the last crustal layer of global digital crustal database CRUST 2.0. Using the values of -17.3 and 4.46 km for the mean and standard deviation, respectively, values that resulted from the Airy model, it was not possible to diminish the disagreement between the empirical covariance function of the gravity anomalies (Fig. 3) and the co-variance function of the gravity response of the layers at sea surface, when a heuristic tuning of the statistical parameters within acceptable ranges was applied. For this reason the values of -12.2 and 2.7 km, which were taken from the CRUST 2.0 model, were used instead. With the values of the initial parameters for the second interface shown in Table 5, row 2 an almost perfect agreement was achieved between the empirical covariance function of the gravity anomalies and the model covariance function of the gravity response of the layers.

In Fig. 5, the model covariance functions of the two interfaces is shown, based on the parameters of Table 5.

The statistics of the estimated depths to the interfaces 1 and 2 are shown in Table 6.

Table 5. Statistical characteristics of the two interfaces used for the LSC inversion of the gravity anomalies.

| Interface | Mean value (km) | Standard deviation (km) | Correlation length (km) | Density contrast (kg m^{-3}) | Correlation to previous layer |
|-----------|--------------------|----------------------------|----------------------------|--|-------------------------------|
| 1 | -4.2 | 1.09 | 180.0 | 1.700 | 1.000 |
| 2 | -12.2 | 2.70 | 200.0 | 0.610 | -0.975 |

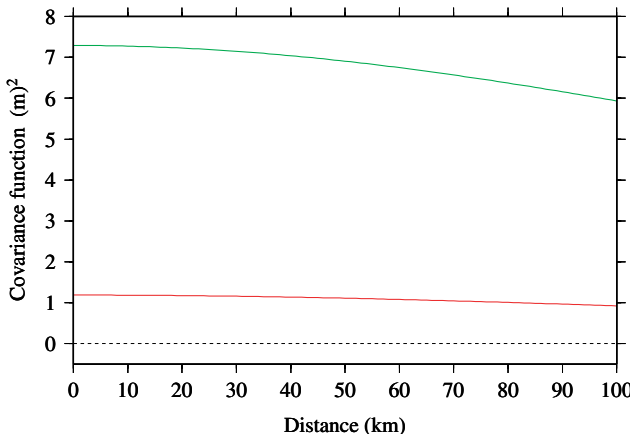


Fig. 5. Model covariance functions of the two interfaces based on the parameters of Table 5. The red line corresponds to the covariance function of interface 1 and the green to covariance function of the interface 2.

Table 6. Statistical characteristics of the estimated depths to interfaces 1 and 2. Unit is km.

| Interface | Mean value | Standard deviation | Minimum | Maximum |
|-----------|------------|--------------------|---------|---------|
| 1 | -4.441 | 0.567 | -6.890 | -0.130 |
| 2 | -12.143 | 0.944 | -19.760 | -7.280 |

4. Assessment of the Estimated Moho Depths in the Indian Ocean

4.1. Based on the comparison with CRUST 2.0

A comparison of the statistical characteristics of the estimated depths to interface 2 (Table 6, row 2) with the corresponding of CRUST 2.0 (Table 3) results in considerable differences in terms of the standard deviation and the minimum and maximum values. However, a direct comparison is not possible due to the different resolution of the two models.

4.2. Based on isostatic reductions on JASON 1 altimeter data using Airy or the computed model

The assessment of the estimated interfaces was also carried out comparing the results of topographic as well as of isostatic reduction of altimeter data

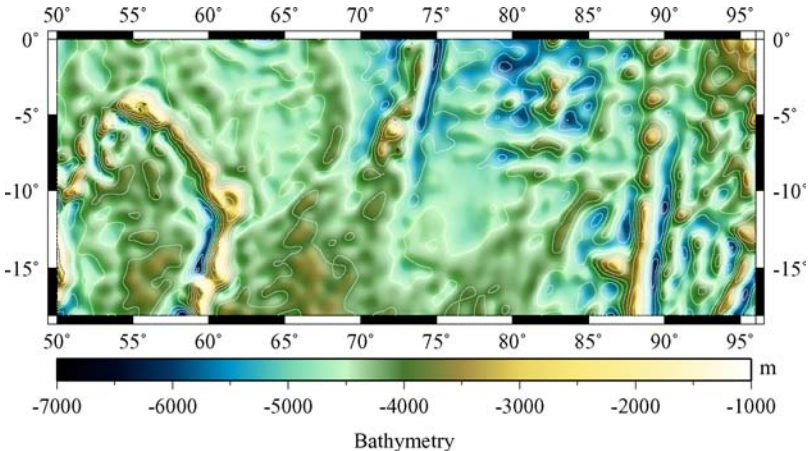


Fig. 6. The estimated bathymetry model in the Indian Ocean.

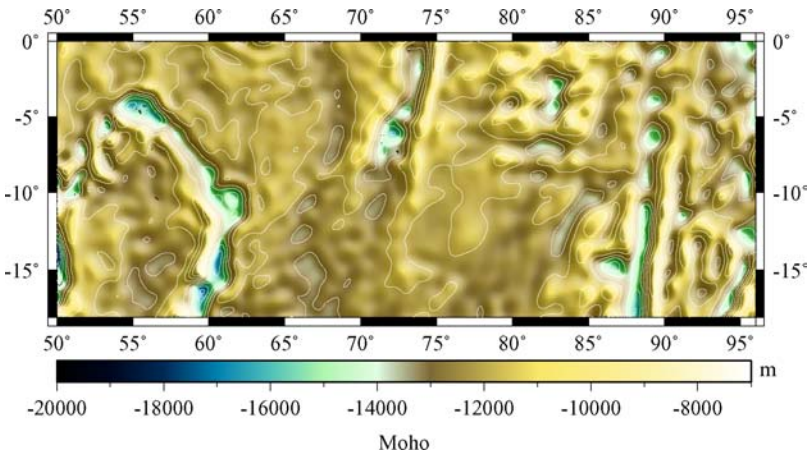


Fig. 7. The estimated Moho interface in the Indian Ocean.

from JASON-1 mission using depths from DTM2002, from the Airy isostatic model and from the estimated interfaces. According to Table 4 (column 5) the density values 2.727 and 3.337 kg m^{-3} were adopted for the lithosphere and the underlying denser layer.

In Table 7 the results in terms of the statistics of topographic reductions of SSH using (i) DTM2002 and (ii) the estimated layer 1 are shown. Topographic masses up to a distance of 30 km from the computation point were taken into account in both computations.

Table 7. Results in terms of the statistics of the topographic reduction of SSH (28,934 point values) using (i) DTM2002 and (ii) the estimated depths from the LSC inversion of the gravity anomalies. Unit is m.

| | Mean value | Standard deviation | Minimum | Maximum |
|----------------------------------|------------|--------------------|---------|---------|
| (i) DTM 2002 | | | | |
| Topographic reduction | -8.25 | 2.36 | -12.00 | -0.06 |
| Reduced SSH | -53.18 | 14.62 | -87.44 | -16.48 |
| (ii) Estimated depths of layer 1 | | | | |
| Topographic reduction | -8.96 | 1.02 | -12.09 | -3.98 |
| Reduced SSH | -52.47 | 15.25 | -87.36 | -16.87 |

Table 8. Results in terms of the statistics of the topographic reduction of SSH (28,934 point values) using (i) DTM2002 and (ii) the estimated depths from the LSC inversion of the gravity anomalies. Unit is m.

| | Mean value | Standard deviation | Minimum | Maximum |
|---|------------|--------------------|---------|---------|
| (i) DTM 2002 and Airy | | | | |
| Isostatic reduction | -6.88 | 1.58 | -8.54 | -0.80 |
| Reduced SSH | -54.55 | 14.97 | -89.53 | -18.00 |
| (ii) Estimated depths of layers 1 and 2 | | | | |
| Isostatic reduction | -9.75 | 8.08 | -35.10 | -60.18 |
| Reduced SSH | -51.68 | 10.13 | -92.73 | -25.98 |

In Table 8 the results in terms of the statistics of the isostatic reduction of SSH using (i) DTM2002 and Airy isostatic model and (2) the estimated interfaces are shown. In both cases the isostatic reduction was carried out taking into account masses up to 350 km from the computation point.

In Table 7 it is shown that the results of the topographic reduction of the SSH using DTM2002 are better than the corresponding using the estimated depths to the interface 1, at least with respect to the standard deviation of the reduced SSH. This was expected, since our model for the representation of the upper crust cannot account for the several peaks exceeding the sea surface. This is obvious also from the comparison of the maximum heights of DTM2002 (Table 2) and the estimated interface 1 (Table 6, row 1).

The results of the isostatic reduction of Table 8 are superior in the case of using the depths of the estimated interfaces, showing a very satisfactory compensation of the topographic masses.

A further computation regarding an additional isostatic reduction is presented in Table 9. It refers to the CRUST 2.0-deduced isostatic

Table 9. Results in terms of the statistics of the topographic reduction of SSH (28,934 point values) using (i) DTM2002 and (ii) the estimated depths from the LSC inversion of the gravity anomalies. Unit is m.

| | Mean value | Standard deviation | Minimum | Maximum |
|-------------------------|------------|--------------------|---------|---------|
| CRUST 2.0 (final layer) | | | | |
| Isostatic reduction | -0.14 | 32.15 | -32.94 | 96.99 |
| Reduced SSH | -61.30 | 26.01 | -139.10 | -21.91 |

reductions and the corresponding reduced SSH. Applied was the exact layer formation, as provided by CRUST 2.0 for the geometrical data of the seventh crustal layer describing, according to the model, the depth of the Moho interface for each of the $207\ 2^\circ \times 2^\circ$ cells that define the test area. The computations reveal a rather weak compensation of the CRUST 2.0-induced Moho structure. The obtained isostatically reduced SSH are characterized by rough statistical values, the overall computations do not comply with a compensating mechanism and this leads to the preliminary assumption that the crustal structure information provided by CRUST 2.0 for the specific oceanic region has to be assessed in more detail.

5. Conclusions

The application of the LSC algorithm for the prediction of the geometry of certain crustal interfaces may prove itself as an efficient tool in the frame of Moho-related investigations. This effort can be assisted from the current availability of digital databases for the topography, bathymetry, and crustal structure. However, the inhomogeneous and sometimes questionable accuracy of these databases and most importantly their different spatial resolution deserve a very cautious and critical application and interpretation of the final results. The investigations presented in this paper demonstrated that the LSC approach is in principle applicable for the task of predicting the structure of the Moho interface using gravity anomalies obtained from satellite altimetry data. The method has been applied successfully over a region defined at the Indian ocean, which indicated the significance of the method in areas such as oceans, where in most cases the only available primary observables with a very dense coverage (at least for the time being) are observations of satellite altimetry. The numerical investigations led to two major issues that are related with the present research and deserve further investigations

(i) the fine tuning of the statistical parameters, which is essential for the construction of the involved covariance functions, and (ii) the bad performance of CRUST 2.0 over the specific region of the Indian Ocean. As far as the first point is concerned, one should probably investigate the possibility of introducing different families of covariance functions into the LSC algorithm, such that certain local tectonic characteristics may be taken into account. On the other hand the overall performance of crustal database CRUST 2.0, should be assessed further by defining more regional test windows of the model globally and interrelate the CRUST 2.0-inherited characteristics with regional independently obtained geophysical observations and corresponding models.

References

1. H. Moritz, *Advanced Physical Geodesy* (Wichmann Verlag, Karlsruhe, 1989).
2. D. Arabelos, *IAG Proc.* **119** (1997) 105–112.
3. C. C. Tscherning, R. Forsberg and P. Knudsen, in *Mare Nostrum*, Geomed Report 4 (Eds. D. Arabelos and I. N. Tziavos) (Ziti Publishing, Thessaloniki, 1994), pp. 133–145.
4. J. Saleh and N. Pavlis, in *3rd Meeting of the IGGC*, (Ed. I. N. Tziavos) (Ziti Editions, Thessaloniki, 2002), pp. 207–212.
5. C. Bassin, G. Laske and G. Masters, *EOS Trans. AGU* **81** (2000) F897.
6. O. B. Andersen and P. Knudsen, *J. Geophys. Res.* **103**(C4) (1998) 8129–8173.
7. G. Mantzios, Master Thesis (The Polytechnic Faculty, School of Rural and Surveying Engineering, Thessaloniki, 2005).
8. D. Tsoulis, *J. Geodesy* **78** (2004) 7–11, DOI: 10.1007/s00190-003-0360-3.

POST EARTHQUAKE DEBRIS MANAGEMENT — AN OVERVIEW

RAJU SARKAR

*Department of Civil Engineering
G.B. Pant Polytechnic
New Delhi – 110 020
sarkar.raju@yahoo.com*

Every year natural disasters, such as fires, floods, earthquakes, hurricanes, landslides, tsunami, and tornadoes, challenge various communities of the world. Earthquakes strike with varying degrees of severity and pose both short- and long-term challenges to public service providers. Earthquakes generate shock waves and displace the ground along fault lines. These seismic forces can bring down buildings and bridges in a localized area and damage buildings and other structures in a far wider area. Secondary damage from fires, explosions, and localized flooding from broken water pipes can increase the amount of debris. Earthquake debris includes building materials, personal property, and sediment from landslides. The management of this debris, as well as the waste generated during the reconstruction works, can place significant challenges on the national and local capacities. Debris removal is a major component of every post earthquake recovery operation. Much of the debris generated from earthquake is not hazardous. Soil, building material, and green waste, such as trees and shrubs, make up most of the volume of earthquake debris. These wastes not only create significant health problems and a very unpleasant living environment if not disposed of safely and appropriately, but also can subsequently impose economical burdens on the reconstruction phase. In practice, most of the debris may be either disposed of at landfill sites, reused as materials for construction or recycled into useful commodities. Therefore, the debris clearance operation should focus on the geotechnical engineering approach as an important post earthquake issue to control the quality of the incoming flow of potential soil materials. In this paper, the importance of an emergency management perspective in this geotechnical approach that takes into account the different criteria related to the operation execution is proposed by highlighting the key issues concerning the handling of the construction and demolition debris following an earthquake.

1. Introduction

Every year natural disasters, such as fires, floods, earthquakes, hurricanes, landslides, tsunami, and tornadoes, challenge various communities of

the world. Natural disasters strike with varying degrees of severity and pose both short- and long-term challenges to public service providers. As a result of a natural disaster or conflict, large quantities of the building stock and infrastructure are often damaged beyond economic repair and require demolition with subsequent removal of debris. The management of this debris, as well as the waste generated during the reconstruction works, can place significant challenges on the national and local capacities. If these wastes are not properly managed, they can subsequently impose serious environmental and economical burdens on the reconstruction phase. This also includes the negative effect that debris can have on the general municipal waste collection and handling operations, which is one of the major challenges following disasters.

Earthquakes generate shock waves and displace the ground along fault lines. These seismic forces can bring down buildings and bridges in a localized area and damage buildings and other structures in a far wider area. Secondary damage from fires, explosions, and localized flooding from broken water pipes can increase the amount of debris. Earthquake debris includes building materials, personal property, and sediment from landslides. Earthquake debris removal is a major component of every post earthquake recovery operation. Much of the debris generated from earthquake is not hazardous. Soil, building material, and green waste, such as trees and shrubs, make up most of the volume of earthquake debris. Most of this debris can be recycled into useful commodities. Debris from earthquake and other natural disasters like floods, landslides, hurricanes, tornadoes, and fires falls into a few major categories as shown in Table 1.

Table 1. Major categories of disaster debris.

| | Damaged buildings | Sediments | Green waste | Personal property | Ash and charred wood |
|-------------|-------------------|-----------|-------------|-------------------|----------------------|
| Earthquakes | X | X | X | X | X |
| Floods | X | X | X | X | |
| Landslides | X | X | X | X | |
| Hurricanes | X | X | X | X | |
| Tornadoes | X | | X | X | |
| Fires | X | | | X | X |

2. Post Earthquake Debris Separation

Under any earthquake disaster situation, it may not be practical to employ a system of debris separation where hazardous debris is identified and isolated from other debris. This would be the ideal system; however, it would not be practical or even feasible, due to the magnitude of the earthquake-related debris and the time and labor it would require to identify the potential hazardous debris. In addition, there may not be previously organized debris management practice in most or all of the earthquake-affected areas; most of the hazardous debris recycled or reused along with other debris. Even in countries with an organized system of hazardous earthquake debris separation, it becomes hard to implement when an earthquake occurs.

It will be most effective for the country to separate and dispose of the earthquake debris based on the classifications, vegetative and non-vegetative. This separation of vegetative debris from the non-vegetative debris could take place at either the collection points or temporary staging areas.

2.1. *Vegetative debris*

The vegetative debris includes trees, stumps, brush, and leaf. The disposal of vegetative debris does not typically result in groundwater contamination; such debris can be collected, stockpiled, land filled, used for firewood, as compost or as mulch.

2.2. *Non-vegetative debris*

This non-vegetative debris is the largest portion of the debris produced during an earthquake disaster. The materials that remained after the earthquake includes aggregates, wood, metals, gypsum, plastics, bricks, tiles, and asbestos roofing. The materials from the construction and debris class of debris can generally be recycled, however, materials containing asbestos need to be handled very cautiously. These materials should ideally be handled wet, and if possible, bagged and buried.

Two of the main classes of non-vegetative earthquake debris are aggregates and construction and demolition debris. Aggregate debris, such as asphalt pavement and concrete, results from the destruction of roadways. These materials, if separated, can be stockpiled and reused after reprocessing them to the specifications used for road base aggregate or

solid fill material. The second class, construction and demolition debris is also a large component of earthquake debris. This debris is the result of the destruction of homes, commercial and non-commercial buildings, and other structures. Most of the non-vegetative debris can also be reused or recycled. Any non-vegetative debris that cannot be reused or recycled must be carefully disposed in a properly managed dumpsite to avoid groundwater pollution. Based on site-specific conditions of geology and hydrogeology, a debris disposal site could be strategically located above the groundwater table and over a layer of densely pack soil, such as clay, that would act as a barrier to leachate entering the groundwater supply. Another alternative would be investing in a lined landfill that would help to prevent leachate penetration into groundwater.

3. Post Earthquake Debris Management Plan

Any community likely to be faced with significant debris from an earthquake disaster should develop a debris management plan (Fig. 1). To facilitate coordination, this plan could be a specific task under the community's general emergency plan. This guide, based on experiences of other communities, suggests some helpful planning considerations. It describes:

1. Steps a community can take to prepare for dealing with the waste created by earthquake and to speed recovery after such earthquake; and
2. Ways communities can reduce the burden on their municipal solid waste management systems in the event of an earthquake.

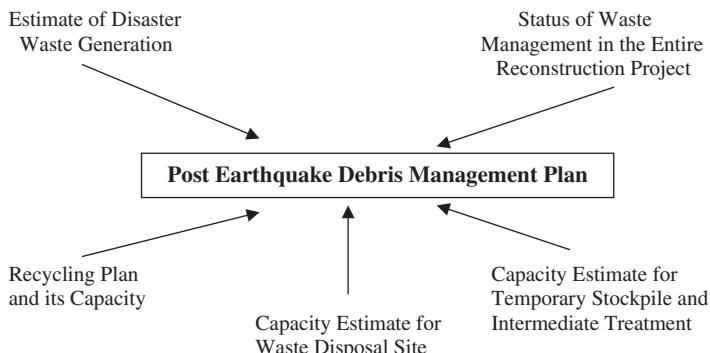


Fig. 1. Flow chart for disaster waste management plan.

This guide does not provide all the tools, a planner will need to write a debris management plan, however. The development of an earthquake debris management plan usually requires input from neighboring communities, state officials, local contractors, and a variety of local agencies. This guide is intended to help a planner begin the development process.

Preparing an earthquake debris management plan in advance can pay off in the event of an earthquake disaster. Planning can help a community identify its debris collection, recycling, and disposal options. Although the recovery process will take a long time, perhaps even years, careful planning will prevent costly mistakes, speed recovery, and avoid creation of more waste. A plan also can save money by identifying cost-effective debris management options and sources of help, increasing control over debris management in the community, and improving administrative efficiency.

4. Selection of Post Earthquake Debris Collection and Storage Sites

The most common suggestion from communities that have experienced earthquake disaster is to pre-select debris staging sites that will be used for temporary storage and processing of debris. Convenient local sites allow collection crews to reduce travel time when transferring debris to processing or disposal facilities and result in faster street clearing. Site operators can sort debris for recycling or disposal, as well as answer questions from the public. These sites can be used to store green waste before transferring it to another facility, or they can be used to chip and mulch green waste on site. Communities also can use these sites to distribute free mulch or wood to the public.

Selection of the sites should be based on planned activities, such as staging, collection, storage, sorting, recycling, land-filling, and burning of debris. Pre-selection of sites speeds the implementation of the debris management plan. Also consideration should be made for access to heavy equipment, lack of impact on environmentally sensitive areas, and convenience to collection routes. Investigate possible impacts on adjacent housing, since the sites could produce noise at levels deemed unacceptable by residents or attract rodents that may carry disease. Evaluate and document the condition of these sites prior to use. The government agencies

involved will be responsible for returning these sites to their original condition. Be sure to establish agreement on the schedule for return of the property to the owners and the degree of rehabilitation to the property.

If residents will be asked to bring earthquake debris to collection sites, the concern community should include these locations in its disaster communication strategy, so that information is immediately available to the public in the event of an earthquake. Schedules and staffing plans for these sites should take into account that the busiest times for residents dropping off home-related debris are likely to be evenings and weekends.

5. Types of Earthquake Debris Disposal Sites

Disposal of debris is a major concern following an earthquake. No matter what state a person live in, the type of debris the person will encounter after an earthquake will be much the same: damaged buildings, downed trees, building materials, and household and other types of hazardous waste. What varies is the way in which each state disposes of the debris. Some states have particular issues, such as soils, which limit the areas in which debris can be stored. Since debris cannot be stored or buried in floodplains, coastal areas cannot be used for debris management. In the mountains, many of the sites that seem the best for dumping are at the bottom of a hollow — right in the middle of the floodway.

In the past, debris from earthquake was simply buried or burned in the community. As demonstrated by recent earthquake, burying or burning debris as a means of waste management may not be acceptable. Citizens do not want to inhale the smoke from open burning. Municipalities do not want to risk contamination of drinking water and soil from uncontrolled burial of debris. Under normal circumstances, much municipal solid waste is recycled. The remainder is disposed of in sanitary landfills or in sophisticated combustors, both of which are equipped with devices to control pollutants. Often, however, these standard waste disposal options are not sufficient to handle the overwhelming amount of debris left after an earthquake. Further adding to the disposal dilemma is the fact that many municipalities are reluctant to overburden or deplete their existing disposal capacity with earthquake debris. Scarcity of available sites always leads to severe problem to secure

ample debris disposal space in developing countries. There are three different types of systems available based on the degree of control of leachate from the reclaimed debris:

1. Least controlled landfill sites for safe and stable debris
2. Controlled landfill sites for safe but unstable debris
3. Strictly controlled landfill sites for hazardous debris.

As shown in Table 2, the debris generated from an earthquake is basically construction waste in general. Construction waste amounts to about 20% of all industrial wastes, and includes concrete and brick, plastic, glass and ceramic, metal, rubber, sludge, wood, and oil wastes. The five categories can be disposed of at “least controlled” landfill sites because they are safe and stable materials for reclamation.

6. Transportation of Post Earthquake Debris

Transportation of post earthquake debris is another important activity after the earthquake. Debris is generally transported either to temporary storage locations or final disposal sites. Due to heavy or partial collapse of road network, many debris-transporting vehicles become an additional cause of traffic congestion. The lack of coordination between the capacity of the access road and the upper limit of daily capacity of the vehicles at the disposal sites may lead to further traffic congestion. So, local government authority or non-governmental organization should take necessary arrangement or should make necessary plan so that due to traffic congestion no further development works suffer.

Table 2. Generation of post earthquake debris and the type of recycling material.

| No. | Debris generation | Type of recycling material | Purpose |
|-----|------------------------|----------------------------|----------------------------|
| 1 | Non-combustible debris | Concrete | Reclamation Construction |
| | | Metal | Steel manufacture |
| 2 | Combustible debris | Wood | Pulpwood, fuel, fertilizer |

7. Temporary Storage and Intermediate Treatment

If onsite separation of debris is not possible due to insufficient land available, debris material is not acceptable until such waste goes through a separation and size reduction process. So possibility of stockpile of mixed debris therefore increased at open spaces designated as temporary storage. This debris can be separated into three piles: incombustible debris, wooden debris, and residential debris. As a means to reduce the amount of debris and also for sanitary reasons, illegal incineration at temporary stockyard may be continued for a longer period if local government bans it completely. In other cases, demolition contractors may dump and incinerate the debris illegally. Air pollution from ashes and odor may become an issue for the neighbors, so the Environmental Agency in collaboration with local government should conduct a field investigation. Illegal incineration always causes more psychological dissatisfaction for the citizens living around the temporary storage locations.

8. Post Earthquake Debris Management Related to Various Phases after the Disaster

There are three phases involved in the earthquake debris management after the disaster and they are:

1. *Immediate response phase:* In this phase for the first several days after the earthquake, debris should clear for search and rescue of disaster victims by both local residents and emergency officers such as fire-fighters, policemen, and the defense forces everywhere in the impacted area.
2. *Recovery phase:* In this phase, some of the collapsed buildings and highway bridges can also be demolished and removed by the local and national government authority to secure the trunk road networks for recovery operations.
3. *Restoration phase:* In this phase, debris clearance generated by the individual houses and private buildings should begin and it becomes a serious issue to coordinate the entire process from the application for debris clearance to the processing at the final disposal site.

Table 3. Post earthquake debris management related to each phase after the disaster.

| No. | Phase | Required content |
|-----|--------------------------|--|
| 1 | Immediate response phase | Rescue, prevention of secondary earthquake, and security of life |
| 2 | Recovery phase | Security of road network |
| 3 | Restoration phase | The basis for restoration process. Preservation of property |

Debris clearance operations should begin immediately after the earthquake as shown in Table 3.

9. Basic Rules for the Post Earthquake Debris Management

Since there is always an upper limit for debris disposal space, there are three basic rules for the debris management and they are:

1. *Minimization of debris generation:* There has been practice in many ways and they are
 - (i) Size reduction by milling and shredding
 - (ii) Incineration
 - (iii) Dehydration
 - (iv) Desiccation
2. Practice of making the debris sanitary
3. *Promotion of recycling:* The debris may be either disposed of at a reclamation landfill site as soil material or reused as material for construction.

In order to practice these three rules, it is important to coordinate all the tasks required for waste management in the following stages:

1. Demolition
2. Transportation
3. Intermediate treatment
4. Final disposal at landfill site.

10. Post Earthquake Debris Management Related to Night Soil, Garbage Collection, and Collapsed Structures

The processing of excrement is the first issue of the post earthquake debris management program, because the water supply system and the sewage system face heavy damage due to the earthquake (Fig. 2).

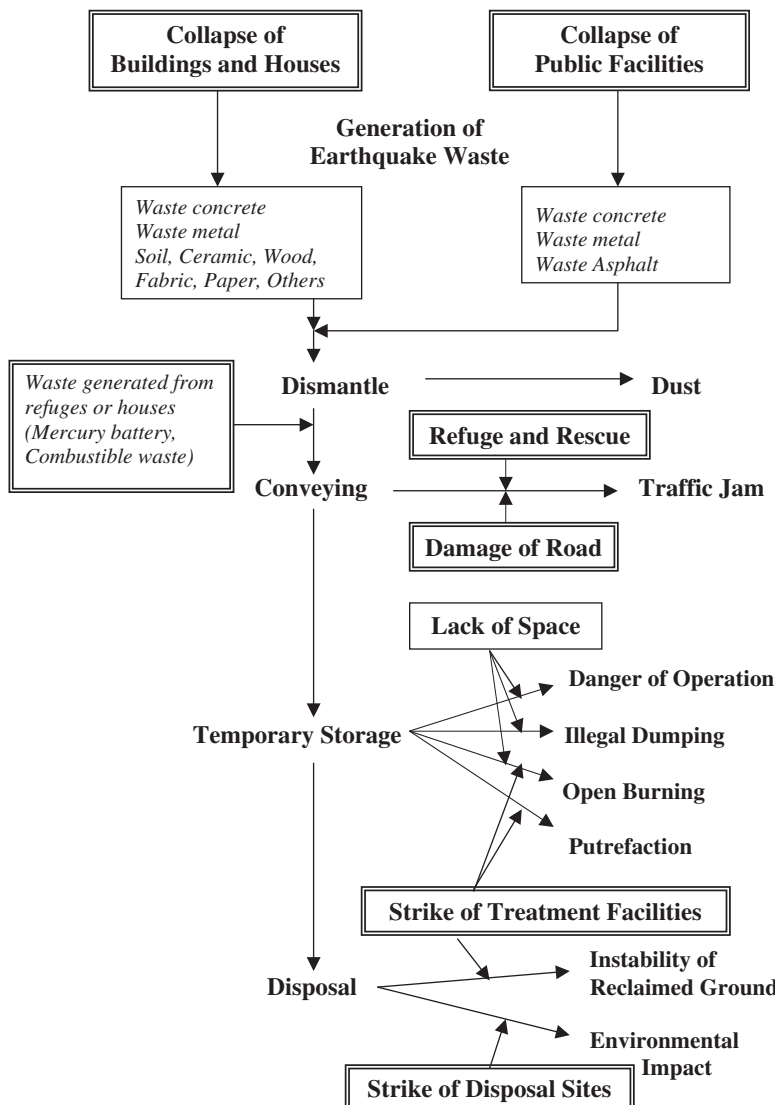


Fig. 2. Outline of post earthquake debris management and its impact.

The stockpiling of residential solid waste on streets is another distinctive earthquake debris management problem. Many food and drink containers and bulky waste are generated soon after the earthquake. The garbage collection system may be delayed due to unseen circumstances which may lead to stockpiling on the streets. When this debris is removed to a temporary storage location, garbage may be stockpiled in a different form from the rest of the wastes. However, the pile of garbage can remain in the parent position for many days even after the regular garbage collection and combustion service restored.

Another big concern is the environmental impact due to rough treatment of damaged or abandoned electric appliances containing hazardous chemicals, such as refrigerators containing fluorocarbons. As a result of a great effort by the local government in cooperation with volunteer groups these abandoned refrigerators can be collected and the fluorocarbon can be extracted from them safely for the environmental protection.

Again another major issue of post earthquake debris is the management of the collapsed houses, buildings, and other public facilities. The debris from houses and buildings includes not only the waste timber, steel and concrete blocks, but also soils, cloths, furniture, electric appliances, and so on. In most cases they are mixed up with each other. For collapsed buildings and public facilities, the debris contains mainly concrete and scrap steel. On site separation of the debris may therefore be easier than for individual ordinary houses.

11. Emergency Management Perspectives for Post Earthquake Debris Clearance

It is important to treat the debris clearance issue as one of the most important emergency management issues. Since the debris clearance issue adopted a construction waste processing scheme as the model for its operation, civil engineers in this field tended to regard debris clearance as a matter of securing ample space for temporary stockpiling and disposal. From the geotechnical perspective however, it would be of great concern to have an incredible amount of material less qualified for reclamation. The future of the post earthquake debris reclaimed land might be jeopardized unless proper precaution has been taken to consider the geotechnical engineering aspects to control the quality of incoming reclaimed material. For this purpose, information about the entire debris clearance management program and the coordination based on such information are indispensable.

12. Conclusion

The first response to an earthquake must place its emphasis on saving human life. This includes emergency rescue activities as well as restoring life lines such as water, electricity, and gas. In addition to these crucial activities, there also lies a requirement to deal with the large quantities of construction and demolition debris which are generated after the earthquake. A strategy for the management of this debris stream must include measures to ensure that the debris are sorted into recyclables, transported to recycling depots, and processed into recycled materials which can be utilized in the ensuing reconstruction works. The opportunities to recycle large proportions of the earthquake debris have been presented from several past earthquakes the challenge now lies in the preparation of “emergency earthquake debris management system” before the actual earthquake occurs. Such a system should be integrated with the household waste management operations, and must take into account the sustainability of any systems implemented.

References

1. F. Baycan and M. Petersen, *Disaster Waste Management-C&D Waste*, (Ministry of Environment, Ankara, Turkey).
2. Department of Environmental Engineering Sciences, *Recommended Management Practices for the Removal of Hazardous Materials from Buildings Prior to Demolition* (University of Florida, Disasters Database, <http://www.cred.be/emdat/disdat2.htm>, 2001).
3. FEMA, *Planning for Disaster Debris, Handbook*.
4. H. Hayashi and K. Katsumi, *Generation and Management of Disaster Waste, Special issue of Soils and Foundations* (Japanese Geotechnical Society, 1996), pp. 349–358.
5. Y. Kobayashi, *Proceedings of the International Earthquake Waste Symposium*, Osaka, UNEP Technical Publication Series 2, (1996).
6. N. Kuramoto, *Proceedings of the International Earthquake Waste Symposium*, Osaka, UNEP Technical Publication Series 2, (1996).
7. E. K. Lauritzen, *Proceedings of the International Earthquake Waste Symposium*, Osaka. UNEP Technical Publication Series 2, (1995).
8. E. K. Lauritzen, *Disaster Waste Management*, (ISWA Yearbook 1996/1997).
9. F. T. Saatcioglu *et al.*, *2nd National Earthquake Engineering Conference*, Istanbul (1993).
10. J. H. Skinner, *Proceedings of the International Earthquake Waste Symposium*, Osaka. UNEP Technical Publication Series 2, (1995).
11. UNDP, *Regional Management Plan for the Rubble in the Marmara Earthquake Region*, Final Report (1999).

OCEAN SCIENCE (OS)

This page intentionally left blank

BURIED AND SURFACE POLYMETALLIC NODULE DISTRIBUTION IN THE EASTERN CLARION–CLIPPERTON ZONE: MAIN DISTINCTIONS AND SIMILARITIES

R. KOTLINSKI*,† and V. STOYANOVA‡,§

†*Interoceanmetal Joint Organization,*

9, Cyryla i Metodego, 71-541 Szczecin, Poland

‡*Institute of Marine Science, University of Szczecin,
13, Waska, 71-415 Szczecin, Poland*

**r.kotlinski@iom.gov.pl,*

§*v.stoyanova@iom.gov.pl*

The distribution pattern, abundance variations, morphology, chemical and mineralogical composition of buried polymetallic nodules in the eastern Clarion–Clipperton Zone (CCZ) are presented. Our observations are based on data collected from 59 boxcore stations, which comprise about 22.6% of all sampled stations in the Interoceanmetal exploration area site B₂ in the eastern CCZ, with recorded buried and surface polymetallic nodules. The majority of stations with buried nodules (>90%) is below 4300 m water depth and is associated mainly with seafloor hills and slopes of ridges and depressions. Buried nodules lie completely beneath the active sediment–water boundary layer (with thickness range from 0 to 15 cm), and they are vertically recorded down to the 45 cm in sediment cores. Abundance of buried nodules varies from 0.2 to 22.1 kg/m², averaging 3.2 kg/m². By comparison, surface nodules are more abundant, varying from 0 to 20.2 kg/m², averaging 10.3 kg/m². As a general rule the size of buried nodules is larger than surface nodules, and >27% of recovered buried nodules exceed 10 cm in diameter. It is assumed that more than 90% of analyzed buried nodules have a diagenetic origin; however, the identification of factors and conditions responsible for their formation still remains unknown.

1. Introduction

Polymetallic nodule deposits occur in various areas of the World Oceans: on shelves, abyssal plains, hills, seamounts, and rises.

Nodules are also found throughout the sediment column, but often they lie on the water–sediment interface and partly buried in the sediment. They vary greatly in abundance, in some cases they can cover more than 70% of the deep seafloor.¹

The most promising polymetallic resources in terms of nodule abundance and high contents of the base metals (nickel, copper, manganese, and cobalt) occur in the Clarion–Clipperton Zone (CCZ), an area that has been allocated by the International Seabed Authority (ISA) for exploration by several contractors: DORD (Japan), COMRA (China), Government of the Republic of Korea, IFREMER/AFERNORD (France), Interoceanmetal (IOM) (a consortium formed by Bulgaria, Cuba, Czech Republic, Poland, Russian Federation, and Slovakia), Yuzhmorgeologiya (the Russian Federation), and BGR (Germany).^{2–4} Another prospective area, similarly allocated, lies in the Mid-Indian Basin and is a subject of exploration by the Government of India.^{5,6}

The CCZ is located in the eastern part of the Pacific plate and is bounded by the Clarion and Clipperton sublatitude transform faults in the north and south, respectively.² The area allocated for the IOM exploration activity under a contract with the ISA, covers 75,000 square km in the eastern part of the CCZ and extends longitudinally over 510 km with mean width of 150 km.

During 2001–2005, IOM carried out three sea-going cruises which collected bathymetric data using a multi-beam echo-sounder system “Simrad”, and bottom sampling at 261 boxcore stations. For the first time in the IOM’s exploration area, buried nodules were recorded, occurring at 8–45 cm below the seafloor. They were found at 59 stations representing about 22.6% of all sampled stations within the entire IOM exploration area. This paper summarizes the distribution pattern, abundance, types, and chemical composition of buried nodules and compares their main features to surface nodules which have been collected within the IOM contract area.

2. Geological Setting of the IOM Exploration Area

The seafloor within the boundaries of the IOM exploration area forms an undulating (4300–4400 m below sea level) hilly plain, crossed by a system of longitudinal horsts (4100–4300 m depth) and grabens (4400–4750 m). Surface relief of the hilly plain is generally less than 100 m, with hills and ridges exceeding 100 m in places. Less common are volcanic structures (~30%), characterized by slopes of more than 7°.

The seabed of the IOM exploration area is composed of sediments representing the Early Miocene–Late Oligocene Marquesas formation as well as the Pliocene–Early Quaternary Clipperton formation (Fig. 1).³

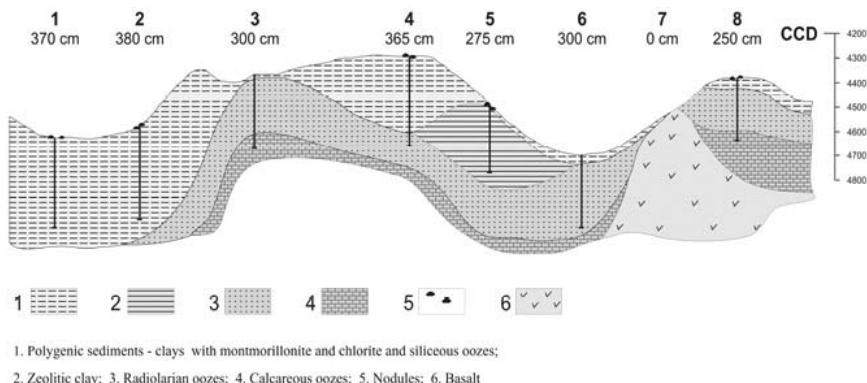


Fig. 1. Vertical distribution of sediments within the IOM exploration area.

The Marquesas formation sediments can be divided into the following three units (from the bottom up): calcareous and nanofossil-containing ooze (70 cm thick), siliceous (radiolarian) ooze (250 cm thick), and zeolitic red clay (270 cm thick); the amorphous silica content of these sediments averaging 18%.

The uppermost layer (up to 3.5 m thick) belongs to Clarion–Clipperton formation, and sediment consists of clays and oozes with montmorillonite and chlorite; the amorphous silica content varies from 1 to 20%.

The seafloor sediment is topped by siliceous ooze and siliceous clayey oozes of the geochemically active layer (2–12 cm thick) on which surface polymetallic nodules are formed and partly embedded.

3. Nodule Types and Distribution Pattern

The IOM exploration area features all the morphological and genetic nodule types known from the Clarion–Clipperton nodule field: hydrogenetic type (*H*), hydrogenetic–diagenetic type (*HD*), and diagenetic type (*D*).^{2,3}

It is considered that the mineral and chemical composition of nodules, particularly the relationship between hydrogenetic minerals (e.g., iron and manganese hydroxide, vernadite) and diagenetic minerals (e.g., todorokite and birnessite), as well as the Mn/Fe ratio and concentration of Ni, Cu, and Co, reflects the major processes responsible for nodule formation. As a rule, large nodules with rough surfaces are enriched with Mn, Ni, Cu, and Mo, and birnessite is dominant; whereas the smaller, smooth nodules are relatively rich in Co, Fe, and have higher vernadite content.

The surface nodule abundance within IOM exploration area varies from 0.2 to 22.6 kg/m², averaging 8.4 kg/m². There does not appear to be any spatial relationship of nodules distribution with topography as high nodule abundance was observed both on hilltops and in depressions.

4. Buried Nodules Phenomenon

Buried nodules were found at 59 stations, mainly between latitudes 119°50'W and 120°50'W, and at depths >4300 m (90.2%), including 42.7% of all stations being located at depths >4400 m.

Buried nodules lie completely beneath the geochemically active layer sediment, and they are vertically recorded down to 45 cm in sediment cores (Fig. 2).

4.1. Relationship with topography and sediments

Most of the stations (~55%) were located on the gently undulating plains; about a third (32.9%) were located on sloping parts of the bottom (slopes of horsts and troughs), while 9.8 and 2.4% of the stations were situated on horst tops and on slopes of volcanic hills, respectively.

As a rule (~90% of all sampled stations), buried nodules are found in polygenic clays, while at six stations buried nodules are located in zeolitic clays.

4.2. Vertical distribution pattern

Most often (~89% of the stations), buried nodules form a single layer; five stations revealed two layers, while three and five layers were found at a single station each. In the latter cases, high nodule abundance (up to 21.9 kg/m²) was recorded.

As revealed by boxcore samples, buried nodules are deposited basically within 10–15, 20–25, and 30–35 cm in the sediment.

4.3. Size

The highest number of surface nodule (64.3%) occurs in the size class 6–10 cm, while the dominant size class (42.4%) of buried nodules is 2–6 cm (Table 1).

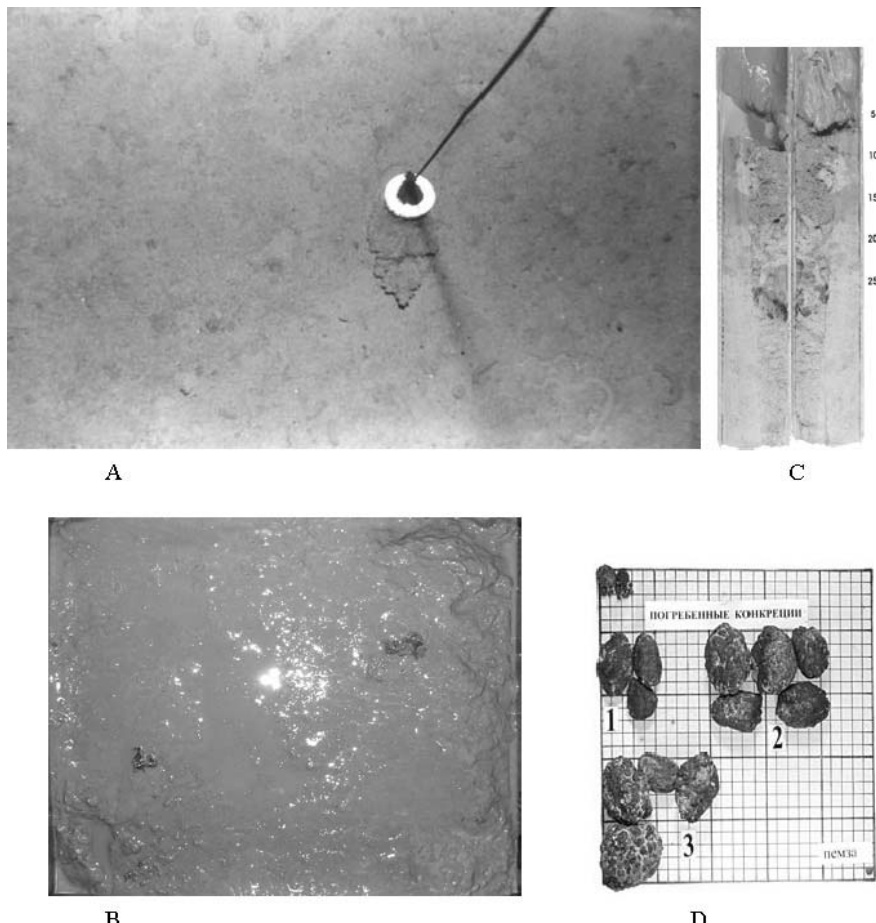


Fig. 2. Nodule photographs at #2189 boxcore sample station situated within the IOM exploration area, eastern Clarion–Clipperton Zone, water depth 4462 m. (A) Bottom photograph, taken by GFU6-8 camera type in scale $\sim 1:10$, with relatively very small nodule abundance. (B) Onboard photograph, taken by Olympus C-4000 camera type of the boxcore sample with two surface nodules. (C) Core cross-section with buried nodules occurring at 15 and 25 cm depth. (D) Template data with 12 buried nodules (1, 2, and 3) and two small surface nodules (upper, left).

At the same time, buried nodules larger than 10 cm in diameter, occurred in 27.1% at stations, while only 7.1% of the stations contained surface nodules >10 cm in diameter. Most often, at one sampling station, buried nodules are larger than those found on the sediment surface (Fig. 2D).

Table 1. Dominant size class (cm in diameter) of surface and buried nodules collected in boxcore samples based on data at 59 stations randomly distributed within the IOM exploration area (eastern Clarion–Clipperton Zone, North Pacific). Three stations within studied area showed the presence of buried nodules only.

| | Size class, cm | | | |
|-----------------|----------------|-----------|-----------|-----------|
| | 0–2 | 2–6 | 6–10 | >10 |
| Surface nodules | Not found | 16 (28.6) | 36 (64.3) | 4 (7.1) |
| Buried nodules | 1 (1.7) | 25 (42.4) | 17 (28.8) | 16 (27.1) |

Note: Data in brackets show percent of all stations with recorded buried ($n = 59$) and surface nodules ($n = 56$).

4.4. Appearance

Buried nodules differ from those found on the surface. They always show traces of dissolution, and are dark-gray, not black.

The buried nodules either completely lack the microrelief (granularity of the bottom part, equatorial belt) or it is very weak. Not infrequently, the surface of buried nodules shows light-gray or gray-clayey coatings, differing in their texture and color from the surrounding sediment.

4.5. Abundance

At 23 stations, nodule abundance exceeded 1.0 kg/m^2 ; 11 stations showed more than 5 kg/m^2 , abundances exceeding 10 kg/m^2 were recorded at five stations. Buried nodules were found, but not examined, at six stations.

The abundance of buried nodules was at six stations higher than that found on the seafloor surface, the difference being substantial at three stations, where the ratio is $32 \leq r \leq 99$. Moreover, three stations showed the presence of buried nodules only.

4.6. Chemistry

In their elemental composition, buried nodules differ from the surface ones only slightly (Table 2). Nevertheless, they do show, in most cases, higher concentrations of Co and Fe and lower concentrations of Ni and Mo.

Statistically, Mn and Cu are only slightly different in buried nodules.

Table 2. Nodule abundance and metal contents of surface and buried nodules based on data at 59 boxcore stations randomly distributed within the IOM exploration area (eastern Clarion–Clipperton Zone, North Pacific).

| Observed parameter | Surface nodules | Buried nodules |
|-------------------------------------|---------------------|-------------------|
| Nodule abundance, kg/m ² | 10.34 ± 5.77 (n=59) | 3.19 ± 4.9(n= 53) |
| Metals, % | n = 54 | n = 35 |
| Mn | 32.04 ± 1.53 | 32.33 ± 1.82 |
| Fe | 5.39 ± 0.84 | 5.61 ± 1.80 |
| Ni | 1.31 ± 0.1 | 1.18 ± 0.12 |
| Cu | 1.27 ± 0.1 | 1.28 ± 0.11 |
| Co | 0.175 ± 0.022 | 0.201 ± 0.044 |
| Mo | 0.061 ± 0.008 | 0.051 ± 0.007 |
| Zn | 0.15 ± 0.02 | 0.13 ± 0.02 |

Note: Data represent average ± standard deviation, n denotes number of analyses.

5. Discussions

Due to the limited scope of studies on buried nodule phenomena, many questions remain unanswered. Some of the questions are:

1. What might be the geological factors responsible for the buried nodules formation?
2. What might be the correlation between particular sedimentation process (including sedimentary hiatuses) and nodule growth within the studied area?
3. Which key parameters would be useful as indicators of buried nodules?
4. How do we integrate the data on buried nodules when estimating the nodule reserves that could be mined from contract area?
5. What alteration in mining system design could be used to ensure collection of buried nodules?
6. What might be the impact of buried nodule exploration on the marine ecosystem?

6. Conclusions

The data on buried nodules bear evidence of the complexity and length of processes leading to their formation.

Factors and conditions responsible for the buried nodules formation are still unknown and they may include specific features of deep-sea environment in which buried nodules form.

Acknowledgments

This work was supported by the Interoceanmetal Joint Organization sponsoring states. We would like to thank Mr. Mikhail Zadornov for his early comments on geological setting of the studied area. We would like to express our appreciation to reviewers Mr. Jianping Gan and Mr. Tim McConachy for editing the text and helpful comments.

References

1. J. L. Bischoff and D. Z. Piper, eds., *Marine Geology and Oceanography of the Pacific Manganese Nodule Province*, Marine Science Series, Vol. 9 (Plenum Press, New York, 1979).
2. R. Kotlinski and K. Szamalek, eds., *Surowce mineralne morz i oceanow* (Wyd. Nauk Scholar, 1998).
3. R. Kotlinski and M. Zadornov, *Minerals of the Ocean, International Conference Abstracts* st. Petersburg (2002), p. 164.
4. E. F. Shnjukov, G. N. Orlovsky, S. A. Kleshchenko, V. P. Reznik, A. P. Ziborov and A. A. Schiptsov, 2001. *Ferromanganese Nodules from the Indian Ocean* (National Academy of Sciences of Ukraine, Kiev, 2001), p. 330.
5. P. Jauhari and J. N. Pattan, in *Handbook of Marine Minerals Deposits*, ed. D. S. Cronan (Press LLC, 2000).
6. Ch. L. Morgan, in *Handbook of Marine Minerals Deposits*, ed. D. S. Cronan, (CRC Press, 2000), pp. 145–170.
7. U. von Stackelberg, in *Handbook of Marine Minerals Deposits*, ed. D. S. Cronan (CRC Press, 2000), pp. 197–239.
8. http://www.isa.org.jm/en/publications/IA_ENG/ENG3.pdf.

IRON ORGANIC COMPLEXATION IN THE OLIGOTROPHIC SUBTROPICAL WATERS IN THE TASMAN SEA

FENG TIAN^{*,†}, RUSSELL FREW[†], ROBERT STRZEPEK[‡] and MICHAEL ELLWOOD[§]

[†]*Department of Chemistry,
University of Otago, Dunedin, New Zealand*

[‡]*Department of Chemistry,
National Institute of Water and Atmosphere,
Research Centre of Chemical and Physical Oceanography,
University of Otago, Dunedin, New Zealand*

[§]*National Institute of Water and Atmosphere,
Hillcrest, Hamilton, New Zealand*

**Ftian@chemistry.otago.ac.nz*

As part of a larger program focused on understanding the biogeochemistry of the Tasman Sea, we participated in the Characterizing Oligotrophic Subtropical Waters (COST) voyage conducted in February 2005. Measurements of dissolved iron (Fe) and Fe organic speciation in the upper water column of two stations located south and north of the Tasman Front along 170°E in the Tasman Sea are presented. On-deck multifactorial incubation results confirm that both regions are typical of oligotrophic waters, in being dominated by picophytoplankton and cyanobacteria. The dissolved Fe concentrations were low (< 0.2 nM) in the surface waters and increased with depth below 150 m. The chemical speciation of Fe was dominated by organic complexation at both stations and the ligand concentrations ranged between 0.4 and 1.0 nM, with complex stability $\log K'_{FeL} = 22.1\text{--}23.9$. The Fe-complexing ligands in the upper 50 m water column were consistently higher at the northern station compared to at the southern station. This difference in ligand concentrations contrasts with that of the concentrations of total dissolved Fe, which were slightly higher at the southern station. The vertical profiles of the ligands showed a maximum consistent with the potential biological sources for ligand production.

1. Introduction

Photosynthetic carbon fixation by marine phytoplankton and the subsequent export of particulate organic carbon to the ocean interior represent a biological

carbon pump that regulates atmospheric CO₂ concentrations and the global climate. Iron (Fe) plays a key role in ocean productivity as it is known to be a limiting micronutrient in high-nutrient low chlorophyll (HNLC) regions,^{1,2} in some coastal regions,^{3–5} and possibly also in some oligotrophic oceans.⁶ Current models suggest that approximately half of the world's oceans are chronically or seasonally Fe-deplete.⁷ The low concentrations of dissolved Fe found in surface seawater are a product of the low solubility⁸ of the thermodynamically favored redox state Fe(III). The chemical speciation of Fe(III) in seawater has been found to be dominated by complexation with natural organic ligands,^{9–11} which increase the overall solubility and are thought to be more bioavailable^{12,13} to phytoplankton. Thus it is of great importance to study the organic speciation of Fe in seawater, if we aim to better understand the link between the climate forcing and iron dynamics in the oceans.

Previous studies of chemical speciation of Fe have been performed mainly in the HNLC regions. Very few data exist on the organic complexation of Fe in oligotrophic seawaters. However, most of the ocean shows near-complete nutrient utilization. The New Zealand's 200 mile Economic Exclusion Zone is dominated by subantarctic and subtropical water. Although it is established that the subantarctic surface water as a whole is classified as a HNLC water body and has an Fe-limited phytoplankton population,^{14,15} there have been relatively few measurements to date that examine phytoplankton limitation in subtropical open ocean waters. The oligotrophic subtropical waters found in the Tasman Sea to the north of New Zealand are transported to the North Island coast by the Tasman Front (TF). This is a very understudied area and so any biogeochemical/biological measurements are unique to this region.

In an effort to further understand the biogeochemistry of Fe in the ocean, we present organic speciation results for Fe along a transect across a frontal zone, the TF, at 170°E in the oligotrophic subtropical waters of the Tasman Sea. The Fe speciation data are also compared with the shipboard incubation results and some other biochemical parameters.

2. Materials and Methods

Seawater samples were collected during the austral summer, from February 3, 2005 to February 17, 2005, during the Characterizing Oligotrophic

Subtropical Waters (COST) voyage aboard the R.V. *Tangaroa*. The study area is located north of New Zealand (Fig. 1). The Tasman Front,^{16–17} a band of eastward-flowing water near 32°S, extends across the northern Tasman Sea from the East Australian Current toward New Zealand and is characterized by high salinity and high temperature indicative of its subtropical origin. It separates the warmer waters of the Coral Sea from

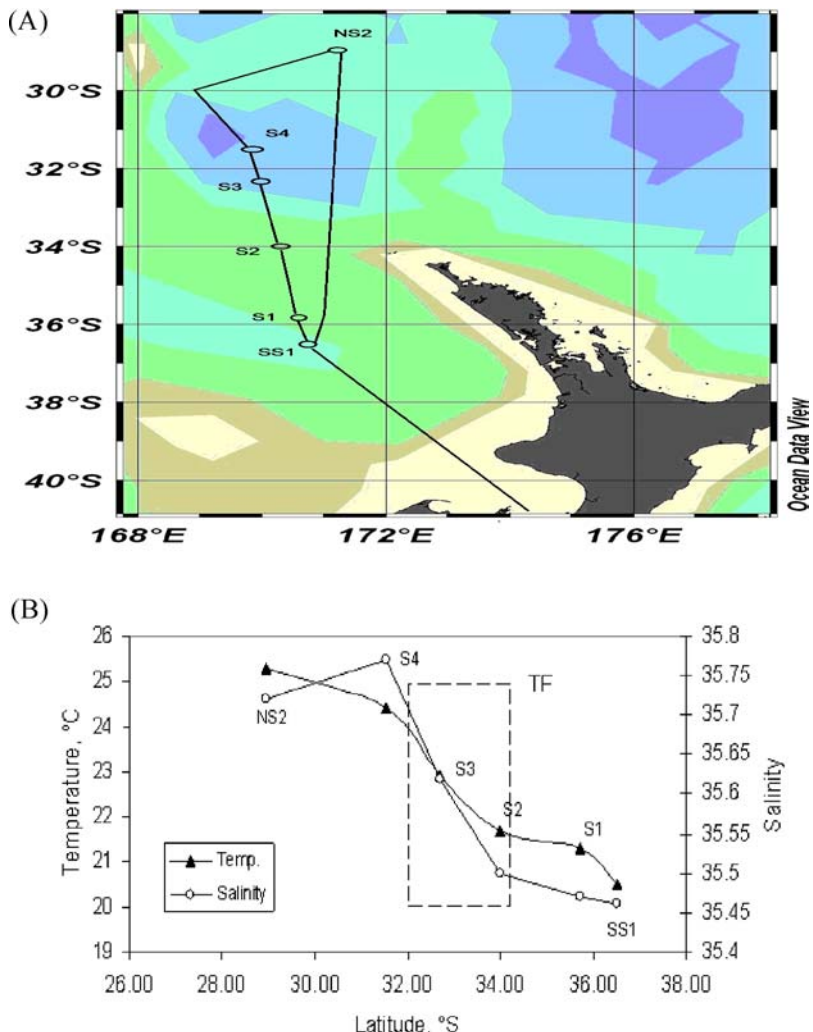


Fig. 1. (A) Location map showing the sampling stations. (B) Temperature and salinity in surface waters across the Tasman Front for a section around 170°E.

the colder waters of the Tasman Sea. This flow provides much of the subtropical inflow for the warm currents along the eastern New Zealand coast. For this reason, the temperature of New Zealand is 2–3°C warmer than it would have been without. It is therefore important for the country's climate.

Water column samples were collected using 10 L acid-cleaned Teflon-coated Go-Flo bottles deployed on Kevlar hydrowire, from the upper 500 m at two stations. All samples were filtered through a 0.2 µm polycarbonate filter and stored frozen in acid-cleaned low-density polyethylene bottles (Nalgene). The bottle depths were checked with a SIS pressure and temperature sensor. While *Tangaroa* was steaming, surface seawater samples were collected using a “fish” system deployed on the starboard side of the ship at five stations across the TF. All sampling, filtration, and sample manipulations were carried out using trace-metal clean techniques in the clean laboratory onboard.

Fe speciation was carried out using the methodologies described by Tian *et al.*¹¹. Briefly, twelve 10 mL aliquots of seawater were pipetted into twelve 60 mL Teflon vials and buffered at pH 8.0 with 1.0 M of stock EPPS buffer. Fe spikes were added to all but two of the vials. The added Fe was allowed to equilibrate with the natural ligands for 1 h at room temperature. After this equilibration, 10 µL of 10 mM methanolic TAC solution was added and the sample was left to equilibrate overnight. Labile Fe concentrations were then determined by cathodic stripping voltammetry (CSV). Speciation data were calculated using the nonlinear regression fitted for a single ligand model.¹¹

Total dissolved Fe concentrations were determined on q-HCl acidified ($\text{pH} < 1.8$) samples in the land-base laboratory using a combination of solvent extraction techniques described by Danielsson *et al.*¹⁸ and Bruland *et al.*¹⁹ Fe in the extracts was determined by graphite furnace atomic absorption spectrometry using a Perkin-Elmer 4100 ZL with Zeeman background correction. Recovery efficiencies were determined by standard addition analysis of previously extracted seawater and blanks were determined by analyzing Milli-Q water or previously extracted seawater. Extraction efficiencies were $93 \pm 5\%$, blanks were $< 0.03 \text{ nM}$, and the detection limit was 0.05 nM (2σ).

Nutrient samples were also collected from the Go-Flo bottles and the “fish” sampling system. They were determined immediately onboard on an Astoria Flow Injection Analysis system using standard methods.²⁰ Salinity and temperature profiles were measured on separated CTD casts at each

station using a Seabird CTD system. Hydrographic data (e.g., salinity and temperature) were collected by NIWA personnel, and were made available to other voyage participants.

3. Results

3.1. *Surface transect*

The surface transect began offshore the west coast of the North Island (36.5°S , 170.7°E) in relatively low temperature (20.5°C) salinity (35.46) oligotrophic water of the Tasman Sea (Fig. 1). The TF was clearly observed along the voyage track approximately between 32°S and 34°S as there was a strong temperature gradient. North of the TF, the ship moved into warmer (25.3°C) higher-salinity (35.72) subtropical waters. The surface waters were depleted in nutrients, though the core of the front showed a slightly higher phosphate concentration of $0.23\text{ }\mu\text{M}$ and silicic acid concentration of $0.65\text{ }\mu\text{M}$ (Fig. 2A). All nitrate concentrations were at subnanomolar levels which are below the detection limit of the conventional spectrophotometric technique (M. Woodward, unpublished data). Dissolved Fe concentrations were low (0.2 nM) and decreased slightly northwards across the TF to less than 0.1 nM (Fig. 2B). The total dissolved Fe-complexing ligand concentrations ranged between 0.4 and 0.7 nM and increased slightly northwards across the TF (Fig. 2B).

3.2. *Vertical profiles/subsurface waters*

3.2.1. *Hydrology, macronutrients, and biomass*

In an attempt to compare the organic Fe complexation in the waters to the north and south of the TF, two vertical profiles were obtained at sampling stations NS2 and SS1 (Fig. 1). In general, the warmer and more saline subtropical waters were observed at station NS2, north of the TF. The surface temperatures were about 4.5°C higher than that of station SS1 and salinities were 0.3 higher. During this summer voyage, both stations had similarly shallow mixed layer depths ($<20\text{ m}$). Below the mixed layer, water temperature decreased rapidly with depth from the mixed layer temperature to the much colder deep water. At both stations, the top of the thermocline was observed at the upper 150 m zone, with a higher temperature gradient of $0.06^{\circ}\text{C}/\text{m}$. Below 150 m , water temperatures

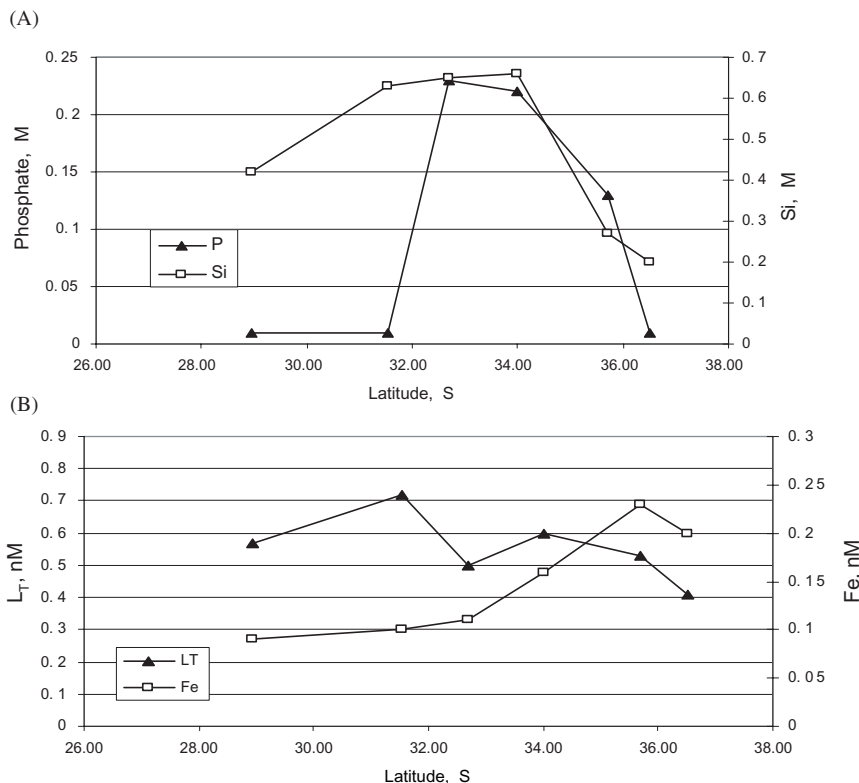


Fig. 2. Data from the surface transect: (A) dissolved phosphate (P) and silicic acid (Si) concentrations. (B) total dissolved Fe concentrations and concentrations of the total dissolved Fe-binding ligands (L_T).

decreased much slower at $0.01^{\circ}\text{C}/\text{m}$ between 150 and 1200 m. Salinities were fairly uniform at the upper 150 m, then decreased gradually with depth.

The upper 75 m of the water column was nutrient deplete (Fig. 3). The nutrient concentrations then increased with depth. At 410 m depth, nitrate concentrations were $12 \mu\text{M}$ at station SS1 and $6 \mu\text{M}$ at station NS2, phosphate concentrations were $1 \mu\text{M}$ for both stations. At station SS1, silicic acid concentrations ranged between 0.1 and $6.2 \mu\text{M}$. At station NS2, silicic acid concentrations ranged between 0.4 and $4.7 \mu\text{M}$. Based on previous cruises to the region it appears that waters north of the TF are permanently oligotrophic. The waters south of the front are seasonally oligotrophic (C. Law, personal communication).

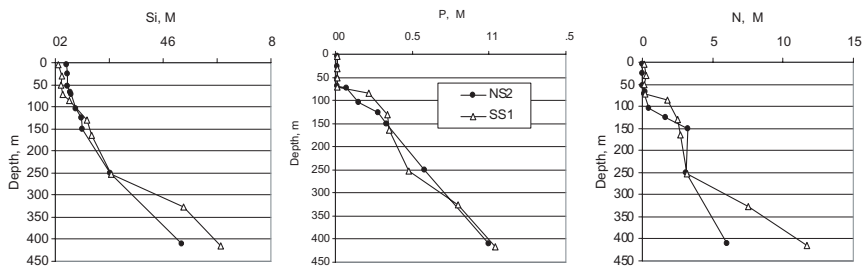


Fig. 3. Vertical profiles of dissolved nutrients for station NS2 (north of the TF) and SS1 (south of the TF).

Vertical distributions of size-fractionated chlorophyll *a* (Chl *a*) concentrations at the two stations showed that both stations were dominated by picophytoplankton and cyanobacteria as the percentage of the <2 µm fraction was greater than 90% (Fig. 4). The biomass showed a distinct subsurface maximum at depth between 50 and 100 m. Flow cytometry demonstrated the *Prochlorococcus* were the numerically dominant phytoplankton group at station NS2 (Fig. 5).

3.2.2. Dissolved iron and iron complexation

Figure 6 presents the Fe speciation data from the two vertical profiles. At Station SS1 south to the TF, dissolved Fe concentrations were low (~ 0.2 nM), showed slight surface enrichment: a minimum at 50–100 m, then increasing Fe values at depth below 100 m. The NS2 station north to the TF showed a nutrient-like profile. Dissolved Fe concentrations were very

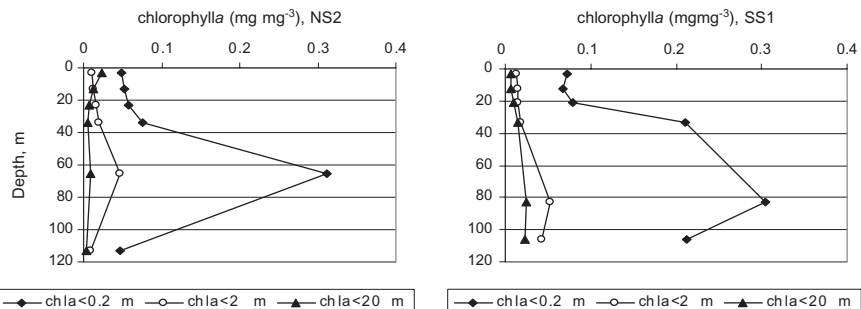


Fig. 4. Vertical profiles of size-fractionated Chl *a* concentrations at station NS2 and SS1.

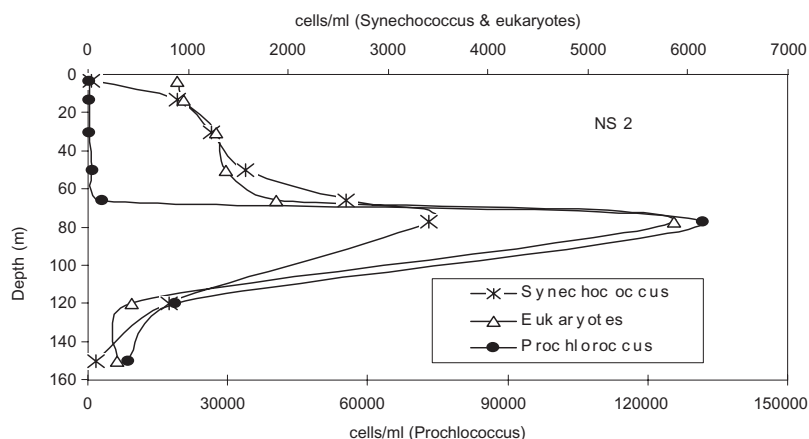


Fig. 5. Phytoplankton abundance as determined by Slow cytometry at station NS2 (J. Hall and K. Safi unpublished data).

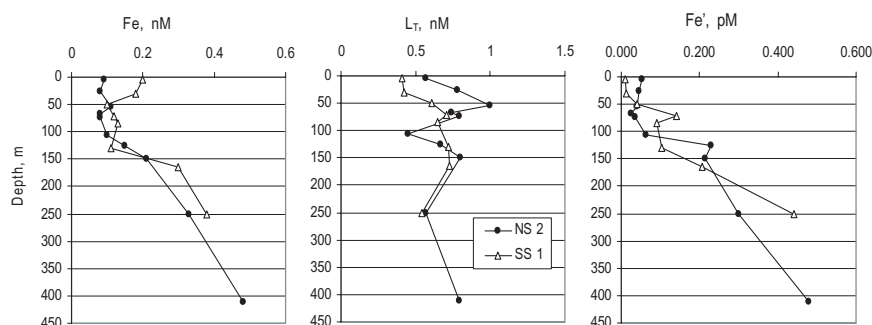


Fig. 6. Vertical profiles of dissolved Fe, Fe-binding ligands and Fe' for station NS2 (north of the TF) and SS1 (south of the TF).

low (0.1 nM) in the surface mixed layer and increased gradually to 0.5 nM at 410 m.

In this study, we found no justification for using a two-ligand system, so the one-ligand one-metal model²¹ was applied to all sample speciation calculations. In general, the dissolved Fe was fully complexed by natural organic ligands, the organic species of Fe were the dominant fraction throughout the water columns.

The vertical profile for Fe-complexing ligands from NS2 (Fig. 6) showed a maximum ligand concentration at 50 m (1 nM), then decreased slightly with depth. The ligand concentrations ranged between 0.5 and 1.0 nM.

Estimated values of the free inorganic Fe concentration (Fe') showed an increasing trend below 100 m. The water from 410 m was found to have a high Fe' ($\sim 0.5 \text{ pM}$), significantly higher than the waters in the upper 100 m ($\sim 0.05 \text{ pM}$). At station SS1, ligand concentrations ranged from 0.4 to 0.7 nM, a slight enrichment in waters at 50–150 m. Similarly, the estimated values of Fe' showed a increasing trend below 50 m, with a significantly higher value (0.4 pM) at 250 m.

In general, the Fe-complexing ligand concentrations were very low (not higher than 1 nM) and there was no significant variation between the two stations. Values of the conditional stability constants ranged from $10^{22.1}$ to $10^{23.9}$, indicating a strong Fe-complexing stability.

4. Discussion

4.1. Iron organic speciation

Though the Tasman Sea is considered to receive significant external Fe forcing via dust input from Australia, eolian Fe deposition is episodic and the regional dust transport pathways are more diverse than the previously thought west–east route.^{22,23} This partially released Fe is then removed from the water column relatively quickly via both biotic and abiotic pathways.²⁴ The low surface dissolved Fe concentrations observed in the study area suggest that the Fe supply from atmospheric input was not significant during the study period in the Tasman Sea north of New Zealand. The other trace-metal concentrations (e.g. Zn, Cu), observed during the voyage, were also very low at subnanomolar levels (M. Ellwood, unpublished data).

In the surface and subsurface waters obtained from NS2 and SS1, dissolved Fe concentrations show slight variations in response to eolian Fe deposition, water mixing, competitions between particle scavenging and phytoplankton/bacteria uptake and removal.^{25,26} The downward increase of dissolved Fe concentrations at 150–400 m at both stations is consistent with a nutrient-type behavior for Fe. The nutrient-type distribution of dissolved Fe in the upper 400 m suggests that the microbial decomposition of sinking organic matters carrying that Fe may be the major route by which Fe in surface water is transported into the deep ocean.²⁷

The naturally occurring Fe-binding ligands were detected in all samples and their concentrations were in excess of the dissolved Fe concentrations. The vertical profiles of the ligands obtained from both stations showed

increasing concentration with depth in the upper water column, with a distinct maximum at 50–70 m (Fig. 6), close to the subsurface Chl *a* maximum (Fig. 4). Similar trends were also observed in the vertical profiles of the “excess” ligands (the concentrations of total dissolved Fe-binding ligands minus the concentrations of total dissolved Fe) at both stations. These results suggest the potential biological origin for these Fe-binding ligands.

The high Fe-binding stability determined by CSV suggests that these ligands could be siderophores. In fact, siderophore production by marine bacteria under Fe-limited conditions has been well documented.^{28–32} The coincidence of the subsurface maxima in dissolved Fe-binding ligand concentrations with the sharp maximum concentration of the dominant *Prochlorococcus* may suggest that *Prochlorococcus* is the main producer of Fe-binding ligands. The strong Fe-binding ligands may be secreted by this marine cyanobacterium to aid in Fe uptake in the low ambient Fe environment. However, for the present work, we cannot distinguish between ligand production from cyanobacteria or eukaryotes. Moreover, the maximum of ligand concentration around deep chlorophyll maximum (DCM) may be subject to complex processes of dissolved organic matter production and degradation/removals.

Ligand concentrations at depths greater than ~150 m at both stations were similar. The ligand concentrations in the upper 50 m water column at the northern station, NS2, were about 0.3 nM higher than the ligand concentrations at the southern station, SS1. This difference in ligand concentrations for the upper 50 m water column contrasts with that of the concentrations of total dissolved Fe, which were slightly higher at station SS1. This is also reflected in the “excess” ligand concentrations, which were about 0.4 nM higher at NS2 compared to SS1. This difference in ligand concentration across the TF may represent slight differences in algal biomass. A previous study also showed the Fe-binding ligand concentrations were consistently higher (~0.5 nM) in the subtropical waters than in the subantarctic waters across the subtropical convergence over the Chatham Rise.¹¹

In general, the total dissolved Fe-binding ligands observed in the austral summer oligotrophic subtropical Tasman seawaters were at relatively low concentrations. The ligand concentrations ranged between 0.4 and 1.0 nM with a mean value of 0.65 ± 0.15 nM. Larger variability is observed in the concentrations of Fe-binding ligands measured in the world’s oceans. Rue and Bruland found 1.5 nM ligands in the central north Pacific¹⁰ and

0.5 nM ligands in the equatorial Pacific.³³ The ligands were observed in the concentrations of 3–5 nM in the North Atlantic,^{9,34} 2–6 nM in the Arabian sea,³⁵ and 4–12 nM in the Mediterranean sea.³⁶ In Southern Ocean, Croot *et al.*³⁷ found the ligand concentrations of 1–3 nM, while Boye *et al.*²¹ had a much lower value of 0.7 nM.

The vertical profiles of [Fe'] obtained from both stations show an interesting, systematic difference: very low [Fe'] at the upper 50 m water column, compared with much higher [Fe'] at 150 m and increase with depth. The estimation of Fe' provides an indication of the size of the most labile Fe pool available to phytoplankton. The minimum [Fe'] associated with the [L] and Chl *a* maximum is presumably due to the dual effect of uptake of Fe' by phytoplankton, the production of Fe-ligands and subsequent complexation of Fe'. The significantly higher Fe' below 150 m is related to the increasing [Fe] together with the lower concentration of Fe-complexing ligands. This is presumably in line with the fact that phytoplankton have to live in the euphotic zone. However, it is now apparent that bacteria and eukaryotic phytoplankton in the open ocean are able to access Fe bound to strong organic ligands.^{38–40} The mechanisms of Fe acquisition by plankton community in oceanic regions are not fully understood yet and may involve multiple pathways and Fe species.

4.2. Deck incubation results

Shipboard incubation experiments were also carried out during the voyage using methodologies described by Ellwood.⁴¹ The incubation experiments provided evidence for the nitrogen-limitation of phytoplankton yields in these oligotrophic subtropical waters (Fig. 7). The addition of ammonium N alone produced significant increases in Chl *a* concentrations, and eukaryotic and prokaryotic cell numbers compared to the unamended controls.

The coincidence of the subsurface minima in dissolved Fe concentrations with the DCM at NS2 may have important implications for phytoplankton ecology in the subtropical Tasman Sea. Our data suggest that the biological utilization of Fe by phytoplankton, growing at the depth of the DCM, must contend with low Fe availability. During the austral summer in the subtropical Tasman Sea, phytoplankton biomass in the DCM was dominated by the cyanobacterium *Prochlorococcus* (Fig. 5), the smallest known photosynthetic organism (they measure only $\sim 0.6 \mu\text{m}$).⁴²

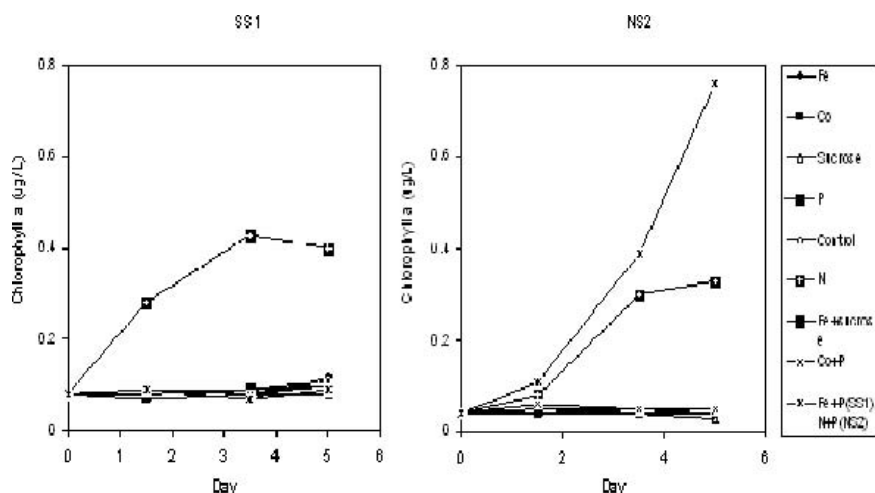


Fig. 7. Chlorophyll *a* determined for station SS1 and NS2 incubation experiments. Additions of metals and nutrients were as follows: control, no addition; +Fe (2 nM); +Co (1 nM); +sucrose (1 µM C); +P (0.48 µM); +N (8 µM NH₄).

Marine cyanobacteria, including species of *Prochlorococcus* and *Synechococcus*, are prominent constituents of the ocean that account for a significant percentage of oceanic primary productivity.^{42,43} Within the DCM, *Prochlorococcus* are believed to maintain a competitive advantage over other phytoplankton with respect to their high surface/volume ratio resulting from their very small cell size⁴⁴ and through their ability to grow under conditions of very low irradiance.^{45,46} However, they must also possess either unusually small nutrient requirements or an extremely efficient capacity to scavenge elements. Mann and Chisholm⁴⁷ argued that dissolved Fe concentrations of ~ 0.02 nM were limiting the growth rate of *Prochlorococcus* in the eastern equatorial Pacific. Similarly, Fe co-limitation of *Prochlorococcus* may develop in the surface oligotrophic subtropical Tasman seawater where subnanomolar Fe concentrations are encountered. This was partially evidenced by the deck incubation experiments. During the incubation, there was an additional response in the Fe+P treatment (Fig. 8) but a lack of response by the P addition treatment for NS2 experiment. This suggests that the dissolved Fe could be a co-limiting factor for the primary production in these waters. However, the Fv/Fm response was too low to say that significantly different to the others. Obviously, more experiments are necessary for the clear demonstration of the Fe co-limitation of these waters.

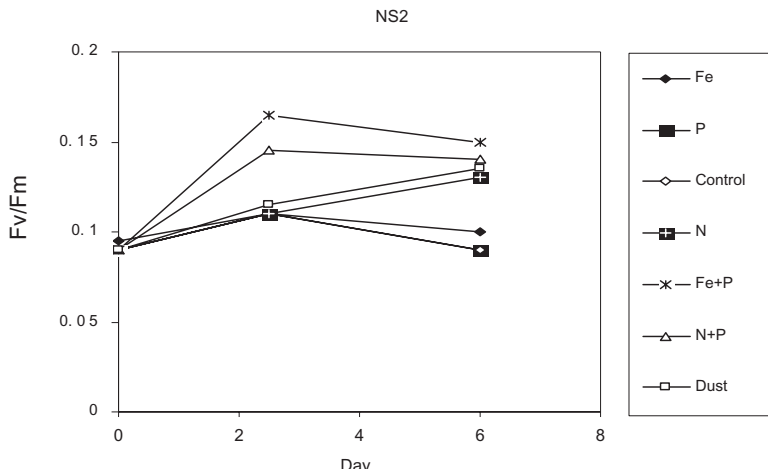


Fig. 8. The potential photochemical efficiency of photosystem II (F_v/F_m) measured by fast repetition rate fluorometry for deck incubation experiments at station NS2.

Acknowledgments

This research was funded by grants from NIWA's Ocean Fronts research programme. Thanks to Julie Hall, Karl Safi, Karen McCluskie, Karine Leblanc, Cliff Law, Sarah Bury, and Stu Pickmere for incubation, chlorophyll *a* and nutrient data, and the officers and crew of *Tangaroa*. F. Tian is grateful to Phil Boyd and Cliff Law for their invitation for joining the COST voyage. Finally, we thank the anonymous referees for reviews that help to improve the manuscript.

References

1. J. H. Martin, K. H. Coale, K. S. Johnson, S. E. Fitzwater, R. M. Gordon, S. J. Tanner, C. N. Hunter, V. A. Elrod, J. L. Nowicki, T. L. Coley, R. T. Barber, S. Lindley, A. J. Watson, K. V. Scoyer, C. S. Law, M. I. Liddicoat, R. Ling, T. Stanton, J. Stockel, C. Collins, A. Anderson, R. Bidigare, M. Ondrusek, M. Latasa, F. J. Millero, K. Lee, W. Yao, J. Z. Zhang, G. Friederich, C. Sakamoto, F. Chavez, K. Buck, Z. Kolber, R. Greene, P. Falkowski, S. W. Chisholm, F. Hoge, R. Swift, J. Yungel, S. Turner, P. Nightingale, A. Hatton, P. Liss and N. W. Tindale, *Nature* **371** (1994) 123–129.
2. P. W. Boyd, A. J. Watson, C. S. Law, E. R. Abraham, T. Trull, R. Murdoch, D. C. E. Bakker, A. R. Bowie, K. O. Buesseler, H. Chang, M. Charette, P. Croat, K. Downing, R. Frew, M. Gall, M. Hadfield, J. Hall, M. Harvey,

- G. Jameson, J. LaRoche, M. Liddicoat, R. Ling, M. T. Maldonado, R. M. McKay, S. Nodder, S. Pickmere, R. Pridmore, S. Rintoul, K. Safi, P. Sutton, R. Strzepek, K. Tanneberger, S. Turner, A. Waite and J. Zeldis, *Nature* **407** (2000) 695–702.
3. D. A. Hutchins and K. W. Bruland, *Nature* **393** (1998) 561–564.
4. D. A. Hutchins, C. E. Hare, R. S. Weaver, Y. Zhang, G. F. Firme, G. R. DiTullio, M. B. Alm, S. F. Riseman, J. M. Maucher, M. E. Geesey, C. G. Trick, G. J. Smith, E. L. Rue, J. Conn and K. W. Bruland, *Limnol. Oceanogr.* **47** (2002) 997–1011.
5. G. F. Firme, E. L. Rue, D. A. Weeks, K. W. Bruland and D. A. Hutchins, *Global Biogeochem. Cycles* **17**(1) (2003) 1016.
6. M. J. Behrenfeld and Z. S. Kolber, *Science* **283** (1999) 840–843.
7. J. K. Moore, S. C. Doney and K. Lindsay, *Global Biogeochem. Cycles* **18** (2004) Art. No. GB4028.
8. X. Liu and F. J. Millero, *Mar. Chem.* **77** (2002) 43–54.
9. M. Gledhill and C. M. G. van den Berg, *Mar. Chem.* **47** (1994) 41–54.
10. E. L. Rue and K. W. Bruland, *Mar. Chem.* **50** (1995) 117–138.
11. F. Tian, R. Frew, S. Sander, K. Hunter and M. Ellwood, *Mar. Freshw. Res. CSIRO* **57** (2006) 533–544.
12. D. A. Hutchins, A. E. Witter, A. Butler and G. W. Luther, *Nature* **400** (1999) 858–861.
13. M. T. Maldonado, R. F. Strzepek, S. Sander and P. W. Boyd, *Global Biogeochem. Cycles* **19** (2005) GB4S23.
14. J. M. Bradford-Grieve, F. H. Chang, M. Gall, S. Pickmere and F. Richards, *NZ J. Mar. Freshw. Res.* **31** (1997) 201–224.
15. P. Boyd, J. LaRoche, M. Gall, R. Frew and R. M. McKay, *J. Geophys. Res.* **104** (1999) 13395–13408.
16. B. R. Stanton, *NZ J. Mar. Freshw. Res.* **13** (1979) 201–214.
17. R. A. Heath, *NZ J. Mar. Freshw. Res.* **19** (1985) 79–124.
18. L. Danielsson, B. Magnusson and K. Zhang, *Anal. Chim. Acta* **144** (1982) 183–188.
19. K. W. Bruland, R. P. Franks, G. A. Knauer and J. H. Martin, *Anal. Chim. Acta* **105** (1979) 233–245.
20. M. J. Ellwood and W. A. Maher, *Mar. Chem.* **80** (2003) 145–159.
21. M. Boye, C. M. G. van den Berg, J. T. M. de Jong, H. Leach, P. Croot and H. J. W. de Baar, *Deep-Sea Res.* **48** (2001) 1477–1497.
22. H. A. McGowan, G. H. McTainsh and P. Zawar-Reza, *Earth Surf. Processes Landforms* **25** (2000) 633–647.
23. P. W. Boyd, G. McTainsh, V. Sherlock, K. Richardson, S. Nichol, M. Ellwood and R. Frew, *Global Biogeochem. Cycles* **18**(1) (2004) Art. No. GB 1029.
24. R. D. Frew, D. A. Hutchins, S. Nodder, S. Saundo-Wilhelmy, A. Tovar-Sanchez, K. Leblanc, C. E. Hare and P. W. Boyd, *Global Biogeochem. Cycle* **20** (2006) GB1S 93.
25. C. I. Measure and S. Vink, *Deep Sea Res.* **46** (1999) 1597–1622.

26. T. D. Jickells, Z. S. An, K. K. Andersen, A. R. Baker, G. Bergametti, N. Brooks, J. J. Cao, P. W. Boyd, R. A. Duce, K. A. Hunter, H. Kawahata, N. Kubilay, J. laRoche, P. S. Liss, N. Mahowald, J. M. Prospero, A. J. Ridgwell, I. Tegen and R. Torres, *Science* **308** (2005) 67–71.
27. K. W. Bruland, K. J. Orians and J. P. Cowen, *Geochim. Cosmochim. Acta* **58** (1994) 3171–3182.
28. R. T. Reid, D. H. Live, D. J. Faulkner and A. Butler, *Nature* **366** (1993) 455–458.
29. C. G. Trick and S. W. Wilhelm, *Mar. Chem.* **50** (1995) 207–217.
30. S. W. Wilhelm, K. MacAuley and C. G. Trick, *Limnol. Oceanogr.* **43**(5) (1998) 992–997.
31. B. L. Lewis, P. D. Holt, S. W. Taylor, S. W. Wilhelm, C. G. Trick, A. Butler and G. W. Luther, *Mar. Chem.* **50** (1995) 179–188.
32. J. Granger and N. M. Price, *Limnol. Oceanogr.* **44**(3) (1999) 541–555.
33. E. L. Rue and K. W. Bruland, *Limnol. Oceanogr.* **42**(5) (1997) 901–910.
34. M. Boye, A. P. Aldrich, C. M. G. van den Berg, J. T. M. de Jong, M. Veldhuis and H. J. W. de Baar, *Mar. Chem.* **80** (1995) 129–143.
35. A. E. Witter, B. L. Lewis and G. W. Luther, *Deep-Sea Res.* **47** (2000) 1517–1539.
36. C. M. G. van den Berg, *Mar. Chem.* **50** (1995) 139–157.
37. P. L. Croot, K. Andersson, M. Ozturk and D. R. Turner, *Deep-Sea Res.* **51** (2004) 2857–2879.
38. D. A. Hutchins, A. E. Witter, A. Butler and G. W. Luther, *Nature* **400** (1999) 858–861.
39. M. T. Maldonado and N. M. Price, *Deep-Sea Res.* **46** (1999) 2447–2773.
40. M. T. Maldonado, R. F. Strzepek, S. Sander and P. W. Boyd, *Global Biogeochem. Cycles* **19** (2005) GB4S23.
41. M. J. Ellwood, *Mar. Chem.* **87** (2004) 37–58.
42. F. Partensky, W. R. Hess and D. Vaulot, *Microbiol. Mol. Biol. Rev.* **63** (1999) 106–127.
43. F. Partensky, J. Blanchot and D. Vaulot, *Mar. Cyanobacteria* **19** (1999) 457–475.
44. S. W. Chisholm, P. G. Falkowski and A. D. Woodhead (eds.) (Plenum Press, 1992) pp. 213–237.
45. T. S. Bibby, I. Mary, J. Nield, F. Partensky and J. Barber, *Nature* **424** (2003) 1051–1054.
46. C. S. Ting, G. Rocap, J. King and S. W. Chisholm, *Trends Microbiol.* **10** (2002) 134–142.
47. E. L. Mann and S. W. Chisholm, *Limnol. Oceanogr.* **45**(5) (2000) 1067–1076.

This page intentionally left blank

COASTAL PROCESSES WITH IMPROVED TIDAL OPENING IN CHILIKA LAGOON (EAST COAST OF INDIA)

GIRIJA JAYARAMAN and ANUMEHA DUBE

*Centre for Atmospheric Sciences,
Indian Institute of Technology,
Hauz Khas, New Delhi — 110016, India*

Chilika Lagoon ($19^{\circ}28' - 19^{\circ}54'N$ and $85^{\circ}06' - 85^{\circ}36'E$) is the largest brackish water lagoon with estuarine character. Interest in detailed analysis of the ecology of the lagoon and the various factors affecting it is due to the opening of the new mouth on September 23, 2000 to resolve the threat to its environment from various factors — Eutrophication, weed proliferation, siltation, industrial pollution, and depletion of bioresources. The opening of the new mouth has changed the lagoon environment significantly with better socio-economic implications. There is a serious concern if the significant improvement in the biological productivity of the lagoon post-mouth opening is indeed sustainable. The present study focuses on the changes in the coastal processes as a result of the additional opening of a new mouth. Our results based on mathematical modeling and numerical simulation compare the dynamics, nutrient, and plankton distribution before and after the new mouth opening. The model could confirm the significant increase (14–66% depending on the sector) in the salinity after the new mouth opening, the maximum change being observed in the channel which connects the lagoon to the sea. The constriction in the lagoon which blocks the tidal effects entering the lagoon must be responsible for maintaining the main body of the lagoon with low salinity. The ecological model is first tested for different sectors individually before a complete model, including the entire lagoon area, is included incorporating their distinct characteristics. The model is validated with available observations of plankton and nutrients made before the opening of the new mouth. It predicts the annual distribution of plankton in all the sectors of the lagoon for post-mouth opening which is to be verified when the data will be forthcoming.

1. Introduction

Management of a coastal lagoon involves constant monitoring of the tidal openings, which affect the exchange of water between the sea and the lagoon and hence its water quality and biological productivity. The management

strategy often includes artificial opening of a new mouth in addition to the existing mouth. The success of the strategy and the choice of the new mouth opening location is assessed by comparing the data on salinity, biological productivity, dissolved oxygen, sediment distribution, etc., obtained after the new mouth opening with those of the pre-mouth opening conditions. Numerical models of transport processes combined with accurate observational studies can be effectively used as management tools. In conjunction with monitoring programs and laboratory experiments, there is a need to formulate quantitative models to predict, to guide assessment, and to direct intervention. Assessment based on modeling approach will depend on: (i) hydrodynamic models, (ii) models depicting the spatio-temporal behavior of the biological species, (iii) water quality studies, and (iv) models for sediment transport in the lagoon corresponding to both the situations — pre- and post-mouth opening and their comparison. The credibility of a model depicting the transport processes in a coastal lagoon depends on how accurately the model responds to the perturbations (e.g., a new mouth opening).

The circulation/dynamic models are fundamental for any further understanding of the biological processes, since the circulatory pattern regulates the supply of dissolved inorganic nutrients. With the advancement of computational techniques and technological sophistication in recording the data at several spatial locations, a holistic approach leading to spatio-temporal models is getting popular.^{1–5} The objective of the mathematical modeling of ecological problems is quantitation of the interaction within and between species and their inorganic environment, and the investigation of the temporal/spatial variation of groups of individual of various species.

Chilika Lagoon, on the east coast of India, offers an interesting study to understand, through mathematical modeling and numerical simulation, the changes that a lagoon can undergo after the governmental implementation of a managerial decision to open an additional mouth. The opening of the new mouth is claimed as an historic and most successful intervention in the history of the restoration of the ecosystem. According to Chilika Development Authority (CDA), opening of the new mouth has made positive impacts on the lagoon ecosystem: increase in salinity level, autorecruitment of fish and prawn, reduction in eutrophication/weed infestation, and dramatic improvement in the fish landing and productivity of the lagoon (<http://www.chilika.com>).

In our earlier paper,⁶ we modeled the dynamics and salinity distribution of Chilika, and validated the model with the available observations. Our

model could effectively simulate the currents and salinity corresponding to (i) the southwest and northeast monsoon seasons and (ii) pre- and post-mouth opening conditions. In this study, our earlier model is complemented with an ecological model which is validated with the available data for pre-mouth opening conditions. The model predicts the modifications in the biological productivity due to the additional mouth and needs to be validated with credible data which is yet to be available.

2. Description of Study Area and Details about the New Mouth Opening

Chilika Lagoon ($19^{\circ}28'$ – $19^{\circ}54'$ N and $85^{\circ}06'$ – $85^{\circ}36'$ E) on the Orissa coast, India, is one of the unique ecospheres in the world. The water-spread area of the Chilika Lagoon varies between 1165 and 906 sq km during the monsoon and summer, respectively.⁷ A significant part of the freshwater and silt input to the lagoon comes from river Mahanadi and its distributaries.⁸ Based on the physical and dynamical characteristics of the lagoon, the lagoon is divided into four sectors (Fig. 1). The northern sector receives discharge of the floodwaters from the rivers. It is the shallowest region of the lagoon and has the highest nutrient concentrations, which are brought in by the river waters draining in the lagoon basin. The northern sector shows the lowest salinity levels (1–8 ppt) in the entire lagoon. The southern sector is relatively smaller and does not show much seasonal variation in any of the hydrographic parameters. Salinity in southern sector ranges from a low of 1 ppt during the southwest monsoon season to 20 ppt during the northeast monsoon season. It is the deepest of all the three sectors and is poor in nutrients. The central sector has features intermediate of the other two sectors, salinity in the central sector is high as compared to the northern and southern sectors (6–20 ppt). The lagoon is separated from the Bay of Bengal by a sand bar 60 km in length. A distinct salinity gradient exists along the lagoon due to the influx of freshwater from the rivers and the inflow of seawater through the outer channel. The width of the original and natural tidal mouth opening is about 1.5 km.

Due to choking of the outer channel and northward shifting of the tidal mouth,⁹ exchange of water and sediment between the lagoon and the sea was affected. To preserve the rich biodiversity of Chilika, the Indian Government, through CDA, initiated many conservation measures and the opening of the tidal mouth on September 23, 2000 is considered as one

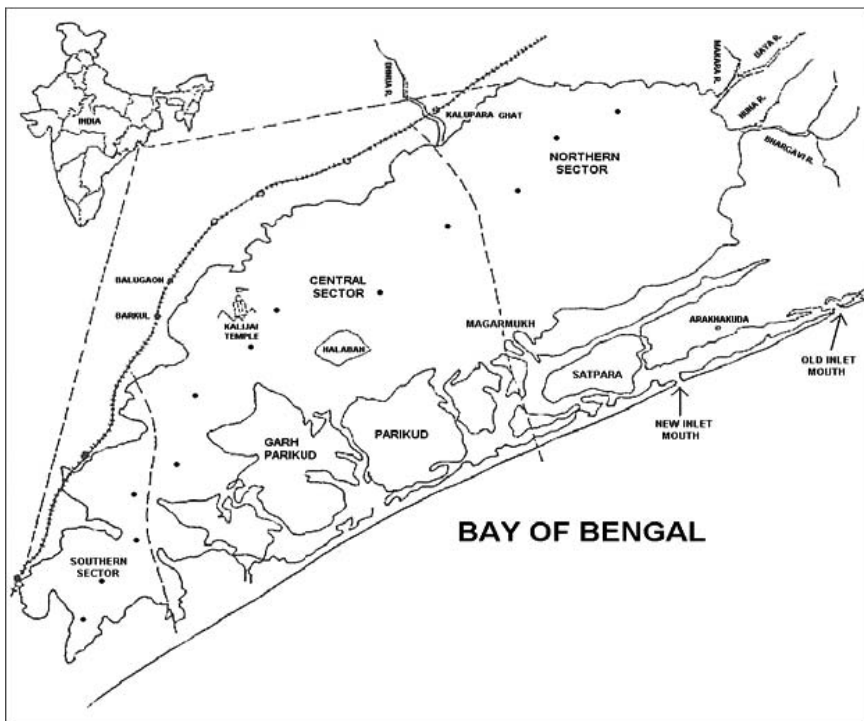


Fig. 1. Map of Chilika showing different sectors.

of the major accomplishments (<http://www.chilika.com>). The new tidal opening is also situated in the northeastern end of the lagoon and the distance between the old mouth and the new mouth is around 17 km along the coastline (Fig. 1). Opening of the new mouth has significantly changed the lagoon environment resulting in major changes in the hydrography and ecology of the lagoon. Increase in the salinity of the lagoon waters after the opening of the mouth provides the desirable sense of direction for the eurohaline forms to enter into the lagoon from the sea. This is facilitating the autorecruitment of fish, prawn, and crab juvenile into the lagoon. As against the annual average fish landing of 1600 metric tons, recorded during the past 6 years, the fish landing during the year 2001–2002 has improved to 11,988.88 metric tons, which is a record production, and an all-time high in the history of Chilika. The total prawn and crab landing were 2478.82 and 149.81 metric tons, respectively, which are considered as all-time high record (<http://www.chilika.com>).

It is essential to compare and model the pre- and post-mouth opening conditions, particularly, the changes in circulation patterns and salinity structures and their effect on the lagoon ecology, since seasonal studies based on such a model will help in understanding if the significant improvement in the biological productivity of the lagoon after post-mouth opening is sustainable.

3. Observations for Surface Water Current, Salinity, and Plankton of Chilika Lagoon (Pre- and Post-mouth Opening)

Maximum current velocity was observed in the channel (tidal effect) and near the northern sector (river water flux). Tidal amplitudes were examined at three important points such as the Satpada and Magarmukh (Fig. 1). During January, the maximum tidal amplitude was observed as 0.76 m near Sipakuda which gradually declined at Satpada (0.37 m) and at Magarmukh (0.25 m). These measurements were taken in the interior side of the lagoon where there are other influences due to the seasonal change and this could be responsible for slightly lower values in July.

Salinity variation in the lagoon is significant which ranges from almost freshwater (0.2 ppt) to little less than saline water (22 ppt) in the pre-mouthopening condition and from 0.4 to 33 ppt in the post-mouth opening condition during summer. The observed salinity concentration in the outer channel is high but in the northern sector, which receives freshwater from Mahanadi river system, the salinity is almost zero during SWM. Salinity gradient is lower in the southern and central sectors and increases gradually in the direction of the outer channel.¹⁰ The impact of new tidal mouth on salinity variation is very significant in the central sector and the channel.

Chilika Lagoon constitutes a typical environment for the study of marine algae because of its variable hydrological conditions from place to place and from season to season.¹¹ Biological production in Chilika was studied in the form of total chlorophyll pigment found in the lagoon waters. Chlorophyll *a* showed much higher concentrations in the northern sector as compared to the southern sector.^{10,12}

The total biomass of phytoplankton is observed to be the highest in the Northern Sector followed by the central sector, and lowest phytoplankton concentration was observed in the southern sector. Seasonally, phytoplankton are seen to be maximum in summer followed by

winter and the rainy seasons. The primary peak is found to occur during March–May followed by a secondary peak in November.¹³ Sector wise, a high nutrient concentration was observed in the northern sector where the effect of freshwater was more.¹⁴

4. Modeling the Circulation, Salinity, and Ecology of Chilika Lagoon (Pre- and Post-mouth Opening)

4.1. *Modeling the hydrodynamics and salinity of Chilika Lagoon*

Our depth-averaged model developed was used to obtain information on the response of Chilika waters to: (i) tidal effects, (ii) wind forcing, and (iii) freshwater input was solved numerically for two seasons: (i) Southwest monsoons and (ii) northeast monsoons. The model is forced by the climatological mean winds representative of the months of July and January (chosen as the representative months for SWM and NEM, respectively). During July, the wind direction is almost southwest (200°) with a uniform speed of 6.5 m/s and in January the direction of the wind is almost northeast (40°) with uniform speed of 2 m/s over the entire lagoon area.¹⁵ Numerical experiments were carried out with each of the forcing factors (wind, tides, and freshwater influx) individually and collectively in order to analyze their effect on the circulation. Also, results were analyzed separately for circulation corresponding to flood, ebb, and mean, where the mean was taken over a tidal period after the steady state was achieved. We present here only the results for southwest monsoon season and these are depicted in the Figs. 2–5. Figures 2 and 3 show the mean circulatory pattern, and Figs. 4 and 5 depict the mean salinity structure for pre- and post-mouth opening. More details related to the model, resulting circulation and salinity patterns for pre- and post-mouth opening conditions, and corresponding to ebb and flood conditions can be found in Jayaraman *et al.*⁶ and Jayaraman and Dube.¹⁶

The tides at both the tidal openings are considered to be in phase owing to the short distance of 17 km between the two tidal openings. The circulatory patterns for both the cases are found to be qualitatively very similar showing that the residual circulation is not affected qualitatively by the opening of the new tidal mouth. The only changes are in the outer channel region and the central sector due to an increase in the tidal influx which is attributed to the opening of the new tidal mouth. An overall

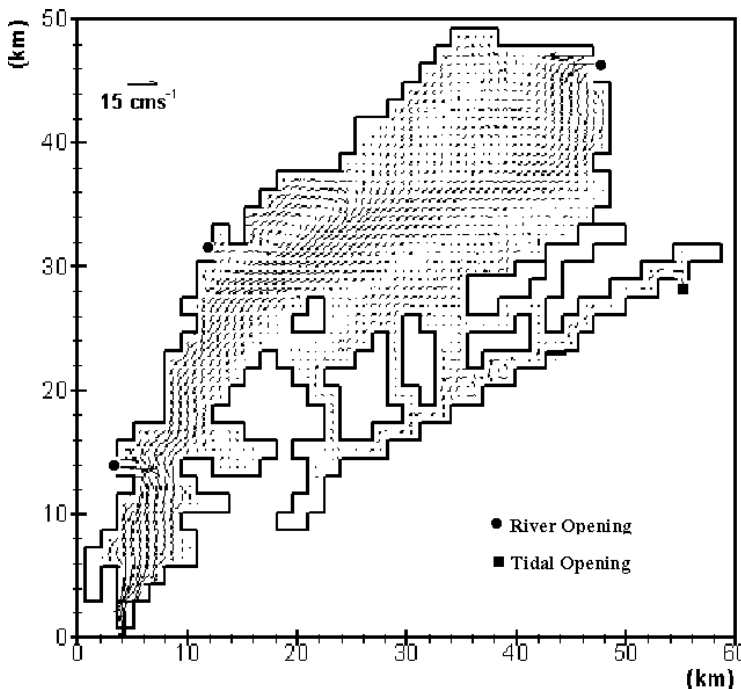


Fig. 2. Mean circulation as a result of tide, July wind, and freshwater influx (old inlet).

increase in the current intensity is observed due to the new tidal opening. For both the cases (pre- and post-mouth opening) the mean circulation profile suggests ebb current is stronger than flood current.

All discussions for the salinity patterns in the lagoon are based on the mean salinity profile. The salinity changes were analyzed within a tidal range, i.e., for the flood and ebb cases. It was observed from the model results that the flood and ebb salinity profiles did not show a lot of variations, particularly in the main body of the lagoon. This can be attributed to the narrowness of channel which obstructs the flow from the sea into the main body of the lagoon and hence the changes in salinity within a tidal period are seen only in the outer channel region rather than the main body of the lagoon. The salinity values show an overall increase due to the new mouth. The results confirm that the region of maximum salinity is the channel and there is a steady decrease in salinity near the mouth to where the channel ends and the central sector begins, where it takes on a plume-like structure. A large plume dominates the

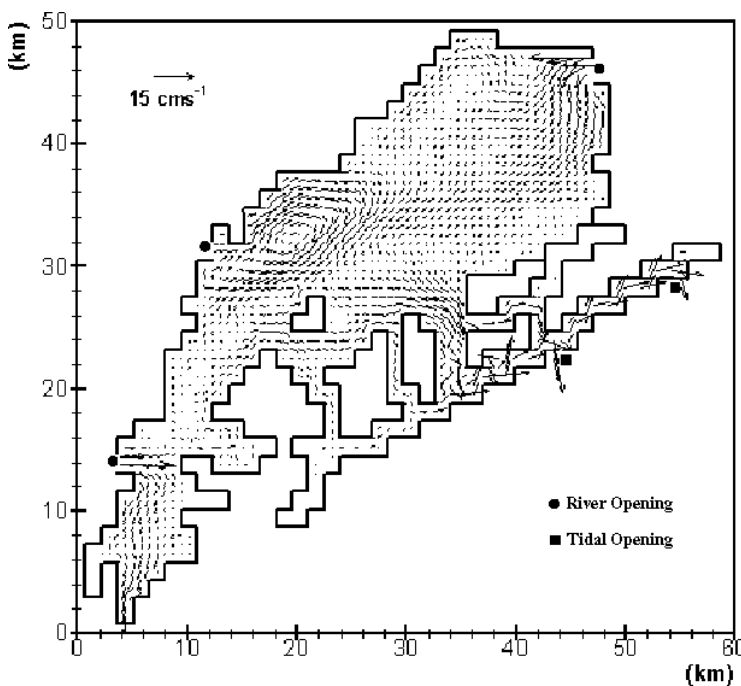


Fig. 3. Mean circulation as a result of tides, July wind, and freshwater influx (both inlets).

central sector and has higher salinity (8–10 ppt) as compared to the one-mouth plume (6–8 ppt). In the central sector salinity ranges from 8 to 10 ppt (as against 4–6 ppt for single mouth). Northern sector also shows an increase in the salinity levels (2–8 ppt) as compared to the single mouth case (1–4 ppt). In general, the new tidal mouth affects salinity values throughout the main body of the lagoon except in the northernmost and the southernmost regions. The results have been validated against the available observations and found to be in good agreement (Table 1).

4.2. Ecological model

There is a significant change in the nutrient concentration and plankton distribution after the new mouth opening making it essential to compare the biological production in the lagoon for the pre- and post-new mouth opening cases. The present paper is aimed at studying the effect of new

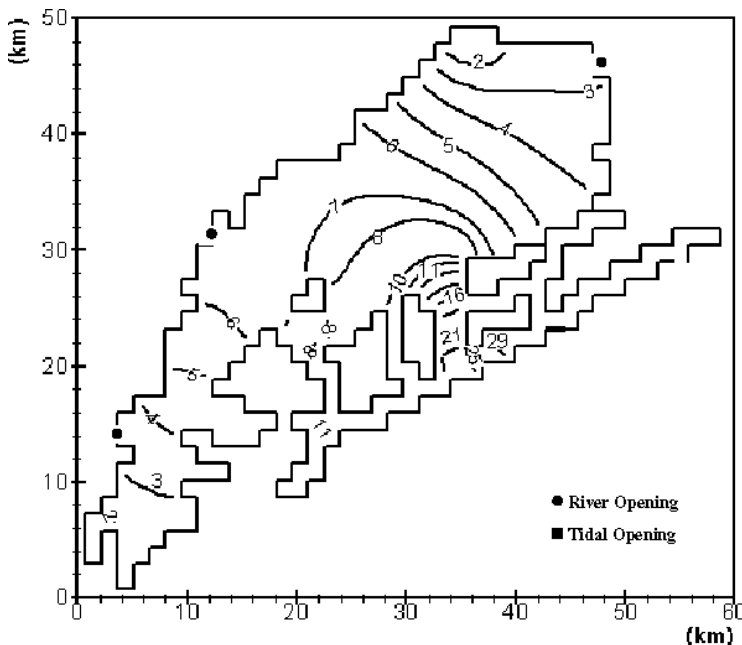


Fig. 4. Horizontal salinity in ppt as a result of tide, July wind, and freshwater influx (old inlet).

mouth opening on the biological productivity of the lagoon by a three-compartment (nutrient, phytoplankton, and zooplankton) ecological model. Details about the basic ecological model are given in the Appendix. The model is solved for different sectors of the lagoon which have distinct characteristics in terms of depth, light penetration, nutrients, and hence planktonic growth.

The model is solved twice: firstly, with appropriate initial conditions for pre-mouth opening conditions; and secondly, for the initial conditions of the postmouth opening case. Salinity variations are introduced in the model as in Griffin *et al.*² The analysis done in this paper is for the total phytoplankton for the pre- and post-mouth opening conditions for each of the sectors. Some of the model parameters which are specific to Chilika are not known but in order to reduce the trial and error, and make a rough estimate of the range of parameters involved, a local stability analysis of the system of equations with N_0 as constant was undertaken. For the validation of the simulated results, fine tuning and sensitivity analysis of the parameters were required. The values of the parameters used in the

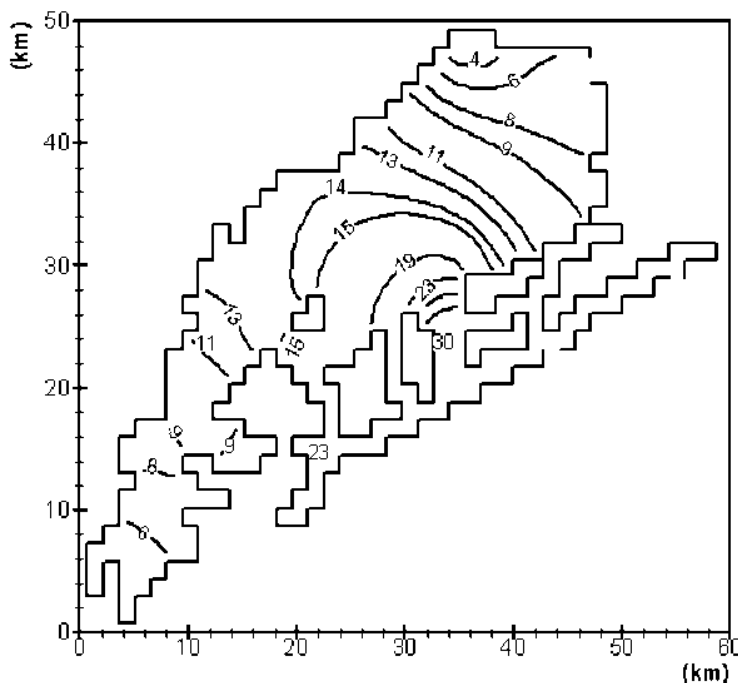


Fig. 5. Horizontal salinity in ppt as a result of tide, July wind, and freshwater influx (both inlets).

model are given in Table 2. Due to the unavailability of data for the post-mouth opening case the validation is done for the total phytoplankton of the pre-mouth opening conditions only. Therefore, for the post-mouth opening case we can only predict the response of phytoplankton to changes in salinity. The result of the total phytoplankton distribution along with the observations for the pre-mouth opening conditions for the northern, central, and southern sectors are given in Figs. 6(a–c).

Table 1. Comparison of observed and computed salinity values (ppt) for July.

| Sectors | Pre-mouth Observed | Pre-mouth Simulated | Post-mouth Observed | Post-mouth Simulated |
|----------|-----------------------|------------------------|------------------------|-------------------------|
| Northern | 0.4–1.3 | 1.0–4.0 | 0.4–4.4 | 0.4–5.6 |
| Central | 4.6–9.2 | 4.0–10.0 | 0.4–12.7 | 1.0–14.0 |
| Southern | 8.0–11.2 | 4.0–6.0 | 12.7–20.2 | 6.0–10.0 |

Table 2. Parameter values used in the model

| Parameter | Definition | Northern sector | | Central sector | | Southern sector | |
|----------------------------|---|-----------------|--------------|----------------|--------------|-----------------|--------------|
| | | Pre-mouth | Post-mouth | Pre-mouth | Post-mouth | Pre-mouth | Post-mouth |
| $K_{N,1}$ (mg/l) | Nutrient uptake | 10.0 | 10.0 | 10.0 | 20.0 | 15.0 | 10.0 |
| $K_{N,2}$ (mg/l) | half saturation | 10.0 | 10.0 | 20.0 | 20.0 | 20.0 | 10.0 |
| N_0 (mg/l) | Nutrient source ¹⁹ | | 150.89 | | 107.95 | | 91.25 |
| r_1 (day ⁻¹) | Respiration rate | 0.25 | 0.25 | 0.1 | 0.1 | 0.3 | 0.1 |
| r_2 (day ⁻¹) | of phytoplankton | 0.25 | 0.25 | 0.15 | 0.1 | 0.1 | 0.1 |
| m_1 (day ⁻¹) | Vertical diffusion rate | | 0.05 | | 0.07 | | 0.07 |
| c (day ⁻¹) | Grazing rate | | (0.058–0.06) | | (0.07–0.076) | | (0.07–0.076) |
| p_1 | Palatability of freshwater phytoplankton to zooplankton ¹⁸ | | 0.4 | | 0.4 | | 0.4 |
| p_2 | Palatability of marine phytoplankton to zooplankton ¹⁸ | | 0.4 | | 0.4 | | 0.4 |
| K_Z (mg/l) | Grazing half saturation | | (30.0–65.0) | | (55.0–82.0) | | (50.0–75.0) |
| P_0 (mg/l) | Grazing threshold | | (5.0–9.0) | | (5.0–8.0) | | (1.0–3.0) |
| e | Assimilation efficiency | | (0.8–0.92) | | (0.8–0.85) | | (0.3–0.6) |

(Continued)

Table 2. (Continued)

| Parameter | Definition | Northern sector | | Central sector | | Southern sector | |
|--------------------------|---|-----------------|--------------|----------------|--------------|-----------------|--------------|
| | | Pre-mouth | Post-mouth | Pre-mouth | Post-mouth | Pre-mouth | Post-mouth |
| g (day $^{-1}$) | Loss rate of zooplankton | | (0.03–0.045) | | (0.01–0.018) | | (0.01–0.013) |
| D (m) | Depth ⁶ | | 1.5 | | 2.0 | | 2.5 |
| σ_1 (ly $^{-1}$) | Low light | | 0.4 | | 0.4 | | 0.4 |
| σ_2 (ly $^{-1}$) | photosynthetic slope ¹⁷ | | 0.02 | | 0.02 | | 0.02 |
| Q_1 (day $^{-1}$) | Maximum photosynthetic | | 2.3 | | 2.3 | | 2.3 |
| Q_2 (day $^{-1}$) | rate ¹⁷ | | 3.2 | | 3.2 | | 3.2 |
| k_1 (day $^{-1}$) | Light attenuation by | | 0.0 | | 0.0 | | 0.0 |
| k_2 (day $^{-1}$) | plankton ¹⁷ | | 0.1 | | 0.1 | | 0.1 |
| S_{OPT} (ppt) | Optimal salinity (freshwater plankton) ² | | 14.0 | | 14.0 | | 14.0 |
| S_{OPT} (ppt) | Optimal salinity (marine plankton) ² | | 20.0 | | 20.0 | | 20.0 |
| β | Value of $f(S)$ when $S = 2S_{OPT}^2$ | | 2.0 | | 2.0 | | 2.0 |
| β | Value of $f(S)$ when $S = 0^2$ | | 2.5 | | 2.5 | | 2.5 |

Suffix 2 corresponds to Marine Species of Phytoplankton.

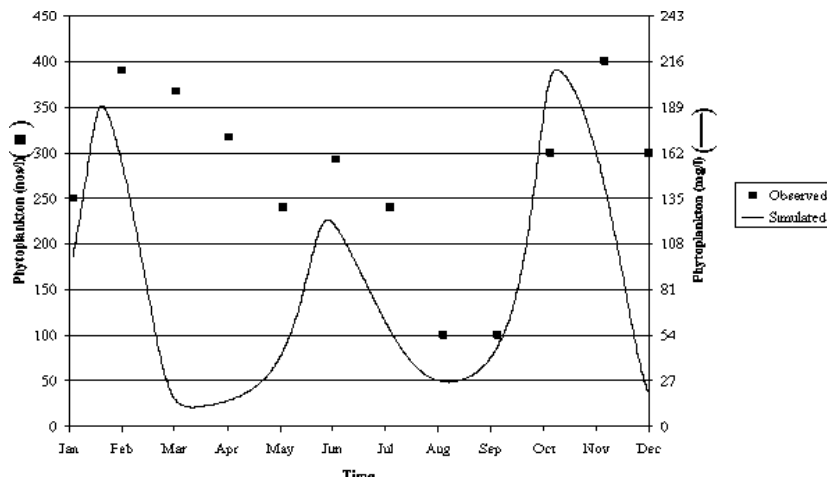


Fig. 6(a). Annual phytoplankton distribution in northern sector.

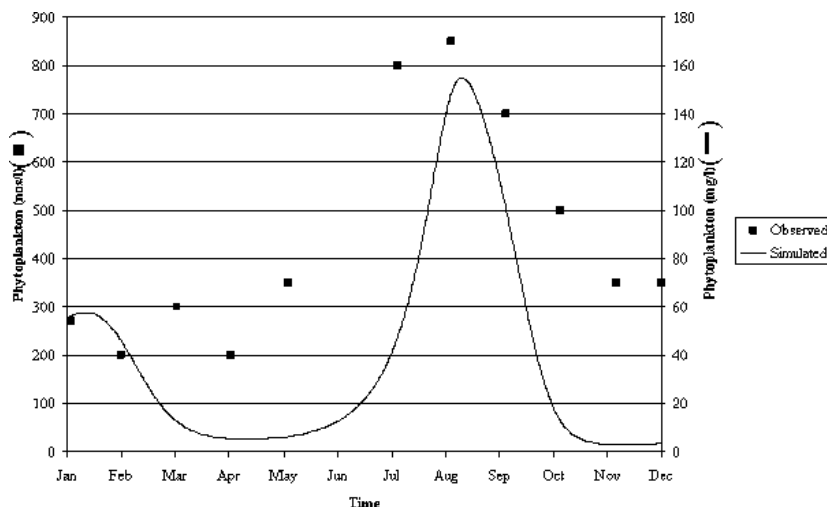


Fig. 6(b). Annual phytoplankton distribution in central sector.

Figures 7(a-c) give a comparison of the phytoplankton distribution for the pre- and post-mouth opening cases in each of the sectors. From Fig. 7(a), which depicts the total phytoplankton in the northern sector for the pre- and post-mouth opening cases, it can be seen that the phytoplankton concentrations are very low for the post-mouth opening

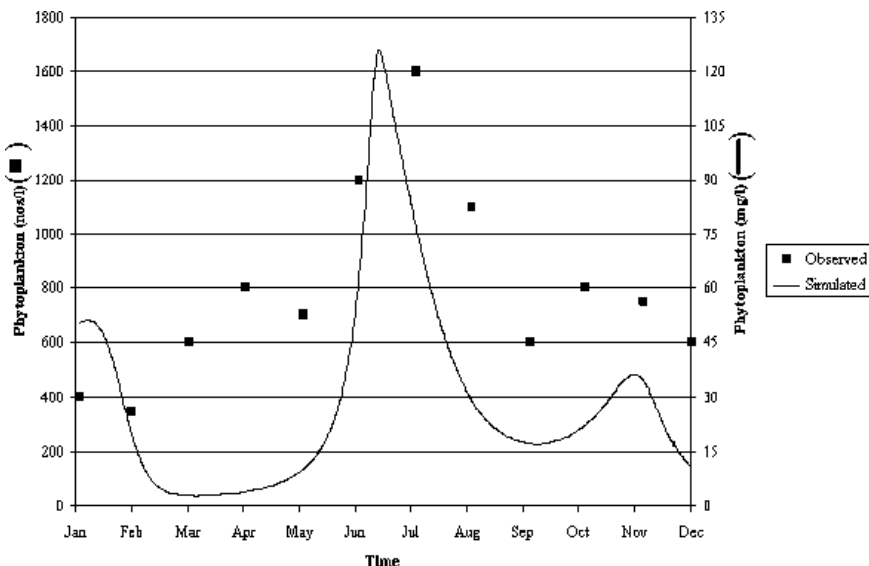


Fig. 6(c). Annual phytoplankton distribution in southern sector.

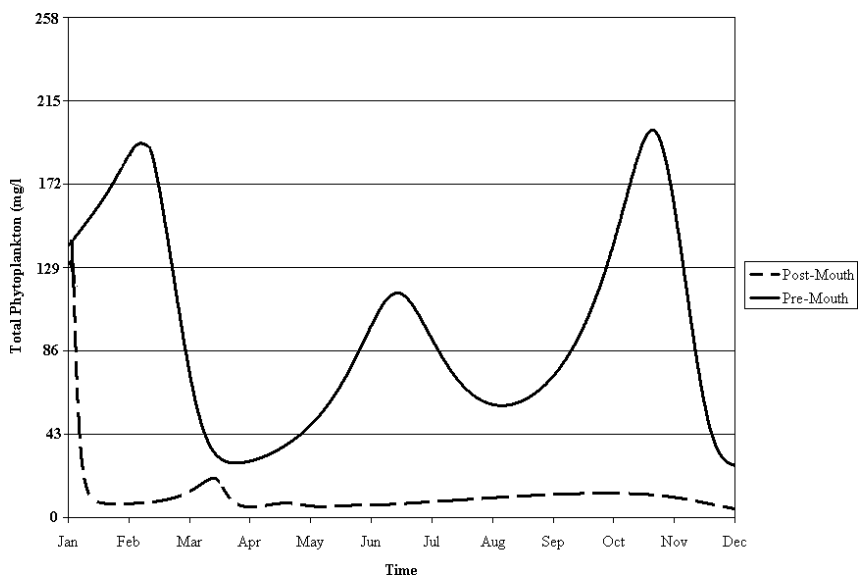


Fig. 7(a). Total phytoplankton in northern sector (pre-and post-mouth).

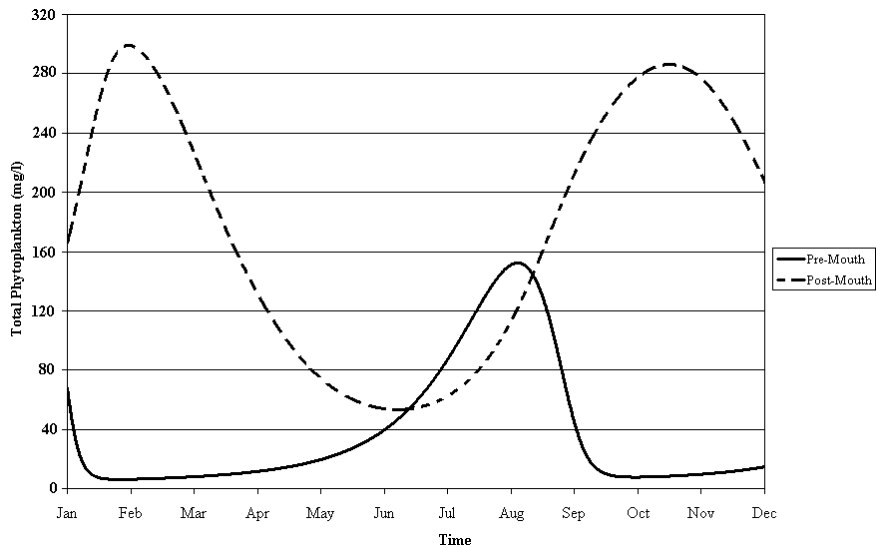


Fig. 7(b). Total phytoplankton in central sector (pre- and post-mouth).

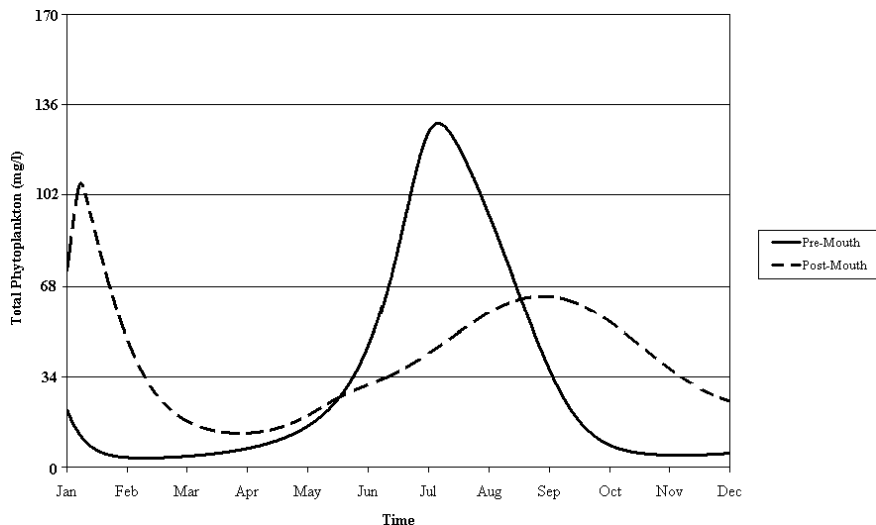


Fig. 7(c). Total phytoplankton in southern sector (pre- and post-mouth).

case. This can be attributed to the fact that the northern sector is mostly dominated by the freshwater-adapted species and an increase in salinity due to the opening of the new mouth leads to a decrease in their population. Figure 7(b) shows a comparison between the phytoplankton for the pre- and post-mouth opening cases for the central sector. The central sector constitutes of brackish water and has both freshwater and marine species of phytoplankton. The phytoplankton population in this sector shows an increase in the post-mouth opening case as compared to the pre-mouth case. This increase may be due to the increase in salinity which makes the environment favorable for the marine species of phytoplankton to grow and hence the total phytoplankton population shows an increase. Figure 7(c) depicts a comparison between the pre-mouth and post-mouth distribution of phytoplankton in the southern sector. The phytoplankton population shows a decrease in the post-mouth opening case which may be due to an increase in salinity. For the pre-mouth opening case the salinity levels in the southern sector are favorable for the freshwater phytoplankton and unfavorable for the marine species. But after the opening of the new mouth the salinity levels increase and become unfavorable for the freshwater species. This increase in salinity is not able to reach to a level which may be favorable for the marine species. This leads to a decrease in the total phytoplankton population in the southern sector.

5. Conclusions

The results for the hydrodynamic model show that although the second opening has helped in increasing the tidal influx and hence the salinity, its influence is still not felt far interior of the lagoon due to the constriction of flow area between the lagoon and the channel area. The simulated results have been validated against the limited observations and found fairly in good agreement. Our model simulation results show that out of the different terms in the growth rate, changes in light-limited growth rate and nutrient-limited growth rate are the controlling factors for phytoplankton population. The results are validated against the observed values for 1989²⁰ and are found to be in good agreement. With the status of data at the present time, only a qualitative validation of the numerical results is possible. We have verified for different years (1987, 1998, 1999, 2000, and 2001) using the discrete data we have from various authors.

This model can be used to study the impact of the new mouth opening which has resulted in an increased biological productivity, once more

sophisticated field observations are available for the post-mouth opening conditions. It can also be used to compare the pre- and post-mouth opening plankton distributions. For a holistic and complete understanding of the influence of physical processes, freshwater discharges, and tidal forces on the seasonality of phytoplankton in Chilika Lagoon, a physico-biological model linking our earlier study⁶ with the present analysis needs to be formulated. The conclusions based on a systematic study of dynamics, salinity, and ecology of the lagoon will help in analyzing if the significant improvement observed in the biological productivity of the lagoon after post-mouth opening is sustainable.

References

1. C. Pinazo, S. Bujan, P. Douillet, R. Ficchez, C. Grenz and A. Maurin, *Coral Reefs* **23**(2) (2004) 281–296.
2. A. L. Griffin, H. Michael and D. P. Hamilton, *Ecol. Eng.* **16** (2001) 373–394.
3. M. R. Flindt, M. A. Pardal, A. I. Lillebø, I. Martins and J. C. Marques, *Acta Oecol.* **20**(4) (1999) 237–248.
4. V. A. Ryabchenko, V. A. Gorchakov and M. J. R. Fasham, *Global Biogeochem. Cycles* **12** (1998) 501–530.
5. T. Oguz, H. Ducklow, P. Malanotte-Rizzoli, S. Tugrul, P. N. Nezlin and U. Unluata, *J. Geophys. Res.* **101**(7) (1996) 16585–16600.
6. G. Jayaraman, A. D. Rao, A. Dube and P. K. Mohanty, *J. Coastal Res.* (2007) (To appear in April 2007).
7. S. Z. Siddiqi and K. V. Rama Rao, *Fauna of Chilka Lake, Wetland Ecosystem, Series 1* (Edited by the director, Zoological Survey of India, Calcutta, 1995), pp. 11–136.
8. P. K. Mohanty, S. K. Dash, P. K. Mishra and A. S. Murty, *Indian J. Mar. Sci.* **25** (1996) 184–188.
9. P. Chandramohan and B. U. Nayak, *J. Coastal Res.* **10** (1994) 909–918.
10. J. Rath and S. P. Adhikary, *Seaweed Res. Utilization* **25**(1/2) (2003) 127–130.
11. J. Rath and S. P. Adhikary, *Algal Flora of Chilika Lake* (Daya Publishing House, Delhi, 2005), pp. 127–130.
12. B. K. Nayak, B. C. Acharya, U. C. Panda, B. B. Nayak and S. K. Acharya, *Indian J. Mar. Sci.* **33**(2) (2004) 164–169.
13. R. C. Panigrahy, *J. Indian Ocean Stud.* **7**(2/3) (2000) 222–242.
14. D. Panda, S. K. Tripathy, D. K. Patnaik, S. B. Choudhary, R. Gouda and R. C. Panigrahy, *Indian J. Mar. Sci.* **18** (1989) 286–288.
15. S. Hastenrath and P. J. Lamb, *Climatic Atlas of the Indian Ocean, Part-1: Surface Climate and Atmospheric Circulation* (The University of Wisconsin Press, 1979), pp. viii–xi.
16. G. Jayaraman and A. Dube, in *Modelling and Simulation: Life Sciences, Materials and Technology*, eds. A. Avudainayagam, P. Misra and S. Sundar (Narosa Publishing House, New Delhi, 2005), pp. 143–171.

17. G. T. Evans and J. S. Parslow, *Biol. Oceanogr.* **3**(3) (1985) 327–346.
18. G. T. Evans, *Limnol. Oceanogr.* **33**(5) (1988) 1027–1036.
19. A. V. Raman, Ch. Satyanarayana, K. Adiseshasai and K. Phani Prakash, *Indian J. Mar. Sci.* **19** (1990) 274–277.
20. S. P. Adhikary and J. K. Sahu, *Jpn J. Limnol.* **53**(3) (1992) 197–205.

Appendix

The basic general equations that give the time evolution of a chemical or biological quantity are given by

$$\frac{dB_i}{dt} = S_i + D_i \quad i = 1, 2, \dots \quad (\text{A.1})$$

where B_i represents the concentration of the i th chemical or biological species, S_i is the source term, and D_i the decay term which is defined for each variable B_i by a function depending upon the concentration of some other variables B_j as well as B_i itself.

We propose a purely ecological model for nutrients (N), phytoplankton (P), and zooplankton (Z). The specific governing equations for these variables considered in this study are:

$$\frac{dN}{dt} = - \left[\frac{\bar{\alpha}N}{K_N + N} - r \right] P + \frac{m_1}{D} N_0(t) \quad (\text{A.2})$$

$$\frac{dP}{dt} = \left[\frac{\bar{\alpha}N}{K_N + N} - r \right] P - \frac{c(P - P_0)Z}{K_z + P - P_0} \quad (\text{A.3})$$

$$\frac{dZ}{dt} = \frac{e \times c \times (P - P_0) \times Z}{(K_z + P - P_0)} - g \times Z \quad (\text{A.4})$$

where the concentrations of nutrients, phytoplankton, and zooplankton are measured in mg/l, t is time, $\bar{\alpha}$ (day $^{-1}$) is the light-limited growth rate, and r (day $^{-1}$) is the metabolic, respiratory loss rate of the phytoplankton. K_N (mg/l) and K_z (mg/l) are the half-saturation coefficients for nutrient uptake and zooplankton grazing, respectively, c (day $^{-1}$) is the grazing rate and P_0 (mg/l) is the grazing threshold. $N_0(t)$ is the source of nutrients, m_1 (m/day) is the vertical diffusion rate and D is the depth in meters. e is the grazing efficiency and g (day $^{-1}$) is the loss of zooplankton to carnivores. The formulation for the light-limited growth rate of the phytoplankton has been adopted from Evans and Parslow.¹⁷

ATMOSPHERIC SCIENCE (AS)

This page intentionally left blank

SEMI-IDEALIZED COAMPS^{®a} SIMULATIONS OF SUMATRA SQUALL LINES: THE ROLE OF BOUNDARY FORCING

Lan Yi*† and Hock Lim‡

†*Temasek Laboratories, Nanyang Technological University,
Singapore*

‡*Temasek Laboratories, National University of Singapore,
Singapore*

*yilan@ntu.edu.sg

Sumatra squall line is a fairly impactive convective storm that often forms along the Malacca Straits and sweeps across Singapore in the early mornings of April to November each year. To understand and better predict this phenomenon, cloud resolving simulations with COAMPS^a at 3 km horizontal resolution are performed in a 3-D semi-idealized framework starting from a horizontally uniform atmosphere initialized by observed radiosonde data. Realistic boundary forcing effects by land-sea distribution, radiative fluxes, topography, and sea surface temperature (SST) are evaluated. Five ellipsoidal warm bubbles are prescribed to line up along the Malacca Straits to spawn a squall line. The bubbles are excluded in some cases to see if the squall line can be triggered without the initial external perturbation. Results demonstrate that line convection can be initiated by SST heating under no initial thermal perturbation; warm SST is conducive to kicking off convection. The diurnal circulations driven by the land sea thermal contrast play an important role in the intensification of the Sumatra squall line and its eastward migration. The shallow convection is enhanced by the convergence resulting from colliding land breezes from the west and the east coast of the Malacca Straits. It is found that the high relieves along west Sumatra and northwest Malaysia act to veer the low to mid tropospheric westerly winds into northerly flows, which converge into the strait with the southwest monsoonal flows from the south. The low-level convergence may then trigger and sustain the squall line.

1. Introduction

Malacca Straits is a narrow waterway separating the Malay Peninsular and the Sumatra Island of Indonesia. A number of vessels pass through

^aCOAMPS stands for Coupled Ocean/Atmosphere Mesoscale Prediction System. COAMPS is a registered trademark of the US Naval Research Lab.

it every day carrying nearly half the world's oil supplies and one-third of the global trade.¹ Being one of the transit chokepoints, Malacca Straits grows in economic and military importance.² The most significant weather around the area is the Sumatra squall line.

Sumatra squall lines, named "Sumatras" by locals, are moving lines of thunderstorms that form along the Straits of Malacca during night, pre-dawn, morning and afternoon hours in April to November. They often propagate eastwards, affecting the west coast of Malaysia and Singapore. Like the squall lines in US³ and other countries, "Sumatras" are usually hundreds of kilometers in length with several hours life span, and accompanied by gusty winds and heavy rains.

Limited studies of the "Sumatras" have been performed by Watts,⁴ Pakiam *et al.*,⁵ Lim⁶ and perhaps others a few to several decades ago. The structure and dynamics of tropical squall lines in locations such as South America and Africa were investigated by Betts *et al.*,⁷ Houze,⁸ Moncrieff and Miller,⁹ and Zipser.¹⁰ The relevance of these works to the "Sumatras," however, is not assessed and validated. As the tropical maritime continental region is well devoid of data, the research progress on "Sumatras" has been rather slow.

A state-of-the-art numerical weather predication model COAMPS developed by US Naval Research Lab¹¹ is adopted herein to investigate the "Sumatras." The present study aimed to assess the impacts of boundary forcing effects of land sea distribution, radiative fluxes, sea surface temperature (SST), and topography on the generation and development of Sumatra squall lines. Semi-idealized numerical simulations using the COAMPS model are performed.

This paper is organized as follows: Sec. 1 gives a brief introduction of the Sumatra squall lines; Sec. 2 describes the COAMPS model configuration for the semi-idealized simulations; Sec. 3 explains how the numerical experiments are designed and conducted; Sec. 4 presents the simulation results on four separate areas: (1) initiation and timing of a squall line, (2) interaction between convection and land-sea circulations, (3) migration and enhancement of the squall line, and (4) topographic effects. A summary of this study is followed at the end in Sec. 5.

2. Model Configuration

The non-hydrostatic COAMPS model is used as a cloud resolving model with $156 \times 117 \times 58$ grids (geographic domain is shown in Fig. 1); 3 km

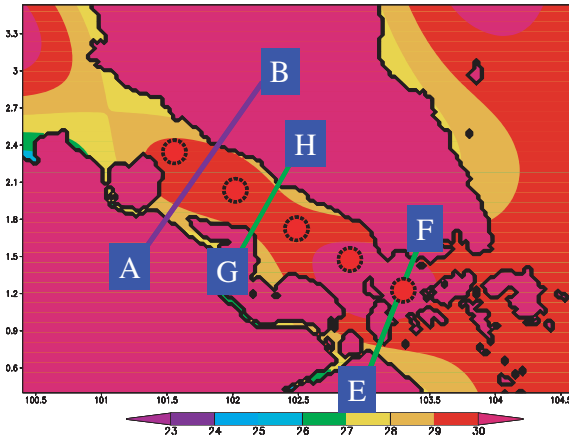


Fig. 1. Model domain and the initial distributions of ground surface temperature (T_g) and SST in color shades at $\tau = 0$. X-axis is longitude in degree, and Y-axis is latitude in degree. Cross-section locations at lines AB, EF, and GH are also shown. Dotted circles indicate locations of the five ellipsoidal warm bubbles prescribed in experiment “Wet_bub.”

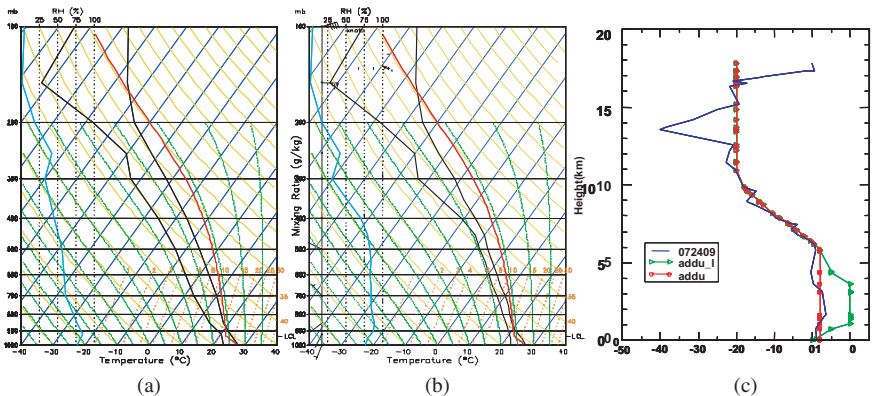


Fig. 2. Initial RH profiles (light blue on the left), T and Td profiles (black) used in the experiments (a) “Wet” and (b) Wet_RH. Wind profiles shown in (c) are used in the experiments Wet_addu (the red curve with circles) and Dry_addu_1 (the green curve with triangles). The blue curve in (c) is the observed wind at 09Z July 24, 2002. The CAPE values of the soundings are 1887 J kg^{-1} for (a) and 1812 J kg^{-1} for (b).

horizontal grid spacing; and 50–500 m stretched vertical resolutions. An observed sounding at Singapore at 09Z July 24, 2002 is adapted as model initial conditions (see Fig. 2a). The thermodynamic and wind profiles are applied horizontally homogenously over the entire model domain. Realistic

boundary conditions are imposed, such as real land sea mask and Navy Operational Global Atmospheric Prediction System (NOGAPS) analysis SST. Initially the ground surface temperature ($T_g = 300\text{K}$) is fixed over land, and uniform albedo (0.2 for land, 0.07 for water), surface roughness (0.01 for land, ~ 0 for sea), and ground wetness (0.1 for land, 1 for sea), are specified. Diurnal radiative forcing and surface fluxes are switched on. The radiation module follows the methods of Harshvardhan *et al.*¹¹ The surface layer parameterization follows the Louis (1979) scheme,¹¹ and a level 2.5 boundary layer scheme (Mellor and Yamada 1982)¹¹ is used. Open boundary conditions are set at x and y directions. Kessler warm-rain cloud microphysics parameterization is applied. For simplicity, ice physics is turned off. The central latitude of the model domain is 2°N . The Coriolis parameter is accordingly set. All simulations start from 12Z [8pm local time (LT)] and persist for 24 h.

3. Experiment Design

Table 1 lists all the simulations conducted. Variations are made among the experiments in their initial atmospheric conditions, moist physics option, topographic setting, and initial temperature perturbations (warm bubbles). The v component of wind is set to 0 m s^{-1} in all cases. In one simulation, a line of five ellipsoidal warm bubbles with horizontal radius 24 km and vertical radius 75 m are prescribed along the Malacca Straits (see Fig. 1). The maximum potential temperature excess of the bubbles is 1 K. The warm bubbles are switched off in other simulations to see if the squall line can be born naturally. Please note in the present study we only evaluate

Table 1. Outline of experiments with varied initial, boundary, and moist physics conditions.

| Moist physics | Terrain | Initial atmospheric conditions | | | Warm bubbles | |
|-----------------|---------|--------------------------------|-----------|--------------|--------------|-----|
| | | T | RH | U | | |
| Wet_bub | On | No | Fig. 2a,b | 62%, Fig. 2a | 0 | Yes |
| Wet | On | No | Fig. 2a,b | 62%, Fig. 2a | 0 | No |
| Dry | Off | No | Fig. 2a,b | 62%, Fig. 2a | 0 | No |
| Wet_RH | On | No | Fig. 2a,b | 83%, Fig. 2b | 0 | No |
| Wet_addu | On | No | Fig. 2a,b | 62%, Fig. 2a | Fig. 2c | No |
| Dry_addu_l | Off | No | Fig. 2a,b | 62%, Fig. 2a | Fig. 2c | No |
| Dry_addu_l_topo | Off | Yes | Fig. 2a,b | 62%, Fig. 2a | Fig. 2c | No |

isolated boundary effects and their interaction with convection and local circulations. Simulations with mixed effects that are closer to real situations will be investigated at a later stage.

Additionally, we adjust the mid-level relative humidity averaged between 850 and 400 hPa from 62 to 83% (see Fig. 2a, b) to assess the effect of mid-level moisture on the squall line development. Low-level (0–5 km) mean wind is altered (Fig. 2c) as well to help elucidate the terrain effect, and the propagation characteristics of the squall line.

4. Simulation Results

4.1. Initiation and timing

A line of five ellipsoidal warm bubbles are placed along the Straits of Malacca to spawn a squall line. In a previous study by Yi and Lim,¹² warm bubbles triggered linear convective cells in less than 1 h over a flat land without the effects of radiation and surface fluxes, but in the present case the model atmosphere is cooled by outgoing long wave radiation during the first 12 h of the simulation, the convective cells thus appear 3 h later.

It is seen in Fig. 3 that the ground surface temperature (T_g) experiences pronounced diurnal variation in response to the diurnal forcing of the incoming solar radiation, while the change of SST is small due to higher heat capacity of water. The largest change of T_g occurs between 11 am and 2 pm LT. The line convection moves from central Straits eastward and westward after 11 am and develops into two vigorous line squalls along the east coast of Sumatra and the west coast of the Malay Peninsular. Although the model is static at first, local winds driven by distinct radiative forcing between land and sea must have played a role in the position shift of the squall line and the formation and intensification of the later squall lines. This will be discussed in more details in Sec. 4.2. Notably, during night, the tallest and strongest convective cell is developed right above the warmest SST region west of Singapore at the lower southern part of the Malacca Straits. This is possibly because the long-wave radiative cooling near the cloud top intensifies the convective system during night through destabilization.

To test the role of SST in triggering convection, a similar simulation that excludes the initial warm bubbles is carried out with results shown in Fig. 4. Notable shallow convective cells are initiated first over the southern and northern Straits, where warmer SSTs are observed. Apparently, warmer SST is conducive to kicking off convection. Before 11 am, convective cells

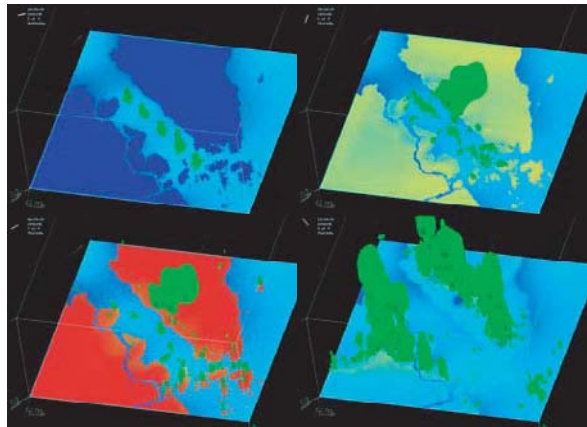


Fig. 3. Convection development in experiment “Wet_bub” at $\tau = 6$ h (2 am LT, upper left), 15 h (11 am LT, upper right), 18 h (2 pm LT, lower left), and 24 h (8 pm LT, lower right). Clouds are represented by isosurfaces of q_c (cloud water mixing ratio) $> 0.01 \text{ g kg}^{-1}$. Also drawn is ground and sea surface temperature in color shades.

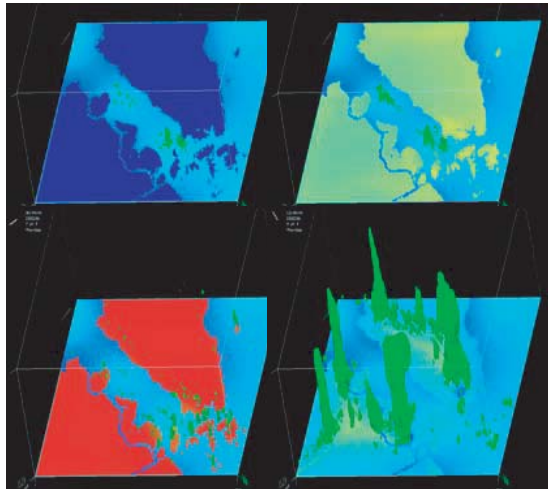


Fig. 4. Same as Fig. 3 except for experiment “Wet” at $\tau = 12$ h (8 am LT, upper left), 15 h (11 am LT, upper right), 18 h (2 pm LT, Lower left), and 24 h (8 pm LT, lower right).

are pushed and clamped by land breezes to the central Straits, and then sea breezes shift, reorganize and strengthen them into two line convective systems over both coasts of the Straits. For the studied region with its particular geographic setup of land and sea, given an initially static

and homogenous atmosphere, it appears that the transition from shallow, somewhat sporadic convection to organized, linear and deep convection can be accomplished by boundary forcing itself without initial external forcing. The diurnal circulations are seen to help enhance the convective organization and strength.

The simulated line convection shows up in the coastal areas such as Singapore in late morning rather than early morning or pre-dawn as observed. Lack of mean wind in these simulations is one reason. We also examine radiative fluxes at the surface and radiative cooling/heating in the lower troposphere, and find out that although the net surface radiative flux is positive (downward) from 8 to 11 am LT (Fig. 5a), the atmosphere is still being cooled above surface (Fig. 5b) because of outgoing long wave cooling. The turbulent mixing in the boundary layer is not able to develop sufficiently to transfer the surface heat upwards during this period. Therefore, an early development of the squall line is suppressed.

4.2. Land-sea circulation and convection interaction

Several cross-sections are chosen in Fig. 1 to obtain pictures of the diurnal circulations in the boundary layer of the Malacca Straits. Line EF crosses the warmest SST area with maximum forcing and expects the strongest

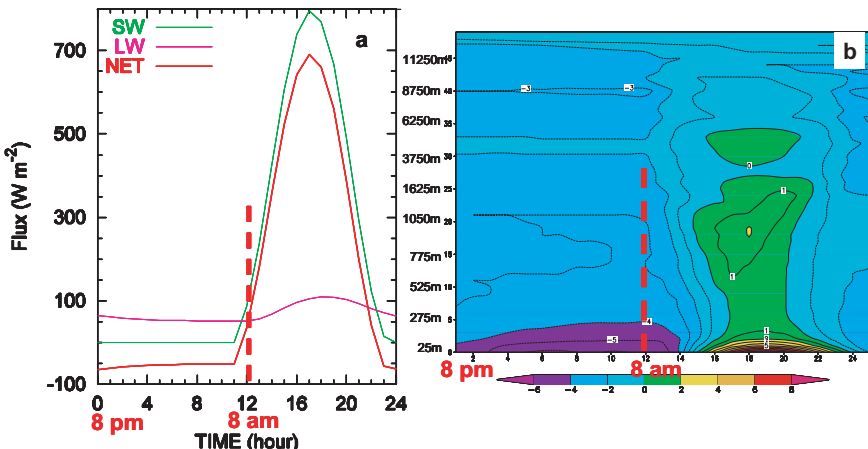


Fig. 5. (a) Time evolution of incoming, outgoing and net surface radiative fluxes in experiment “Wet.” X -axis represents the model time; (b) time-height evolution of radiative heating (or cooling) rate (C day^{-1}) in experiment “Wet.” Y -axis denotes model sigma levels (with height in meter to the left).

convection. Line AB traverses another warmer SST area with a little reduced strength. The diurnal circulation in the least cloudy area along the Malacca Straits may be represented by the cross-section GH.

A change of diurnal circulations from land breezes to sea breezes along the cross-section line AB is shown in Fig. 6. The change takes place from 11 am to 2 pm LT when T_g is experiencing the most significant rise in a day. Under clear skies (moist physics is switched off), sea breezes are intense and much higher (to about 2 km); land breezes are weaker and shallower, reaching to only about 1 km. But this is altered by convection formed under the SST forcing in the boundary and lower troposphere. Convective scale updrafts and outflows act to enhance the land breezes,

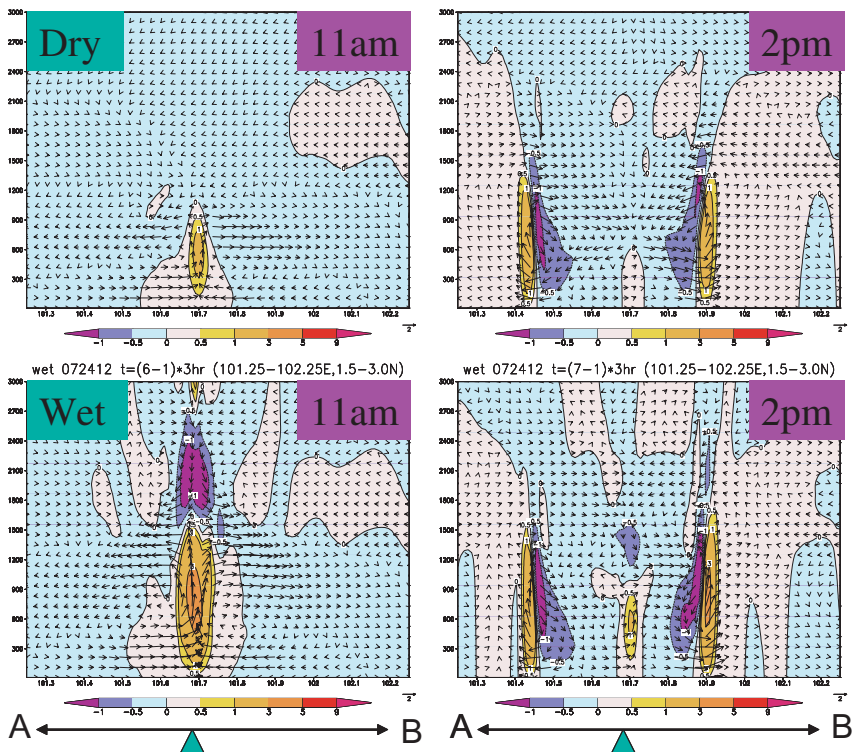


Fig. 6. Circulations (horizontal wind in ms^{-1} , vertical wind in cm s^{-1}) along the vertical cross-section AB in experiments “Dry” (upper panels) and “Wet” (lower panels) at 11 am LT (left panels) and 2 pm LT (right panels). Vertical motion is also contoured and shaded with color scale at the bottom of each plot. Y-axis is height in meter, X-axis is longitude in degree.

double the depth of the circulations and make them reach to almost the same level as the sea breezes. Offshore winds from the east coast of Sumatra and west coast of Malay Peninsular blow toward the central Straits, and converge there. Upward motion thus produced in the land breeze circulations coincidentally couples with convective updrafts, creating much stronger and deeper vertical transport. The sea breezes blowing from the central Straits are somehow weakened, and shrank in horizontal dimension, and lowered by about 200–300m in depth. This is because the convective scale circulation develops in between the two sea breeze circulations, and counteracts, and squeezes them apart.

Similar patterns of land and sea breezes are found along the cross-section EF (figure not shown). The low-level convection enhances land breezes and weakens sea breezes in almost the same way. Circulations of land and sea breezes along the cross-section GH remain unaffected because inappreciable convection is observed at this location (figure not shown). There appears to be a well-organized structure of the land and sea breezes under clear and cloudy conditions across the Malacca Straits (see Fig. 7). The bottom branch of the land breezes is very close to the sea surface, while that of the sea breezes is about 300m above the sea surface. In

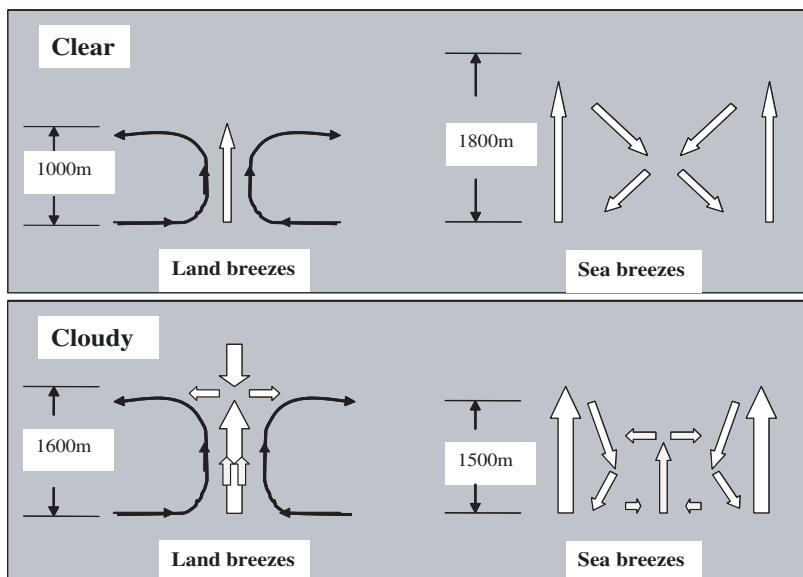


Fig. 7. A schematic illustration of land/sea breezes across the Straits of Malacca under clear and cloudy conditions without consideration of terrain and mean wind.

central Straits, erect upward motion is seen with land breezes, while slanted downward motion is associated with sea breezes. Please note Fig. 7 is only an idealized depiction of the local diurnal circulations driven by only land–sea contrast without consideration of terrain and mean wind.

4.3. Enhancement and migration

The effects of mid-level moisture (Fig. 2b) and mean wind at lower levels (Fig. 2c) on convective organization under the boundary forcing are also investigated. As in the idealized simulations by Yi and Lim,¹² more mid-level moisture promotes stronger and deeper convective cells in the present case as well (Fig. 8). Weak, constant ($u = 2 \text{ m s}^{-1}$) low-level winds speed up the eastward movement of the shallow convective cells, pulling clouds over Singapore several hours earlier, but under this windy condition no convective cells pop up near the second warmer SST center at the northern part of the Malacca Straits (Fig. 9). The upper-level easterly wind shear seems responsible for the formation of high-level stratiform clouds during the late simulation, and low-level winds (although weak) seem to have dissipated the low-level clouds during this period (also Fig. 9). It is inferred that stronger low-level mean westerly winds are disadvantageous to the development of the line convection possibly due to the enhanced mixing thus incurred. This conforms to a local weather forecaster's experience (personal communication).

4.4. Topographic effect

The topographic effect is examined with enlarged model domain to cover north Sumatra and north Malay Peninsular. Two simulations are performed with and without terrain. Mean wind of 10 m s^{-1} is imposed at $1\text{--}3 \text{ km}$ altitude (Fig. 2c) in the initial conditions. Figures 10 and 11 show the circulations at $z = 200 \text{ m}$ and $z = 800 \text{ m}$. The blocking effect of the terrain is quite obvious at both levels. Due to the existence of the mountain range along the west Sumatra and the north Malay Peninsular, air flows bifurcate around the high relief in the two areas. Deflected air streams from westerly to northwesterly generate a strong northerly component of wind into the Malacca Straits, which might converge with the southwest monsoon, providing low-level convergence favorable for the Sumatra squall lines.

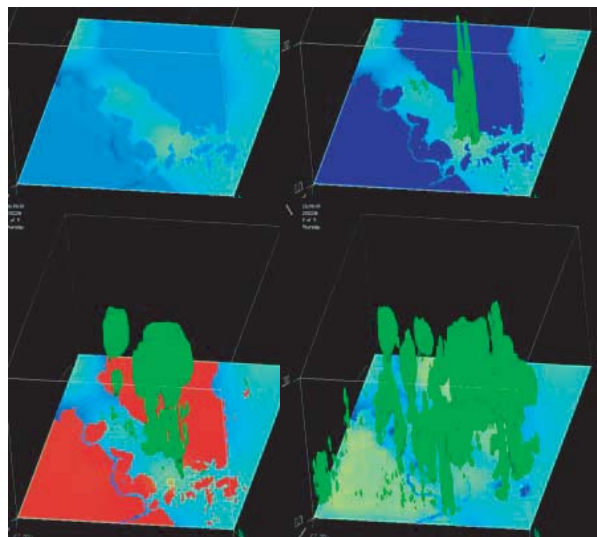


Fig. 8. Same as Fig. 3 except for experiment “Wet_RH” at $\tau = 3$ h (11 pm LT, upper left), 12 h (8 am LT, upper right), 18 h (2 pm LT, lower left), and 24 h (8 pm LT, lower right).

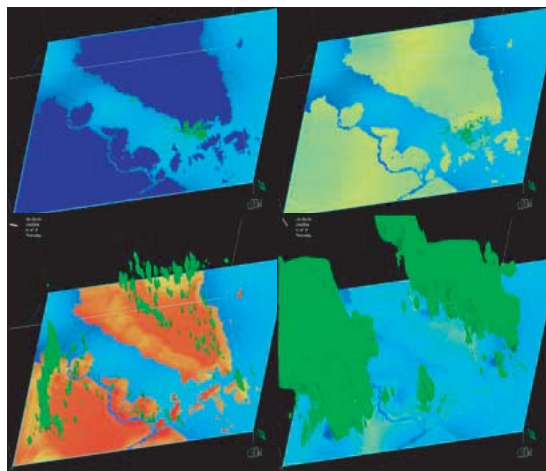


Fig. 9. Same as Fig. 3 except for experiment “Wet_addu” at $\tau = 12$ h (8 am LT, upper left), 15 h (11 am LT, upper right), 21 h (5 pm LT, lower left), and 24 h (8 pm LT, lower right).

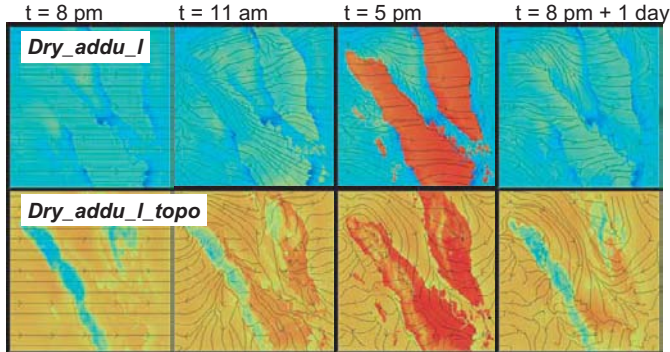


Fig. 10. Simulated streamlines at $z = 200$ m at different model times (see time tag at top) in experiment “Dry_addu_1” and experiment “Dry_addu_1_topo.” Also shown are T_g and SST in color shades.

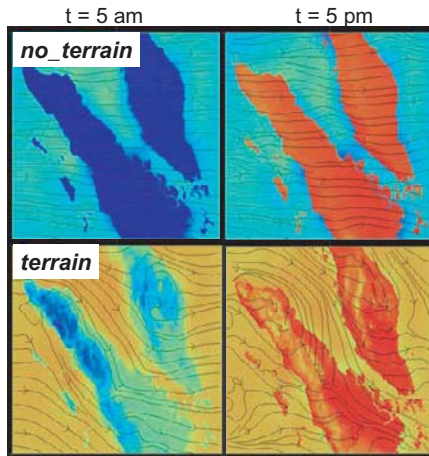


Fig. 11. Same as Fig. 10 except $z = 800$ m. Note “no_terrain” equals “Dry_addu_1,” and “terrain” equals “Dry_addu_1_topo”.

5. Conclusion

In this study, we have investigated several boundary forcing effects on the generation and development of Sumatra squall lines. Because the maritime continent where Sumatra squall lines often occur has a quite sparse and very limited observation network, we adopt the US Navy’s non-hydrostatic mesoscale model COAMPS as a cloud resolving model at 3 km

horizontal resolution to carry out semi-idealized simulations. The semi-idealized simulations are helpful to isolate various boundary forcing effects and identify the impact of each of them on the squall line development. The simulation results indicate that:

1. Line convection can be initiated by SST heating, and organized and sustained by diurnal thermal contrast between land and sea. Warmer SSTs are conducive to kicking off convection.
2. Diurnal boundary layer circulations can help enhance the organization and strength of the line convection. In turn, convection alters the land and sea breezes.
3. More mid-level moisture supports stronger convection. Low-level mean wind from west is helpful to speed up convection propagation but detrimental to its strength.
4. Air flows bifurcate around high relieves in west Sumatra and north Malay Peninsular. Terrains around the Malacca Straits deflect low-level wind from westerly to northwesterly, promoting low-level convergence with the southwest summer monsoon.

Although all of the simulations conducted in this study are in a semi-idealized context, the result about the role played by the local land and sea breezes in the development of the squall lines is consistent with that from most previous studies (see Sec. 1). This study further identified and demonstrated the roles of SST and topography. It also sheds a bit light on the role of mid troposphere moisture and low-level wind shear in the squall line development. The focus of this study is the boundary forcing effects on the “Sumatras” convective development under a semi-idealized framework. Another study¹² about the dynamics and self-organizing features of the squall lines in idealized settings is also carried out.

Boundary forcing is considered to be mainly static with little daily variations. Since “Sumatras” are not taking place every day, it should be stated here that boundary forcing effects are not sufficient but perhaps necessary conditions for the Sumatra squall lines to initiate and develop. Large-scale flow disturbances and convective instability are suspected to play a leading role in controlling the timing, propagation and strength of the “Sumatras.” Further research along this line is being planned.

Acknowledgments

The authors thank the US Naval Research Lab for its support in applying the COAMPS model to the weather study in Singapore. Discussions with Mr Keng Gaik Lam and Ms Yihong Hu of Meteorological Service Division, National Environment Agency of Singapore have helped this work. This study was conducted under grants from Singapore Defense and Science & Technology Agency.

References

1. J. H. Noer, Southeast Asian Chokepoints: Keeping Sea Lines of Communications Open. Strategic Forum, December 1996, http://www.ndu.edu/inss/strforum/SF_98/forum98.html (accessed 15 September 2006).
2. M. Zubir and M. N. Basiron, The Straits of Malacca: the rise of China, America's intentions and the dilemma of the littoral states, Maritime Institute of Malaysia online articles (2005) (<http://www.mima.gov.my/mima/htmls/papers/online.html>) (accessed 15 September 2006).
3. C. A. Doswell, ed., *Severe Convective Storms*, Meteorological Monographs, Vol. 28 No. 50 (American Meteorological Society, 2001).
4. I. E. M. Watts, *Equatorial Weather* (University of London Press, London, 1955).
5. J. E. Pakiam, H. C. Koo, L. Hock, et al., *Radar Study of Thunderstorms Over Singapore, 12th Annual Congress* (Canadian Meteorological and Oceanographic Society, 1978).
6. T. K. Lim, *Empirical Orthogonal Function Analysis of the Spatial Patterns of Daily Rainfall in Singapore*, internal report (Meteorological Service Singapore).
7. A. K. Betts, R. W. Grover and M. W. Moncrieff, *Q. J. Roy. Meteorol. Soc.*, (1976) 395–404.
8. R. A. Houze, *Mon. Weather Rev.* (1977) 1540–1567.
9. M. W. Moncrieff and M. J. Miller, *Q. J. Roy. Meteorol. Soc.* (1976) 373–394.
10. E. J. Zipser, *Mon. Weather Rev.* (1977) 1568–1589.
11. R. M. Hodur, *Mon. Weather Rev.* (1997) 1414.
12. L. Yi and H. Lim, in *Proceedings of the 26th Conference on Hurricanes and Tropical Meteorology*, Miami, FL, USA (American Meteorological Society, 2004), p. 500.

SAND DUST WEATHER IN BEIJING FROM THE LATE 19th CENTURY

XUE ZHEN ZHANG*,† and XIUQI FANG†,‡

†*School of Geography, Beijing Normal University*

Beijing 100875, China

‡*Institute of Geographic Sciences and Natural Resources Research*

Beijing 100101, China

**xuezhen8108@163.com*

Based on an ancient Chinese diary named *Weng Tonghe Diary* written in the late Qing Dynasty, daily weather entries were extracted, excluding the months with more than 4 absent recording days. From the data, monthly sand dust days (SDD) and monthly colder days from 1860 to 1898 are reconstructed. Then, based on the records of complementary rainfall/sunshine days, monthly rainfall/snowfall days are reconstructed. The results reveal that sand dust weather of the later half of the 19th century is more frequent than the mid-1980s, and especially the 1990s. The monthly distribution of the past differs to the recent several decades. The spring contribution to the total frequency during the later 19th century and during the years 1961–2000 is 70 and 60%, respectively. The spring SDD is significantly correlated with local meteorological conditions during the later 19th century. However, based on the present data, it would be difficult to attribute a dynamical mechanism as the prime meteorological factor responsible for the sand dust frequency distribution.

1. Introduction

Investigation of past sand dust weather is helpful in understanding the correlation between climate change and sand dust weather and to reveal how serious is the sand dust weather of recent decades. Based on the documented record of sandstorms since 300 AD, it is concluded that a colder and drier climate corresponded to more frequent sandstorms in the north of China.^{1–4} Nevertheless, most of the data of previous studies were extracted from local gazettes (*Difangzhi*) or official chronicles that mainly described stronger sandstorm weather. In comparison with these archives, the descriptions in private diaries are more detailed.

In Beijing (39.62° N, 116.46° E), as the capital in a long history, there are plenty of historical documents available. A private diary named *Weng Tonghe Diary*, which described, in detail, daily nature phenomena of Beijing in the later half of 19th century, is one of them. Based on the diary, it is possible to investigate the past sand dust weather of Beijing, and to compare it with several recent decades.

In this paper, we focus on the sand dust weather of Beijing during the later 19th century. In order to do this, data evaluation and the reconstruction of monthly sand dust days (SDD) are presented in Sec. 2. Section 3 presents the statistical results and finally some conclusions are summarized in Sec. 4.

2. Materials and Methods

2.1. Description of the data source

In this paper, the data were mainly extracted from *Weng Tonghe Diary*, which is written in the later half of the 19th century and has been edited in two recent decades. There is a total of six volumes, published by China Press.^{5–10} The author *Weng Tonghe* was the tutor of the third and second last Chinese emperors, Emperor *Tongzhi* (reign 1862–1874 AD) and Emperor *Guangxu* (reign 1875–1908). *Weng Tonghe* was also one of the most important politicians in the later Qing Dynasty. He had worked twice in the Ministry of Military-political-affair (*Jun Ji Chu*), which was a core department of the central government in the Qing dynasty.¹¹ He kept his diary from July 31, 1858 to June 27, 1904. From January 23, 1860 to June 30, 1898, there were more than 90% entries written in Beijing, of which 0.4% were absent, and the others mentioned were from Changshu (31.64° N, 120.74° E), in Jiangsu Province.

During the periods from January 23, 1860 to September 19, 1868; January 7, 1869 to May 31, 1872; August 4, 1874 to August 23, 1877; and November 21, 1877 to June 30, 1898, he lived in Beijing. His home was outside old Beijing city. As the imperial tutor and a key officer of the central government, he traveled to the forbidden city from his home, nearly for everyday. This was a good opportunity for him to observe daily weather. As a result, there were many descriptions of natural atmospheric phenomena in his diary, including rainfall, snow, wind, sand dust, fog, frost, ice and plant phenology. The descriptions of these phenomena were very detailed. For example, on April 1, 1865, he wrote: “It’s warmer and there

was sun, but the sun was obscure. There is no wind, but the air was full of dust.” For a further example on March 30, 1880, he wrote: “There was heavy fog, it’s moist, and the clothes had been wet. At the division of Chensi (ancient Chinese time: 7:00–9:00 AM) and Sishi (referring to: 9:00–11:00 AM), it started to be strongly windy, there was yellow sand dust in the sky, and the sun had been obscure. It’s like so, till the night. However, the wind still continues during the whole night.” Totally, 335 entries about sand dust weather are extracted from *Weng Tonghe Diary*.

Another data source is also the private diary named *Yue Man Tang Diary*,¹² written by *Li Ciming*, contemporary with *Weng Tonghe*. However, the description in this diary is obviously much briefer. For most of the entries, a few Chinese characters are employed to describe daily weather. In comparison with *Weng Tonghe*, *Li Ciming* was much less descriptive. It is evident that much sand dust weather had been ignored in *Yue Man Tang Diary*. This paper will mainly extract the description about rainfall and snowfall from it to complement absent entries in the *Weng Tonghe Diary*, when counting monthly rainfall and snowfall days.

2.2. Data assessment

Firstly, it is impossible for the author to make incorrect entries, especially about the daily weather. This is because keeping a diary is the author’s daily habit or vocation, and a private diary is generally not available to anyone else. Moreover, there is no correlation between the daily weather and the author’s political and economic welfare. So, there is no reason for the author to fictionalize entries about the daily weather in his diary.

Secondly, all these entries appear to be correct with very few suspect ones. The author was a literator of the old China, who mastered Chinese words. So he could freely select the most correct words to describe the natural phenomena and his impressions of the current weather.

Thirdly, some of the sand dust weather extracted from the *Weng Tonghe Diary* can also be detected in the *Yue Man Tang Diary*. For instance, on May 1, 1871, *Weng Tonghe* wrote: “It is very cloudy. In the morning, it would be rainy. Strong wind since the fifth-Geng (ancient Chinese time: 3:00–5:00 AM) lasted during the whole day, and the air was full of sand dust, it looks yellow.” On the same day, *Li Ciming* wrote: “It was windy and cloudy in the morning. Afternoon, it was slight sunny. After Bushi (ancient Chinese time: 3:00–5:00 PM), the wind was stronger, and

it started to blow sand dust.” Some of the records from the *Weng Tonghe Diary* could also be identified in the Draft History of the Qing Dynasty (*Qingshigao*), the official chronicle of the Qing Dynasty.

For the above reasons, it is concluded that entries about sand dust weather in the diary are reliable, but SDD recorded in the diary may be fewer than in reality owing to the following three reasons. First, the author left Beijing for other locations on several days, so he knew little about the daily weather of Beijing on those days. Second, he lived in Beijing, but he did not keep a diary, or kept a diary without weather description on several days, for instance, when he was so ill that he could not venture outdoors. Third, even though he kept a diary with weather descriptions of Beijing, some sand dust observations might be absent, because only sand dust weather that he actually observed would be described in his diary. For example, some of the sand dust weather that occurred at night might have disappeared before the following day or, was so slight it was not apparent, so would be absent in diary.

According to the Standard of Ground Meteorological Observation of China,¹³ sand dust weather can be distinguished as dust storm, blowing dust and suspended dust. However, it is difficult to distinguish between these groups based on the description in the diary. So classification into these sand dust weather groups will not be carried out in this paper.

2.3. Method

In this paper, we define an absent day as an entry without Beijing weather information, including the days on which the author left Beijing for other locations or kept a diary but without including a weather description of Beijing. In the period from January 1, 1860 to June 30, 1898 (462 months, 14,061 days), there was a total of 1677 absent days, compared to 1121 days.¹⁴

Figure 1 shows the absent recorded days by month for the period January 1, 1860 to June 30, 1898. There are 334 (72.3%) months without absent days, and 53 (11.5%) months with 1–4 absent days. The absent entries were dispersed in most of the months with 1–4 absent days. In other words, in these months any two absent entries were not adjacent to each other. Because sand dust weather in Beijing is usually caused by cyclonic conditions, with strong wind and cloud and occasionally rain, if there was sand dust weather on the absent days, the related atmospheric phenomena

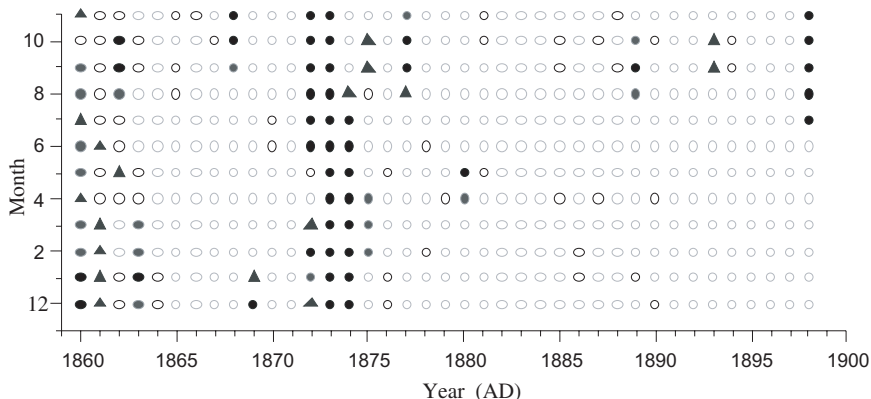


Fig. 1. Monthly days of absent weather entries of Beijing in the *Weng Tonghe Diary* during 1860–1898. Every year begins with prior December, ends with current November. Black dot, gray dot, black triangle, black circle, and gray circle represent absent recording days of more than 20, 11–20, 5–10, 1–4, and no absent entries, respectively.

and the impact on daily life should be described on the adjacent days. According to the weather preceding or following adjacent days of the absent day and reference to the author's activities on these days in Beijing (if it is available), there was no such description. So, it is concluded that there was no sand dust weather on the absent days. As a result, these months could also be considered to contain no absent entries. However, for the months with more than 4 absent days, many absent days are adjacent each other. So, in this paper, only the months with 0–4 absent days are regarded as no absent data, and used for the analysis.

In addition, because of the limitation of description characteristics, it is also difficult to determine if the sand dust weather observations were being described past 8:00 PM, which is the dividing time of the day in modern meteorological observations. So, in this paper an SDD is classified according to the original description.

In order to investigate the correlation between sand dust weather and climate, monthly rainfall and snow fall days are incorporated into a wet/dry index based on the complementary *Weng Tonghe Diary* with *Yue Man Tang Diary*, and monthly colder days described by the author comprise the cold/warm index. Counting monthly colder days and monthly rainfall/snowfall days applies only for the months with 0–4 absent days based on the *Weng Tonghe Diary*, similar to the SDD statistical criterion.

In this paper winter, spring, summer and autumn refer to, December–February, March–May, June–August, and September–November, respectively. So, the whole year refers to the December–November period.

3. Analysis Results

3.1. Yearly sand dust days

Based on the 24 years without absent entries in any month (Fig. 2), there were 10.4 SDD per year on average, with a 95% confidential interval of 8.3–12.5 days, a maximum of 23 days (1870) and a minimum of 4 days (1882, 1890). There were 23, 7.7, 9.1 days per year, respectively, between the years 1961 and 1990, 1991 and 2000, and 1986 and 2000.¹⁵ On annual basis, SDD between 1860 and 1898 were significantly more than during the 1990s at the confidence level.

Beijing SDD during both periods 1860–1898 and 1961–2000 occurred mostly during the spring months. From 1860 to 1898, 70% sand dust weather arose in spring with a correlation of 0.88 (significant at 0.99 confidence level) with yearly SDD, winter accounted for about 20%, and summer/autumn combined, accounted for the smallest number of about 10% (Table 1). On a monthly basis, April had the most (28%), followed by May (24.8%), and then the March (17.6%). To compare with the 1961–2000 period, the spring months of the 1860–1898 period were weighted more than the spring months of 1961–2000. For the spring period from 1860–1898

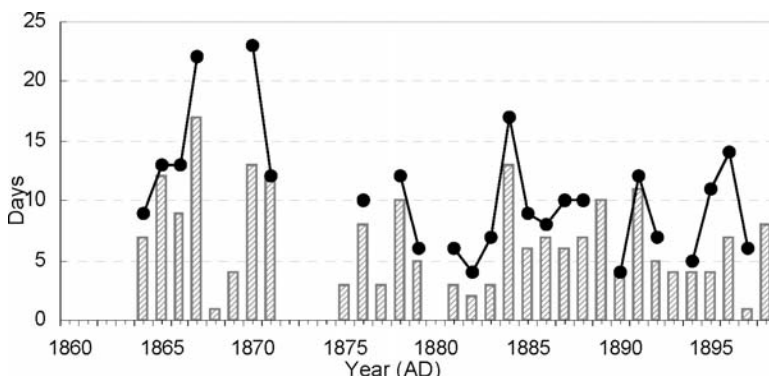


Fig. 2. Sand dust days for the whole year (full line with solid black dot) and spring (bar). The years without solid black dots or bars means that there is at least 1 month with more than 4 absent days of recording.

Table 1. Comparison on monthly (seasonal) distribution of sand dust days between 1860–1898 AD and 1961–2000 AD in Beijing.

| Period | March | April | May | June–November | December | January | February |
|-----------|-------|-------|-------|---------------|----------|---------|----------|
| 1860–1898 | 17.6% | 28% | 24.8% | 10% | 4.4% | 7.6% | 7.6% |
| 1961–2000 | 16.1% | 26.3% | 17.1% | 13.2% | 7.3% | 10.2% | 9.8% |

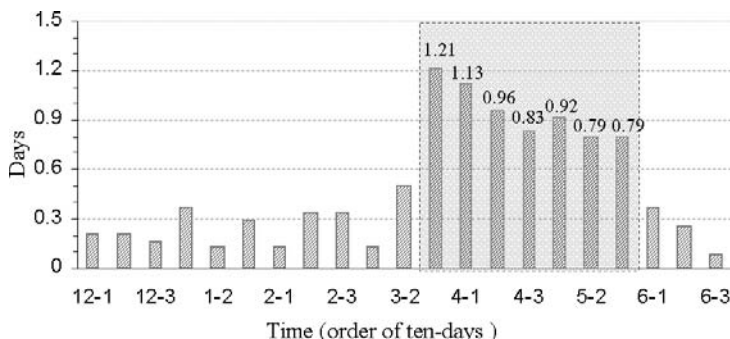


Fig. 3. The sand dust days per 10 days. X-coordinate begins with the first 10 days of December, and ends with the last 10 days of June. The shadow indicates the duration with higher frequency of sand dust weather. The figures on the bars indicate the SDD during the corresponding 10 days.

the weight was about 10% more than during the 1961–2000 period, and specifically the difference for May between the two periods was about 7.7%. In other words, during the 1860–1898 period, sand dust weather in spring was relatively more frequent than during the years 1961–2000.

SDD per 10 days from the first 10 days of December to the last 10 days of June indicated that during 1860–1898 the sand dust weather was most frequent from the last 10 days of March to the first 10 days of May (Fig. 3). For this duration, there was a minimum of 0.8 SDD per 10 days, which was more than the maximum of 0.5 SDD per 10 days at other times.

3.2. Correlation between sand dust days in spring and wet/dry and warm/cold

According to the above analysis, it is evident that the annual SDD distribution is heavily influenced by spring. In this section, the correlations between spring SDD and monthly rainfall and snow days of the previous

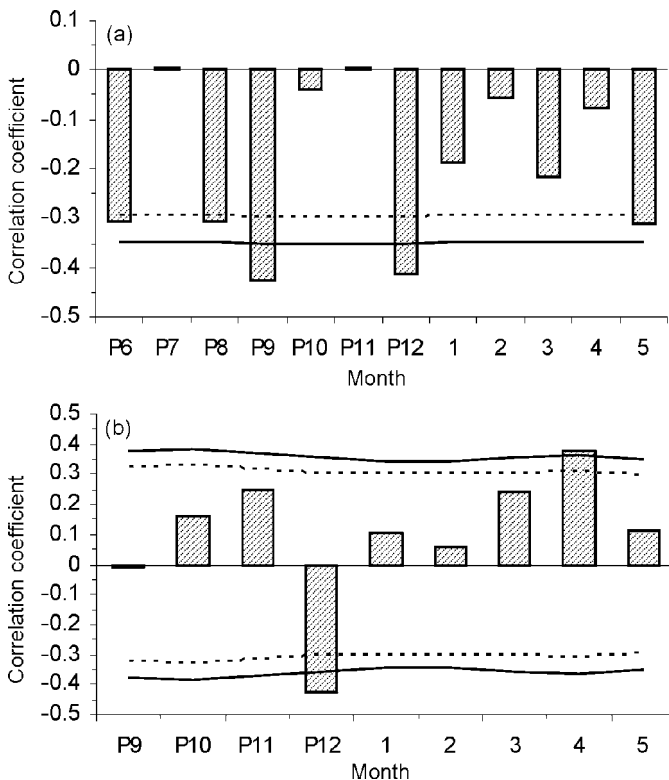


Fig. 4. The correlation coefficient between spring SDD and monthly rainfall and snow days (a) and monthly colder days (b). The X -coordinate begins with previous June in (a) and previous September in (b) and end with the current May. Y -coordinate is correlation coefficient; the solid line and dashed line represent the confidence levels of 0.05 and 0.1, respectively.

June to current May, and monthly colder days of the previous September to current May, are investigated. The results are shown in Fig. 4.

Firstly, for nearly all months, the correlations between spring SDD and monthly rainfall/snowfall days are negative. This is verified by recent ground-based observed data.¹⁷ Moreover, the correlations of spring SDD and the June, August, September, December of previous year, and May of current year are significant at confidence level of either 0.1 or 0.05. This implies that the higher the precipitation, the less the spring SDD, especially for the prior Autumn and Winter.

Secondly, the correlations with monthly colder days demonstrate that the greater the number of monthly colder days, the greater the number of

SDD in spring, but it is the reverse for the prior December. In this case, both a negative correlation with the prior December and a positive correlation with the current April are significant at the 0.05 confidence level.

4. Discussion and Conclusion

This study reveals that the sand dust weather frequency in northern China is lower, since the mid-1980s, and especially since the 1990s, in comparison with not only recent decades of the 20th century, but also in comparison with the later decades of the 19th century. There is a little difference in the monthly distribution of SDD between the later half of the 19th century and recent decades of the 20th century. The spring frequency in the later half of the 19th century was higher than in recent decades. It is not possible from the data to determine the main meteorological factor responsible for the sand dust weather. It is possible to say only that the sand dust weather of Beijing is determined by local meteorological factors, however the correlation between the SDD of Beijing and local meteorological factors is statistically significant.

Acknowledgments

The authors thank Prof. Wang Shaowu for helpful comments, and also thank Dr. Milton Speer for corrected English. Besides, the authors would like to thank our colleagues for valuable suggestions on this work. This work was supported by the National Natural Science Foundation of China (Grant No. 40331013, 40571165).

References

1. D. Zhang, *Chin. Sci. Bull.* **294** (1982) (in Chinese).
2. D. Zhang, *Sci. China B* **278** (1984) (in Chinese).
3. H. Deng and W. F. Jiang, *Geograph. Res.* **403** (2005) (in Chinese).
4. Q. Y. Zhang and J. Fei, *Arid Zone Res.* **108** (2004) (in Chinese).
5. T. H. Weng (origin author) and Y. J. Chen (editor), *Weng Tonghe Diary*, Vol. I (China Press, Beijing, 1989) (in Chinese).
6. T. H. Weng (origin author) and Y. J. Chen (editor), *Weng Tonghe Diary*, Vol. II (China Press, Beijing, 1989) (in Chinese).
7. T. H. Weng (origin author) and Y. J. Chen (editor), *Weng Tonghe Diary*, Vol. III (China Press, Beijing, 1998) (in Chinese).

8. T. H. Weng (origin author) and Y. J. Chen (editor), *Weng Tonghe Diary*, Vol. IV (China Press, Bejing, 1992) (in Chinese).
9. T. H. Weng (origin author) and Y. J. Chen (editor), *Weng Tonghe Diary*, Vol. V (China Press, Bejing, 1997) (in Chinese).
10. T. H. Weng (origin author) and Y. J. Chen (editor), *Weng Tonghe Diary* Vol. VI (China Press, Bejing, 1998) (in Chinese).
11. J. M. Xie, *Bibliography of Weng Tonghe* (Chinese Press, Beijing, 2000) (in Chinese).
12. M. C. Li, *Yue Man Tang Diary*, Vols. 1–18 (Guang Ling Press, Beijing, 2004) (manuscript, in complex Chinese).
13. Central Meteorological Bureau, *Ground Meteorological Observing Standards* (Meteorological Press, Beijing, 1979) (in Chinese).
14. J. Fei, J. Zhou, Q. Y. Zhang and H. Z. Chen, *Atmos. Environ.* 3943 (2005).
15. G. T. Chen, *J. Des. Res.* **402** (2001) (in Chinese).
16. F. H. Guo, J. F. Hao and J. Xuan, *Meteorol. Monthly* **51** (2002) (in Chinese).
17. X. D. Liu, Z. Y. Yin, X. Y. Zhang and X. C. Yang, *J. Geophys. Res. Atmos.* D16210 (2004).

ENSEMBLE PROJECTION OF CLIMATE CHANGE IN EAST ASIA

CHUNG-MING LIU^{*,†,‡}, YING-CHEN CHEN[†], SHEN-FENG CHEN[†], SAHANA PAUL[†], SHU-HUA LIN[†], YEN-CHIH LEE[†], MING-CHIN WU[‡], REN-YOW TZENG[§], HUNAG-HSUNG HSU[‡] and CHENG-TA CHEN[¶]

^{*}*Global Change Research Center, National Taiwan University
Taipei, Taiwan, R.O.C.*

[†]*Department of Atmospheric Science, National Taiwan University
Taipei, Taiwan, R.O.C.*

[‡]*Department of Atmospheric Science and Institute of Atmospheric Physics
National Central University, Chung-li, Taiwan, R.O.C.*

[¶]*Department of Earth Sciences, National Taiwan Normal University
Taipei, Taiwan, R.O.C.*

*liucm@ntu.edu.tw

In the present study, the statistical super-ensemble approach is applied on three regional climate model's outputs initiated by the same global circulation model for the projection of future climate change. The results indicate that the average temperature in summer over East Asia is projected to be increased up to 3.5°C in summers of 2040–2050 and 6°C in summers of 2090–2100 with respect to 1990–2000, respectively. The Pacific high is simulated to be intensified. As a result of this fact, an enhancement of northward transport of air from the South China Sea toward mainland is observed. The northward component of wind over land area is projected to be increased about $0.1\text{--}1 \text{ m s}^{-1}$ in 2040s and $1\text{--}2.7 \text{ m s}^{-1}$ in 2090s than that in 1990s, respectively. Therefore, the temperature is simulated to be increased over land than that over ocean, and increased over northern latitudes than that over southern region. Furthermore, the intensification of the Pacific high favors more precipitation over most of the part of mainland China and which gradually extends in more amounts northward into northern China.

1. Introduction

The global circulation models (GCM) are the only primary tools for projecting the future climate. However, due to their low spatial resolution, it is hard to demonstrate regional climate characteristics

associated with complicated terrain and land surface condition. As an alternative, it is possible to produce detailed climate simulation for selected region by embedding a high resolution regional climate within coarse scale GCM.^{1,2} The initial conditions and the lateral boundary conditions that are necessary to drive the regional model are provided by the GCM.

A number of studies have been performed on the downscaling of coarse resolution GCM to high resolution regional scale model by several researchers.^{2–6} Having benefited from these efforts done on downscaling problem in the past, the future climate has been projected by different regional models in different regions.^{7,8}

In the present study, three regional climate simulation outputs initiated by the same GCM have been employed to project the summers of 2040–2050 and 2090–2100. The three regional climate models (RCMs) used here are MM5 (The Fifth-Generation NCAR/Penn State Mesoscale Model),⁹ NCEP RSM (NCEP Regional Spectral Model),¹⁰ and PRM (Purdue Regional Model).¹¹ The GCM data are obtained from ECHAM4/OPYC3.¹² SRES A2 future scenario outlined by IPCC¹³ is adopted in these simulations.

Due to the differences in individual structure of each RCM, the results from their simulations are different from each other. These differences in individual structure of different RCMs have been discussed in Sec. 2, even if in response to the same dynamic and radiative forcing. It has been noted that, the outputs from different RCMs produce skillful result in different regions of the simulated domain. Therefore, an average of all these outputs with each other is expected to correct the deficiency of one model by other and produce a better output. Super-ensemble approach, i.e., the equal and unequal weighted averages of RCM outputs are the commonly applied method to merge the outputs of these simulations.^{14–17} According to the previous studies, these methods are expected to provide a statistically reasonable projection. The two super-ensemble methods, applied in this study, are equal weighted ENSEMBLE method and the other is unequal weighted inverse square error of summation (ISES) method.¹⁷ Among these two methods ISES is more skillful than ENSEMBLE.¹⁷ Therefore, in the present case, finally ISES method is chosen for future projection. Four variables, i.e., temperature at 2 m height, the mean sea level pressure, accumulated precipitation, and the wind vector are selected in this study.

2. Data and Methodology

In this study, three regional climate simulation outputs have been employed to project the summers of 2040–2050 and 2090–2100 to assess the climate change after 50 and 100 years with respect to present days.

The RCMs have been driven by the GCM data that are obtained from ECHAM4/OPYC3.¹² The SRES A2 future scenario outlined by IPCC¹³ is adopted in these simulations. RSM used in this study is the NCEP version (97v) by Juang and Kanamitsu¹⁰ and Juang *et al.*¹⁸ Juang and Kanamitsu¹⁰ and Juang *et al.*¹⁸ developed the RSM based on the global spectral model at National Centres for Environmental Prediction. The PRM has been developed over the past 15 years at Purdue University, and has been used for atmospheric numerical simulations,^{19–22} covering a wide range of spatial and temporal scales. A complete summary of PRM physics can be found in Chern²² and Haines *et al.*²³ The PSU/NCAR mesoscale model, MM5, is a limited area, nonhydrostatic, terrain following sigma coordinate model designed to simulate or predict mesoscale atmospheric circulation. The model is supported by several pre-or post-processing programs, which are referred collectively as the MM5 modeling system. Table 1 gives necessary information about grid sizes, model domains, lower boundary condition, and boundary layer physics used in all the three models.

It has been mentioned earlier that different RCMs provide different results, in response to same dynamis and radiative forcing, due to the difference in their basic structure. In addition, the performance of different RCMs is skillful in different regions of the selected domain super-ensemble approach. Super-ensemble approach is a well known approach to merge the outputs of their simulations^{25,26} to get an improved result. Actually, the super-ensemble of outputs from different RCMs corrects the deficiency of one model by other and produces an improved output. For example, in Fig. 1, the simulated decadal means of surface temperature over East Asia by MM5, NCEP RSM, and PRM show that different models are skillful in different regions. In Yellow and Bohai Sea area, NCEP RSM and PRM simulations are that close to the observation. But, in case of land, MM5 and NCEP RSM are giving better result than PRM. Therefore, by averaging through super-ensemble method, a moderate output can be obtained.

The statistical method, super-ensemble, designates a weighting coefficient to each model according to their performance. This method provides a new simulation data from linear combinations of these model outputs. Here, two different procedures have been used to calculate the

Table 1. Information about grid sizes, model domains, lower boundary condition, and boundary layer physics used in the three regional circulation models.

| RCM | Grid size | Model domain | Lower Boundary Condition | | Boundary layer physics | Terrain |
|-----|------------------------|-------------------------|---|---|--|---|
| | | | Land surface process | Topography | | |
| PRM | Resolution in 50 km | 10°–40°N; 100°–140°E | Three layer land surface parameterization scheme | Truncation error significantly reduces near complex topography | The planetary boundary layer parameterization | Terrain follows normalization pressure coordinates (sigma) in vertical and staggered (Arakawa C) grid in horizontal |
| MM5 | 45 km resolution | 95°–145°E; 5°–50°N | LSM: Noah LSM, Cloud and radiation schemes: Cloud and precipitation physics: shallow convection, Grell scheme for cumulus convection, with simple ice. Cloud radiation: CCM2 radiation scheme | USGS 30s global data set (for topography, vegetation, and soil) | MRF scheme: Efficient scheme based on Troen-Mahrt representation of counter-gradient term and K profile in the well mixed PBL, as implemented in the NCEP MRF model ²⁴ | Terrain follows sigma coordinate model |

(Continued)

Table 1. (Continued)

| RCM | Grid size | Model domain | Lower Boundary Condition | | Boundary layer physics | Terrain |
|-----|------------------|------------------------------|---|--|--|--|
| | | | Land surface process | Topography | | |
| RSM | 50 km resolution | 96.3°–144.6°E; 3.951°–43.3°N | Primitive hydrostatic system of virtual temperature, humidity surface and mass continuity prognostic equations on 28 terrain-following sigma coordinates as the forcing NCEP reanalysis. Use momentum equation to simplify lateral boundary condition. Monin-Obkhov similarity theory surface layer | Used topography is for smooth orography from the model | New diffusion scheme representing the model horizontal diffusion on pressure surface, which replaced the origin scheme of fourth order diffusion on sigma surface. Nonlocal vertical diffusion ²⁴ | Used terrain for observation orography |

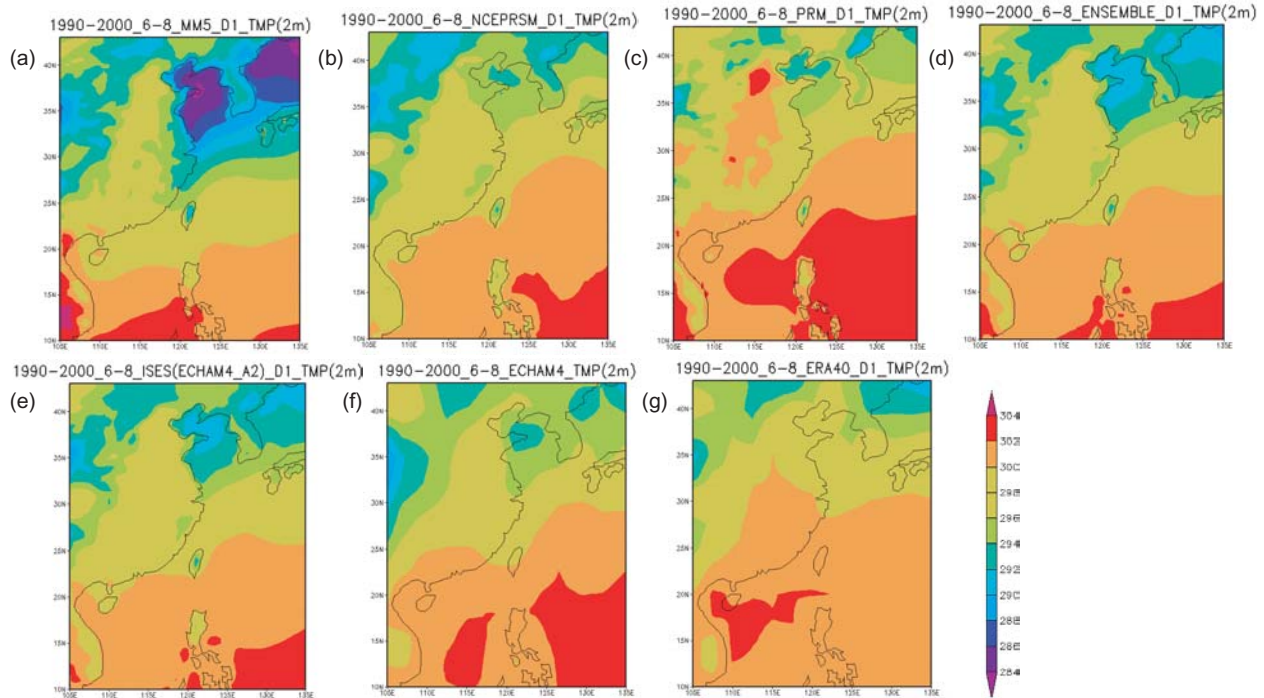


Fig. 1. Simulated decadal mean of the surface temperature at 2 m above sea level over East Asia during June–August of 1990–2000 by (a) MM5, (b) NCEP RSM, and (c) PRM. The ensemble mean of these three outputs is shown in (d) and the ISES method is (e), with the output of (f) ECHAM4/OPYC3 and the reanalysis data of (g) ERA40.

weighting factors of different super-ensemble methods. In order to represent the monthly variability in summer, the anomaly of model and observation data (obtained from monthly mean subtracted by 11-year long-term mean of that month) have been used here in calculating the super-ensemble. The used two methods of super-ensemble calculation are described below:

1. *Ensemble mean (ENSEMBLE)*: Here simply the average of the outputs of three regional models has been taken as the final result. Therefore, the weighting coefficient (W_i), of each model is 1/3.

2. *Inverse of square error summation*: Here the weights are not same. The weights of each model depend on their performance. The weighting coefficient of each model has been determined by

$$W_i = \frac{e_i^{-2}}{\sum_{i=1}^N e_i^{-2}}$$

where the error is

$$e_i = \sum_{t=0}^{t-\text{train}} [O(t) - M_i(t)]$$

and W_i is inversely proportional to the inverse squares of error (e_i). This e_i is the difference between observation anomaly, $O(t)$, and simulated models anomaly, $M_i(t)$.²⁶ Therefore, the better the model simulated anomaly are, the greater W_i it has, and the sum of W_i of each model is equal to 1.

From the above discussion, it is clear, that the weights of ISES are calculated from the deviation between simulated model anomaly and observation anomaly. The weights are higher when the model anomaly is closer to the observation anomaly. So, here the main concern is the accuracy of the anomaly pattern with respect to the observation, which counts the performance of the model as well.

According to Chen *et al.*,¹⁷ among these two methods, ISES is more skillful. In their study, three RCMs, i.e., MM5, NCEP RSM, and PRM have been employed to study the future summer data of 2 m temperature. But, here also, even if, the RCMs are initiated by same GCM data (ERA40), they come out with different results. The RCMs were run by GCM, ERA40, for the case of 2 m temperature. The results of super-ensemble simulations suggest that the ENSEMBLE method cannot effectively sieve out the more precise data from single model because taking average with equal weighting results produces lack of selective ability. In area analysis, either in different

subdomains or in the whole simulation domain, the ISES method showed the better performance in RMSE, APCC, and EVSS than the ensemble simulation. Hence, it is capable to make up the deficiencies of single model and improve the skill in regional climate simulation.

Following the above result, here in this study, the ISES method has been taken as better method for projecting the future climate. However, it is seen that both the ENSEMBLE and ISES method's results are deviating largely from observation (Fig. 1). The observation data used here are the monthly mean of surface temperatures of ERA40 data set available in the website http://data.ecmwf.int/data/d/era40_mnths/. This is happening due to the driving GCM, ECHAM4 A2 scenario data, which is deviated largely from observation data. It is seen all the RCM and both the ENSEMBLE and ISES simulations are affected by the GCM. Therefore, the results will definitely vary from observation (Fig. 1). But, in case of Chen *et al.*,¹⁷ the driving GCM for all three RCMs was ERA40, which is the reanalysis data and closer to observation. Therefore, their verification results were skillful. In the present case, it is not worth to compare these results with observation.

Before adopting the simulation outputs during 2040–2050 and 2090–2100, the inconsistency in between the regional simulations and observation during 1990–2000 should be identified first. Here, the main inconsistency is common for all the three models and can be identified as the effect of GCM (Fig. 1). In addition, it is also observed that the super-ensemble means are very much close to the GCM and it differ from observation. Therefore to reach the RCMs and super-ensemble closer to the observation, the GCM result should be followed by some adjustment to agree with the observation. This picture then helps to get an in-depth understanding of the spatial distribution of climate parameters, after those inconsistencies are removed from the projected outputs of the future periods. This approach is commonly named as bias correction and the adjusted results can be used for future projection. Basically, the method needs to calculate the deviation in between the model results and observation data, and then add this deviation to model projected future results. Such effort is expected to provide no interference of the inconsistency from the GCM to check the climatic change of meteorological parameters.

According to the results of Chen *et al.*,¹⁷ it is clear individual models are failing to simulate an improved data. But due to the application of super-ensemble approach the results have been improved. Among the super-ensemble approaches, ISES seems to be more promising than ENSEMBLE.

Table 2. Model weights for ISES. The four different parameters are temperature at 2 m height (TMP (2 m)), the mean sea level pressure (MSLP), accumulated precipitation (PCP) and the wind vector (UWIND, VWIND).

| | TMP (2 m) | MSLP | UWIND | VWIND | PCP |
|----------|-----------|-------|-------|-------|-------|
| MM5 | 0.271 | 0.283 | 0.310 | 0.255 | 0.334 |
| NCEP RSM | 0.422 | 0.313 | 0.298 | 0.303 | 0.558 |
| PRM | 0.307 | 0.404 | 0.397 | 0.442 | 0.108 |

Therefore, in the present study, ISES method has been considered to project the future climate. So, the weights of each model for each parameter have been presented in Table 2. The weighting factors show that higher weighting factors are coming from RCM with good skills.

3. Climate Change in 2040–2050 and 2090–2100 with Respect to 1990–2000

To understand the climate change over East Asia after 50 and 100 years, the super-ensemble ISES approach has been applied in order to project the climate change in 2040s and 2090s (shown in Fig. 2 and 3, respectively) with respect to 1990s. Fig 2 presents the decadal change in 2040s with respect to 1990s. In 2040–2050, the Pacific high is simulated to be much more intensified than 1990s. A lower pressure with respect to 1990s is simulated over the mainland and extends toward northward. That helps the northward transport of water vapor from South China Sea toward the mainland. The northward component of the wind flow over land area is simulated to increase about $0.1\text{--}1\text{ m s}^{-1}$ in 2040s with respect to 1990–2000. The prevailing southerly from South China Sea to inland of China is stronger than the GCM projection. Therefore, the surface temperature over ocean in 2040–2050 will increase by $1\text{--}2^\circ\text{C}$ than that in 1990–2000. However, for the land, temperature will be increased to about $1.1\text{--}5^\circ\text{C}$ than that in 1990–2000. Furthermore, the increase of the northward movement of warm and moist air from the South China Sea will affect the intensity of rainfall over Southern China. Some parts of China will have higher rainfall increased up to 500 mm. But, over some areas, it is simulated to have lower rainfall decreased up to 150 mm. The adjusted super-ensemble ISES mean projection shows more rainfall in China than the GCM projection.

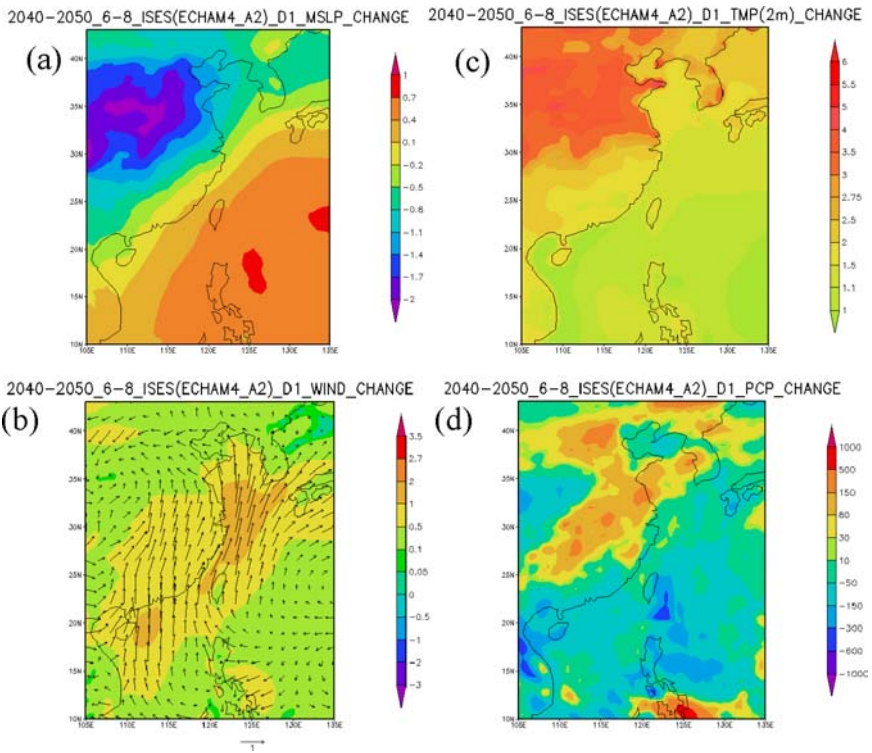


Fig. 2. The ISES of the projected decadal change of the (a) mean sea level pressure, (b) wind flow, (c) surface temperature at 2 m above sea level and (d) accumulative precipitation (mm) during June–August of 2040–2050 from that of 1990–2000 under SRES A2 scenario.

Figure 3a–3d shows the ISES super-ensemble average of the projected decadal change of the meteorological parameters during June–August in 2090–2100. The mean sea level pressure pattern in 2090s is similar to that in 2040s. But, the Pacific high is simulated to be extended by area and strengthen by 1 hPa than that in 1990–2000. The Pacific high is simulated to be much more stronger than that of 1940s. Over the South China Sea area, the wind speed is simulated to increase to about 2.7 m s^{-1} in 2090s than that in 1990s. In addition, the surface temperature is simulated to elevate all over East Asia and over all the inland it will be increased up to $3\text{--}6^\circ\text{C}$ with respect to 1990s condition. Besides, the simultaneous decrease and increase of pressure over mainland China and ocean, respectively, explains increase of precipitation over mainland and decrease over the ocean (Fig. 3d).

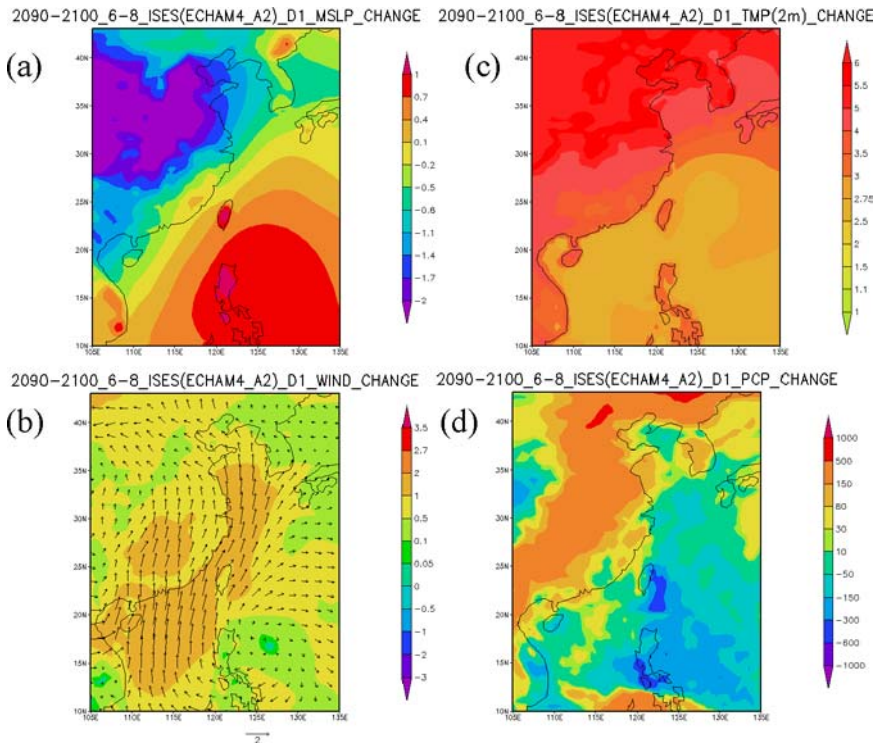


Fig. 3. Same as Fig. 2, but for 2090–2100 under SRES A2 scenario.

Moreover, the accumulated rainfall is simulated to increase and extend over land up to 1000 mm. But, over the Ocean, the rainfall is projected to decrease over 150 mm to 30 mm with respect to 1990s.

4. Conclusion

The ISES method is expected to be the suitable choice for the projection of future climate change of 2040–2050 and 2090–2100. So, ISES method has been adopted for this study. The results indicate that the mean sea level pressure at Pacific is projected to be intensified and the low pressure structure in China is projected to reduce in future projection. The Pacific high is simulated to increase by 0.4–1 hPa in summers of 2040–2050 and 0.7–1 hPa in summers of 2090–2100 under SRES A2 scenario in most of the area of Pacific. Meanwhile, the northward component of wind flow over land

area is simulated to increase to about $1\text{--}1\text{ m s}^{-1}$ in 2040s and $1\text{--}2.7\text{ m s}^{-1}$ in 2090s than that in 1990s. The temperature over the sea of 2040–2050 and 2090–2100 is simulated to increase to about $1\text{--}1.5^\circ\text{C}$ and $2.75\text{--}4^\circ\text{C}$ higher than that in 1990–2000, respectively. Moreover, the temperature is projected to increase higher at higher latitudes. As for the land, the simulated increment in temperature is about $1.1\text{--}3.5^\circ\text{C}$ higher in 2040–2050 while in 2090–2100 it is about $3\text{--}6^\circ\text{C}$ higher with respect to 1990s. The simulated intensified Pacific high is caused by the rise of temperature over mainland in future. Furthermore, as for the simulation of precipitation, the data showed that the change of precipitation is about 80–1000 mm on the land and -150 to -30 mm on the ocean in the future. Moreover, the intensified northward movement of warm and moist air from the South China Sea toward the mainland is simulated to increase the rainfall over this region.

Acknowledgments

This study is supported by the National Science Council of ROC grant NSC93-Z-2621-002-033, NSC 94-2621-Z-002-004, and NSC95-2621-Z-002-004. The authors appreciated the generosity of MPI and DKRZ for providing ECHAM4 data sets in this work.

References

1. R. E. Dickinson, R. M. Errico, F. Giorgi and G. T. Bates, *J. Climate* **15** (1989) 383–422.
2. F. Giorgi and G. T. Bates, *Mon. Wea. Rev.* **117** (1989) 2325–2347.
3. M. R. Marinucci and F. Giorgi, *J. Geophys. Res.* **97** (1992) 9989–10009.
4. J. D. Horel, J. B. Pechman, A. N. Hahman and J. E. Geisler, *J. Climate* **7** (1994) 56–71.
5. J. O. Roads and S.-C. Chen, *J. Geophys. Res.* **105** (D24) (2000) 529–539.
6. B. T. Anderson, J. O. Roads and S.-C. Chen, *J. Geophys. Rev.* **105** (D19) (2000) 24455–24467.
7. D. Conway, *Prog. Phys. Geogr.* **22** (1998) 350–374.
8. P. H. Whetton, J. J. Katzfey, K. J. Hennesey, X. Wu, J. L. McGregor and K. Nguyen, *Clim. Res.* **16** (2001) 181–201.
9. G. A. Grell, J. Dudhia and D. R. Stauffer, *Technical Report NCAR/TN-398+STR* (National Center for Atmospheric Research, Boulder, Co, 1994).
10. H.-M. H. Juang and M. Kanamitsu, *CAS/JSC Research Activities in Atmospheric and Oceanic Modeling*, report no. 19 (1994).
11. P. A. Haines, J. D. Chern and W. Y. Sun, *Tellus* **49A** (1997) 595–612.

12. E. Roeckner, J.M. Oberhuber, A. Bacher, M. Christoph and I. Kirchner, *Clim. Dyn.* **12** (1996) 737–754.
13. Intergovernmental Panel on Climate Change (IPCC), *Special Report on Emission Scenarios* (Cambridge University Press, Cambridge, 2000), p. 570.
14. F. Giorgi and R. Francisco, *Clim. Dyn.* **16** (2000) 169–182.
15. F. Giorgi and R. Francisco, *Geophys. Res. Lett.* **27** (2000) 1295–1298.
16. R. Weisse, H. Heyen and H. von Storch, *Mon. Wea. Rev.* **128** (2000) 3631–3642.
17. S. F. Chen, C. M. Liu, S. H. Lin, M.-C. Wu, R.-Y. Tzeng, H.-H. Hsu and C.-T. Chen, *Climate Change and Sustainable Development* (Global Change Research Center, National Taiwan University, Taipei, Taiwan, ROC, 2005), pp. 16–23.
18. H. M. H. Juang, S. Hong and M. Kanamitsu, *Bull. Am. Meteorol. Soc.* **78** 2125–2143.
19. W.-Y. Sun and J.-D. Chern, C.-C. Wu and W. R. Hsu, 1991, *Mon. Wea. Rev.* **119** (1991) 2558–2573.
20. W.-R. Hsu and W.-Y. Sun, *Mon. Wea. Rev.* **122** (1994) 324–340.
21. W.-Y. Sun and J.-D. Chern, *J. Atmos. Sci.* **51** (1993) 191–209.
22. M. G. Bosilovich and W.-Y. Sun, *J. Climate* **12** (1999) 1490–1505.
23. J.-D. Chern, *Ph. D. Dissertation* (Purdue University, West Lafayette, IN, 1994), p. 178.
24. S. Y. Hong and Pan, H. L., *Mon Wea. Rev NWS/NCEP*, (1996) **244**.
25. T. N. Krishnamurti *et al.* *Science* **285** (1999) 1548–1550.
26. P. Xie and P. A. Arkin, *J. Clim.* **9** (1996) 840–858.

This page intentionally left blank

ATMOSPHERIC DEPOSITION OF NUTRIENTS AND ITS ROLE ON COASTAL EUTROPHICATION IN SOUTHEAST ASIA

SUNDARAMBAL PALANI^{*,†}, RAJASEKHAR BALASUBRAMANIAN^{‡,§},
SATHRUGNAN KARTHIKEYAN[‡] and PAVEL TKALICH[†]

[†]*Tropical Marine Science Institute, NUS*

14 Kent Ridge Road, Singapore 119223

[‡]*Division of Environmental Science & Engineering,*

NUS, Singapore 117576

^{*}*tmssp@nus.edu.sg*

[§]*eserbala@nus.edu.sg*

Human activities often lead to increased inputs of nutrients and organic matter (as point or non-point sources) into the coastal environment. The excess nutrients input into coastal waters may cause increases in eutrophication of coastal regions and food web alteration in oligotrophic pelagic regions. As point sources originate from discrete and identifiable locations, their loads and impacts can be quantified using respective well-developed methods. However, non-point sources such as atmospheric deposition are diffused and highly variable. Among the distributed sources of nutrients in the coastal zone, the role of atmospheric deposition is least understood due to the paucity of comprehensive observational data in Southeast Asia (SEA). In view of recurring forest fires in SEA on a large scale especially during the 1997–1998 El Niño period and the abundant rainfall in this tropical region, the wet and dry deposition fluxes of nutrients from the atmosphere to the ocean are thought to be significant. Results obtained on atmospheric deposition of nutrients show that this process may be an important contributor to nutrient loading of coastal zones in SEA. Relatively higher concentrations of nutrients were observed in rainwater and airborne particles during the 1997–1998 smoke haze as compared with non-haze period. The fluxes of atmospheric nutrients ammonium, nitrate, and phosphate estimated in this study were 0.44, 4.74, and 0.05 g/m²/year for wet deposition; and 0.02, 0.31 and 0.11 g/m²/year for dry deposition, respectively.

1. Introduction

Eutrophication of coastal waters has been considered one of the major threats to the health of marine ecosystems for more than 30 years.^{1–3}

Even though seawater has assimilation capacity, the combined effect of additional pollutants with the nutrient load may cause outbreak of harmful algal bloom, excessive eutrophication, and loss of natural habitat. Among effects and consequences caused by eutrophication are increase in nutrient concentrations, changes in N:P:Si ratio, phytoplankton primary production and biomass, reduction of biodiversity, microbial loop and the pelagic system, light reduction and increase in sedimentation, and depletion of oxygen concentrations. Another alarming change in coastal waters is the increased abundance of gelatinous organisms that displace the traditional crustacean grazer food webs.⁴ Transport via the atmosphere is recognized as an important route by which nutrients and particles are delivered to the sea surface in addition to that caused by riverine outflow, direct wastewater discharge, and stormwater runoff.⁵ Estimates of the atmospheric fluxes of nutrients to the oceans suggest that the atmosphere can be a major source in terms of mass^{6,7} and plays a major role in the oceanic biogeochemical cycling.^{8,9}

The increase in the concentration of nutrients in coastal environments in countries within Asia and the Pacific can be due to both point and non-point sources. The point sources such as domestic sewage and industrial outfalls discharge continuously with little variation over time from discrete and identifiable locations; their impacts can be measured and controlled directly. However, non-point sources such as atmospheric deposition are diffused, highly variable, and linked to seasonal or irregular events such as heavy precipitation, smoke haze episodes (caused by forest fires), etc. There are three major processes of direct atmospheric deposition to natural water bodies, namely dry deposition, wet deposition, and gas exchange across air–water interface (Fig. 1). Dry deposition is composed of small particulates that fall from air or collected from aerosol, while wet deposition involves dissolved chemical compounds that occur in rainfall. In general, wet deposition is more important than dry deposition for components associated with small particles, which are mainly those produced by gas to particle conversion. Atmospheric inputs may deposit directly onto the oceanic euphotic zone. Some of the organic and inorganic pollutants can have acute and long-term impacts on the marine environment. In particular, USEPA¹⁰ studies show that 21% of the nitrogen (N) pollution entering Chesapeake Bay comes from the air.

Increasing population, industrialization, agricultural activities, and uncontrolled forest fires are expected to increase the atmospheric deposition of a wide variety of fixed and organic nitrogen (ON) as well as phosphorous

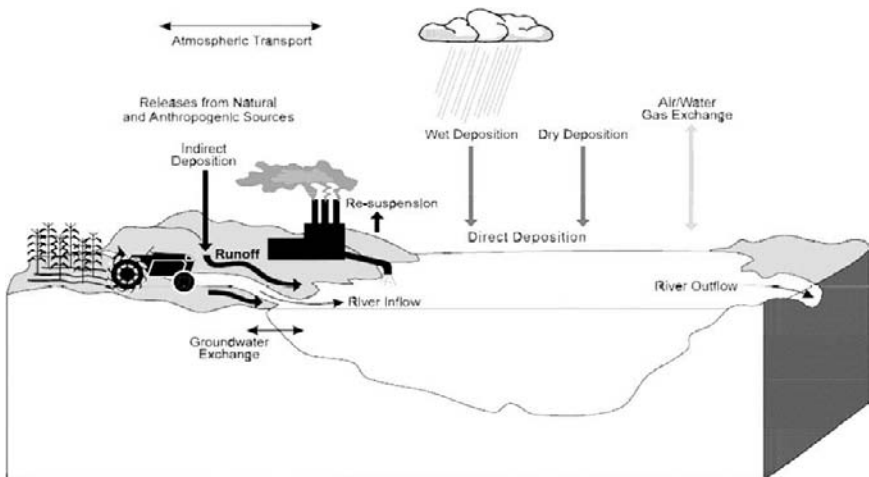


Fig. 1. A schematic illustration of atmospheric deposition processes.¹⁰

(P) species to both the pelagic and coastal oceans. Many development activities, both within and outside the coastal zone, have taken place without due regard to environmental considerations and impacts on ocean environment.¹¹ As a result, the sustainable capacity of many coastal ecosystems, particularly mangroves, coral reefs and estuaries, has been threatened, or deteriorated from a combination of air and water pollution. The estimates of atmospheric inputs of nutrients to the oceans and some coastal areas are needed as the evidence is growing that these inputs significantly modify oceanic chemistry^{12,13} and biogeochemical processes in estuarine and coastal waters before mixing with the ocean in a variety of complex and poorly understood ways.

Atmospheric wet and dry deposition includes several familiar biologically active inorganic N species. In addition, the atmospheric ON deposition may be equal to or perhaps greater than the inorganic nitrogen flux to the ocean.¹⁴ The ON is known to be biologically active, but its sources and chemical form are not fully known yet. Developed regions of the world are predicted to show relatively small increase in the fixation of N over this time period, while rapidly developing areas will contribute very significantly to increased human-derived fixed N. For example, Asia is predicted to account for approximately 40% of the global increase from energy-derived fixed N and approximately 87% of that from fertilizer.¹⁵ The dissolved ON is of anthropogenic origin, and the human activities

have increased fixed-N fluxes to the ocean from $(3\text{--}8) \times 10^{12}$ mol/year to $(6.5 - 19) \times 10^{12}$ mol/year, implying an even more massive perturbation of the global nitrogen system than previously believed.¹⁴ Galloway *et al.*¹⁶ developed maps of the recent (1980) and expected (2020) annual deposition of the oxidized forms of N from the atmosphere to land and ocean surfaces by a deposition modeling study. Increases in deposition from 1.5 to 3 times, and in some limited areas up to 4 times, are projected to occur over large areas of the coastal and pelagic ocean¹⁷ (this estimate does not include possible changes in reduced N and ON fluxes). This leads to the possibility of regional biogeochemical impacts in the coastal and pelagic oceans.

There have been no systematic measurements and quantifications done yet on atmospheric nutrient deposition of N and P species in Singapore seawater and the rest of the SEA either. This paper describes the first attempt to quantify the atmospheric deposition of N and P compounds (both inorganic and organic forms). The preliminary results obtained on wet and dry deposition fluxes of N and P compounds are presented and discussed. In addition, a 3-D water quality model (NEUTRO),³⁹ used to gain further insights into atmospheric deposition of nutrients, is also discussed.

2. Background

Several literature reviews have highlighted the importance in addressing the nutrients input from the atmosphere into the Singapore coastal waters and SEA.^{a9,14,18} The Indonesian forest fires, that took place in Kalimantan and Sumatra during the 1997–1998 dry season, deteriorated the regional air quality in SEA (Bangkok Post, September 27, 1997).¹⁹ Both airborne particulate matter and other air pollutants were spread over six Southeast Asian countries, with peak levels of particulates in Kuala Lumpur, Singapore, and many Indonesian cities far exceeded ambient air quality standards.²⁰ The Air Pollution Index, which is a measure of SO₂, NO₂, CO, ozone and dust particles, reached a critical level of 839 on September 23, 1997 in Malaysia. It should be mentioned that levels of 100–200 are considered “unhealthy”; levels of more than 300 are equivalent to smoking 80 cigarettes a day and are “hazardous.” Measurement of NO₂ shows that its concentration was $8.4 \pm 5.5 \mu\text{g}/\text{m}^3$ at various sites throughout

^aThe first attempt to quantify atmospheric deposition fluxes of macro-nutrients (N and P components) on Coastal waters of SEA is briefly explained in this study.

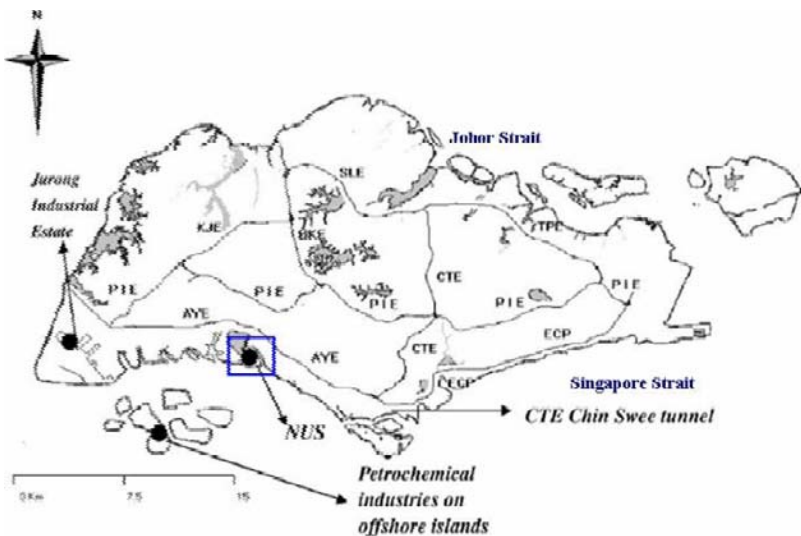
Brunei Darussalam during October 1997 and February 1998.²¹ Air quality in terms of Pollutant Standards Index (PSI, as introduced by USEPA) became worse during hazy days as evident from the increase in PSI to 101–200, 5% of days unhealthy in 1994 and 3% of days unhealthy in 1997. The deterioration in air quality was due to the trans-boundary smoke haze from the land and forest fires in Indonesia.²²

Due to abundant rainfall in SEA region and the recurring forest fires on a large scale, the significant quantities of N species are delivered from the land to the ocean via the atmosphere. N is now considered the biggest pollution problem in coastal waters.^{23–25} Reactive N is overused in the coastal areas of Pacific Ocean, which causes significant environmental impacts, particularly eutrophication in the coastal areas and surface water.²⁶ Since atmospheric inputs do occur all year round, the flux of N from the air may not only trigger summer blooms, but also contribute to the water column nitrogen standing stock, and hence the magnitudes of the spring bloom. The emissions from the forest fires cause several environmental impacts on human health and marine organisms. Burning of crop residues due to the uncontrolled (Indonesian) forest fires seems to be a major source of reactive N in SEA in spring.²⁷ During the intense El Niño event of 1997–1998, extensive coral bleaching occurred on coral reefs worldwide^{28,29} due to mobilization and deposition of nutrients released from natural forest fires.

Little is known about inputs and impacts of atmospheric N and P species to the Singapore coastal waters compared to coastal waters of the USA and Europe, and also about the role of atmospheric inputs in relation to those from runoff and outfall. ON deposition in SEA was 41% of TN³⁰ and they are important components of atmospheric N deposition.³¹ Nutrients deposited from the atmosphere include N species [total nitrogen (TN), nitrate (NO₃), nitrite (NO₂), ammonium (NH₄) and organic nitrogen (ON)] and P species [total phosphorus (TP), phosphate (PO₄) and organic phosphate (OP)]. Thus the present research is important to assess impacts of these N and P compounds on the water quality and the marine environment of SEA. A water quality model is used to understand the role of biogeochemical processes in eutrophication of tropical coastal water, and to predict how it might be affected by environmental changes or perturbations to the system by an atmospheric input. The manifestation of adverse effects of eutrophication in coastal marine environments is closely related to hydrodynamic processes (physical processes such as advection, the development of stratification, establishment of fronts, and the mixing of water masses).

3. Methodology

Singapore is a small urban country with total land area of 699 km² (temperature ranging from 21.1 to 35.1°C, annual average rainfall of 2136mm, latitudes 1°06'N and 1°24'N; longitudes 103°24'E and 104°24'E, 137 km north of the equator), with small water resources and limited coastal ocean space around the island. It therefore needs to protect and conserve its precious resources for sustainability. In addition, as the Singapore Straits lies at the crossroads of the Malacca Strait and South China Sea, its coastal water quality is also influenced significantly by transboundary inputs from its neighboring countries. It is therefore necessary to quantify the atmospheric macro nutrients and micronutrients inputs to the seawater through wet and dry deposition studies.³² The amount of nutrients deposited from the atmosphere needs to be quantified to assess their potential impacts on the marine environment and to identify their most probable sources, and factors involved in reaching seawater and pathways of transportation. The sampling site (Fig. 2) is approximately 1 km away from the open sea, and is free of any major emissions. Chemical industries are situated to the South-West (SW) of the station while heavy industries are found to the North-West (NW).



Note: AYE, BKE, CTE, ECP, KJE, PIE, SLE and TPE are expressways.

Fig. 2. Map showing the sampling location in Singapore.

The methodologies used for air sampling and laboratory analysis of nutrients are described below. Dry deposition (Airborne Particulate Matter) samples were collected on Whatman quartz microfiber filters using a high-volume sampler (Hi-Q Environmental Products Q5; model 3800 AFC) for a stipulated period, and wet deposition samples were collected using an automated wet only sampler (Ecotech Model 200) at NUS atmospheric research station located at the rooftop of building E2 (67 m above sea level) (Fig. 2). The air sampling and the chemical analysis of atmospheric samples were carried out according to standard protocols. Measuring total dissolved nitrogen (the inorganic and organic components together) involves releasing the nitrogen from the organic molecules, by chemical oxidation to NO_3^- . The resulting TN was measured, and with the initial concentrations of the inorganic ions, bulk dissolved ON concentration can be determined by difference ($\text{ON} = \text{TN} - \text{initial inorganic nitrogen}$). The ON chemical species result from direct emissions of ON compounds or from the interaction between nitrogen and biogenic or anthropogenic and natural sources. Speciation of ON in the atmosphere is poorly understood.

Dry deposition filter samples were taken as a fraction, for example, 1/4 or 1/8th part of total filter area and 20 or 50 ml Milli Q water was added in a tapered bottle. It was sonicated for 30–60 min and then the extracts were filtered using a syringe filter. Rain water samples were taken after filtration for laboratory analysis. Samples were refrigerated prior to analysis in the original polyethylene collection bottle. No other precaution was taken against biological activity in the stored sample, however, if necessary, samples were filtered through a 0.45- μm filter prior to analysis. Wet and dry samples were analyzed for ammonium by ion chromatography (IC) (Model ICS-2000; Dionex Corporation) using a cation column according to our standard laboratory procedure.

Wet and dry samples were analyzed for oxidized nitrogen ($\text{NO}_3 + \text{NO}_2$) by an IC anion column.³³ To determine TN, the samples were placed in a bottle with an oxidizing reagent (potassium persulfate–sodium hydroxide) and borate buffer solution. The bottles were placed in a pressure cooker at 100°C (3–4 psi) for 60 min for sample digestion so that all N species could be converted into nitrate. After the samples are cooled to room temperature, the digested samples were filtered through a 0.45- μm filter. A boric acid–sodium hydroxide buffer was added to bring the pH of the sample within the range 7–8. If IC was used for TN determination, the digested sample pH should be adjusted to alkaline condition to avoid spoiling the IC columns. The sample was then ready for the determination

of total oxidized nitrogen using IC as nitrate. EDTA standards were used for calibration.

Wet and dry samples were analyzed by the IC anion column for PO₄ and by the Ascorbic Acid method for TP.³⁴ The digested sample was used for TP determination as per standard phosphate procedure. OP flux was quantified by subtracting the PO₄ fluxes from the TP flux. The quality of the methods for both N and P species was verified by a known NIST SRM 1648 (urban particulate matter) standard sampling procedure and a standard addition method.

4. Results and Discussions

The PM₁₀ air samples collected from August 1997 to November 1997 during smoke haze period (PSI > 50, signifying that the ambient air was polluted with PM) and the rainwater samples collected from May 2005 to May 2006 (average precipitation of 51.4 mm) were analyzed in the laboratory to estimate the nutrients (TN, NH₄, NO₃+NO₂, TP, and PO₄) present in dry and wet atmospheric deposition, respectively. Table 1 shows the measured concentrations of nutrients in atmospheric dry deposition, wet deposition, and seawater baseline. The amount of nutrients (both N and P) deposited by wet deposition is significantly higher than that by dry deposition and the seawater baseline water quality. If all nutrients are assumed to be deposited into ocean, it may have considerable effect on seawater quality and thus

Table 1. Measured concentrations of nutrients (nitrogen and phosphorous components) in atmospheric dry deposition ($n = 10$), wet deposition ($n = 12$), and seawater baseline in Singapore.

| Nutrients | Dry deposition* | | Wet deposition* | | Seawater baseline |
|----------------------------------|-----------------|-------------|-----------------|-------------|-------------------|
| | Mean | Min–Max | Mean | Min–Max | Mean |
| TN | 1.260 | 0.256–2.355 | 3.903 | 0.913–8.961 | 0.1129 |
| NH ₄ | 0.107 | 0.001–0.431 | 0.206 | 0.004–0.961 | 0.0133 |
| NO ₂ +NO ₃ | 0.830 | 0.121–2.085 | 2.218 | 0.131–5.553 | 0.02 |
| ON | 0.406 | 0.132–1.578 | 1.496 | 0.596–2.489 | 0.0796 |
| TP | 0.425 | 0.073–0.887 | 0.251 | 0.085–1.069 | 0.0251 |
| PO ₄ | 0.176 | 0.006–0.699 | 0.023 | 0.001–0.056 | 0.0116 |
| OP | 0.296 | 0.022–0.676 | 0.241 | 0.083–1.069 | 0.0135 |

Note: The units of all parameters are in $\mu\text{g}/\text{m}^3$ for dry deposition, in mg/l for wet deposition, and for seawater baseline.³⁹

*Dry deposition and wet deposition data are based on the present study; n = number of samples.

increase the algal bloom due to nutrient enrichment. The net nutrient flux due to wet deposition depends on the amount of rainfall in the region.

The current paucity of high-quality dry deposition and rainwater composition data from most countries in Asia makes a quantitative survey of dry and wet deposition across the whole region impossible at present.³⁵ By selecting data from sites well away from the major urban and industrial centers, the results obtained from the Australian study can be taken to define a "baseline" for an unpolluted continental setting³⁶ when compared to Asian locations that is expected, on the basis of regional emissions, to be anthropogenically influenced. The two salient points drawn by Ayers and Yeung³⁷ were: (i) that very substantial increases in emissions over decadal time scales have already occurred and will continue to occur in Asian countries, and (ii) the total regional emissions comprise a large fraction of global emissions. The latter point is underscored by global emissions estimates during 1980 for NO_x from industrial activities/fossil fuel use of 22 TgN/yr.³⁸ The published, relatively unpolluted locations are in Indonesia (at Bukit Koto Tabang & Sumatra by Gillett *et al.*,⁴⁰) and Katherine in Australia.³⁷ The annual mean pH calculated from volume weighted mean concentration of H^+ was 4.20 in Singapore, which is a typical acidic value.⁴¹ The published nominal annual average dry deposition concentration of nutrients in SEA are 13.67 ($\mu\text{mol/l}$), 19.87 ($\mu\text{mol/l}$), and 0.18 ($\mu\text{mol/l}$) in Malaysia during 1996–1997,^{35,37} respectively, for NH_4 , NO_3 , and PO_4 , 0.88 (mg/l) for NO_3 in Indonesia during 1990,⁴² 40.45 ($\mu\text{g/dm}^3$) for NO_3 in Hong Kong during 1997⁴³ and 16.79 ($\mu\text{eq/l}$) and 17.27 ($\mu\text{eq/l}$) for NH_4 and NO_3 in Singapore during 1997–1998,⁴¹ respectively.

The smoke haze occurrences were due to advection of biomass burning impacted air masses from the Indonesian provinces, Sumatra and Kalimantan (Borneo), where extensive forest fires took place.⁴⁴ These islands are situated around Singapore from southeast (SE) to southwest (SW). The areas of forest fires ranged from several hundred kilometers to about 2000 km from Singapore. The severity of the fires episodes was also linked to the occurrence of the El Nino/Southern Oscillation, which has historically brought drought conditions to the SEA, creating conditions ripe for fires. With the wind generally blowing from the SE/SW direction during southwest monsoon (SWM, June to September) period, the combustion generated gaseous pollutants and fine particles emitted from the biomass burning were transported to Singapore, Malaysia and Thailand.⁴⁵ At the end of October, the onset of the northeast monsoon (NEM, November to March) brought a sudden return to PSI levels below 50 and good air quality.

4.1. Dry deposition fluxes

Quantifying dry atmospheric input to natural surfaces is a difficult task due to the complex physical and chemical processes involved. In the most widely used formulation for dry deposition it is assumed that the dry deposition flux is directly proportional to the concentration of the chemical component being deposited. Dry deposition fluxes ($\text{g/m}^2/\text{year}$) F_d of nutrients and other chemical components in the aerosol phase are estimated using the following equation:

$$F_d = C_a V_d \quad (1)$$

where C_a is the concentration measured from the atmospheric particles collected in the aerosol phase (g/m^3); V_d is the dry deposition velocity (m/year). The magnitude of V_d depends on the chemical components [2, 1.2, 0.6 cm/s for phosphate, nitrate and ammonium, respectively⁶ 0.18 cm/s for NO_2 .⁴⁶ The advantages of this formulation of dry deposition are that all of the complexities of the process are represented in one single parameter, the deposition velocity. The disadvantage is that V_d depends on many different physical and chemical properties and therefore can be quite difficult to quantify. During the 1997 haze period, the dry deposition flux ($\text{g/m}^2/\text{year}$) of NH_4 , $\text{NO}_3 + \text{NO}_2$ and PO_4 were estimated in this study as 0.02, 0.31 and 0.11, respectively. Nominal annual average dry deposition fluxes ($\text{meq/m}^2/\text{year}$) published elsewhere in SEA for NO_2 were 33.08 in Malaysia during 1993–1998^{46,47}; 45 in Indonesia during 1992 and 1996,⁴⁰ and 1.7 in Australia during 1991.³⁷

4.2. Wet deposition fluxes

The wet atmospheric deposition fluxes ($\text{g/m}^2/\text{year}$) F_w of nutrients are calculated from the precipitation rate and the concentration of the nutrients and other chemical components in rainwater using the following equation:

$$F_w = C_{\text{rain}} P_r \quad (2)$$

where C_{rain} is the concentration measured in precipitation (g/m^3) and P_r is the precipitation rate (m/year). The annual average rainfall of Singapore is 2136 mm.⁴⁸ Precipitation contains a variety of organic and inorganic species, including many N and P compounds. The dissolved phase in rainwater is regarded as an approximation of its bioavailable fraction. The particulate fraction in rainwater that enters the marine surface layer

partly dissolves, however, but this contribution is assumed low; dissolution processes in clouds are driven by mainly pH variations and involve acidic pH values.^{49,50} It is likely that the remaining particulate fraction is little soluble. Moreover, the dissolution of atmospheric particles depends greatly on their origin (lithogenic or anthropogenic) and on biological processes such as ingestion by zooplankton,⁵¹ and it is difficult to quantify this remaining particulate fraction. When the rainfall amount is less than 1 mm, the event is not taken into account for flux calculations, firstly for analytical convenience, and secondly because even when the nutrient concentration is high, such events yield low or negligible nutrient loads. The estimated wet deposition fluxes ($\text{g/m}^2/\text{year}$) of TN, NH_4 , NO_3+NO_2 , ON, TP, PO_4 , and OP were 8.34, 0.44, 4.74, 3.19, 0.54, 0.05, and 0.52 in this study which are significant and are higher than those published for Australia [0.079 (NH_4) and 0.308 (NO_3) by Ayers and Yeung³⁷], respectively, in SEA. Nominal annual average wet deposition fluxes ($\text{meq/m}^2/\text{year}$) published elsewhere in SEA for NH_4 and NO_3 are 39.83 and 58.17 in Malaysia during 1993–1998^{46,47}; 76.67 and 28.07 in Indonesia during 1992 and 1996⁴⁰; 4.37 and 4.97 in Australia during 1991, and 24.34 and 37.48 in Hong Kong during 1988–1991,³⁷ respectively.

4.3. Water quality model

Numerical 3-D water quality model NEUTRO^{39,52,53} used in the study predicts nutrient dynamics with respect to seawater baseline characteristics and transport of industrial and domestic effluents discharged in coastal waters or estuaries. The model description and eutrophication model kinetics were published elsewhere,³⁹ and the fundamental equation is given in Appendix A. This model provides information on nutrient concentrations (NH_4 , NO_3+NO_2 , PO_4 , Silica, ON, and OP), primary production (phytoplankton and zooplankton), dissolved oxygen [carbonaceous biochemical oxygen demand and dissolved oxygen (DO)] bacteria, and total suspended solids necessary to estimate large-scale ecological effects. The model is capable of simulating relevant fluxes due to physical, chemical and biological processes and external forcing such as point sources. The water quality model is being used for both short-term and long-term forecast studies, and for environmental impact assessment in Singapore. The model domain covers the main island of Singapore and its surrounding coastal waters, extending from approximately 1°0'N to

1°33'10.43"N (latitude) and from 103°20'E to 104°20'E (longitude). The typical hydrodynamic forcings (tidal currents and turbulence diffusion) are obtained from 3-D hydrodynamic model (TMH).⁵⁴ The water quality baseline for the model is calibrated using a typical hydrodynamic output data from TMH with a horizontal grid of 500 m × 500 m with 10 vertical layers at depths of 0, 2.5, 5, 7.5, 10, 20, 40, 60, 80, and 120 m. The previous version of NEUTRO³⁹ did not include information on non-point sources such as atmospheric inputs onto sea surface. It is essential to include these phenomena in the model along with/without land-based sources. The water quality and the plankton community in the Singapore waters undergo significant short-term variations induced by tidal changes and seasonal variations induced by monsoon cycles. In order to understand the long-term response of the coastal ecosystem to anthropogenic activities and the potential for eutrophication of the coastal waters of Singapore, it is necessary to establish current baseline conditions of the physical, chemical, and biological attributes of the coastal waters over a range of space and time scales. The present research is important for identifying causes and effects of atmospheric deposition of nutrients in SEA.

4.4. Case study for Singapore coastal water eutrophication

Following the atmospheric deposition onto the surface of the seawater, the nutrients are transported to the water column as well as spatially distributed by the action of tidal currents. As a preliminary study, the atmospheric contribution to nutrient load is specified as a constant concentration (g/m³) uniformly distributed over the model domain area at all time steps. The model calculates the nutrient flux by using concentration, precipitation (wet deposition), and settling velocity (dry deposition). For scenario analysis, the model is run with SW monsoon tidal current and atmospheric deposition source on the surface of seawater. With the estimated atmospheric load, the computed concentrations of NO₃+NO₂ and OP changed significantly from baseline value. Due to this increase in concentration, there is a marginal increase in phytoplankton and zooplankton concentration observed. In order to get in-depth knowledge on this nutrient change due to "new" source on plankton growth, more data from field measurement should be acquired and also further fine tuning of the model kinetics/phenomena is needed to incorporate the "new" source accurately. Figure 3 shows typical time series computed concentrations

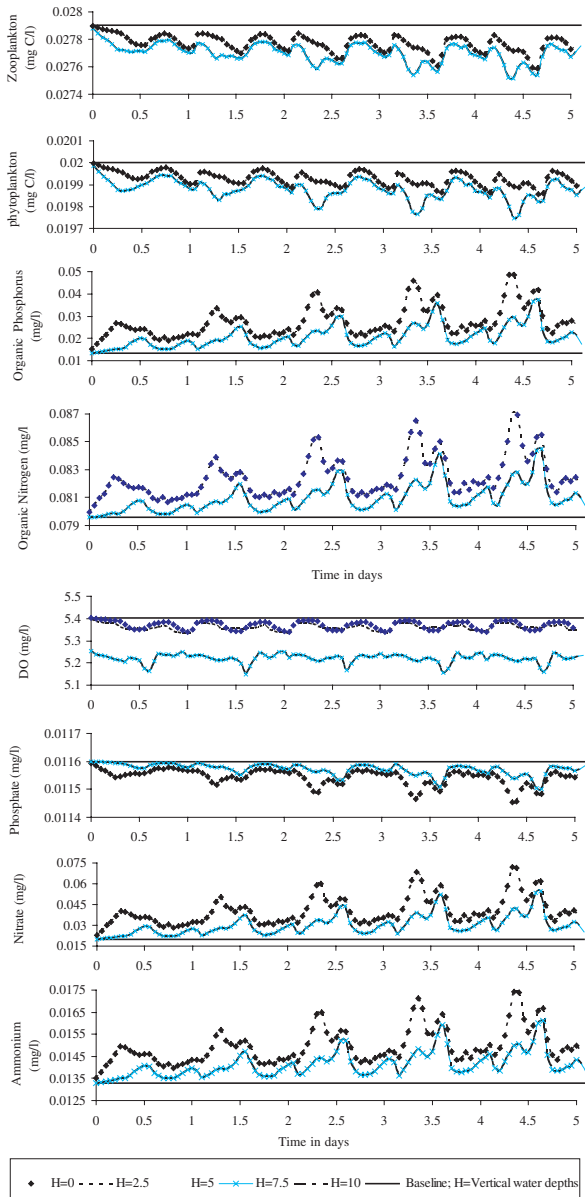


Fig. 3. Typical time series computed concentrations of nutrients, dissolved oxygen and plankton at a location in the model domain of Singapore seawater (*Note:* The straight line indicates the baseline values of seawater).

of nutrients, DO, phytoplankton and zooplankton at a location in the Singapore seawater. The computed model result is compared with the ASEAN criteria for marine waters⁵⁵ to identify the water quality changes from standards.

5. Conclusions and Outlook

Atmospheric deposition in Singapore and surrounding countries appears to provide significant fluxes of nutrients of environmental concern and to play an important role in the coastal eutrophication. The smoke haze events (arising from forest fires and a strong El Niño influence) in SEA are likely to affect atmospheric inputs of nutrients and other pollutants into aquatic ecosystems. Atmospheric dry and wet deposition will be monitored over a long-term to understand their seasonal trends and the factors that influence nutrient deposition into coastal water and the open ocean in SEA. A numerical 3-D water quality model (NEUTRO) was used for the simulations of coastal eutrophication. The expansion of the model and the fine tuning of kinetics are in progress to incorporate the “new” atmospheric nutrient input and related phenomena so that their impact on the Singapore coastal waters can be predicted accurately. Nutrient deposition data are particularly needed to determine the input levels into the coastal zone at which negative environmental effects occur and to predict where impacts can be expected. The effect of haze events and atmospheric input into coastal zone of SEA will be identified by further monitoring and field investigation. The present research is important for assessing the eutrophication processes and the proper management of marine ecosystems.

Acknowledgments

This work is a part of the main author’s ongoing PhD research. We would like to thank Elisabeth Rianawati and Umid Man Joshi for their technical assistance and TMSI, NUS for supporting the pursuit of this research project.

References

1. J. H. Ryther and W. M. Dunstan, *Science* **171** (1971) 1008.
2. S. W. Nixon, *Ophelia* **41** (1995) 199.

3. R. Elmgren, *Ambio* **30** (2001) 222.
4. E. L. Mills, *Helgoländer Meeresunters* **49** (1995) 29.
5. H. W. Paerl, *Ophelia* **41** (1995) 237.
6. R. A. Duce, P. S. Liss, J. T. Merrill, E. L. Atlas, P. Buat-Menard, B. B. Hicks, J. M. Miller, J. M. Prospero, R. Arimoto, T. M. Church, W. Ellis, J. N. Galloway, L. Hansen, T. D. Jickells, A. H. Knap, K. H. Reinhardt, B. Schneider, A. Soudine, J. J. Tokos, S. Tsunogai, R. Wollast and M. Zhou, *Global Biogeochemical Cycles* **5** (1991) 193.
7. J. M. Prospero, K. Barrett, T. Church, F. Dentener, R. A. Duce, J. N. Galloway, H. Levy, J. Moody and P. Quinn, *Biogeochemistry* **35** (1996) 27.
8. T. Jickells, *Marine Chemistry* **48** (1995) 199.
9. H. W. Paerl, *Limnology Oceanography* **42 (5 part 2)** (1997) 1154.
10. USEPA, in *Second Report to Congress*, (Office of Air Quality Planning and Standards, North Carolina, 1997), EPA-453/R-97/011. Retrieved from EPA web site <http://www.epa.gov/air/oaqps/gr8water/2ndrpt/report97.html>
11. The Straits Times, in Article: *Ocean's carbon intake threatens ecosystem-NOAA*, (Singapore Press Holdings, Singapore, 2004) July 2004.
12. GESAMP, *Reports and Studies* **38** (1989) p. 32.
13. GESAMP, UNEP Regional Seas Reports and Studies **115** (1990) p. 111.
14. S. Cornell, A. Rendel and T. Jickells, *Nature* **376** (1995) 243.
15. J. N. Galloway, W. H. Schlesinger, H. Levy, A. Michaels and J. L. Schnoor, *Global Biogeochemical Cycles* **9(2)** (1995) 235.
16. J. N. Galloway, H. Levy II and P. S. Kasibhatla, *Ambio* **23(2)** (1994) 120.
17. J. N. Galloway, W. H. Schlesinger, H. Levy II, A. Michaels, and J. L. Schnoor, *Global Biogeochemical Cycle* **9(2) (D17)** (1995) 235.
18. J. A. Nerilie, K. G. Michael, T. M. Malcolm, C. John and S. H. Wahyoe, *Science* **301** (2003) 952.
19. GEO 2000, in *Global Environment Outlook 2000* (UNEP, Nairobi, 2000) p. 398. Derived from <http://www.grida.no/geo2000/index.htm>
20. World Bank, in *1997 World Development Indicators* (The World Bank, Washington DC, 1997), p. 280.
21. M. Radojevic, *Environmental Scientist* (1997) p. 1. Derived from <http://www.chemsoc.org/chembytes/ezine/1998/radojevic.htm>
22. C. Y. Koh, in *workshop Better Air Quality in Asian and Pacific Rim Cities (BAQ 2002)* (BAQ 2002, Hong Kong, 2002) p. 6. Derived from http://www.cse.polyu.edu.hk/~activi/BAQ2002/BAQ2002_files/Proceedings/Sub-workshop2/sw2a-6Koh_paper.pdf
23. National Research Council (NRC), in *Clean Coastal Waters: Understanding and Reducing the Effects of Nutrient Pollution*, (National Academy Press, Washington, DC, 2000) p. 405.
24. R. W. Howarth, D. P. Swaney, T. J. Butler, and R. Marino, *Ecosystems* **3** (2000) 210.
25. N. Rabalais, *Ambio* **31** (2002) 102.
26. J. N. Galloway, M. Bekunda, Z. Cai, J. W. Erisman, J. Freney, R. W. Howarth, L. A. Martinelli, M. C. Scholes and S. P. Seitzinger, in *Third*

- International Nitrogen Conference*, 3rd INI Conference proceeding, (Institute of Soil Science Chinese Academy of Sciences, China, 2004) p. 270.
- 27. Y. Kondo, Y. Morino, N. Takegawa, M. Koike, K. Kita, Y. Miyazaki, G. W. Sachse, S. A. Vay, M. A. Avery, F. Flocke, A. J. Weinheimer, F. L. Eisele, M. A. Zondlo, R. J. Weber, H. B. Singh, G. Chen, J. Crawford, D. R. Blake, H. E. Fuelberg, A. D. Clarke, R. W. Talbot, S. T. Sandholm, E. V. Browell, D. G. Streets, and B. Liley, *Journal of Geophysical Research* **109** (2004) D15S12.
 - 28. GEO 2003, in *Global Environment Outlook 2003* (UNEP, Nairobi, 2002) p. 426. Derived from <http://grida.no/geo/geo3/english/index.htm>.
 - 29. UNEP, GeoYear Book 2003, United Nations Environment Programme (Earthscan Publications Ltd, London, 2004).
 - 30. S. C. Cornell, T. D. Jickells, J. N. Cape, A. P. Rowland and R. A. Duce, *Atmospheric Environment*, **37** (2003) 2173.
 - 31. J. C. Neff, E. A. Holland, F. J. Dentener, W. H. McDowell and K. M. Russell, *Biogeochemistry* **57** (2002) 99.
 - 32. P. Sundarambal, R. Balasubramanian, S. Karthikeyan and P. Tkalich, in *AOGS 2006*, AOGS Conference Proceeding (AOGS, Singapore, 2006) p. 1202.
 - 33. S. Karthikeyan, S. See and R. Balasubramanian, *Analytical Letters* **40** (2007) 1.
 - 34. APHA, in *Standard Methods for the Examination of Water and Wastewater*, (AWWA & WEF, 21st Edition, Washington, 2005) p. 1368.
 - 35. G. P. Ayers, Environmental Monitoring Assessment **19** (1991) 225.
 - 36. N. Kato and H. Akimoto, *Atmospheric Environment* **26A** (1992) 2997.
 - 37. G. P. Ayers and K. K. Yeung, *Atmospheric Environment* **30** (1996) 1581.
 - 38. J. Dignon, *Atmospheric Environment* **26A** (1992) 1157.
 - 39. P. Tkalich and P. Sundarambal, *Singapore Maritime and Port Journal* (2003) 122.
 - 40. R. W. Gillett, G. P. Ayers, P. W. Selleck, H. Tutimhw and Harjanto, *Water, Air, and Soil Pollution* **120** (2000) 205.
 - 41. G. P. Hu, R. Balasubramanian and C. D. Wu, *Chemosphere* **51** (2003) 747.
 - 42. S. Asiati, T. Budiwati, L. Q. Avia, *Water, Air and Soil pollution* **130** (2001) 1571.
 - 43. T. Peter and W. F. Tam, *Water, Air, and Soil Pollution* **122** (2000) 433.
 - 44. R. Balasubramanian, T. Victor and R. Begum, *Journal of Geophysics Research* **104** (1999) 26,881.
 - 45. M. Brauer and H. Hashim, *Journal Environmental science and technology* **32** (1998) 404A.
 - 46. G. P. Ayers, L. C. Peng, L. S. Fook, C. W. Kong, R. W. Gillett and P. C. Manins, *Tellus* **52** (1999) 60.
 - 47. G. P. Ayers, L. C. Peng, R. W. Gillett and L. S. Fook, *Water, Air, and Soil Pollution* **133** (2002) 15.
 - 48. Singapore Department of Statistics, Singapore in Figures 2005, (2005). Derived from <http://www.singstat.gov.sg/keystats/annual/yos/climate.pdf>.
 - 49. L. J. Spokes, T. D. Jickells and B. Lim, *Geochimica et Cosmochimica Acta*, **58** (1994) 3281.

50. K. D. Desboeufs, R. Losno, F. Vimeux and S. Cholbi, *Journal of Geophysical Research* **104** (1999) 21,287.
51. R. M. Moore, J. E. Milley and A. Chatt, *Oceanologica Acta* **7** (1984) 221.
52. P. Sundarambal and P. Tkalich, in *Joint AOGS 1st Annual Meeting & APHW 2nd Conference*, Conference Proceeding (AOGS, Singapore, 2004) p. 756.
53. P. Sundarambal and P. Tkalich, in *AOGS 2005*, AOGS Conference Proceeding (AOGS, Singapore, 2005) p. 1155/1428.
54. W. C. Pang and P. Tkalich, *Environmental hydraulic and sustainable water management-environmental hydraulic*, 14th IAHR-APD Congress Proceeding Vol.1, (Taylor & Francis Group, London, 2004) p. 489.
55. ASEAN, in *ASEAN State of the Environment 1995* (Unpublished, Association of South-East Asian Nations, 1995).

Appendix A: Neutro model³⁹ transport equation

The 3D transport equation for dissolved and suspended constituents in a water body accounts for all materials entering and leaving through direct and diffuse loading; advective and dispersive transport; physical, chemical, and biological transformation. Consider a coordinate system with x - and y -coordinates in the horizontal plane and the z -coordinate in vertical. The 3-D advective-diffusive equation is described as follows:

$$\begin{aligned} \frac{\partial C_j}{\partial t} + \frac{\partial C_j U}{\partial x} + \frac{\partial C_j V}{\partial y} + \frac{\partial C_j (W - w_j)}{\partial z} - \frac{\partial}{\partial x} \left[E_x \frac{\partial C_j}{\partial x} \right] \\ - \frac{\partial}{\partial y} \left[E_y \frac{\partial C_j}{\partial y} \right] - \frac{\partial}{\partial z} \left[E_z \frac{\partial C_j}{\partial z} \right] = \frac{Q(S_j - C_j)}{\Delta h \Delta x \Delta y} + R_j \\ C(t_0) = C_B \end{aligned} \quad (\text{A1})$$

where C_j = concentration of j th pollutant (mg/l); S_j = contamination of the source with j th pollutant (mg/l) from point or non-point sources; Q = discharge of the liquid source or quantity of atmospheric source (m^3/s); the model atmospheric flux (F) is quantified by source term $F = QS_j$. R_j = chemical reaction terms, corresponding to the interaction equations for j th state variable (eutrophication kinetics are described mathematically by a set of equations in Ref. 39); E_x, E_y, E_z = turbulent eddy coefficients; $\Delta x, \Delta y, \Delta z$ = computational grid sizes in x -, y -, and z -directions, respectively; Δh = thickness of water layer affected with initial dilution; $C(t_0)$ = concentration of j th pollutant at zero simulation time; C_B = initial (baseline) concentration of each state variable obtained from field measurements; w_j = settling velocity of j th pollutant; U, V, W = tidal

current in x , y , and z directions, respectively. The values of U , V , and W , E_x , E_y and E_z are computed using the 3-D hydrodynamic model (TMH⁵⁴) and are used as input to NEUTRO. Values of concentration (C) are computed at the nodes of a 3-D grid at different instances of time using Equation (A1).

STUDY OF TEMPORAL VARIATION OF EQUATORIAL TROPOPAUSE DUE TO ATMOSPHERIC WAVES IN CPEA CAMPAIGN 2004 AT KOTO TABANG, INDONESIA

S. K. DHAKA^{*,†}, RANGOLI BHATNAGAR[†], Y. SHIBAGAKI[‡], S. FUKAO[§],
T. KOZU[¶], V. MALIK[†], S. MALIK[†] and A. DUTTA^{**}

[†]*Department of Physics, Rajdhani College, University of Delhi, India*

[‡]*Osaka Electro-Communication University, Osaka, Japan*

[§]*Research Institute for Sustainable Humanosphere*

Kyoto University, Uji, Kyoto, Japan

[¶]*Faculty of Science and Engineering, Shimane University, Shimane, Japan*

^{**}*Department of Physics and Astrophysics, University of Delhi, Delhi, India*

**skdhaka@yahoo.com*

Variation in the wind and temperature data over 1 month is investigated using daily GPS radiosonde as a part of Coupling Processes in the Equatorial Atmosphere over Koto Tabang (100.32°E , 0.20°S), Indonesia. Composites of temperature and wind variations are shown near tropopause region ($\sim 17\text{ km}$ altitude) from April 10 to May 9, 2004. Strong correlation coefficient (0.64) between zonal wind and temperature in the close vicinity of tropopause indicates presence of Kelvin waves. Results show that these waves modulate the cold point tropopause (CPT) height. Kelvin waves and CPT height variation with wave period of $\sim 7\text{--}8$ days were found dominant in the altitude region of $\sim 17\text{ km}$.

1. Introduction

Tropopause represents the boundary between the troposphere and stratosphere and is marked by large changes in thermal, dynamical and chemical structure of the atmosphere. The tropical tropopause region or tropical tropopause layer is the region between the convective equilibrium of troposphere and the radiative equilibrium of stratosphere. It is a transition zone where both stratospheric and tropospheric processes interact.¹ The cold point tropopause (CPT) is the coldest temperature in the tropopause region. Its height corresponds to the tropopause height. The height of tropopause is sensitive to temperature changes in troposphere and

stratosphere. Its height is about 15–17 km over the tropics and 10 km near the poles. It also varies seasonally as well as with occurrence of deep convection. The height of tropopause and its stability is also found to have a dynamical link with the atmospheric convective system dominant just below the tropopause.^{2–8} The atmospheric wave systems are supposed to be responsible for the change of tropopause height and hence the change in CPT.

The equatorial region is the source of many unique atmospheric processes that couple the entire atmosphere vertically from bottom to top and horizontally from equator to pole. The Coupling Processes in the Equatorial Atmosphere (CPEA) program had been initiated by Japan to understand the basic processes in the equatorial atmosphere by conducting various observations in the Indonesian equatorial region.⁹ The role of atmospheric waves until now is poorly understood for the large-scale variation in the upper troposphere region. The aim of this paper was to study the signatures of atmospheric waves in the upper troposphere region over Indonesia and to study their role in modulating the tropopause height.

2. Data

The wind and temperature data were collected as a part of a well-coordinated intensive observation period (IOP) carried out under the first (CPEA) campaign conducted at Koto Tabang, West Sumatra, Indonesia from April 10, 2004 to May 9, 2004 using the radiosonde.⁹ Wind and temperature data were used with a height resolution of 150 m. Though data were available at a fine interval, however, it is averaged at each 150 m so that spurious peaks could be eliminated. The temperature sensor of capacitive wire type was used in GPS radiosonde that can cover temperature range from 60 to –90°C with a resolution of 0.1°C and accuracy of 0.3°C. The pressure sensor of silicon type was used that covered pressure range from 1080 to 3 hPa with 0.1 hPa resolution and 0.5 hPa accuracy. The data over 1 month were analyzed in order to examine the phase relationship and correlation coefficient between temperature and wind components (both zonal and meridional) from 15 to 20 km heights. The CPT and its altitude were noted daily from temperature profile data. In order to investigate the temporal variation and inter-relationship between the temperature and wind components (zonal and meridional) near tropopause height, we plotted and analyzed these parameters during IOP.

3. Results and Discussion

Figure 1 shows the temporal variation of tropopause height during IOP. We examined the variation of all parameters to understand the interdependency of tropopause vis-à-vis atmospheric waves.

During first few days of observation (April 10–15, 2004), the tropopause height decreased from 18 to 16 km. This was a sharp decrease of about 2 km within 6 days of observation period. However, over next 20 days the tropopause height varied between 16 and 17 km, except in the last week of observation (May 5–9, 2004) where it had gone up to 18 km with a variation of about 500 m.

Tropospheric weather over Indonesia is highly dominated by a complex structure of local convection systems and large-scale convective systems which usually originate from Indian ocean and reach to Indonesian region. In the absence of large-scale convection systems local convection including deep penetration in the troposphere is highly dominating. In the presence of large-scale convection systems [in this observation period three Super Cloud Clusters (SCCs) appeared over Indonesian region starting from April 22, 2004 onwards²], local deep convection was suppressed. Deep convection, starting from April 10, 2004, prevailed and dominated until the large-scale convection systems arrived over the radar site.¹⁰

We employed the power spectrum using maximum entropy method (MEM) to the tropopause height data from April 10 to May 9, 2004. We found variability in the tropopause height with wave periods of 3 and 7 days (shown in Fig. 2).

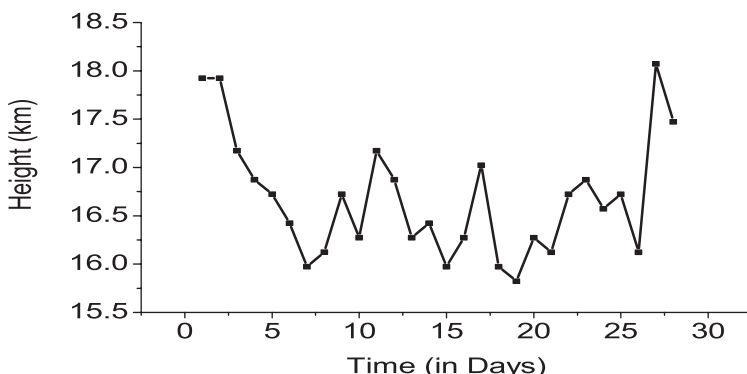


Fig. 1. Temporal variation of tropopause height (km) from April 10 to May 9, 2004 at Koto Tabang, Indonesia.

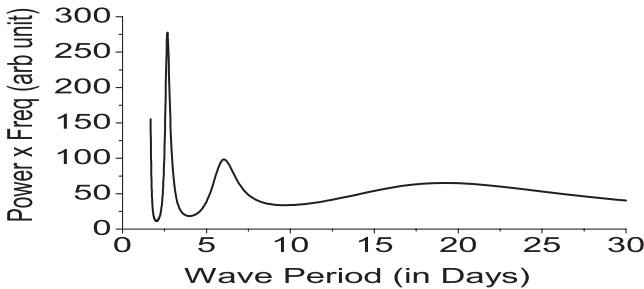


Fig. 2. Power spectrum using MEM for tropopause height variation.

Figure 3 represents the temporal variation of the CPT. The tropopause temperature varied between -84 and -90°C .

However, during the last week of observation the tropopause temperature increased from -90 to -81°C that corresponds to sharp rise in tropopause height, as shown in Fig. 1. The last week of observation is witnessed with presence of strong SCC.² The possible explanation of increase in tropopause height and temperature could be given based on SCC's presence as it might have disturbed the normal day's tropopause height based on the local convection. Power spectrum of the CPT temperature data, shown in Fig. 4, revealed dominant fluctuations with wave periods 2–4 days with a broad peak around 8 days.

The maximum power in Fig. 4 is very close to 2–3 days as found in Fig. 2. Thus, the dominant wave periods of the tropopause height and temperature as shown in Figs. 2 and 4 are similar. In order to determine the possible cause in the tropopause height variation and tropopause

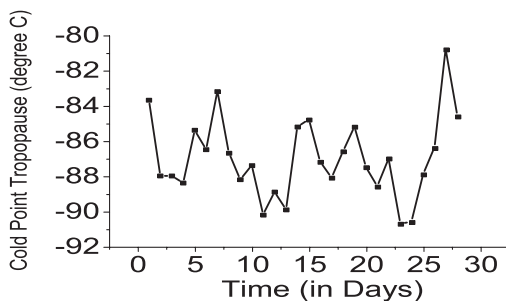


Fig. 3. Time series of CPT temperature. Data are shown from April 10 to May 9, 2004 at Koto Tabang, Indonesia.

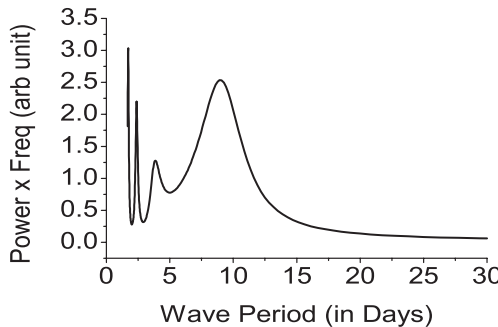


Fig. 4. Power spectrum using MEM for CPT temperature.

temperature, we examined the wind and temperature data variability carefully.

It was most likely that the atmospheric waves with time period of a few days as revealed in Figs. 2 and 4 might have created the temporal variability in the height and temperature of the tropopause.

The data set of wind and temperature is examined for this purpose. Figure 5 shows the variations in zonal wind during IOP. In the upper tropospheric region we have selected 17 km height (average tropopause height) to show the variation of zonal wind and temperature. We notice that zonal wind shows a drastic change both in speed and direction in the last few days of observation.

This change in wind is caused by appearance of SCC as cited before. We examined dominant frequencies in the zonal wind component using MEM.

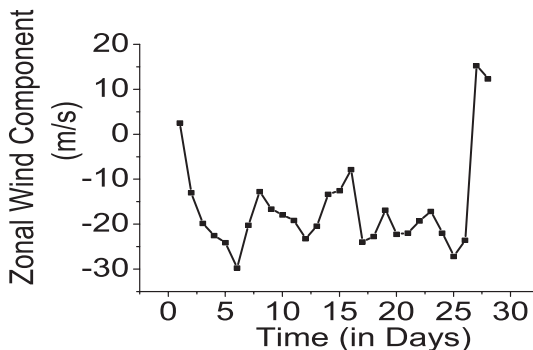


Fig. 5. Temporal variation of zonal wind (U) component from April 10, 2004 to May 9, 2004 at Koto Tabang.

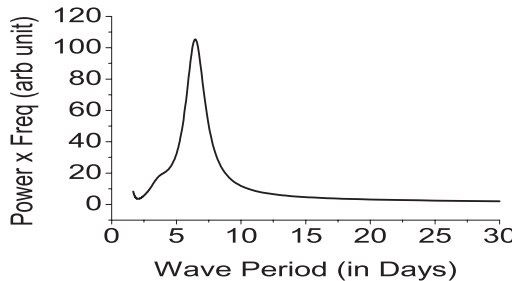


Fig. 6. Power spectrum using MEM for zonal wind component.

Figure 6 shows that a wave period of about 7 days was quite dominating. The power spectra shown in Figs. 2 and 6 clarify that a variability of around 6–7 days was dominant between tropopause height variation and zonal wind component. We found that the zonal wind component and tropopause height varied in consonance in the upper tropospheric region on 6–7 days period; however, broad peak in temperature data (~ 8 days) is also near to these noted peaks. It is evident from Fig. 7 that variability in temperature is very well followed by the zonal wind component. This relation does not exist between the meridional wind and temperature (as shown in Fig. 8). We found that the zonal wind component and temperature varied in consonance in the upper tropospheric region.

During the period from April 15 to May 4, 2004 the temperature was leading the zonal wind by a quarter phase for a dominant wave.

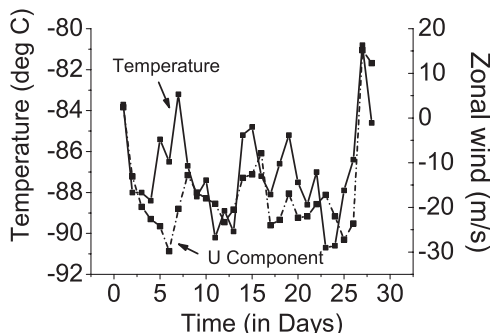


Fig. 7. Time series of zonal wind (m/s) and temperature ($^{\circ}$ C) at about 17 km height Data are shown from April 10, 2004 to May 9, 2004 at Koto Tabang.

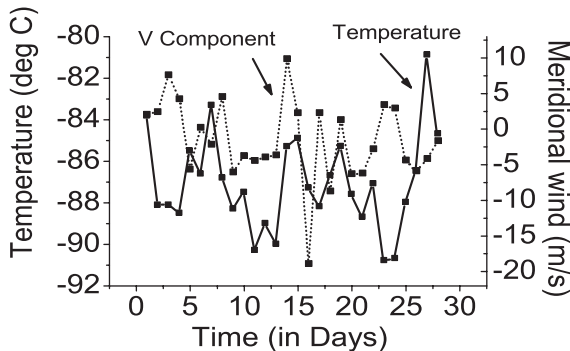


Fig. 8. Time series of meridional wind (m/s) and temperature ($^{\circ}$ C) at about 17 km height. Data are shown from April 10, 2004 to May 9, 2004 at Koto Tabang.

This is an indication of presence of Kelvin wave activity near tropopause region. Usually near tropopause height the atmospheric stability is larger in comparison to the lower and mid troposphere.¹⁰ This is in general valid even during convection, since the effect of convection may cause turbulence in the medium up to 12–13 km heights.

However, above 12–13 km heights ambient atmosphere is stable as the convection terminates in the lower and middle troposphere. In a recent paper by Tsuda et al.¹¹ presence of Kelvin waves is confirmed using several radiosonde stations and CHAMPS/GPS data over Indonesia and nearby region. They have also confirmed some peculiar behavior of Kelvin waves near tropopause region due to the presence of local convection. Hence, atmosphere can support the wave propagation with a change in periods near tropopause region depending upon the environmental conditions.

The correlation coefficient (r_{xy}) was also computed between zonal wind and temperature in a layer of few kilometers adjacent to the tropopause to verify the presence of Kelvin Waves. Table 1 shows the r_{xy} between zonal wind and temperature and the meridional wind and temperature within 15–20 km heights. It is seen from the table that around 16–17 km height r_{xy} is quite strong (0.64) with least value of the probable error. The value of r_{xy} decreases on either sides of this region. The r_{xy} between meridional wind and temperature around 16–17 km heights was weak in contrast to that of zonal wind and temperature. Large value of r_{xy} between zonal wind and temperature further supports the view of presence of Kelvin waves near tropopause height.

Table 1. Correlation coefficient (r_{xy}) of the zonal (U) and meridional (V) wind components with temperature at Indonesia from 15 to 20 km heights.

| Height (km) | Zonal wind component (m/s) and temperature ($^{\circ}\text{C}$) | | Meridional wind component (m/s) and temperature ($^{\circ}\text{C}$) | |
|-------------|--|----------------|---|----------------|
| | r_{xy} | Probable error | r_{xy} | Probable error |
| 15 | 0.38 | 0.11 | 0.37 | 0.11 |
| 16 | 0.60 | 7.88 E-02 | 1.36 E-02 | 0.12 |
| 17 | 0.64 | 7.27 E-02 | -8.99 E-02 | 0.12 |
| 18 | 0.25 | 0.12 | 0.28 | 0.11 |
| 19 | 0.24 | 0.12 | 7.58 E-02 | 0.12 |
| 20 | 0.35 | 0.11 | 0.15 | 0.12 |

Sridharan *et al.*¹² have also verified similar wave characteristics in a recent study using CPEA data over Indonesian region.

4. Conclusion

In this paper, we present the relationship between tropopause height variation and atmospheric wave activity. Tropopause height and hence the tropopause temperature can vary with a time period in consonance with the time period of a wave near tropopause. The lead of temperature fluctuations to wind component by 1–2 days is indicative of Kelvin wave signature. Confirmation of presence of Kelvin waves is supported by recent study cited in the above section. The strong r_{xy} between the zonal wind and temperature also supports the view of the presence of Kelvin wave during IOP. The detection of waves near tropopause can monitor the tropopause height and CPT. The broad peak in the power spectrum of tropopause height, CPT, and zonal wind and temperature noted correspond to wave period of \sim 7–8 days. This confirms the close relationship among these parameters. However, the relationship is not so clear for wave periods of 2–4 days. Since, we have used raw data of wind and temperature without applying any filter, wave signature in wind and temperature could have not been so clear at 2–4 days due to the suppression by strong wave of about 7–8 days. Using CPEA data, Tsuda *et al.*¹¹ and Sridharan *et al.*¹² have indicated high frequency waves with periods of 1–3 days. Such relationships are needed to be examined over a range of wave periods. It would help in understanding the troposphere–stratosphere exchange processes as the stability near tropopause and CPT does vary during severe weather conditions with wave activity in the background wind.

Acknowledgments

The authors are thankful to the reviewers for their critical comments that helped in improving the paper. This work is supported by RESPOND project from ISRO, India. The EAR was established and has been operated by Research Institute for Sustainable Humanosphere (RISH) of Kyoto University, Japan, and the Indonesian Institute of Aeronautics and Space (LAPAN). The authors are also thankful to Dr. A.R. Jain and Dr. T. K. Mandal from National Physical Laboratory (NPL), Delhi for giving useful suggestions that helped a lot in improving the manuscript. S. K. Dhaka is thankful to Dr. Vijay Laxmi Pandit, Principal, Rajdhani College for her kind support.

References

1. A. R Jain, S. S. Das, T. K. Mandal and A. P. Mitra, *J. Geophys. Res.* **III** (2006) D07106, doi : 10.1029/2005JD005850.
2. Y. Shibagaki, T. Kozu, S. Mori, F. Murata, Y. Fujiyoshi, H. Hashiguchi and S. Fukao, *J. Meteorol. Soc. Jpn.* **84A** (2006) 19.
3. S. K. Dhaka, R. K. Choudhary, S. Malik, Y. Shibagaki, M. D. Yamanaka and S. Fukao, *Geophys. Res. Lett.* **29(18)** (2002) 1872, doi:10.1029/2002GL014745.
4. B. V. Krishnamurthy, K. Sathisan, K. Parameswaran, M. N. Sasi, G. Ramkumar, Y. Bhavanikumar, K. Raghunath and M. Krishniah, *Q. J. R. Meteorol. Soc.* **128** (2002) 819.
5. A. Gettleman, M. L. Salby and F. Sassi, *J. Geophys. Res.* **107** (D10) (2002) 4080, doi:10.1029/2001JD001048.
6. M. Fujiwara and M. Takahashi, *J. Geophys. Res.* **106**(22) (2001) 763.
7. T. Tsuda, Y. Murayama, H. Wiryo sumarto, S. W. B. Harijono and S. Kato, *J. Geophys. Res.* **99**(10) (1994) 491.
8. Y. Kawatani, S. K. Dhaka, M. Takahashi and T. Tsuda, *Geophys. Res. Lett.* **30**(8) (2003) 1438 doi:10.1029/2003GL016960.
9. S. Fukao, *J. Meteorol. Soc. Jpn.* **84** (2006) 1.
10. S. K. Dhaka, M. K. Yamamoto, Y. Shibagaki, H. Hashiguchi, M. Yamamoto and S. Fukao, *Geophys. Res. Lett.* **32** (2005) L14820, doi:10.1029/2005GL022907.
11. T. Tsuda, M. Venkat Ratnam, T. Kozu and S. Mori, *J. Meteorol. Soc. Jpn.* **84A** (2006) 277.
12. S. Sridharan, T. Tsuda, T. Nakamura, T. Kozu, S. Mori and J. M. Russell, *J. Meteorol. Soc. Jpn.* **84A** (2006) 259–275.

This page intentionally left blank

THE WINTER ANOMALY OF THE NIGHT-TO-DAY RATIO OF OZONE IN THE MIDDLE TO UPPER MESOSPHERE IN MIDDLE LATITUDES — A COMPARISON BETWEEN MEASUREMENTS AND MODEL CALCULATIONS

GERD R. SONNEMANN^{*,†,‡}, PAUL HARTOGH^{*}, CHRISTOPHER JARCHOW[†],
MYKHAYLO GRYGALASHVILY[‡] and UWE BERGER[‡]

[†]*Max-Planck-Institute for Solar System Research, Germany*

[‡]*Leibniz-Institute of Atmospheric Physics at the University
Rostock, Germany*

**sonnemann@iap-kborn.de*

Long-term ozone measurements by means of the microwave technique at Lindau, Germany (51.66° N, 10.13° E) from December 1998 to December 2005 revealed that the night-to-day ratio (NDR) is markedly enhanced in the middle mesosphere during the winter season compared with the ratio in summer. The anomaly is strongest pronounced in the domain between 65 and 75 km altitude. The winter NDR is more than triple as large as the summer values. The mean ratio shows an annual asymmetry with largest values before winter solstice. The NDR is modulated by oscillation of a time scale in the order of few weeks reminding formally of the well-known winter anomaly of the plasma in the D-region. Model calculations carried out on the basis of our new 3D model LIMA (Leibniz-Institute Middle Atmosphere model) agree in essence with the observations although in some details noticeable differences occur. The strong superimposed variations of planetary time scale point to dynamical processes. A remarkable influence on the winter anomaly of the NDR has the so-called photochemical Doppler-Sonnemann effect consisting in a pronounced impact of the zonal wind on the chemistry. Further influences have to be taken into consideration. We discuss the findings in terms of chemistry and dynamics.

1. Introduction

In the recent past the so-called tertiary ozone maximum of the mixing ratios occurring in the vicinity of the polar night terminator around 72 km was a subject of intense scientific investigation.^{1–7} The term tertiary ozone maximum refers to the historical sequence of its detection and not to the altitudinal order in the atmosphere as it is located between the primary and secondary ozone maximum. In contrast to these permanently

existing maxima the tertiary maximum is a winter phenomenon and extends with decreasing amplitude into middle latitudes only. These facts and its appearance in the middle mesosphere are the reasons to call it middle mesospheric maximum of ozone abbreviated with MMM,⁵ a term we will use in the following sections. The MMM was explained by an increasing imbalance with rising solar zenith angle between the radiation dissociating water vapor and that one dissociating molecular oxygen.³ The photolysis of water vapor which decreases more quickly with increasing solar zenith angle results in the formation of ozone destroying hydrogen radicals whereas the dissociation of molecular oxygen produces ozone by formation of atomic oxygen. As a consequence the ozone concentration should increase. However, the ozone dissociating radiation is almost unabsorbed for grazing incidence in the domain of the MMM producing O(¹D) which is quickly quenched by collisions with air particles.⁵ O(¹D) is able to oxidize water vapor forming two hydroxyl radicals. O itself is involved in different odd oxygen (O and O₃) destroying cycles. A dissociation rate (J) normalized to unity for the constituent x is defined by the relation:

$$J_x^*(\chi, z) = \frac{J_x(\chi, z)}{J_x(\chi = 0, z)} \quad (1)$$

where χ is the solar zenith angle and z is the altitude. There is valid inequality:

$$J_{\text{H}_2\text{O}}^*(\chi, z) \leq J_{\text{O}_2}^*(\chi, z) \leq J_{\text{O}_3}^*(\chi, z) \quad (2)$$

The winter anomaly of the night-to-day ratio (NDR) of ozone consists in the finding that this ratio is enhanced in the winter season. We define a nighttime value as the mean between sunset and sunrise and accordingly a daytime value as the average between sunrise and sunset. The diurnal variation of ozone becomes increasingly more pronounced from the middle to the upper mesosphere. Therefore, a value taken at an arbitrary local time (e.g., noon or midnight) does not represent the behavior at night or day anymore. It is evident that the anomaly of the NDR is closely related to the MMM but it is not the same phenomenon as it also takes into consideration the daytime concentrations behaving differently from the nighttime values. We will present ozone data derived from microwave measurements at a frequency of 142 GHz carried out at Lindau, Germany (51.66° N, 10.13° E) from December 1998 to December 2005. The observations will be compared with model calculations using an advanced 3D model of the dynamics and

chemistry of the middle atmosphere. Finally, the results will be interpreted considering all possible influences.

2. Microwave Measurements of Ozone

A ground-based millimeter wave radiometer detecting the transition of ozone at 142 GHz was used to measure the mesospheric ozone mixing ratio between 35 and 80 km altitude. For more details about the instruments see Refs. 5, 8 and 9. Figure 1 shows the NDR at different heights for the time between December 1998 and December 2005. The dots represent running mean values using a Gaussian function with 8-day full width half maximum

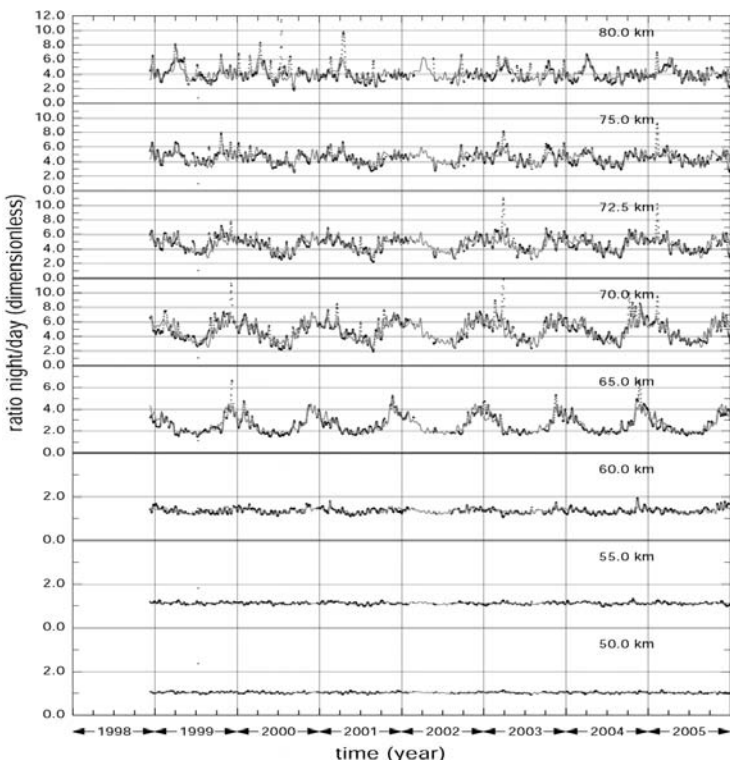


Fig. 1. NDR at different heights for the space between December 1998 and December 2005. The dots represent running mean values using a Gaussian function with 8-day FWHM. The gaps in the observations were linearly interpolated. The closed curve displays the mean of all years derived by a Fourier analysis employing the first 12 harmonics.

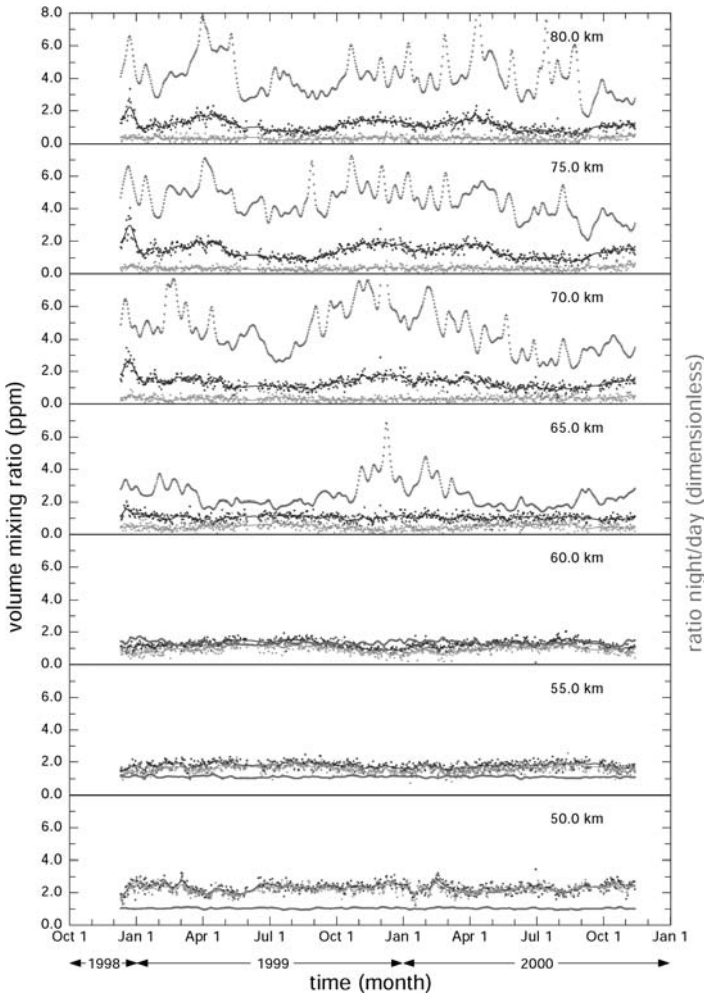


Fig. 2. NDR (uppermost curve) together with the individual measurements (dots) of the night (upper) and day values (lower dots) as well as the sliding means of these values for the first two years of the period showed in Fig. 1.

(FWHM). The gaps in the observations were linearly interpolated. The closed curve displays the mean of all years derived by a Fourier analysis employing the first 12 harmonics. It is, of course, the same variation for all years. Figure 2 exhibits the NDR together with the individual measurements of the night and day values as well as the sliding means of these values for the first two years of the period showed in Fig. 1. The

figure makes clear that the largest wintertime enhancement of the NDR occurs between 65 and 70 km clearly below the Maximum of the MMM. The effect starts weakly at 60 km. In the panels below the NDR is close to unity. At 80 km no pronounced annual but rather an unsystematic variation can be found with exception of an enhancement around spring. This spring maximum is the most interesting feature as it presents a significant deviation from the fluctuating variations outside of this space. The winter-to-summer ratio of the NDR amounts maximum to a factor of 3 at 70 km. There is a marked annual asymmetry. The annual maximum occurs already before winter solstice. The increase of the NDR toward the winter solstice is steeper than the descent toward the summer. As particularly Fig. 2 makes clear the annual variation of the NDR is modulated by variations of a time scale in the order of few weeks.

3. Model Calculations by LIMA

The older versions of our model (called COMMA-IAP: COlogne Model of the Middle Atmosphere of the Leibniz Institute of Atmospheric Physics) calculated climatologic means. It was unable to reproduce events such as sudden stratospheric warmings (SSWs) or to consider the propagation of planetary waves. This model was stepwise improved during the last years. Particularly, the implementation of a new advective transport scheme developed in Refs. 10 and 11 marked by nearly zero numerical diffusion results in the correct calculation of the fields of minor constituents^{5,12,13} as observed by different experiments such as HALOE or microwave monitoring.¹⁴

The longitudinal grid point distance of spherical coordinated increases toward the equator considerably. This non-equidistance is an essential drawback for gravity wave parameterization and the consideration of zonal gradients in the minor constituents particularly in the vicinity of the morning and evening terminators. At the poles the so-called pole-singularities occur meaning no grid point exist at the pole itself. This disadvantage has been addressed by the introduction of triangle, or simplex, coordinates over a sphere. The new model assimilates ECMWF (European Centre for Medium-Range Weather Forecast) data of temperature and horizontal wind components below 35 km. These data contain information about propagating planetary waves according to the running date and geographic position. Based on these input data the dynamic model

calculates the propagation of these waves up to the thermosphere and consequently, it is also able to compute SSW.¹⁵ The dynamical fields calculated in Leibniz-Institute Middle Atmosphere model (LIMA) are used in the chemistry transport model (CTM) consisting of a chemical, a radiation, and a transport code. The transport code considers both the advective and diffusive transport. The diffusion includes turbulent and molecular diffusion, too. It is important also to consider a hydrogen escape flux. The chemistry is as usually based on a family concept but atomic oxygen and ozone have been transported separately. As a consequence the time step has to be reduced to not longer than 100 s. Further information about the CTM can be found in the papers referred above.

Figure 3 shows the annual variation of the NDR calculated by LIMA at the height levels presented in Figs. 1 and 2 for the year 1999. The model calculations reproduce in essential not only the wintertime enhancement of the NDR but also show several differences. The effect starts already some kilometers lower and the amplitudes are larger. Although the annual variation is marked by strong oscillations the agreement with the measurements is rather poor. In the lower panel the NDR are nearly

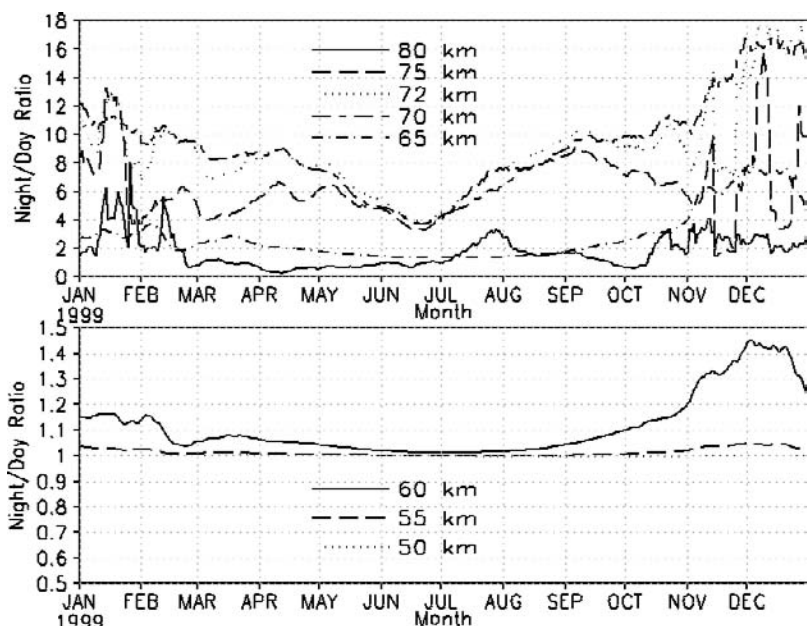


Fig. 3. NDR calculated by LIMA at the height levels presented in Figs. 1 and 2 for 1999.

unity, too. The calculations also make clear (not shown) that the effect is confined to middle and high latitudes whereas in low or equatorial latitudes no annual variation occurs. The amplitude increases considerably toward high latitudes.

4. Discussion

The MMM was interpreted by Marsh *et al.*³ in terms of stronger absorption of radiation that dissociates water vapor resulting in ozone destroying hydrogen radicals than for the radiation that dissociates molecular oxygen when the solar zenith angle increases in the winter season. There is additionally a pronounced annual variation of the water vapor mixing ratio^{13,14} with a maximum in late summer and a minimum in late winter. The average occurring dates depend somewhat on height. The summer-to-winter ratio in high latitudes can amount to more than a factor 2 at 72 km,¹⁴ meaning in the same order varies the production rate of hydrogen radicals for constant solar zenith angle.

The temperature influences the ozone formation by the temperature dependence of the chemical reaction rates. Ozone decreases for increasing temperatures as the rate of its production term decreases and the rate of the main loss process grows with increasing temperature but the concentration of O increases as the production term of ozone is a sink for O and further the O loss terms also decrease with increasing temperature what partly compensates the ozone decreasing effect by rising O concentration. The annual variation of the upper mesospheric temperature shows in winter highest values and in summer lowest ones, meaning the annual temperature variation should damp the influence of the water vapor variation in a limited extent. In a highly complex system it is not trivial to estimate the impact of a varying parameter. There is a transition region around 65 km where the sign of the annual temperature variation changes. In the domain of the occurrence of the winter anomaly of the NDR the annual variations of the temperature are relatively small. The short-term variations become stronger in coherence with SSW when the upper mesosphere cools off and consequently ozone increases.

Figure 4 displays the diurnal variations of the odd oxygen concentration for a latitude close to Lindau (52.5°) at 72 km altitude again according to calculations by LIMA for December 1–3, 1999. The most important result consists in the strong decrease of this quantity in the wake of sunset.

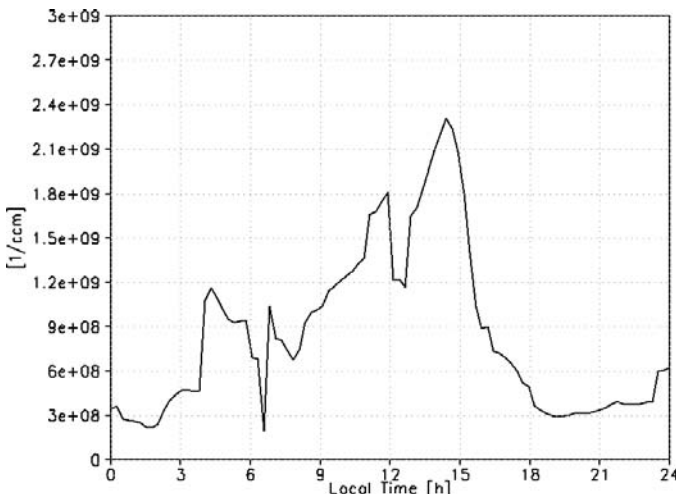


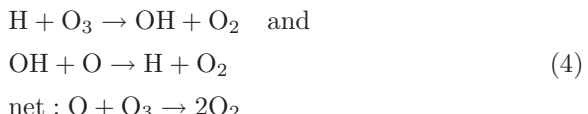
Fig. 4. Diurnal variations during December 2, 1999 of the odd oxygen concentration for 52.5° latitude at 72 km altitude according to calculations by LIMA.

The figure demonstrates the importance of the odd oxygen loss during sunset when atomic oxygen will be transformed into ozone. However, the figure also makes clear that further impacts, such as vertical and meridional transport connected with tidal and gravity wave activity, influences the diurnal variations. Above 60 km (day) and 75 km (night) atomic oxygen is the dominant O_{odd} species and below these altitudes ozone dominates. Atomic oxygen is partly transformed into ozone when the photolysis slows down. This share does not change the odd oxygen concentration. Because simultaneously odd oxygen loss processes act the inequality

$$[\text{O}]_{\text{day}} + [\text{O}_3]_{\text{day}} > [\text{O}]_{\text{night}} + [\text{O}_3]_{\text{night}} \quad (3)$$

is valid.

The chemistry of the middle mesosphere seems to be relatively simple. The catalytic destruction of the odd oxygen constituents (O, O₃) by the odd hydrogen compounds (H, OH, HO₂) in the cycle

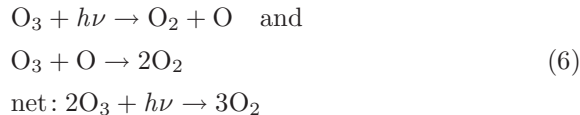


becomes increasingly inefficient with decreasing height because H is removed by the process

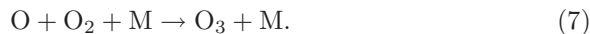


depending quadratically on the air density.

In the lower mesosphere a sink of odd oxygen is given by the scheme



although the largest part of O returns to O₃ by the three-body reaction



Comparing the reaction rates of both processes destroying ozone one will find that for $T = 240\text{K}$ the reaction rate involving H is 6567 times larger than two times that one involving O (two odd oxygen, O and O₃, get lost in this reaction) meaning in order to get the same effect O has to be more abundant by this factor than H. That is only valid below 60 km (varying with different conditions such as local time, season, humidity, etc.).

The loss processes are counterbalanced almost only by the photolysis of molecular oxygen

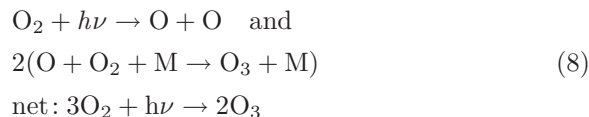


Figure 5 displays the ratio of the dissociation rates normalized to unity of ozone to that of molecular oxygen (upper curve) and those of water vapor to molecular oxygen (lower curve) at 72 km depending on the solar zenith angle. The figure reflects the inequality (2). The ratio of the first curve grows considerably with increasing solar zenith angle, meaning an increasing imbalance will arise during and especially after sunset between the dissociation determining the ozone loss and that one determining its net production.

The reactions of O with OH and HO₂ are very strong. O resulting from the dissociation of O₃ reacts with OH and forms H which will be immediately converted into HO₂. This constituent reacts again with O

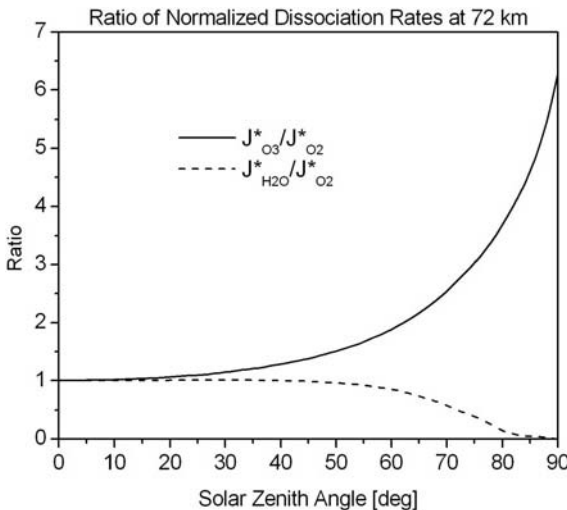
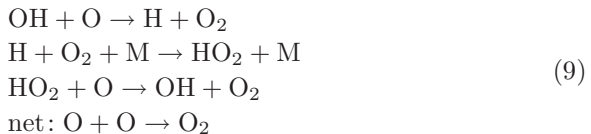


Fig. 5. Ratio of the dissociation rates normalized to unity (J^*) of ozone to that of molecular oxygen (upper curve) and those of water vapor to molecular oxygen (lower curve) at 72 km depending on the solar zenith angle.

and returns to OH so that the following odd oxygen destroying catalytic cycle acts:



Comparing the reaction rates of the reactions of O with OH and O with O_3 one will find that for $T = 240\text{ K}$ again the first reaction is 12,000 times larger than twice the second reaction. In order to get the same effect the ozone concentration has to be by this factor larger than that one of OH. This is only valid within the stratopause region and below so that in the height range of the NDR anomaly the cycle (9) is responsible for the main odd oxygen loss. It is evident that small hydrogen radical concentrations slow down the odd oxygen loss but this effect is at least reduced by the O formation from ozone dissociation for large solar zenith angles.

The characteristic time of the partial O loss in the reaction O with OH only amounts to 2800 s for an OH concentration of 10^7 cm^{-3} — a relatively large concentration. The partial characteristic time for the ozone formation reaction amount to 2680 s at 72 km but only 392 s at 65 km for $T = 240\text{ K}$

again. This means that the transformation of O into O₃ takes place more quickly with decreasing altitude and the loss processes become comparably minor. However, we have to take into consideration that further O₃ returns to O as long as ozone dissociating radiation acts during sunset providing atomic oxygen involved into the loss processes.

The wind system changes principally between summer and winter particularly in middle and high latitudes. The upward wind in summer conveys relatively humid air from the stratosphere into the upper mesosphere whereas in winter the transport is inverse resulting in a drying of the mesosphere. Also the mean meridional wind changes from a transport toward the equator in summer to a transport toward the pole in winter. The zonal wind reverses its direction from a summery east wind regime into a wintry west wind system. Strong wind jets establish in the mesosphere with possible wind speeds exceeding 100 m s⁻¹ in middle to high latitudes in winter. In 2001 Sonnemann¹⁶ introduced the so-called photochemical Doppler effect also abbreviated with DSE (Doppler-Sonnemann effect¹⁷). This effect describes the change of the period of solar insolation for an air parcel moving in zonally direction with or against the rotation of the Earth. For a west wind regime the air parcel moves with the Earth rotation shortening the period and for an east wind regime the period will be prolonged. The shift of the period (DSS) for average climatologic conditions amounts to +4 h in summer and -7 h in winter.¹⁷ The change of the period of insolation affects all diurnal variations of the individual chemical active constituents particularly if the chemical system operates near resonance meaning in a domain around the mesopause region.

Calculations by means of the realistic global three-dimensional model COMMA-IAP revealed an impact of the zonal wind in middle and high latitudes down to 60 km marked by an increase of the ozone nighttime values by more than 60 % and only a slight decrease of the daytime values in winter compared with the case that the zonal wind is zero.¹⁸ The effect was particularly pronounced in the domain of the NDR anomaly but it was almost absent below 60 km. This finding was not analyzed in more detail in the paper referred to. The result is in so far surprising as the characteristic chemical time drops off to few hours or less in the domain under consideration, or in other words, the system operates far from the resonance case as discussed in the paper by Sonnemann.¹⁶

Figure 6 depicts the diurnal variations of the relative deviation of ozone for December 2, 1999 between 50 and 80 km, if calculating on the one hand

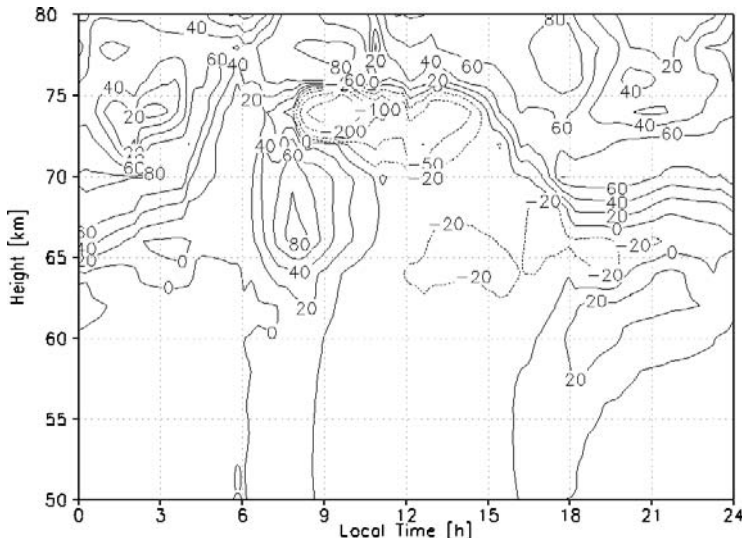


Fig. 6. Diurnal variations of the relative deviation of ozone between 50 and 80 km for the same period as shown in Fig. 4 if calculating on the one hand with the complete wind system and on the other hand if 2 days before solstice the zonal wind was put zero. The quantity R is given by $R = ([O_3]_{\text{with}} - [O_3]_0)/[O_3]_{\text{with}} \times 100 [\%]$.

with the complete wind system and on the other hand if 2 days before solstice the zonal wind was put zero. The quantity R stands for:

$$R = \frac{[O_3]_{\text{with}} - [O_3]_0}{[O_3]_{\text{with}}} \times 100[\%] \quad (10)$$

The calculations were carried out by means of the real date GCM LIMA. As the figure demonstrates, the increase of the nighttime ozone in winter results to a great part from the zonal wind effect whereas the daytime ozone changes only little. However, the comparison with the older model used in Ref. 17 representing climatologic means shows, as already mentioned in the discussion of Fig. 4, that the diurnal variation is essentially more complicated.

The analysis of this finding brought evidence that the shortening of the period of insolation and particularly of the reduction of the duration of sunset by the DSE is responsible for the increase of the winter nighttime ozone concentration. The global calculations made clear that the effect comprises the latitudinal region of the mesospheric west wind jet.

In order to interpret these phenomena one also has to explain why the effect sometimes vanishes although the radiation conditions did scarcely

change. In connection with planetary wave activity and the occurrence of SSWs the aeronomic conditions humidity, temperature, and wind vector alter drastically. Particularly, the zonal wind during sunset influences drastically the nighttime ozone level. The asymmetry of the NDR could result from the fact that SSWs occur more frequent in the second half of the winter season. The differences between observations and model calculations may result from a too coarse integration time step. This discrepancy to solve should be a priority task in future. It demonstrates the sensitive response of the system to small impacts.

5. Conclusion

In conclusion, the MMM and the NDR anomaly in the winter season represent complex phenomena determined by different influences. These are the annual variation of the water vapor concentration with essentially smaller values during the winter season. The increase of the solar zenith angle toward winter solstice entails an increasing imbalance between the normalized photolysis rates of H_2O to that of O_2 . According to Hartogh *et al.*⁵ an inequality is valid that first the water vapor, then the molecular oxygen and finally the ozone dissociation rate noticeable decreases with increasing solar zenith angle. The zonal wind affects particularly the nighttime ozone level by the DSE. The prevailing west wind regime shortens the duration of sunset and consequently the period of ozone decline by $O(^1D)$ and atomic oxygen resulting from the ozone dissociation maintained still after sunset. The annual variation of the temperature tends to decrease the amplitude of the nighttime ozone according to the temperature dependence of the most important reaction rates determining the ozone production and its loss. The modulation of the amplitude of the MMM and the NDR is essentially determined not only by variations of the zonal wind and the temperature but also by a meridional wind transport and, with less extend, by the change of the water vapor concentration due to a changing (vertical) transport.

Acknowledgments

The work was supported by Deutsche Forschungsgemeinschaft, project HA 3261/1-2 and So 263/4-1.

References

1. L. Froidevaux, W. G. Read, T. A. Lungu, R. E. Cofield, E. F. Fishbein, *et al.*, *J. Geophys. Res.* **101** (1996) 10,017.
2. Ch. Jarchow, L. Song, and P. Hartogh, *AGU Fall Meeting* (2000).
3. D. Marsh, A. Smith, G. Brasseur, M. Kaufmann and K. Grossmann, *Geophys. Res. Lett.* **28** (2001) 4531.
4. M. Kaufmann, O. A. Gusev, K. U. Grossmann, F. J. Martin-Torres, D. R. Marsh and A. A. Kutepov, *J. Geophys. Res.* **108** (2003), ACH9-1-ACH9-14 (DOI 10.1029/2002JD002800).
5. P. Hartogh, C. Jarchow, G. R. Sonnemann and M. Grygalashvily, *J. Geophys. Res.* **109** (2004), D18303, doi:10.1029/2004JD004576.
6. D. A. Degenstein, R. L. Gattinger, N. D. Lloyd, A. E. Bourassa, J. T. Wiensz, and E. J. Llwellen, *J. Atm. Sol. Terr. Phys.* **67** (2005) 1395.
7. A. Seppälä, P. T. Verronen, V. F. Sofieva, J. Tamminen, E. Kyrölä, C. J. Rodger and M. A. Clilverd, *Geophys. Res. Lett.* **33** (2006), LO7804, doi: 10.1029/2005GL025571.
8. P. Hartogh, in *Satellite Remote Sensing of Clouds and the Atmosphere II*, 3220 of Proc. SPIE, ed. J. D. Haigh (1997), p. 115.
9. P. Hartogh and G. K. Hartmann, *Meas. Sci. Technol.* **1** (1990) 592.
10. R. P. Walcek, *J. Geophys. Res.* **105** (2000) 9335.
11. R. P. Walcek and N. M. Aleksic, *Atmos. Environm.* **32** (1998) 3863.
12. G. R. Sonnemann and M. Grygalashvily, *J. Atmos. Sol. Terr. Phys.* **67** (2005) 177.
13. G. R. Sonnemann, M. Grygalashvily and U. Berger, *J. Geophys. Res.* **110** (2005) D1530310.1029/2004JD005593.
14. C. Seele and P. Hartogh, *Geophys. Res. Lett.* **26** (1999) 1517.
15. G. R. Sonnemann, M. Grygalashvily and U. Berger, *J. Atmos. Sol. Terr. Phys.* (2006) (in press).
16. G. R. Sonnemann, *J. Atmos. Sol. Terr. Phys.* **63** (2001) 781.
17. G. R. Sonnemann, P. Hartogh, A.s. Medvedev, M. Grygalashvily and U. Berger, *Second International Workshop Mars Atmosphere Modelling and Observations*, 5.1.6, February 27–March 3, 2006, Granada, Spain (2006).
18. G. R. Sonnemann and M. Grygalashvily, *Adv. Space Res.* **32**(5) (2003) 719.

MM5 SIMULATED EVOLUTION AND STRUCTURE OF TYPHOON VAMEI (2001)

FREDOLIN T. TANGANG*,†, LIEW JUNENG†,‡ and CHRIS J. REASON§,¶

†*School of Environmental and Natural Resource Sciences*

Faculty of Science and Technology

National University of Malaysia, Bangi, Selangor, Malaysia

§*Department of Oceanography, University of Cape Town*

Rondebosch, South Africa

**tangang@pkriisc.cc.ukm.my*

†*juneng@pkriisc.cc.ukm.my*

¶*cjr@egs.uct.ac.za*

In this study, the evolution and structure of tropical cyclone Vamei (2001) were simulated using the version 3.6 of the fifth generation of the Pennsylvania State University and the National Center for Atmospheric Research non-hydrostatic model MM5 using one-way nesting and two nested grids. The parameterizations employed include the subgrid-scale convective parameterization of Kain-Fritsch, the grid resolvable Schultz microphysics scheme, the Blackadar parameterization scheme for planetary boundary layer processes, and the CCM2 radiation scheme. The model was initialized and bound by the NCEP global final analyses. The model was integrated for 36 h with an analysis nudging technique employed in the first domain throughout the integration. The second domain was initialized 12 h later with the initial and boundary conditions interpolated from the first domain. The model performed reasonably well in reproducing the track, minimum central pressure, surface maximum sustained wind speed and cloud distribution. During the 36 h of integration, the model clearly shows the evolutionary stages of rapid deepening, maximum intensity, landfall and rapid weakening. The simulated system intensified into a typhoon about 15 h into the model integration time. The thermodynamic and precipitation structures of the simulated system during maximum intensity clearly showed the eye, eyewall, and spiral rainbands. Sensitivity tests indicate that both the sea surface heat transfer and the release of latent heat in clouds contribute positively to the cyclogenesis. Rapid weakening occurred once the system made landfall and there was no longer any latent heat supply from the sea surface.

1. Introduction

On 06:00 UTC December 27, 2001, a very unusual tropical cyclone [named Vamei by the Japan Meteorological Agency (JMA)] formed over the

southern part of the South China Sea (SCS) at about 60 km east of the southern tip of the Malay Peninsula. Tropical cyclone (TC) Vamei was a rare occurrence because its spawning area was located at 1.5°N, 106.5°E where the Coriolis effect is very weak. Chang *et al.*¹ indicated that the formation of TC Vamei was due to the southward intrusion of a northeast monsoon cold surge that later interacted with a Borneo vortex. While strong northeasterlies accompanying a cold surge usually keep this vortex over the land mass of Borneo island, during the formation of Vamei, it remained for an unusually long period of time over the ocean area west of this island.^{1,2} This situation allowed the tropical cyclone to develop without the damping effect of the land mass. Subsequently, the system intensified as it moved toward the Malay Peninsula where it reached typhoon intensity several hours before landfall. Due to the equatorial location of the spawning area, it is of scientific interest to investigate the cyclogenesis of TC Vamei. However, due to its relatively brief lifespan, there were not many observations available other than those from ground radar stations and satellites, particularly during the period when the system was over the SCS. Numerical simulation using models such as the non-hydrostatic fifth generation mesoscale model developed by Pennsylvania State University and the National Center for Atmospheric Research (PSU/NCAR MM5)³ provides an alternative.

The MM5 model has been employed to simulate various tropical cyclones.^{4–7} The investigation of Hurricane Andrew (1992) by Liu *et al.*⁴ using this model is particularly interesting as the model was able to reasonably simulate the thermodynamics and precipitation structures of the hurricane. In the current work, we also employed the MM5 to simulate the evolution, precipitation, and thermodynamic structures of Vamei. In addition, we conducted several other experiments to ascertain the relative roles of various factors in the cyclogenesis. These factors include the latent heat release in clouds, surface heat fluxes, landmass surface friction, and the effects of terrain and elevated orography.

2. Model Configuration

In this study, we use the PSU/NCAR MM5 model version 3.6 that employs a terrain following σ -coordinate system with a total of 24 σ -levels, covering the surface up to 100 hPa. In the horizontal, two grids were used with the coarse domain (45 km resolution) consisting of 100×100 grid points centered

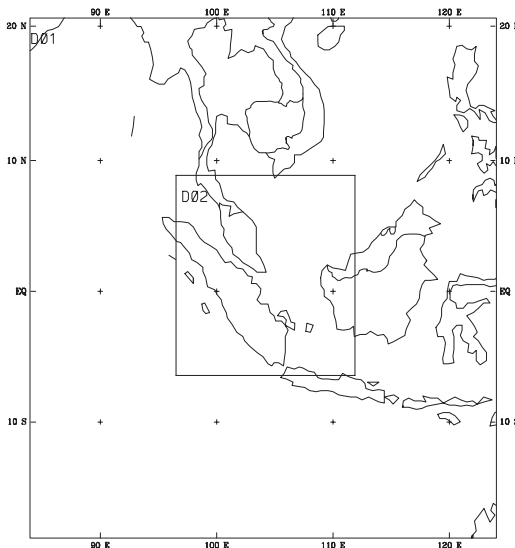


Fig. 1. The domain configuration used for the PSU/NCAR MM5 simulation.

at 102°E; 2.5°N. The inner domain consists of 121×121 grid points with 15 km horizontal resolution one-way nested within the coarser grid. The configuration of the model domains is presented in Fig. 1. It may be argued that the 15 km mesh is still too coarse to resolve the convective structure of the typhoon. However, it is worthwhile to evaluate the performance of the model using this resolution since the mesh ranging from 15 to 20 km is still widely used in limited area operational models.⁵ Lau *et al.*⁵ has successfully reproduced the development of the SCS typhoon Leo using a 18-km mesh. The topography data was taken from the U.S. Geological Survey 5-min resolution data set and interpolated onto the model grids using a Cressman type objective analysis scheme.⁸

The hydrological cycle includes the subgrid-scale convective parameterization of Kain–Fritsch scheme⁹ and a grid resolvable Schultz microphysics scheme by Schultz.¹⁰ The Blackadar parameterization scheme¹¹ is used to represent planetary boundary layer processes. The radiation scheme employed for current study is similar to that in CCM2.¹² The adapted model's physical options have been chosen in the process of numerous sensitivity tests. The global forcing fields are obtained from the NCEP global final analyses of $1^\circ \times 1^\circ$ longitude/latitude. The boundary condition during the model integration is updated every 12 h. The sea

surface temperature (SST) employed is taken from high resolution daily real-time global SST and is available on a grid with a resolution of $0.5^\circ \times 0.5^\circ$.¹³

In this study, the model outer domain is initialized at 00:00 UTC December 26, 2001 and integrated with a grid analysis nudging algorithm throughout the integration period. In this technique, an extra forcing term (known as the analysis-nudging term) is added to the dynamic equations of the model. The second domain is initialized 12 h later at 12:00 UTC December 26, 2001 with the initial and boundary conditions interpolated from the first domain. The 12-h nudging in the first domain allows the model to generate some small-scale features which are then used to initialize the inner domain. This process allows the inner domain to be initialized with a better initial field in the absence of an artificial vortex bogussing scheme. Subsequent analysis nudging processes ensured that the inner domain is forced by enhanced fields which are consistent to the global analyses. The inner domain is integrated for 36 h and the result is analyzed in this paper.

3. Results and Discussion

3.1. Model validation

In this section, the 36-h simulated fields from the inner domain (15 km) are compared to various observations. A comparison between the predicted and observed storm track and intensity revealed a reasonable accuracy of the simulation, especially considering that no initial bogus vortex was inserted during the model initialization. However, the track appears to be less consistent with observations during the initialization period with a slight deviation northward from the Joint Typhoon Warning Center's (JTWC) best track database (Fig. 2). Given that no vortex bogussing scheme was used to initialize the model, there were some uncertainties to the location and strength of the incipient cyclone when the simulation starts (Fig. 2). However, the error became progressively smaller as the system intensified and moved towards the southern tip of the Malay Peninsula. At 06:00 UTC December 27, 2001, several hours before landfall, the gaps between the JTWC's best track and the simulated track was about 60 km.

Figure 3 compares the simulated typhoon intensity to the JTWC's estimation. Both simulation and observation are in general agreement but differ in detail during the 36-h model integration. Initially, the deepening of the system was less prominent in the model simulation. The simulated

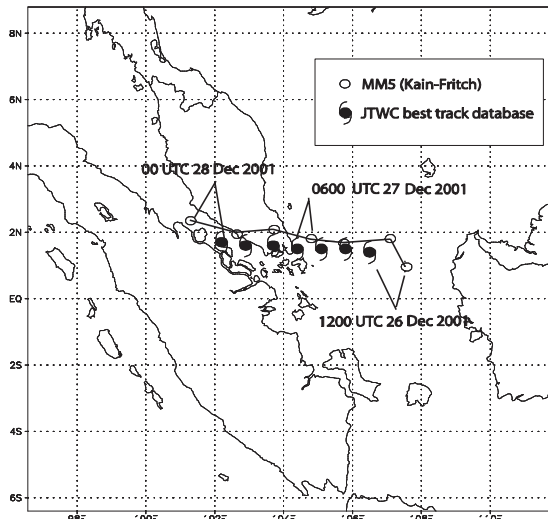


Fig. 2. The JTWC estimated (cyclone symbol) and simulated (solid line) propagation track of Vamei at every 6 h starting 12:00 UTC December 26, 2001. The simulated storm position is computed based on 850 hPa vorticity maxima.

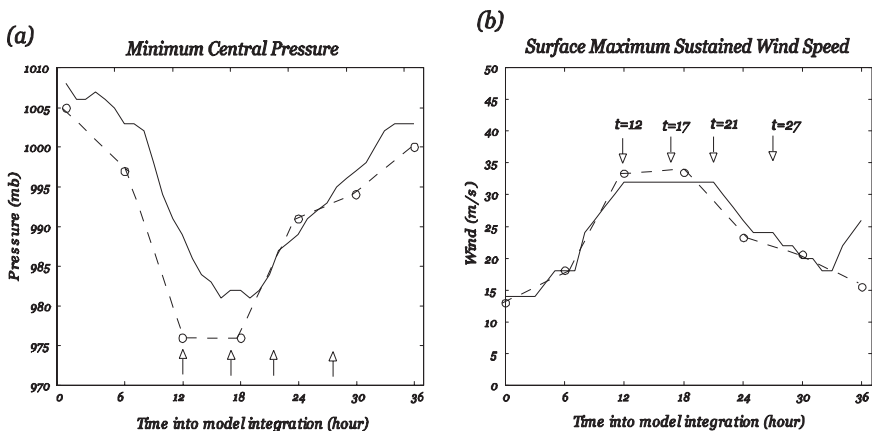


Fig. 3. The TRMM estimated (dashed) and the model simulated (solid) 36 h evolution of (a) minimum central pressure and (b) surface maximum sustained wind speed of Vamei. The arrows mark the times shown in Fig. 5.

cyclone deepened to a minimum central pressure (981 hPa) at around 15 h into model integration time or about 3 h later than observed. After reaching maximum intensity, the system approached land in the next 3–4 h and weakened rapidly. Nevertheless, the simulated intensity corresponds well

with observations during the weakening phase of the system. Consistent with the less accurately simulated storm track, notable differences in the minimum central pressure during the first half of the integration period could partly be due to the fact that there are some uncertainties in the initial condition that cannot be resolved without proper vortex bogussing schemes. However, a comparison between simulated and observed maximum sustained surface wind (Fig. 3b) suggests a more consistent and accurate reproduction of the surface wind characteristics. Based on observed and simulated maximum sustained winds, the system did indeed reached typhoon intensity for a brief period before landfall.

The quality of the simulation is further demonstrated by comparing the hydrometeor characteristics of the simulated storm to that captured by the satellite. Figure 4 (left panel) displays visible satellite imagery of the cloud at 04:00 UTC December 27, 2001, while Fig. 4 (right panel) shows a top view of the hydrometeor of the storm delineated by the 0.02 g kg^{-1} isosurfaces based on the sum of cloud water, ice, rain-water, snow, and graupel mixing ratios. It is interesting to see that there is a remarkable similarity between the simulated and observed storms in terms of general cloud distribution and the location of the system. Although it is not possible to predict the detailed distribution of convective cells along the spiral bands, the model does accurately simulate the cellular convection at the outer edge and the intense and organized (convective and stratiform) clouds in the eyewall.

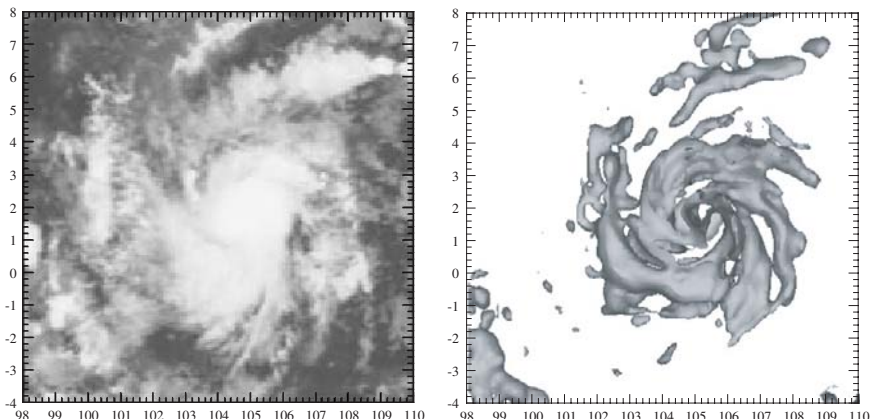


Fig. 4. (Left panel) Visible satellite imagery and (Right panel) top view of the model simulated hydrometeors, as determined by the 0.02 g kg^{-1} isosurface of five precipitation species (cloud, ice, rainwater, snow, and graupel) at 04:00 UTC December 27, 2001. Both panels cover the same area.

Both the model and the observations show the development of organized spiral cloud bands and a relatively dry zone to the southeast quadrant of the vortex. The simulation generally reproduced the storm with reasonable accuracy and the model output can be used for further diagnosis of the storm.

3.2. Horizontal structure

Figure 5 displays the surface wind barb at 12, 17, 21, and 27 h into the model integration, covering the rapid deepening, maximum intensity, landfall, and

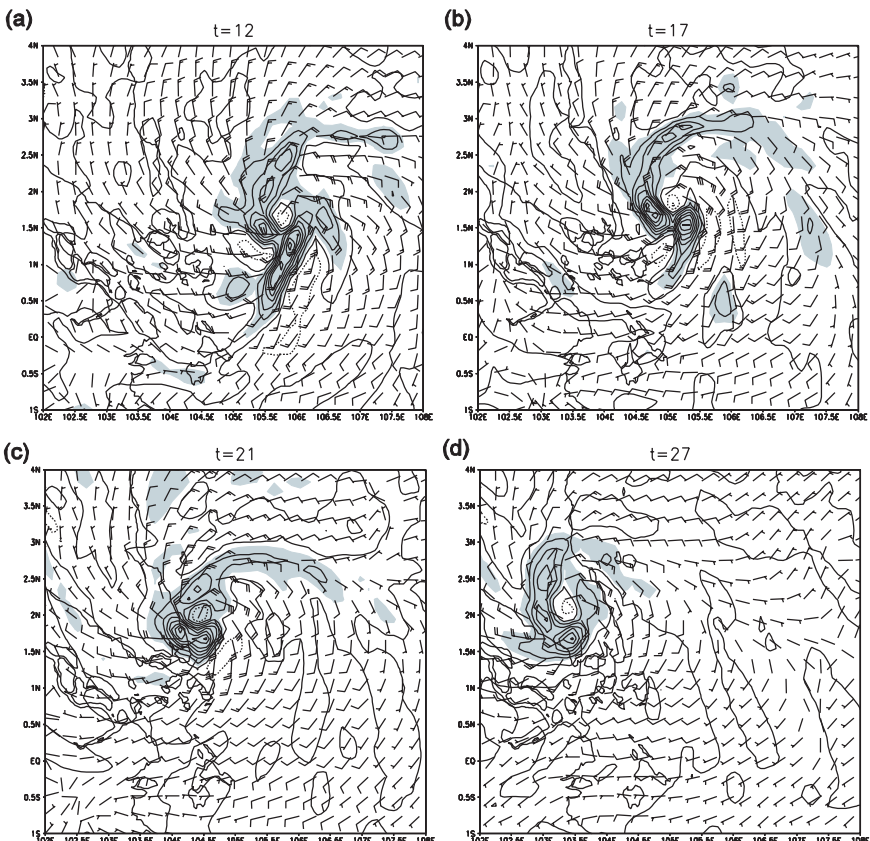


Fig. 5. The simulated surface wind (one full barb is 10 m s^{-1}) and the average low-level (1000–850 hPa) convergence field (contour) (unit: 10^{-5} s^{-1} , interval: $1 \times 10^{-5} \text{ s}^{-1}$) at (a) $t = 12$ h, (b) $t = 17$ h, (c) $t = 21$ h and (d) $t = 27$ h. Area of convergence greater than $1 \times 10^{-5} \text{ s}^{-1}$ is shaded.

the rapid weakening stages of the storm evolution. At 12 h into the model integration, a closed circulation has already developed. The spiral surface wind is at its maximum intensity at the southeast quadrant. The averaged (below 850 hPa) low-level convergence shows a closed convergence region suggesting that at this time the eyewall has appeared. Within this eyewall there exists an intense upward flow (Fig. 6). The largest vertical velocity is observed to the south of the vortex center coincident with the area of maximum low level convergence displayed in Fig. 5.

The system intensified and moved toward the coast at $t = 17$ h with the simulated cyclone showing distortion to its quasi-symmetric structure (Fig. 5b). The spiral band of the convergence zone to the southwest

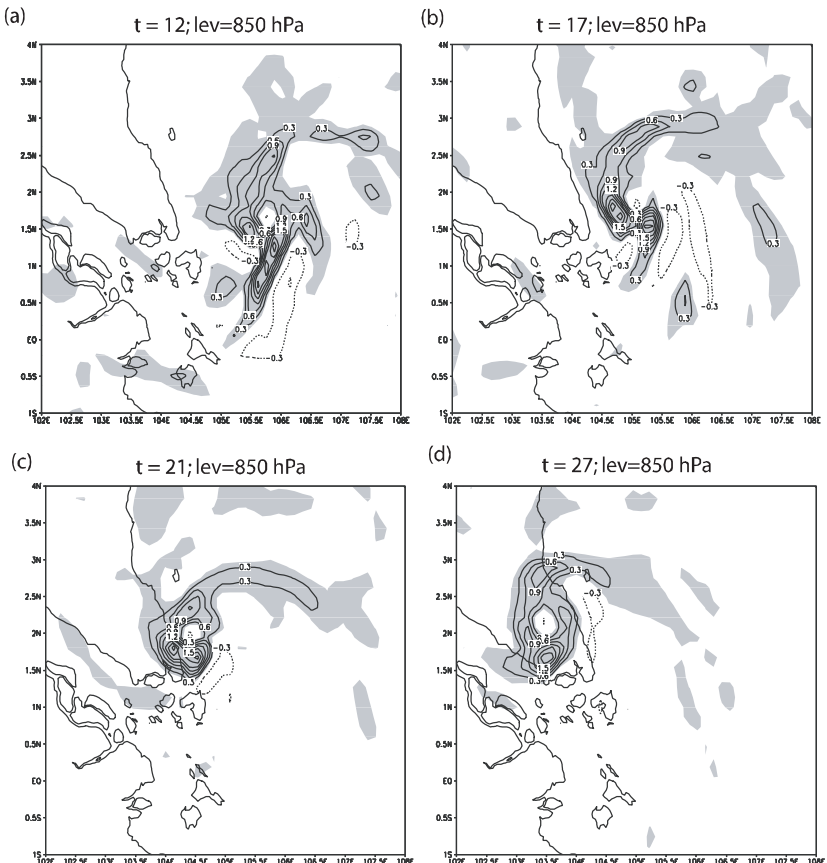


Fig. 6. As in Fig. 5 except for 850 hPa vertical velocity (m s^{-1}).

quadrant of the vortex contracted and the magnitude of the convergence field at this area increased dramatically. This is probably due to the increase of surface roughness and hence surface friction induced convergence as the system moved towards the coastline. The spiral convergence band to the north of the vortex remained strong. A few hours before landfall, during the rapid deepening of the system, conditions in which the distortion of typhoon structure becomes highly asymmetric are frequently reported.¹⁴ Over the southeast quadrant of the vortex, there exists an area of divergence which corresponds to the relatively dry zone shown in Fig. 4 (right panel) while the surface wind speed is at its maximum to the southwest quadrant of the vortex. Figure 7 shows the corresponding upper level divergence fields.

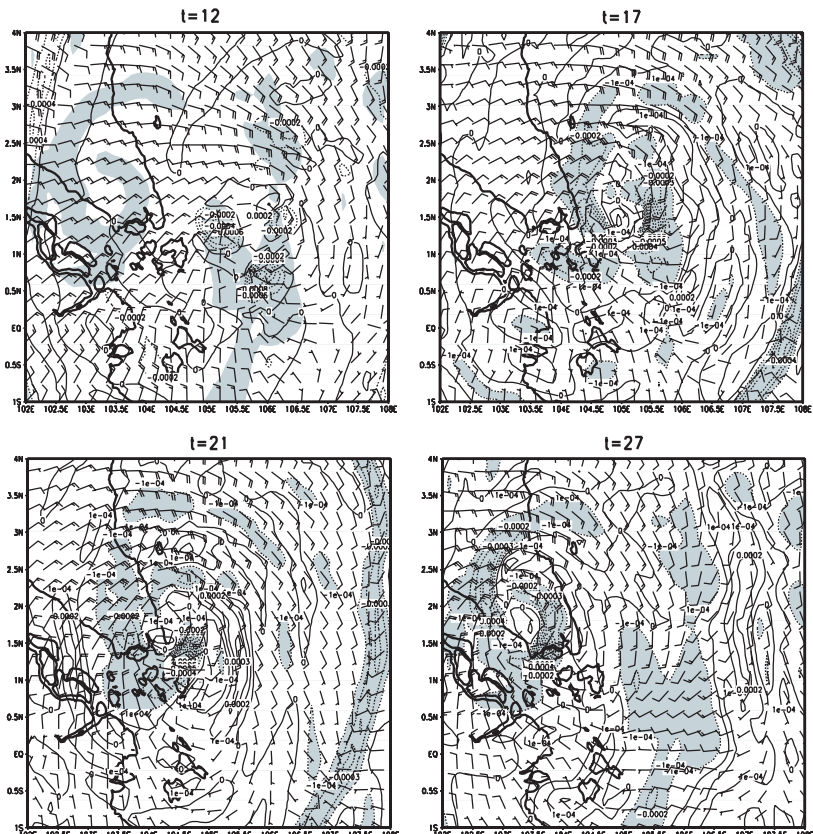


Fig. 7. As in Fig. 5 except for 200 hPa wind velocity (barb) and the convergence field. Area of divergence is shaded.

The maximum upper level divergence area is located in the east quadrant of the system. This situation allows latent heat to be released at the upper layer and subsequently increases the pressure gradient and the outflow of wind. The low convergence–upper level divergence coupling causes a steep increase in the vertical motion (Fig. 6b) to the south of the center.

At 21 h into the model integration, the center of the system was located over the eastern coast of the Malay Peninsula and the system started to weaken rapidly due to the land effect as it moved closer to the Malay Peninsula coastline. The low-level wind and convergence band shows a highly asymmetric characteristic. The strongest convergence is remarkably concentrated to the southern quadrant of the vortex (Fig. 5c). The wind was also at its highest speed at the southeastern and eastern quadrant of the vortex. The northern convergence band remained strong at this point of the model simulation. The upper-level outflow region is largely to the southwest of the center and this is associated with the area of maximum upward motion at 850 hPa. This area is associated with the maximum area of rainfall (figure not shown) together with a thick and wide cloud band as depicted in Fig. 4. The system filled up rapidly upon landfall. At 27 h into the integration, the center of the system was already located inland and the center pressure increased to ~ 993 hPa with the maximum sustained surface wind reduced to $\sim 23 \text{ m s}^{-1}$.

3.3. Vertical structure

The reasonable quality of the simulation enables further diagnosis of the vertical structure of the system. Figure 8 shows the east–west vertical cross-section of the equivalent potential temperature, θ_e at $t = 17$ h (representation of rapid intensification period). θ_e , which is a representation of the static energy of the air parcel is used to understand the thermodynamic structure of the simulated system. It is noted that the θ_e increased rapidly toward the center of the system resulting from the upward transfer of sensible and latent heat fluxes from the underlying warm ocean located east of the system. Over a distance of 80 km toward the center, θ_e increased by 25 K. According to the empirical estimation of hurricane intensity by Malkus and Riehl,¹⁵ using the equation of $P_{\min} = 1000 - 2.5(\max(\theta_e) - 350)$, the maximum intensity of the system, P_{\min} is expected to be 980 hPa. This value is very close to the simulated value of 981 hPa. On the other hand, it is observed that the intense vertical gradients of θ_e occurred

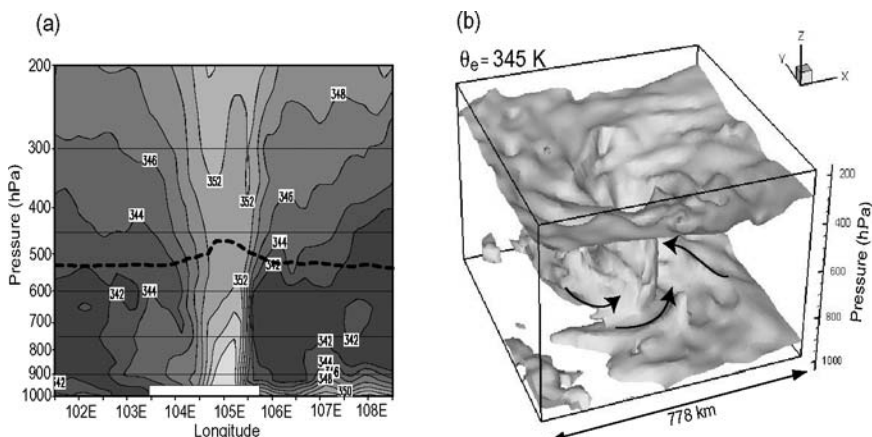


Fig. 8. East–west vertical cross-section at latitude 1.7°N of the (a) simulated equivalent potential temperature, θ_e across the vortex center at intervals of 2 K and (b) a 3D view of the $\theta_e = 245\text{ K}$ isosurface at 04:00 UTC December 27, 2001.

at the top of the maritime boundary layer to the east of the system, with minimum θ_e values near 700 hPa . Such strong vertical θ_e gradients indicate potentially unstable conditions for the development of deep convection and for the strengthening of the system. It is also noted that the central core is characterized by a high θ_e value that is extremely warm but dry as shown in Fig. 9. The lower θ_e air centered at 500 hPa in the system core is mainly due to its extreme dryness.⁴ The high- θ_e air above 450 hPa appears to descend from the upper troposphere, whereas below 800 hPa it is generated by the upward transport of surface fluxes. All these aspects are in good agreement with those revealed by aircraft observations as well as numerical simulations of other tropical cyclone.^{4,16,17}

A 3D view of the corresponding $\theta_e = 354\text{ K}$ isosurface clearly shows the distribution of various features associated with the eye, the eyewall and the spiral rainbands (Fig. 8b). In particular, it can be seen that the spiral bands attained high- θ_e air from the underlying sea to the east of the system and then transported it into a deeper layer as the bands rotate toward the eyewall. At some locations where deep convection is intense, penetrative high- θ_e columns between the surface and the tropopause formed, thereby transporting higher- θ_e air into the upper troposphere.

Figure 9(a–c) depicts the east–west vertical cross-section of different cloud microphysical quantities at latitude 1.7°N during the representative time of intensification period (04:00 UTC December 27, 2001). The 0°C

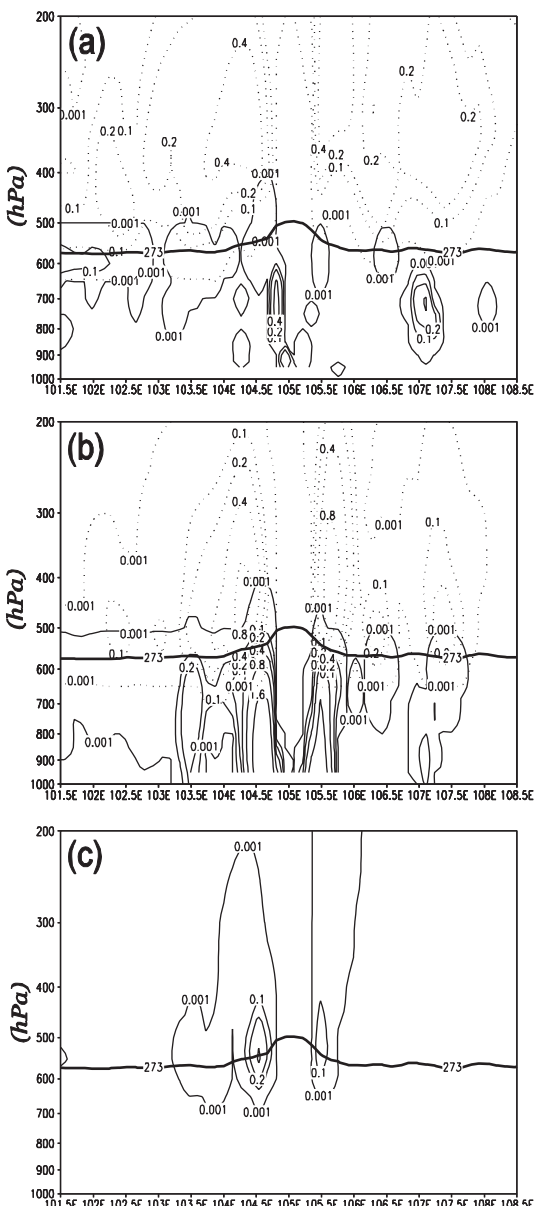


Fig. 9. As in Fig. 8(a) but for the mixing ratios of (a) cloud water/ice (solid/dashed), (b) rainwater/snow (solid/dashed), and (c) graupel at isopleth of 0.001, 0.1, 0.2, 0.4, 0.8, and 1.6 g kg⁻¹. Thick solid line denotes the distribution of 0°C isotherm.

isotherm which indicates the freezing/melting level is also plotted. It is noted that a high concentration of precipitation particles (solid and liquid) are located within the eyewall region and decrease toward the outer ring from the storm core. The distribution of the quantities appears asymmetrical with most of the particles concentrating toward the west of the system. In the center, the air column is dry and warm. Most of the cloud water developed near the 800 hPa level whereas high cloud ice is located at about 300 hPa. The snow which is associated with the cloud ice content tends to have a maximum quantity at about 400 hPa (Fig. 9b). The graupel which forms within the intense updrafts inside the eyewall has maximum values near the 0°C isotherm. Because of their relatively large size, graupel falls rapidly and tends to reside below the maximum level for snow. The graupel grows quickly as a result of repeated collection upon collision with liquid and small ice particles along its path. It then melts into rains and falls through the melting level.

Vamei deepened to typhoon intensity at about 15 h into the model integration within the inner domain and maintained its typhoon intensity for a very short period before filling up rapidly upon approaching the Malay Peninsula. To further our understanding on the cyclogenesis, we performed four sensitivity simulations in addition to the control run. These experiments are summarized in Table 1.

Figure 10 shows the central pressure of the simulated typhoon for various sensitivity experiments. As a comparison, the central pressure from

Table 1. Summary of experimental conditions.

| No. | Experiment Name | Description | Remark |
|-----|-----------------|--|-----------------|
| 1 | NOLHR | Same as the control run except that the latent heat is turned off for D2 during model integration | Mechanism study |
| 2 | NOSFCFLUX | Same as the control run except that the surface flux is turned off for D2 during the model integration | Mechanism study |
| 3 | NOSFCFRIC | Same as the control run except that the surface roughness length is set to 0.0002 m | Impact study |
| 4 | NOTERR | Same as the control run except that the terrain elevation in D2 is set to 0.1 m | Impact study |

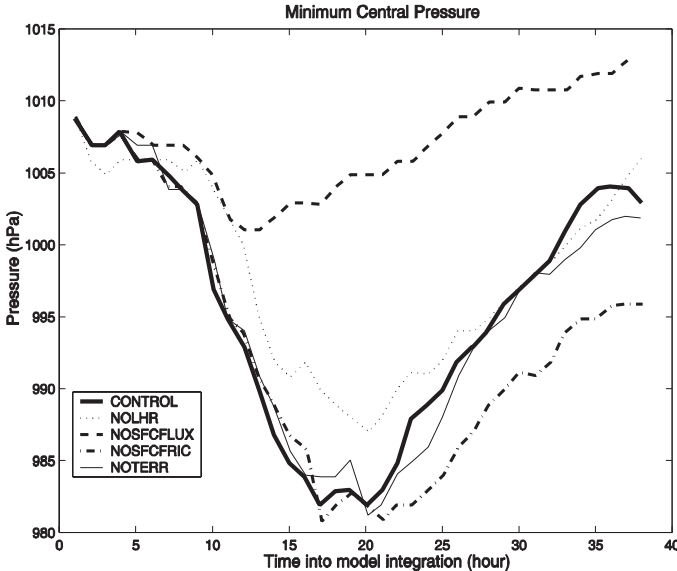


Fig. 10. The simulated minimum central pressure for various experiments. Also shown is the minimum central pressure curve for the control run.

the control run is also superimposed. Experiment NOSFCFLUX has much weaker cyclogenesis with minimum central pressure only reaching 1002 hPa. This result indicates that the removal of surface latent and sensible fluxes affects the intensification of the system more significantly compared to the other factors studied. This positive effect is in agreement with those described in Refs. 18 and 19. Surface fluxes are key to the provision of latent heat and the reduction of static stability.²⁰ Without the contribution of surface fluxes from the sea surface, the simulated system dissipated rapidly after model initialization. The fact that the evolution of Vamei is extremely sensitive to surface fluxes suggests that the simulation may depend critically on the options of PBL schemes. However, a discussion of this issue and its related mechanisms are beyond the scope of this paper and will be addressed elsewhere. Experiment NOLHHR also showed relatively weaker cyclogenesis. The deepening occurred slightly slower than that of the control run and the minimum central pressure reached only 987 hPa (about 5 hPa weaker than that of the control run). This result confirms that the release of latent heat in clouds contributes positively to the cyclogenesis and the results are in agreement with other investigations.^{18,21} For both the NOSFCFRIC and NOTERR experiments, the corresponding minimum central pressure

curves coincide well with that of the control run suggesting that the terrain and surface friction did not influence the deepening of typhoon Vamei.

However, as the system approaches the coastline 18 h into the model integration time, the effect of surface friction is clearly shown. In the control run, the system filled up rapidly after $t = 20$ h when the friction slowed the low level wind (not shown). In the NOSFCRIC experiment, where there was an absence of land surface friction, the system filled up rapidly after $t = 23$ h into model integration, i.e., 3 h later than that of the control run. On the other hand, experiment NOTERR suggests that the presence of mountains and an elevated orography do not have a positive effect on the cyclogenesis. However, the complex orography of the region can have an impact on the propagating track of the system (not shown).

4. Conclusion

The PSU/NCAR MM5 model successfully simulated the rapid deepening, maximum intensity, and rapid weakening upon landfall of the rare near-equatorial typhoon Vamei. The simulated track, minimum central pressure and maximum sustained surface wind compared favorably to the best analysis of JTWC. The simulated cloud distribution also matched very well with the satellite imagery. The ability of the model to produce a better simulation was due to better initialization of the inner domain through an analysis nudging algorithm.

The 36-h model integration clearly captured the evolutionary stages of rapid deepening, maximum intensity, landfall, and rapid weakening. The area of maximum wind speed and maximum upward motion was located to the south of the vortex center. The storm's eyewall formed during an earlier integration with the convergence zone showing quasi-symmetric properties. As the storm strengthened, the vortex became highly axisymmetric with contracted zones of high low level convergence and upward vertical motion to the south of the vortex center. A spiral band of convergence zone persisted in the northern quadrant during rapid intensification and landfall of the storm. As the storm moved closer to the coastline, these features became more apparent. The upper levels showed a strengthening of the outflow wind during the intensification period.

Both the observed and simulated maximum sustained wind speeds indicated that the system did indeed reached typhoon intensity for a brief period before landfall. During the real-time forecasting operation, there

were inconsistencies in the assessment of the peak intensity of Vamei between various operational agencies. JWTC classified Vamei during its peak as a typhoon while JMA categorized it as a tropical storm. Also, warnings issued by the Meteorological Services of Singapore (MSS) at 03:00 UTC December 27 and by the Malaysian Meteorological Services (MMS) at 00:00 UTC December 27 referred to the system as a tropical depression. However, direct Naval ship reports recorded maximum sustained surface winds of 39 m s^{-1} and gust wind of up to 54 m s^{-1} suggesting that the system had actually reached typhoon intensity.¹ The simulation of Vamei's strength in this study supports JTWC's assessment that the system did indeed reach typhoon strength before landfall.

The MM5 model also simulated the thermodynamic and precipitation structures of Vamei reasonably well during its maximum intensity. The east–west vertical cross-section of θ_e through the center of the vortex clearly showed the structure of the central core of high θ_e values, i.e., warm and dry. The 3D structure of the system based on the corresponding $\theta_e = 354\text{ K}$ isosurface clearly showed the eye, eyewall, and the spiral rainbands. This simulated structure is consistent with the observation that this equatorial system is a typhoon.

Conducted sensitivity experiments indicated that both surface heat fluxes and latent heat release have positive effects on the cyclogenesis although the contribution of surface heat fluxes appears to be more crucial. However, both land surface friction and the presence of mountains and elevated orography appear to have a minimal effect on the cyclogenesis. Reducing the surface friction appears to prolong the life of the system in typhoon intensity while the presence of mountains and elevated orography can have effects on the trajectory of the system.

Acknowledgments

This research was funded by the Malaysian Ministry of Science and Technology IRPA Grant 08-02-02-0012-EA215.

References

1. C. P. Chang, C. H. Liu and H. C. Kuo, *Geophys. Res. Lett.* **30** (2003) 1150.
2. C. P. Chang, P. A. Harr and H. J. Chen, *Mon. Wea. Rev.* **133** (2005) 489.
3. G. A. Grell, J. Dudhia and G. R. Stauffer, *NCAR Tech Note NCAR/TN-398 + STR*, (1994), 138 pp.

4. Y. Liu, D. L. Zhang and M. K. Yau, *Mon. Wea. Rev.* **125** (1997) 3073.
5. K. H. Lau, Z. F. Zhang, H. Y. Lam and S. J. Chen, *Meteorol. Atmos. Phys.* **83** (2003) 147.
6. L. Farfán and J. A. Zehnder, *Mon. Wea. Rev.* **129** (2001) 2073.
7. U. C. Mohanty, M. Mandal and S. Raman, *Natural Hazards* **31**, 373 (2004).
8. G. P. Cressman, *Mon. Wea. Rev.* **87** (1959) 367.
9. J. S. Kain and J. M. Fritsch, *Meteor Monogr., Amer. Metro. Soc.* **46** (1993) 165.
10. P. Schultz, *Mon. Wea. Rev.* **123** (1995) 3331.
11. D. L. Zhang and R. A. Anthes, *J. Appl. Meteorol.* **21** (1982) 1594.
12. J. T. Kiehl, J. J. Hack, G. B. Bonan, B. A. Boville, B. L. Williamson and P. J. Rasch, *J. Clim.* **11**(6)(1998) 1131.
13. J. Thiébaux, E. Rogers, W. Wang and B. Katz, *Bull. Amer. Met. Soc.* **84** (2003) 645.
14. J. C. L. Chan and X. Liang, *J. Atmos. Sci.* **60** (2003) 1560.
15. J. S. Malkus and H. Riehl, *Tellus* **12** (1960) 1.
16. H. F. Hawkins and A. M. Imbembo, *Mon. Wea. Rev.* **104** (1976) 418.
17. D. P. Jorgensen, *J. Atmos. Sci.* **41** (1984) 1268.
18. S. W. Chang, T. R. Holt and K. D. Sashegyi, *Mon. Wea. Rev.* **124** (1996) 27.
19. C. A. Davis and K. A. Emanuel, *Mon. Wea. Rev.* **116** (1988) 2469.
20. K. A. Emanuel, *J. Atmos. Sci.* **43** (1986) 585.
21. W. M. Lapenta and N. L. Seaman, *Mon. Wea. Rev.* **120** (1992) 52.

This page intentionally left blank

INFLUENCES OF SECONDARY CHEMICAL GAS PROCESSES ON PM₁₀, PM_{2.5} AND PM₁ CONCENTRATIONS OVER THE KOREAN COAST

Hyo Choi*,† and Milton S. Speer‡,§

†*Department of Atmospheric Environmental Sciences*

Kangnung National University, Kangnung, Korea

‡*Climate and Environmental Dynamics Laboratory*

School of Mathematics and Statistics

The University of New South Wales, Sydney, NSW

Australia

**dus8392@hanmail.net*

§*mss@maths.unsw.edu.au*

An aerosol sampler was installed at Kangnung city in the east coast of Korea to measure mass concentrations of PM₁₀, PM_{2.5}, and PM₁ covering particle diameter sizes ranging from 300 nm to 20 μm from February 14 to 16, 2005. The concentrations of PM₁₀, PM_{2.5}, and PM₁ showed a high morning (09:00 LST) and afternoon (17:00 LST) concentration and a low concentration around midday (12:00 LST). First maximum concentrations of PM₁₀, PM_{2.5}, and PM₁ occurred at 20:00 LST. Secondary maximum concentrations were detected at 01:00 LST, February 15. The distribution of CO and NO_x concentrations showed a similar diurnal distribution to those of PM₁₀, PM_{2.5}, and PM₁, except for the morning of February 14. The first and secondary maximum concentrations of NO_x occurred at the same times as those of PM₁₀, PM_{2.5}, and PM₁. This implies that the increase in NO_x and CO emissions from road vehicles and combustion gases from boilers in residential areas can contribute substantially to the increase in PM concentration. As a result of a typical daytime westerly wind regime over Korea, the rotor action of a lee-side easterly breeze transports PM from Kangnung toward the mountains, which is then recycled toward Kangnung in the westerly airflow at night. Some PM from Wonju city upwind on the western side can also contribute significantly to the secondary maximum at Kangnung city on the eastern or lee side.

1. Introduction

Recently, there has been a research focus on fundamental aspects of aerosol science.^{1–4} Gao and Anderson⁵ investigated characteristics of Chinese aerosols determined by individual particle analysis, where most

measurements of aerosol size were determined by laser technology. Adby and Demster⁶ developed an algorithm as a dependent method while Hansen⁷ and Hansen and O'Leary⁸ utilized the independent L-curve approach. Goldberg,⁹ Michelewicz¹⁰ and Xu *et al.*⁴ applied a genetic algorithm to treat the optimization problem of particle size distribution quite differently from data of multi-spectral extinction measurements.

During the Asian Dust season (Spring) in 2001, the factors of TSP, PM₁₀ and PM_{2.5} affecting the cycle of aerosols and their chemical properties and composition were investigated in the Seoul district of Korea.¹ Also, since 2001, comprehensive studies of particulates and gases at many measurement points in China, Korea and Japan have been carried out.^{11,12} In Korea, routine measurement of aerosols has been established at Gosan, Jeju island and Taean peninsula on the western side of the Korean peninsula by the Korean Meteorological Administration, but the measurement focus has centered on the mass concentration of TSP and PM₁₀ and their chemical composition, while notably excluding the critical PM₁ group. Furthermore, that research does not include particle size distribution of aerosols and the relationship between mass concentration and particle size distribution.

Thus, the objective of this study was to explain the diurnal variation of aerosol concentrations around Kangnung in eastern Korea of not only PM₁₀ and PM_{2.5}, but also PM₁, which greatly influences the effects of local pollution on human health. The 2-day sampling period of February 14 and 15, 2005 includes dust transported downstream from China in a typical spring synoptic scale westerly wind regime. In Sec. 2, the instruments and experiment are outlined including a brief description of the study area topography. A synoptic overview of the meteorology of the 2-day period then follows in Sec. 3. The measurement results are presented and discussed in Sec. 4 followed by the conclusions in Sec. 5.

2. Methodology and Data

2.1. Instruments and experiment

GRIMM sequential mobility particle sizer and counters (Model 1108), was installed at the Gangwon Meteorological Administration office at Kangnung city ($37^{\circ}45'N$, $128^{\circ}54'E$), which is located on the eastern side of the mountainous coastal region of the Korean peninsula. Aerosol particle size distributions ranging from $300\text{ }\mu\text{m}$ to $20\text{ }\mu\text{m}$ and collection of all three

fractions of PM₁₀, PM_{2.5}, and PM₁ were measured by the two aerosol samplers from February 13 to 17, 2005, which included both dust in Korea emanating from dust storms further upstream in China, and also, non-duststorm conditions in Korea.

The sampler is specifically designed for PM₁₀, PM_{2.5}, and PM₁ ambient environmental air analysis using laser light scattering technology. It enables very precise diameter ranges to be determined for all three PM size classifications. The system allows the user to collect all three PM fractions simultaneously without changing sampling heads or weighing filters. Moreover, the 1107 sampler is the only PM instrument monitor to offer dual technology consisting of both optical and gravimetric analysis. It incorporates a removable 47 mm PTFE filter, which allows the user to verify the optical analysis gravimetrically, as well as providing the option for other chemical analyses on the collected residue. It was developed for particulate measurements via 900 laser light scattering and with multiple particle size passes through a flat laser beam produced by a precisely focused laser and several collimator lenses.

The scattered light is detected by a 15-channel pulse height analyzer which is used for size classification. The counts from each size classification are converted to mass by a well established equation. The complete system consists of 165 fiberglass housing, drying temperature control system, 1107 PM dust monitor, sensors for humidity and temperature and 170M sampling system. Real-time data displays of PM₁ and PM_{2.5} and even PM₁ are sampled as often as every 6 s.

The sensitivity of the system is as low as 0.01 $\mu\text{g}/\text{m}^3$ and it can be operated directly as a stand-alone system in the field. The purpose of the 1108 sampler is to count the number of particles from 300 \AA to 20 μm and collect all three fractions of PM₁₀, PM_{2.5}, and PM₁. The Model 1108 different from the Model 1107 is able to count the number of particles from 300 \AA to 20 μm and collect all three PM fraction of PM₁₀, PM_{2.5}, and PM₁.

2.2. Topography in study area and model domain

The study area is located in the mountainous coastal region of eastern Korea (Figs. 1 and 2). The two GRIMM aerosol samplers (Models 1107 and 1108) were installed at Gangwon Meteorological Administration Office in Kangnung city, which is situated adjacent to the East Sea.

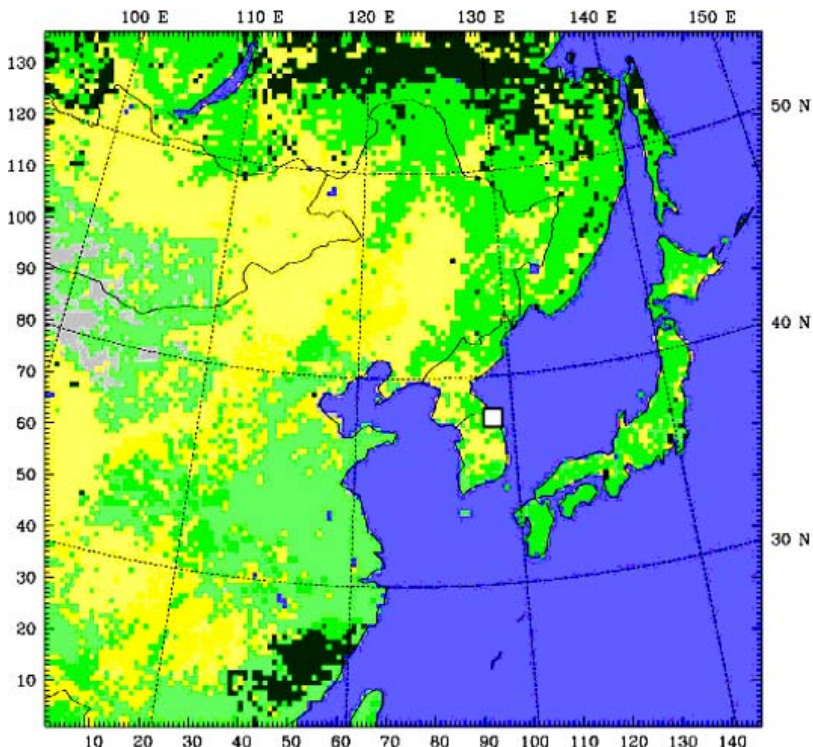


Fig. 1. Map of northeast Asia highlighting land-use data (horizontal resolution 27 km) and the inset box denotes the study area including Kangnung city, Korea.

A horizontal grid interval of 2.5° was used for the largest model domain and simulated streamline and other output obtained from a three-dimensional numerical model called MM5 and 3 km for the fine mesh domain.

3. Synoptic Overview

At 09:00 LST (00:00 UTC), February 14, 2005, high pressure with a central value of 1033 hPa was located over the northern part of the Korean peninsula and another high (1031 hPa) was located over central Japan. Between the two high pressure systems, a weak low-pressure (1028 hPa) was located to the north of Kangnung city over the East Sea (Fig. 3a).

The wind direction observed at the Gangwon Meteorological Administration office was southwesterly due to the influence of the low

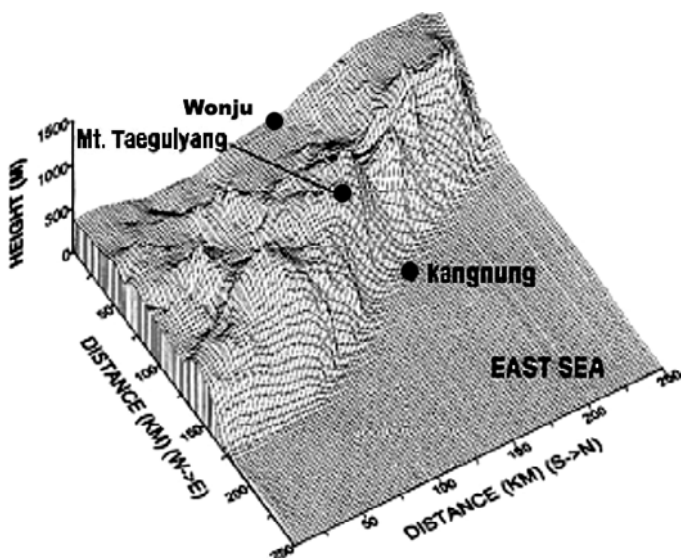


Fig. 2. Map of study area near Kangnung in eastern Korea highlighting topography surrounding Kangnung (horizontal resolution 5 km) and place names mentioned in the text. Kangnung city and Mt. Taegulyang are 20 and 860 m above mean sea level, respectively. Actual north is in 90° left from topographical north in figure.

pressure system, although a northeasterly breeze was evident from 10:00 to 17:00 LST. At 21:00 LST (12:00 UTC), the low pressure centre had strengthened slightly to a value of 1025 hPa and the southern portion of a cold front had edged eastwards while the northern section of the cold front had rotated (anti-clockwise) slightly westwards. A southwesterly wind prevailed at Kangnung city until 09:00 LST, February 15 (Fig. 3b).

From that time, both a high pressure system (1038 hPa) located over Manchuria in China and northern Korea and another low pressure center (1013 hPa) located over the southeastern part of China controlled the synoptic weather pattern. The local observed wind direction until 14:00 LST was northeasterly, thereby providing moisture advection from the sea over inland areas. After 14:00 LST, the wind direction changed to southwesterly until 18:00 LST (Fig. 4a).

At 21:00 LST, February 15, the high and low pressure systems moved further toward the east, with the high pressure center (1043 hPa) located near Vladivostok, Russia and the strengthened low pressure (1010 hPa) now centered over the Yellow Sea near the southwestern side of the Korean peninsula (Fig. 4b). This synoptic scale pressure pattern over the

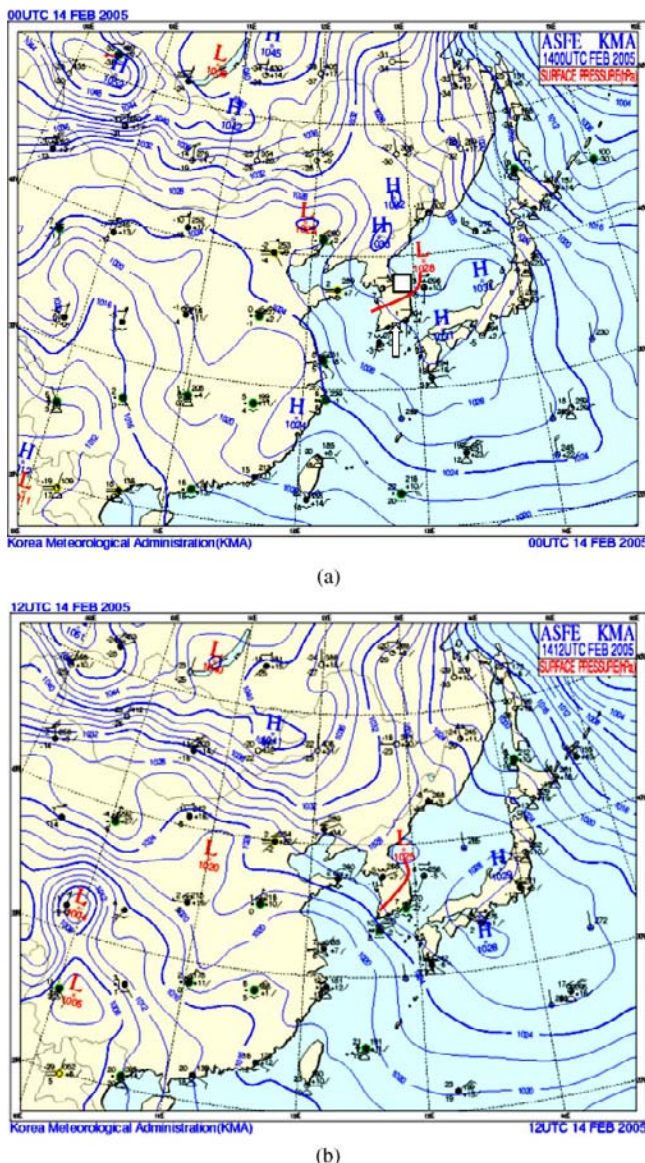


Fig. 3. Weather charts on February 14, 2005 for (a) 09:00 LST and (b) 21:00 LST. The arrow, square, and curved line below the square indicate the Korean peninsula, the study area including Kangnung city, and the cold front, respectively.

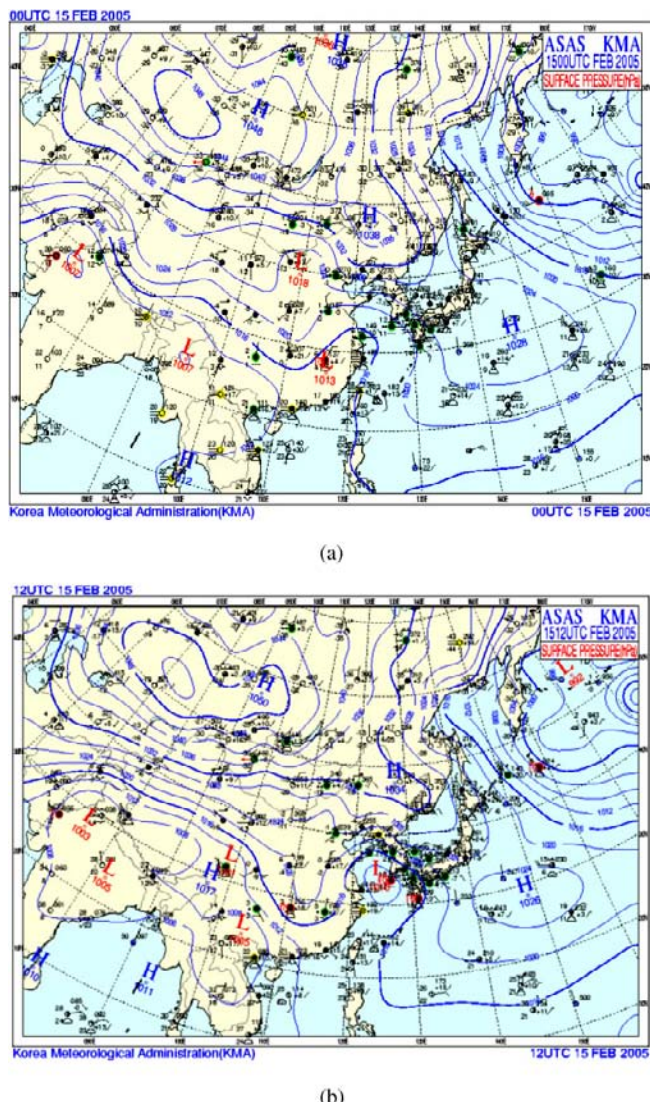


Fig. 4. (a) As in Fig. 2, except for 09:00 LST and (b) 2100 LST, February 15.

topography of the Korean peninsula strongly influences the development of a northeasterly rotor circulation over the coast near Kangnung in the lee of the mountains. Moisture advection from the East Sea, as a result of the northeasterly wind, and subsequent cloud formation, was responsible for a total of 6.5 mm of rainfall at Kangnung city.

4. Result and Discussion

4.1. Aerosol mass concentration

From the 1107 sampler, the distribution of 10-min averaged mass concentration of PM₁₀, PM_{2.5} and PM₁ near the ground at the Kangnung site is shown in Fig. 5. From 00:00 LST February 14 until 00:00 LST, February 15, the mass concentration of PM₁₀ was within the range 50.62–145.12 µg/m³, with the maximum concentration of 145.12 µg/m³ at 14:20 LST occurring after passage of the cold front.

The concentrations of PM_{2.5} and PM₁ had similar variations to PM₁₀. Their concentrations were in the range 15.14–56.19 µg/m³ for PM_{2.5} and 10.73–44.71 µg/m³ for PM₁. From 00:00 LST, February 14, the concentrations of PM₁₀, PM_{2.5}, and PM₁ remained almost unchanged until 17:00 LST, just before peak-hour traffic and near sunset.

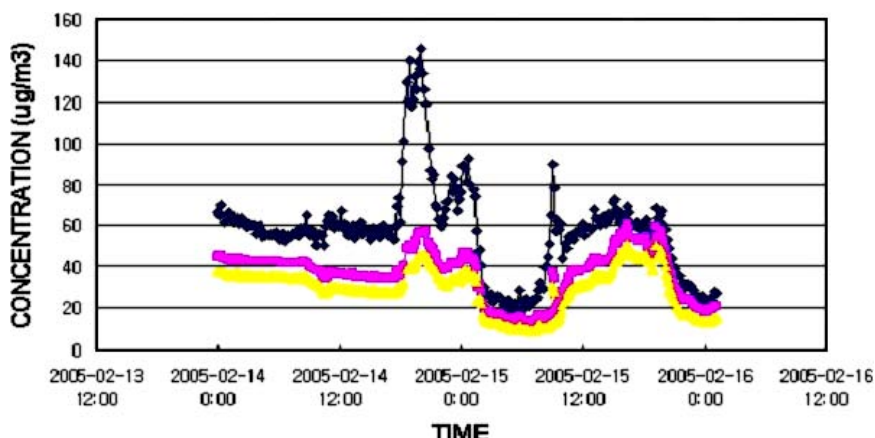


Fig. 5. Hourly concentrations (µg/m³) of PM₁₀ (blue), PM_{2.5} (pink) and PM₁ (yellow) at Gangwon Meteorological Administration Office in Kangnung city from February 14 to 16, 2005.

After 18:00 LST with peak hour traffic increasing, the concentration of aerosols rapidly increased to $145.12 \mu\text{g}/\text{m}^3$ for PM₁₀, $58.93 \mu\text{g}/\text{m}^3$ for PM_{2.5} and $44.71 \mu\text{g}/\text{m}^3$ for PM₁ by 20:00 LST which is about 2 h after sunset. The PM₁₀ concentration decreased to $59.78 \mu\text{g}/\text{m}^3$ at 22:00 LST, February 14, and then increased again to $93.06 \mu\text{g}/\text{m}^3$ at 01:00 LST, February 15. Thus, two maximum concentrations of PM₁₀, PM_{2.5}, and PM₁ were detected with their first maximum at 20:00 LST, February 14 and a secondary maximum at 01:00 LST February 15.

After 01:00 LST, the PM₁₀ concentration continued to decrease to $19.32 \mu\text{g}/\text{m}^3$ by 06:00 LST. A relatively moderate southwest wind in the range from 2.9 to 4.7 m/s occurred at Kangnung city until 10:00 LST. Then the wind speed decreased to less than 2 m/s and the wind direction changed to northeasterly between 11:00 and 17:00 LST, due to the passage of the cold front and easterly sea breeze directed toward Kangnung city. Relative humidity values remained low at below 38%.

The maximum concentration of PM at 20:00 LST, February 14 is most likely due to the increase in vehicle numbers on the roads after office hours. A secondary reason might be as a result of the nocturnal surface inversion layer (NSIL) forming due to the cooling of the surface at night, compared to the depth of the daytime convective boundary layer (CBL) over the city.¹⁴

Choi,¹³ Choi *et al.*,¹⁴ and Choi and Speer¹⁵ indicated that in general, PM generated from industrial and vehicular emissions in the city of Kangnung drifts from the surface to the lower troposphere due to thermal convection and is transported from Kangnung city which is located near the coast, toward Mt. Taegulyang to the west under the influence of an easterly sea-breeze and valley wind until sunset. There, the PM is trapped under a temperature inversion close to the mountain slope.

After sunset, a strengthening downslope wind, reinforced by a katabatic wind and land breeze drives the PM back down the eastern slope of Mt. Taegulyang toward Kangnung city, resulting in a high concentration of particulates around midnight. With a reduction in vehicle numbers after peak hour traffic the PM concentrations also decrease during the night. Thus, a secondary maximum in PM concentration at night is most likely produced by the shallow NSIL and the recycling of some PM from the mountain slope toward the city.

After midnight, PM concentrations rapidly decrease throughout the morning until 09:00 LST, February 15 as most of the PM in Kangnung city has become dispersed over the East Sea. As a result, Kangnung city by this

time is relatively free of PM with values less than $30 \mu\text{g}/\text{m}^3$. The relatively high concentration of PM during the morning of February 14 can most likely be attributed to the transport of some PM from the upwind side of the mountains, where Wonju city is located. The maximum concentration of PM_{10} at 20:00 LST on February 14 also coincided with the maximum concentrations of both $\text{PM}_{2.5}$ and PM_1 .

It is postulated that the gas phases of $\text{PM}_{2.5}$ and PM_1 can contribute significantly to the increase in PM_{10} concentration. Therefore, it is necessary to compare the gas concentrations of CO, NO_x ($= \text{NO}_2 + \text{NO}$) and O_x ($= \text{O}_3 + \text{NO}_2$) at the Kangnung Environmental Monitoring Site, established by Institute of Health and Environment, from February 14 to 16, 2005 (Fig. 6). The CO concentration closely matches that of PM_{10} , $\text{PM}_{2.5}$ and PM_1 . The distribution of NO_x concentration is similar to that of CO, except for the morning of February 14.

When PM_{10} , $\text{PM}_{2.5}$ and PM_1 had their first and secondary maximum concentrations, NO_x also had its first and secondary maximum concentrations, namely, at 20:00 LST on February 14 and 01:00 LST on February 15. This means that NO_x and CO gases resulting from vehicle emissions due to fuel combustion and from boilers in resident areas can contribute significantly to the increase in PM_{10} . O_x is composed with $\text{O}_3 + \text{NO}_2$ and is assumed as permanent capacity of O_3 . O_x concentrations are generally within the range 39–62 ppb, except for 30 ppb on February 15,

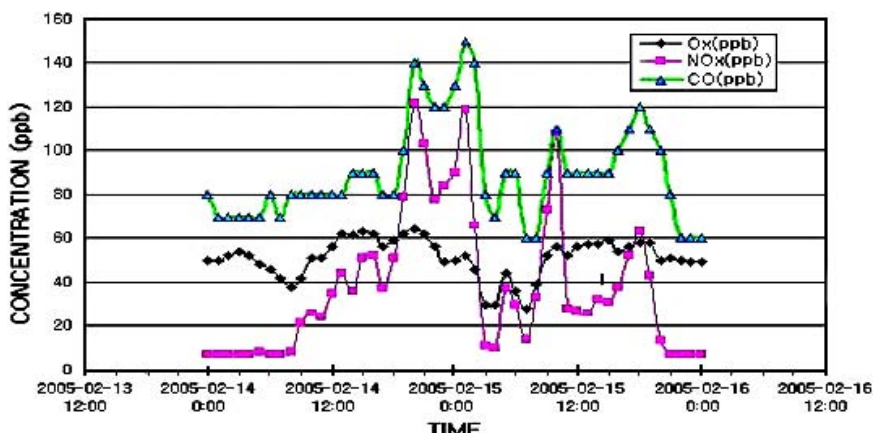


Fig. 6. As in Fig. 5, except for hourly concentrations (ppb) of CO, NO_x (from $\text{NO}_2 + \text{NO}$) and O_x (from $\text{O}_3 + \text{NO}_2$).

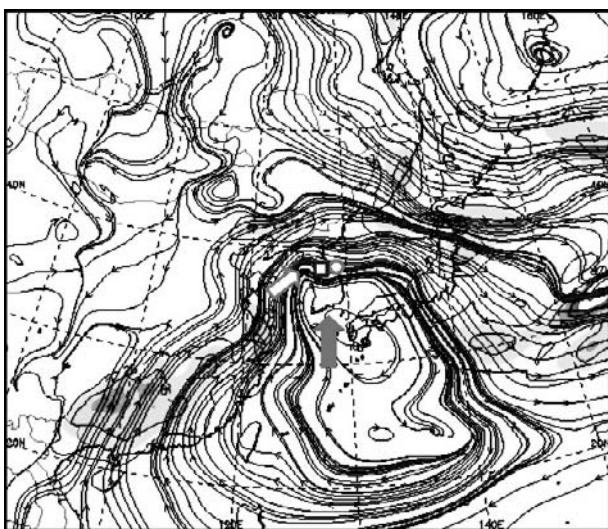
when NO_x concentrations were very low. The distribution of O_x did not reflect the distribution characteristics of CO or NO_x .

4.2. Effect of upwind PM transport

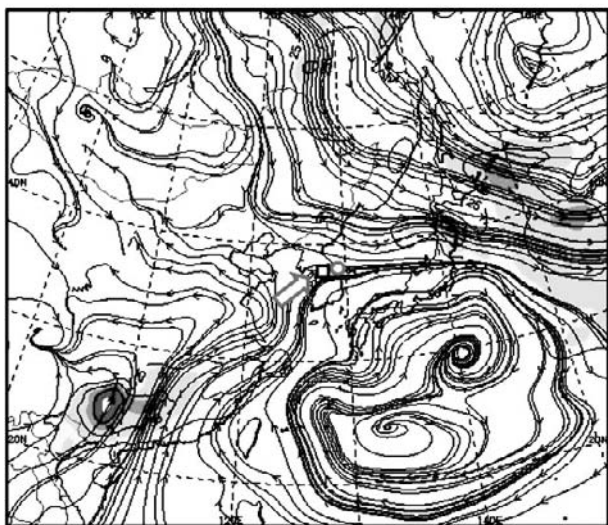
Further consideration was given to the transportation of particulate matter and gases from Wonju city, which is located in the west of Kangnung city (Fig. 2). Figure 7a, b shows streamline output simulated by MM5 (version 3.7), using a horizontal grid spacing of 2.5° at 12 h intervals from 09:00 LST, February 14 to 21:00 LST, February 15. Mass transport occurred from Wonju city downwind toward Kangnung city at 09:00 LST and 21:00 LST, February 14. However, on February 15, Kangnung city was no longer on the downwind side (i.e., upwind side) according to the streamline output, as revealed in Fig. 8a, b.

Only PM_{10} concentration could be measured at Wonju city, due to official PM_{10} measurement and the values ranged from 92 to $136 \mu\text{g}/\text{m}^3$ between 00:00 LST and 19:00 LST (Fig. 9).¹⁶ The PM_{10} concentration at Kangnung city, about 200 km east of Wonju city was approximately $60 \mu\text{g}/\text{m}^3$, or about half the concentration showing at Wonju city. Since the two cities were experiencing westerly and southwesterly winds over this period on February 14, as indicated by the streamlines, the occurrence of high PM concentrations downwind at Kangnung city should be influenced by the transport of some PM from Wonju city, resulting in the PM_{10} concentration of approximately $60 \mu\text{g}/\text{m}^3$.

The concentrations of CO, NO_x and O_x at Wonju are shown in Fig. 10. The NO_x concentration at Wonju city (located on the upwind side on February 14), can influence the amount of NO_x concentration transported to Kangnung city and was generally higher than at Kangnung city. At Kangnung, the NO_x concentration rapidly increased to a value of 108 ppb and then to 163 ppb at 21:00 LST. Even though transport of NO_x from Wonju toward Kangnung over this period could be expected, the amount of NO_x actually transported did not contribute significantly to the occurrence of a maximum concentration of NO_x downwind at Kangnung at 20:00 LST on February 14. However, the transported NO_x might partially contribute to the occurrence of the secondary NO_x maximum at 01:00 LST, February 15. Generally, NO_x concentrations at Kangnung city are known to be very low, but when transport occurs under the influence of a strong westerly wind regime, its concentration increases as noted previously.¹³



(a)



(b)

Fig. 7. Streamlines in northeast Asia simulated by MM5 on February 14 at (a) 09:00 LST; big gray arrow (solid) and small black square (open) in the central part of map denotes Korean peninsula and Wonju city; gray circle (open) denotes Kangnung city and gray arrow (open) denotes upwind side. (b) At 21:00 LST.

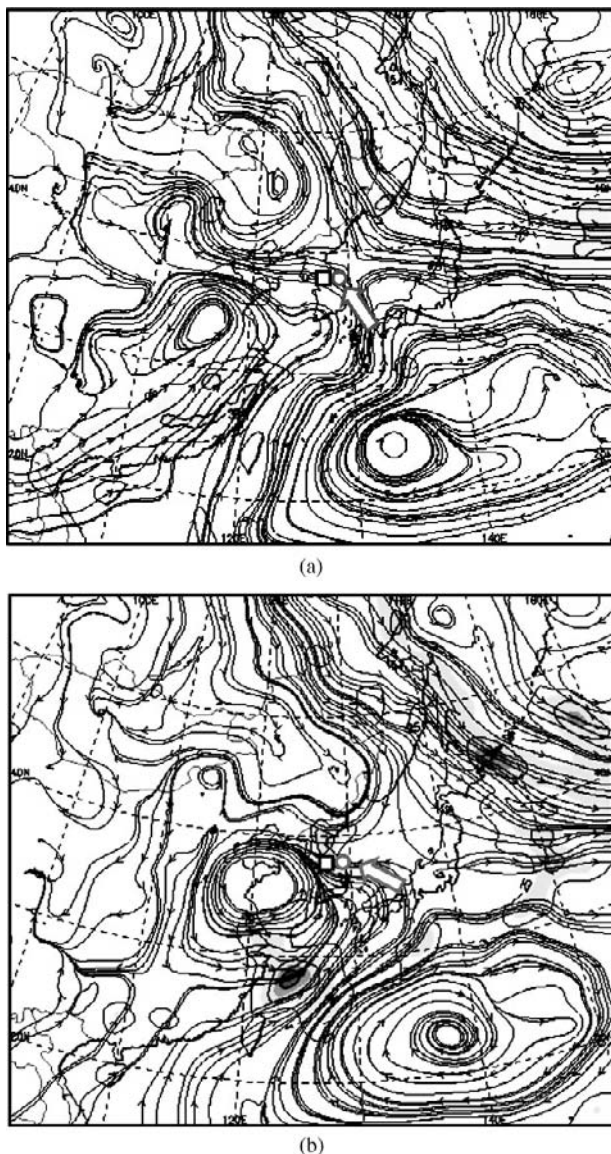


Fig. 8. As in Fig.7, except for (a) 09:00 LST on February 15 and (b) 21:00 LST. Gray arrow (open) denotes upwind side, which has opposite direction to February 14.

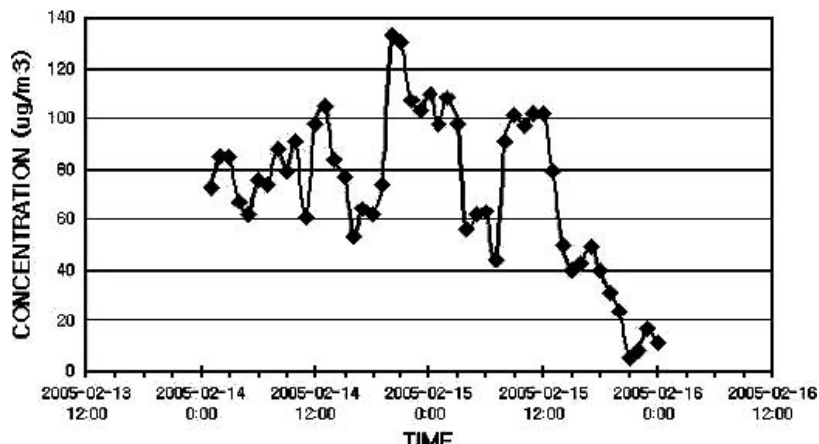


Fig. 9. Hourly concentrations ($\mu\text{g}/\text{m}^3$) of PM₁₀ at environmental site, Wonju city on the upwind side of Kangnung city on February 14, 2005, but the downwind side on 15.

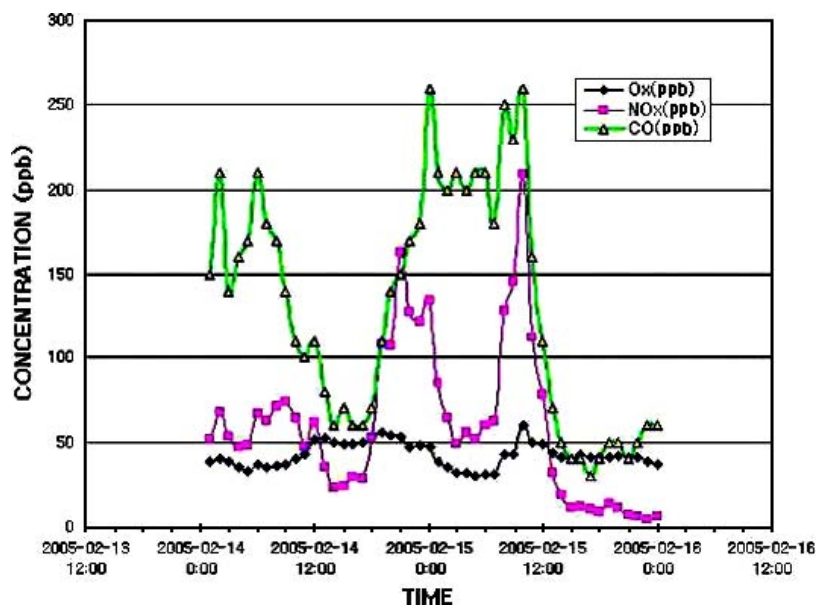


Fig. 10. (a) As in Fig. 9, except Wonju city in the west of Kangnung city.

5. Conclusions

At Kangnung city on the east coast of Korea, diurnal concentrations of PM₁₀, PM_{2.5}, and PM₁ measured over a 4-day period were presented for the two days, February 14 and 15, 2005. The concentrations showed variations consistent with high values around 09:00 LST (within morning peak hour traffic period) and 17:00 LST (within evening peak hour traffic period) and low values near midday. PM₁₀, PM_{2.5} and PM₁ all had their primary maximum concentration at 20:00 LST (about 3 h after sunset) and a secondary maximum concentration at 01:00 LST (just after midnight). When PM₁₀, PM_{2.5} and PM₁ had both their primary and secondary maximum concentrations, NO_x also had a primary and secondary maximum concentration.

The increase in NO_x and CO concentrations resulting from vehicle emissions and combustion gases from residential boilers at night can contribute significantly to the increase in PM concentration. Furthermore, a much shallower NSIL than the daytime CBL can also contribute to an increase in PM concentration. PM concentration decreases after midnight due to the reduction in vehicle numbers on the roads. However, under the influence of a westerly wind regime and resulting easterly rotor effect through Kangnung, the PM that is transported in the return easterly flow from Kangnung along the eastern slope toward Mt Taegulyang is recycled toward Kangnung again in the evening.

Also, PM directed from Wonju located upwind toward Kangnung contributes significantly to the occurrence of the secondary PM maximum. The densities of the particle size distributions, regardless of the particle diameter, were generally much lower in the early morning than in the afternoon or at night.

Acknowledgments

The first author (H.Choi) thanks the Gangwon Meteorological Administration Office located in Kangnung city for allowing measurement of aerosols for the total period from February 5 to April 5, 2005. Mr. Jung Un Ahn of the Korean Branch Company of GRIMM and Mr. Sang Kook Kim, Mr. Nam Won Kim, Mr. Koo Hee Chou of the Gangwon Meteorological Administration Office are also thanked for installing and maintaining the aerosol samplers. This work was supported by the Korea Research Foundation Grant funded by the Korean Government (MOEHRD,

Basic Research Promotion Fund) (KRF-2006-C0044)—“Relation between PM₁, PM_{2.5} and PM₁₀ concentrations and atmospheric boundary layer in the mountain and coast before and after Yellow Dust event” in 2006–2007.

References

1. H. K. Kim and M. Y. Kim, *Atmos. Environ.* **51** (2003) 707.
2. H. Kim, Y. Kang and S. Shim, *J. Geophys. Res.* **102** (1997) 6047.
3. K. W. Kim, Y. J. Kim and S. J. Oh, *Atmos. Environ.* **35** (2001) 5157.
4. L. Xu, G. Shi, J. Zhou and Y. Iwasaka, *China Particulol.* **2** (2004) 256.
5. Y. Gao and J. R. Anderson, *J. Geophys. Res.* **106** (2001) 18037.
6. P. R. Adby and M. A. H. Demster, *Introduction to Optimization Methods* (Chapman & Hall, London, 1974).
7. P. C. Hansen, *SIAM Rev.* **304** (1992) 561.
8. P. C. Hansen and D. C. O’leary, *SIAM J. Sci. Comput.* **14** (1993) 1487.
9. D. E. Goldberg, *Genetic Algorithms in Search, Optimization and Machine Learning* (Addison-Wesley, Massachusetts, 1989).
10. Z. Michalewicz, *Genetic Algorithms + Data Structure = Evolution Programmes* (Springer-Verlag, Berlin, 1996).
11. G. R. Carmichael, M. S. Hong, H. Ueda, L. L. Chen, K. Murano, J. K. Park, H. Lee, Y. Kim, C. Kang and S. Shim, *J. Geophys. Res.* **102** (1997) 6047.
12. J. Xuan and I. N. Sokolik, *Atmos. Environ.* **36** (2002) 4863.
13. H. Choi, *Meteorol. & Atmos. Phys.* **87** (2004) 93.
14. H. Choi, H. W. Zhang and J. Takahashi, *Meteorol. & Atmos. Phys.* **87** (2004) 109.
15. H. Choi and M. S. Speer, *Meteorol. & Atmos. Phys.* **92** (2006) 239.
16. WREO, *Environmental Monitoring Site of Wonju City* (Wonju Regional Environmental Office, Ministry of Environment, 2005).

SEASONAL VARIATION CHARACTERISTICS OF GRADIENT OF REFRACTIVITY OVER A HUMID REGION OF INDIA

S. Duttagupta

*Institute of Radio Physics & Electronics
92, Acharya Prafulla Chandra Road
Kolkata-700009, India
sukla_dg@yahoo.co.in*

The radio wave propagation, which is largely affected by the meteorological parameters, undergo refractive effect due to the variation of refractive index in the atmosphere. This results in changing of direction of the signal or fluctuation in the angle-of-arrival of the beam, thus defocusing it at the receiving end. Hence, to a large extent, the refractive index gradient of the atmosphere, if it departs from the normal lapse rate, is responsible for degradation of microwave signal. The necessity thus arises to determine the characteristic features of the gradient of refractivity at different heights of the near environment. A yearlong study through radiosonde observations determines the existence of such situations during the two extreme climatic conditions prevailing at Kolkata, India, both at sunrise and sunset periods.

1. Introduction

Radio wave propagation under 10 GHz frequency band, used at present for line-of-sight communication, are affected mainly by the irregularities in the refractive index of the atmosphere. The transmitted signal do not follow a straight path, but gets curved due to refraction. If the change of the refractive index with height is less negative than normal, it is termed as sub-refraction. Here, the transmitted ray propagates with a smaller curvature. Whereas, for a refractive index gradient more negative than normal (super-refraction), the ray will then propagate with a much larger curvature. In both these situations the radio signal will undergo defocusing at the receiving terminal and the signal strength shall be subject to fading.^{1,2} A much higher negative refractive gradient, i.e., for dN/dH value exceeding -157 (where ' N ' is the atmospheric refractive index and

' H ' is the vertical height) creates a situation where the radio signal do not reach the receiving antenna at all. Such a meteorological circumstance is known as "ducting," which degrades the signal strength to a large extent.

In a particular location the value of the radio refractive index (RRI) gradient (dN/dH) varies slowly with the season and also during the time of a day.³ This paper encompasses a refractivity gradient profile for the two seasons — summer and winter and the diurnal pattern of dN/dH at a humid location of India. The presence of ducting condition is also determined. The exercise of calculating dN/dH for different seasons and time of the day is necessary to realize the amount of Fresnel zone clearance of any tall structure, either natural or manmade, situated in the pathway of various hops in the vicinity of the area under study. A semi-empirical climatology model to predict the positive refractivity gradient was first done in the USA.⁴ Later, publications on sub-refractive models were also received.⁵

2. Determination of dN/dH

The refractivity of the troposphere is a function of the atmospheric pressure, temperature, and water vapor pressure.⁶

Mathematically, it is represented as,

$$N = 77.7 \frac{P}{T} + 3.73 \times 10^5 \times \left(\frac{e}{T^2} \right)$$

where P is the atmospheric pressure in mbar, T the atmospheric temperature in Kelvin, and e is the water vapor pressure in mbar.

Radiosonde observations taken at Kolkata, India (lat. 22°N; long. 88° E), are utilized to build the refractivity profile. Data for the month of January 2004 are taken at 0:00 GMT (average surface temperature being 287.2 K) and at 12:00 GMT (average surface temperature is 294.7 K) and the RRI are computed. Profiles at surface (height: 4 m) and at elevated heights of 120 and 800 m are plotted and presented in Fig. 1. Similar exercise is conducted for the month of May of the same year for the morning period (average temperature 301.2 K) and in the evening (average temperature 307.5 K). A characteristic graph of the summer RRI is shown in Fig. 2. The RRI gradient (dN/dH) is then determined for various heights from the above two profiles.

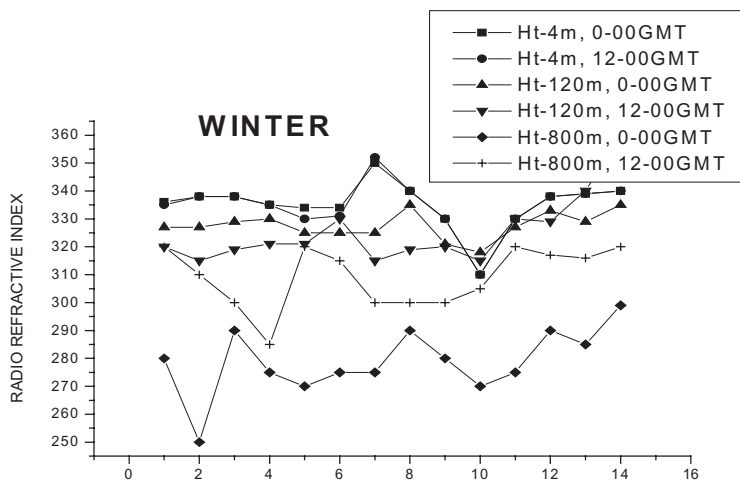


Fig. 1. Radio refractive index profile of winter season.

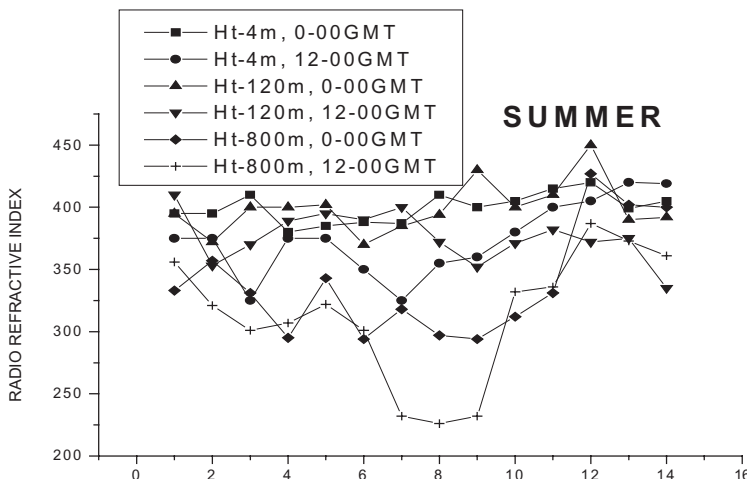


Fig. 2. Radio refractive index profile of summer season.

The gradient of radio refractivity is classified into three broad categories:

1. *Normal refraction*: when dN/dH lies between -40 and -80 .
2. *Sub-refraction*: when dN/dH is greater than -40 .
3. *Super-refraction*: when dN/dH is smaller than -80 .

An extreme case of super-refraction exists when dN/dH has a value more negative than -157 . This condition is called “ducting.”

3. Results

3.1. Season: winter, height: 4–120 m, Time: 0:00 GMT

Figure 3 depicts the refractive index gradient profile in the early hours of winter season at surface to 120 m height level. It is seen here that 58% of the total events has normal refractive atmosphere. In comparison with super-refractive situation (only 10% in this case), sub-refractive condition is more prevailing (31%).

3.2. Season: winter, height: 4–120 m, time: 12:00 GMT

In the evening time observations, with respect to 0:00 GMT, the percentage of $dN/dH < -80$ goes up (19%) whereas the $dN/dH > -40$ comes down (23%) as seen in Fig. 4. The normal refractive gradient remains high at 57%.

3.3. Season: winter height: 120–800 m, time: 0:00 GMT

At higher altitude the atmosphere is much more in the normal state as far as dN/dH is concerned (Fig. 5). Here the normal refraction is observed

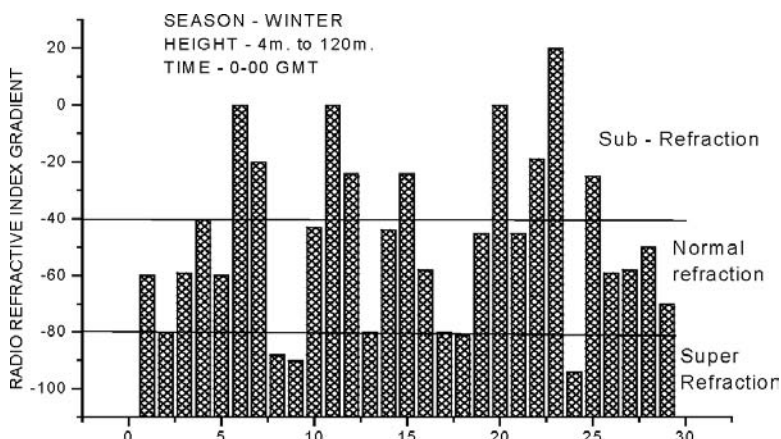


Fig. 3. Ground-based RRI gradient for winter at 0:00 GMT.

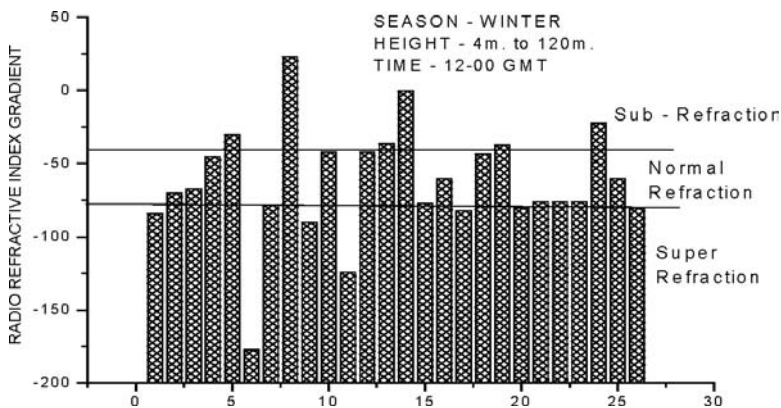


Fig. 4. Ground-based RRI gradient for Winter at 12:00 GMT.

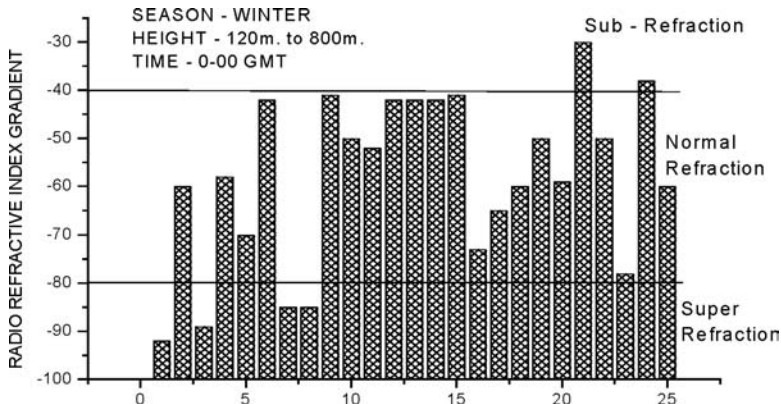


Fig. 5. Elevated RRI gradient for winter at 0:00 GMT.

for 76% of the total time. Sub-refractive phenomenon is very less (8%) as compared to super-refraction, which is slightly higher (16%).

3.4. Season: winter, height: 120–800 m, time: 12:00 GMT

In the 12:00 GMT observations, the winter month at elevated height has a refractive gradient profile similar to that of morning hours. dN/dH normal predominates (76%) over sub-refractive (16%) and super-refractive (8%) as referred in Fig. 6.

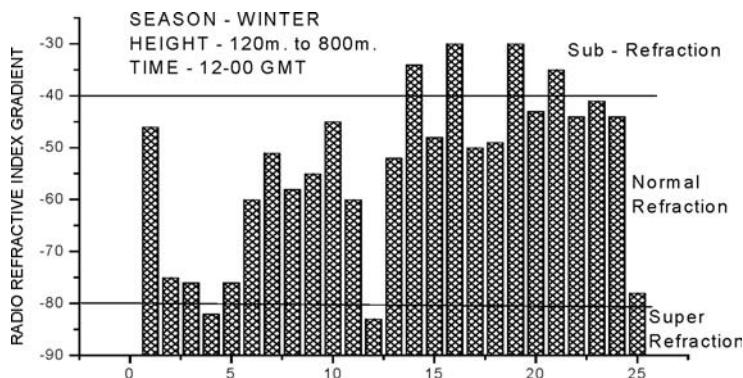


Fig. 6. Elevated RRI gradient for winter at 12:00 GMT.

3.5. Season: summer, height: 4–120 m, time: 0:00 GMT

Figure 7 shows the 0:00 GMT, summer month, ground level refractivity gradient pattern. The atmosphere is different from that observed in winter. A sub-refractive condition prevails almost half of the total time of observation (46%). Equal number of days of normal and super-refraction are also seen (both 27%).

3.6. Season: summer, height: 4–120 m, time: 12:00 GMT

In the sunset period (Fig. 8), the $dN/dH > -40$ situation slowly diminishes, paving the way for a normal refractive (41%) and super-refractive (45%) conditions.

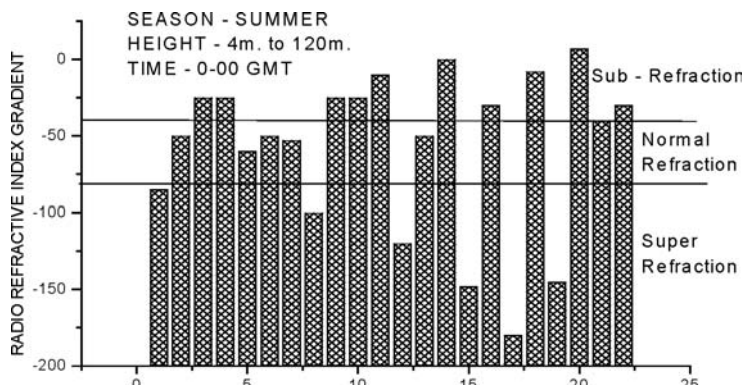


Fig. 7. Ground-based RRI gradient for summer at 0:00 GMT.

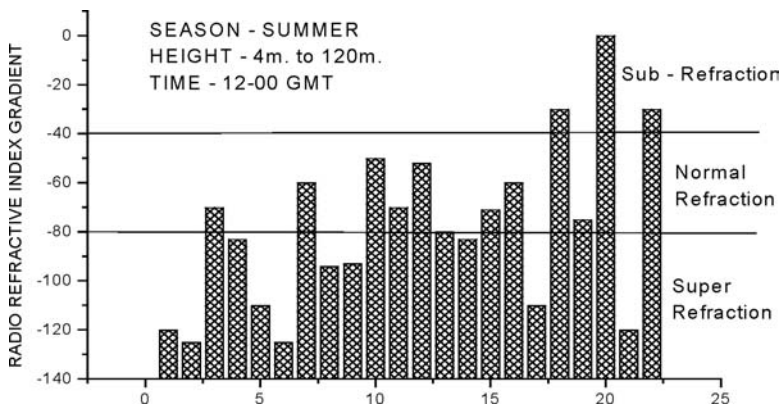


Fig. 8. Ground-based RRI gradient for summer at 12:00 GMT.

3.7. Season: summer, height: 120–800 m, time: 0:00 GMT

In the morning of summer month, at 120–800 m height slab, the refractivity remains more in the $dN/dH < -80$ state (50%). The sub-refractive state is slightly lower (21%) than the normal (29%), as presented in Fig. 9.

3.8. Season: summer, height: 120–800 m, time: 12:00 GMT

As the day progresses, the atmosphere undergoes changes and is more in the normal state (55%), and least in the super-refractive state (16%).

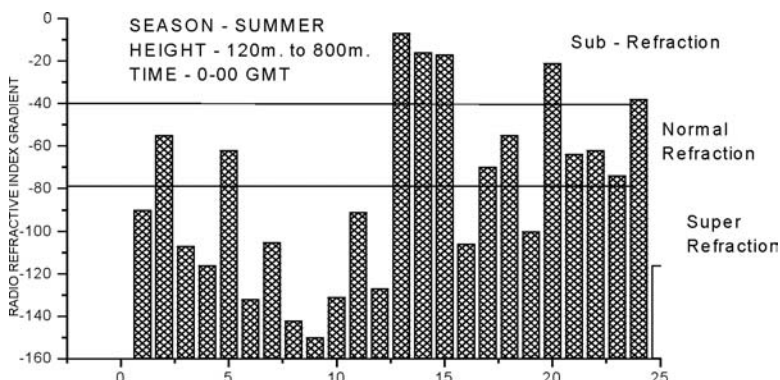


Fig. 9. Elevated RRI gradient for summer at 0:00 GMT.

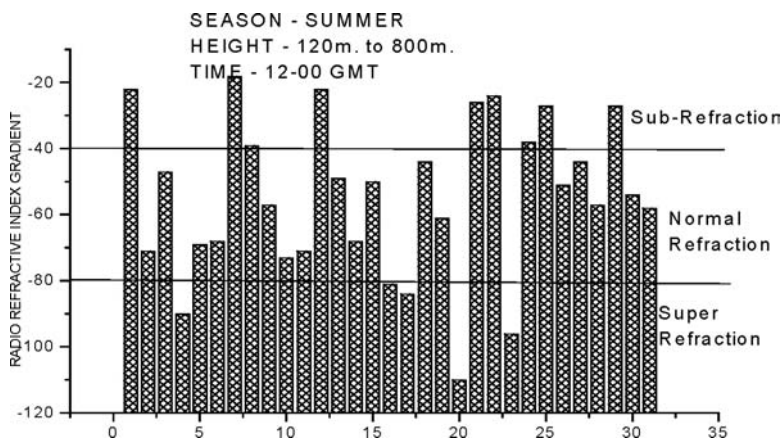


Fig. 10. Elevated RRI gradient for summer at 12:00 GMT.

From Fig. 10, it is seen that about 29% of the time shows sub-refractive atmosphere.

3.9. Ducting condition

Ducting, though a rare atmospheric phenomenon, is nevertheless observed about 4% of the total period under study. The probability of occurrence of ducting is more at the surface in the early morning hours (50%) of the total ducting time. An equal probability of occurrence of ducting is found to be present at the near surface environment in the evening hours (25%) and in the morning hours of higher altitude (25%). No such event is detected in the upper level of 12:00 GMT study. From the seasonal point of view, it is seen that ducting is more probable in summer (75%) than in winter (25%).

4. Discussion and Conclusion

Irrespective of the height or time, the winter season has an atmosphere with predominantly normal refractive index gradient. Conversely, the atmosphere in summer is rather complex. In summer, in the morning period the lower atmosphere has $dN/dH > -40$ in most of the cases, whereas the upper level tends to become super-refractive. The super-refractive environment is also observed at the surface in the evening period of summer observations.

The summer months experience thermal instabilities that result in the formation of planetary boundary layers (PBL) as convection of air takes place.⁷ Due to convective air mixing, the PBL, which occurs in the morning hours, subsides as the evening approaches. The sub-refractive and the super-refractive behavior of the air may be associated with the development and disintegration of PBL in the hot summer season.

Acknowledgments

The author thanks the Department of Science & Technology, Government of India for providing financial support to carry out this research project. The author also thanks The Indian Meteorological Department, Alipore and The British Atmospheric Data Center for providing the necessary atmospheric data, which encompasses this paper.

References

1. J. A. Schiavone, *Symp. IEEE Conf.* 3 (1982), 7B.1.1.
2. A. R. Webster, *IEEE Trans. Antennas Propagation* AP31(1) (1983) 12.
3. S. Sen, *Microwave Propagation Characteristics Under Sub-tropical Environment*, PhD Thesis, 1999.
4. J. A. Schiavone, *Bell Sys. Tech. J.* 60 (1957) 803.
5. R. A. Harvey, *IEEE, Trans antenna propagation* (1987) 832.
6. B. R. Bean and E. J. Dutton, *Radio Meteorology* (Natl. Bur. Stand Monograph, USA (1966), p. 423.
7. H. S. Somal *et al*, *Indian J. Radio phys.* 10 (1981) 137.